





Understanding the behaviour of group V transition metal dichalcogenides for electrocatalysis

Boruch Zadok Epstein

Linacre College

University of Oxford

A thesis submitted for the degree of Doctor of Philosophy in Materials

Trinity 2026

Front Matter

Acknowledgements

I would like to thank all those who have contributed in many ways, major or minor, to this thesis.

To my supervisors Rob Weatherup and Rebecca Nicholls, thank you for your advice, patience and effort. Thank you for your guidance and for the opportunity to pursue this DPhil.

To the other members, current and former of the Weatherup and Nicholls groups. To Jack Swallow and Joshua Gibson, for your mentorship in the early days, and to Leanne, for the electrochemistry advice and help. Namrata Ramesh, for the essential computational advice and Soumyajit Maitra, whom, without our discussions, this thesis would have been much smaller and less interesting. It would be remiss of me not to mention Erik Björklund and Peixi Cong, whose advice on XAS and XPS was invaluable, and of course Longxiang Liu, who along with Leanne and Soumyajit sacrificed time and sleep on my beamtime experiments. Finally, I would like to thank Conor Phelan, who has always been available for an urgent question.

I am grateful for the support of the Engineering and Physical Sciences Research Council (EPSRC) for the funding that allowed me to pursue this degree.

For all that the scientific mentorship, conversation and help was essential, it would not have been possible to reach this point without my parents, to whom I am eternally grateful. To my friends in Oxford, who provided support in the most trying of times, and to the Oxford Chabad, who provided a home away from home, thank you.

Declaration

This thesis is submitted to fulfil the requirements for the degree of Doctor of Philosophy in the Department of Materials at the University of Oxford. I declare that this thesis has not been submitted, in whole or in part, in any previous application for a degree. I declare that, except where specific reference is made to the work of others, or explicit acknowledgement is given, the contents of this dissertation are the results of my own work, and this thesis contains fewer than 40,000 words.

Publication Record

Shalom, B.-O.; Andrés, M. A.; Head, A. R.; Epstein, B. Z.; Brontvein, O.; Pérez-Dieste, V.; Villar-Garcia, I. J.; Walton, A. S.; Polus, K.; Weatherup, R. S.; Eren, B. Chemical State of Nickel Nanoparticles during the Oxygen Evolution Reaction in a Carbonate-Bicarbonate Buffer Solution. *CR-PHYS-SC* **2024**, *5* (9). https://doi.org/10.1016/j.xcrp.2024.102165.

Statement of Authorship

In the appendix, the EDX spectrum was gathered by Soumyajit Maitra under the supervision of Rob Weatherup and Sebastian Bonilla.

Abstract

Transition metal dichalcogenides (TMDCs) are a class of materials that have attracted great interest as electrocatalysts, particularly for the hydrogen evolution reaction but additionally for reactions like the carbon dioxide reduction reaction. A wide range of possible material modifications, such as doping, creating defects, and phase modification are applicable to these materials, however, testing them all in a laboratory is not practicable. To modify these materials in a predictable manner, the computational electronic structure must be experimentally related to the catalytic activity of the materials, and the performance and behaviour of these materials accurately characterised.

To this end, group V TMDCs have attracted great interest, since their basal planes are active and suitable for probing via spectroscopies. The active basal plane also allows a high surface area for higher catalytic activity. However, gaps in our understanding of the behaviour of these materials currently preclude their targeted modification outside of a narrow range of well understood effects.

This thesis attempts to fill in essential lacunae of our understanding of the group V TMDCs. To this end, 2H-NbS_2, 3R-NbS_2, 2H-TaS_2 and 1T-TaS_2 were synthesised as large crystals and powders, while 1T-VS_2 was synthesised as a powder. Raman and XPS spectroscopy established that the crystals readily oxidise on their edges and basal planes. This has consequences for how the performance of these materials are tested and modelled, with the oxides likely contributing to the catalytic activity of the materials.

The specific capacitances of 2H-NbS_2, 3R-NbS_2, 2H-TaS_2 and 1T-TaS_2 were established, and the electrocatalytic performance of the pristine materials was reported using these values. It was found that the specific capacitance and exchange current density were possible empirical

descriptors for catalytic activity to the HER and that adjusting the performance for electrochemical surface area led to substantial differences in reported performance.

Finally, the structural and chemical changes of the group V TMDCs when subjected to strongly reducing potentials (≤ -0.7 V vs RHE) were elucidated. The cause of this structural change was proposed to be a result of hydrogen gas bubbles forming between the material layers. The extent of metal intercalation between the TMDC layers and the electrocatalytic performance of the materials was proposed as an explanation for the different behaviours of the materials, with 3R-NbS_2 and 1T-TaS_2 undergoing no notable changes.

Contents

Front Matter 2

Declaration 3

Publication Record 4

Statement of Authorship 5

Abstract 6

Contents 8

List of Abbreviations 14

Chapter 1. Introduction 16

1.1 Introduction to electrocatalysis 16

1.1.1 Capacitance 20

1.2 The Hydrogen evolution reaction (HER) 20

1.3 References 22

Chapter 2. Background 25

2.0 Abstract 25

2.1 Transition Metal Dichalcogenides (TMDCs) 25

2.2 Design of TMDCs 28

2.2.1 Improving TMDC activity for electrocatalysis 28

2.2.2 Rational design 29

2.2.3 Catalytic Descriptors 30

2.3 Group V TMDCs 31

2.3.1 Vanadium Disulfide 32
2.3.2 Niobium Disulfide 33
2.3.3 Tantalum Disulfide 34
2.3.4 Constructing descriptors for group V TMDCs 34
2.4 Thesis outline 36
2.5 References 37
Chapter 3. Experimental Methods 48
3.1 Spectroscopies and XRD 48
3.1.1 X-ray photoelectron spectroscopy 48
3.1.2 X-ray absorption spectroscopy 53
3.1.3 X-Ray Diffraction 55
3.1.4 Raman spectroscopy 57
3.2 Electrochemical methods 62
3.2.1 The electrochemical cell 62
3.2.2 Linear sweep voltammetry, cyclic voltammetry and series chronoamperometry 64
3.2.3 Electrochemical Impedance spectroscopy 66
3.2.4 Electrochemical procedure 71
3.3 Synthesis methods 72
3.3.1 Introduction to Chemical vapour transport 72
3.3.2 Solid-state (powder) synthesis methods 73
3.3.3 CVT methods 74

3.3.4 Hydrothermal synthesis 75

3.4 References 76

Chapter 4. Computational Methods 80

4.0 Introduction 80

4.1 Methodology 80

4.1.1 The Schrödinger equation and atomic systems 80

4.1.2 Density Functional Theory 81

4.1.3 Dispersion interactions 84

4.1.4 Plane-wave cutoff and k-point spacing. 84

4.1.5 Pseudopotentials 85

4.1.6 Density functional perturbation theory 85

4.2 Calculations 86

4.2.1 1T-VS_2 87

4.2.2 NbS_2 92

4.2.3 TaS_2 94

4.3 References 97

Chapter 5. Synthesis and characterisation of large crystal group V TMDCs 101

5.0 Abstract 101

5.1 Introduction 101

5.2. Synthesis of large group V transition metal chalcogenide crystals 102

5.2.1 3R-NbS_2 synthesis and characterisation 103

5.2.2 2H-TaS_2 synthesis and characterisation 107

5.2.3 2H-NbS_2 synthesis and characterisation 110

5.2.4 1T-TaS_2 synthesis and characterisation 114

5.3. Understanding the spectroscopy of group V TMDC crystals 117

5.4 Conclusion 126

5.5 References 126

Chapter 6. Capacitance, catalysis and electronic structure of the group V TMDCs 131

6.0 Abstract 131

6.1 Introduction 131

6.2 Theoretical Work 134

6.3 Understanding the performance of pristine materials 137

6.3.1 Obtaining the surface area of powdered samples 137

6.3.2 Catalytic performance 142

6.4 Obtaining Specific Capacitance using large crystals 145

6.5 Capacitance and material performance 152

6.5.1 Specific capacitance and activity 152

6.5.2 Pristine material performance with specific capacitance 155

6.6 Use of scan rate cyclic voltammetry for determination of ECSA 158

6.7 Conclusion 161

6.8 References 162

Chapter 7. The behaviour of group V TMDCs under extreme potentials 170

7.0. Abstract 170

7.1 Introduction 170

7.2 Physical observations and Raman spectroscopy 172

7.2.1 Physical observations 172

7.2.2 Raman spectroscopy 173

7.3 X-ray spectroscopy of HNP materials 180

7.3.1 XPS of Ta and Nb in TaS_2 and NbS_2 180

7.3.2 XPS of Sulfur in TaS_2 and NbS_2 184

7.3.3 XAS Data 189

7.4 X-Ray diffraction data 190

7.4.0 Methods 190

7.4.1 1T-VS_2 191

7.4.2 TaS_2 193

7.4.3 NbS_2 195

7.5 Discussion 201

7.5.1 The structure and characterisation of HNP 2H-TaS_2 201

7.5.2 The structure and characterisation of HNP 1T-VS_2 203

7.5.3 The structure and characterisation of HNP 2H-NbS_2 204

7.5.4 Towards an understanding of the cause of HNP phase change 207

7.6 A protocol for detecting thin film VS_2 210

7.7 Conclusion 211

7.8 References 212

Chapter 8. Summary and Future work 218

8.1 Summary 218

8.2 Future work 220

Appendix. Synthesis and characterisation of VS_2 222

A.0 Abstract 222

A.1 Introduction 222

A.2. Understanding the Raman spectroscopy of vanadium disulfide 223

A.2.1 Synthesis of VS_2 related vanadium sulfides. 223

A.2.2 Predicted VS_2 Raman spectrum and the Raman response of VS_2 226

A.2.3 Understanding reported Raman spectra for VS_2 229

A.3 Improving VS_2 yields in the hydrothermal method. 230

A.3.1 C276 and the role of reactor vessel walls 230

A.3.2 Improving hydrothermal VS_2 crystallinity and purity 234

A.4 Conclusion 236

A.5 References 237

List of Abbreviations

TMDC Transition Metal Dichalcogenide

a.u. Arbitrary units

HER Hydrogen Evolution Reaction

CO_2RR Carbon dioxide Reduction Reaction

CDW Charge Density Wave

XAS X-ray absorption spectroscopy

XPS X-ray photoelectron spectroscopy

XRD X-ray diffraction

CV Cyclic Voltammetry

LSV Linear Sweep Voltammetry

EIS Electrochemical impedance spectroscopy

AC Alternating current

CVT Chemical Vapour Transport

APCVD Atmospheric Pressure Chemical Vapour Deposition

DFT Density Functional Theory

GGA Generalised Gradient Approximation

DFPT density functional perturbation theory

ECSA Electrochemical surface area

SEM scanning electron microscopy.

BET Brunauer-Emmett-Teller gas sorption area analysis

C_s specific capacitance (by area)

CPE Constant Phase Element

RHE reversible hydrogen electrode

HNP High/Strong negative potential (≤ -0.7 V vs RHE)

OCP Open circuit potential

Chapter 1. Introduction

1.1 Introduction to electrocatalysis

An electrochemical system, typically contained in a cell, can in the simplest cases be defined as the sum of two half-cell reactions. For the splitting of water, this is the production of hydrogen and oxygen, for which the overall cell reaction is:

$$2H_2O \rightarrow 2H_2 + O_2 \qquad (1-1)$$

This overall reaction is the sum of two separate half-cell reactions, each of which takes place at a different electrode[1]. In an acidic solution, this gives the half-cell reactions:

$$2H_3O^+ + 2e^- \rightarrow H_2 + 2H_2O \qquad (1-2)$$

$$6H_2O \rightarrow O_2 + 4e^- + 4H_3O^+ \qquad (1-3)$$

H_3O^+ is used as a shorthand to represent the protons dissolved in the solution[1]. The Gibbs free energy change of the system is related by the equation:

$$\Delta G = -nFE \qquad (1-4)$$

Where ΔG is the Gibbs free energy change, n is the number of electrons transferred in the reaction, F the Faraday constant and E the cell potential, or electromotive force (emf). E is expressed in volts, (V), and corresponds to the difference between the electrostatic potentials of the two electrodes. The potential of an electrode cannot be measured independently and must be measured relative to another electrode[1].

By convention, the standard hydrogen electrode is chosen as the reference, with a potential of 0 V under standard conditions, and is expressed by:

$$2H^+ + 2e^- \leftrightharpoons H_2 \qquad (1-5)$$

When at non-standard conditions, this is called the RHE, or reversible hydrogen electrode. The potential of the RHE depends on the pH of the solution in a well-defined manner[1].

For equations 1-2 and 1-3, the electrode potentials are 0 V and 1.23 V [2] respectively, leading to an overall cell *E* of -1.23 V. The *ΔG* is positive for this reaction, and therefore the overall reaction is not spontaneous. Spontaneous electrochemical cells are classed as galvanic cells, while non-spontaneous cells are classed as electrolytic cells. The application of an electrical voltage by a power supply to the electrolytic cell shifts the reaction *ΔG* and allows the reaction to occur[1].

For a one-electron transfer:

$$X_{(aq)} + e^-_{(metal)} \leftrightharpoons Y_{(aq)} \qquad (1-6)$$

The net electrical current can be quantified as:

$$I = FAj \qquad (1-7)$$

Where *I* is the current, *F* the Faraday constant, *A* is the area of the electrode, and *j* the reaction flux:

$$j = k_{red}c_{X,0} - k_{ox}c_{Y,0} \qquad (1-8)$$

Where *k* is the rate constant for the reactions and *c* is the concentration of the species. The Arrhenius equation and transition state theory allows them to be defined as:

$$k_n = A_n \exp\left(-\frac{\Delta G_n^{\ddagger}}{RT}\right) \qquad (1-9)$$

where $\Delta G_n^{\ddagger}$ is the Gibbs free energy of activation for the reaction and A_n is the pre-exponential factor for oxidation or reduction (*n*). This, at fixed temperature and pressure is in turn defined as:

$$\Delta G_{red}^{\ddagger} = \Delta G_{red}^{0,\ddagger} + \alpha F\left(E - E_f^0\right) \qquad (1-10a)$$

$$\Delta G_{ox}^{\ddagger} = \Delta G_{ox}^{0,\ddagger} - (1-\alpha) F\left(E - E_f^0\right) \qquad (1-10b)$$

Where $\Delta G_0^{\ddagger}$ is the standard Gibbs activation energy, E is the applied potential and E_f^0 the formal potential[1]. The term α represents the transfer coefficients for the reactions, which in a one-electron transfer process sums to one. The transfer coefficient represents the nature of the transition state as compared to the final state. Values of α close to 0 or 1 indicate a highly asymmetric transition state, resembling one side of the reaction (product, reactant) more strongly than the other[1].

Substituting eq. (1-10) into eq. (1-9) and defining the standard electrochemical rate constant as:

$$k^0 = A_n \exp\left(-\frac{\Delta G_n^{0,\ddagger}}{RT}\right) \qquad (1-11)$$

Allows the construction of the equations

$$k_{red} = k^0 \exp\left(-\frac{\alpha F\left(E - E_f^0\right)}{RT}\right) \qquad (1-12a)$$

$$k_{ox} = k^0 \exp\left(\frac{(1-\alpha) F\left(E - E_f^0\right)}{RT}\right) \qquad (1-12b)$$

Defining α_X as the transfer coefficient for the reactant, and α_Y as the transfer coefficient for products ($\alpha_X+\alpha_Y=1$), while substituting eq. (1-12) back into eq. (1-8) yields the Butler-Volmer equation[1]:

$$j = k^0 c_X \exp\left(-\frac{\alpha_X F\left(E - E_f^0\right)}{RT}\right) - k^0 c_Y \exp\left(\frac{\alpha_Y F\left(E - E_f^0\right)}{RT}\right) \qquad (1-13)$$

In a typical electrochemical cell, sufficient electrolyte is present so that the concentrations of both product and reactant do not significantly change. This is particularly true of the HER and

OER, where the reactant is the solution, and the product evolves as a gas. By assuming that concentrations do not vary and one part of the Butler-Volmer equation dominates (e.g. the reactants), the Tafel law can be derived as a special case of the Butler-Volmer equation, whereby:

$$\ln|I| = -\frac{\alpha F \eta}{RT} + c \qquad (1-14)$$

Where I is the observed current, η is the overpotential ($E - E_f^0$), and α is the transfer coefficient for the reaction[1]. Since α can be extracted from the equation, the Tafel law allows us to reconstruct information about the kinetics of the electrochemical reaction[1].

In the practical electrochemistry literature, the Tafel law is more commonly constructed as the Tafel equation[3]:

$$\eta = A \log_{10} \frac{i}{i_0} \qquad (1-15)$$

Where η is the overpotential, A is the Tafel slope, i is the current density and i_0 is the exchange current density. In the hydrogen evolution reaction (HER), information about reaction thermodynamics can also be extracted from the exchange current density[4,5].

An additional special case of the Butler-Volmer equation applies at electrochemical equilibrium:

$$E = E_f^0 + \frac{RT}{nF} \ln\left(\frac{C_X}{C_Y}\right) \qquad (1-16)$$

This is the Nernst equation, where E is the cell potential, E_f^0 the formal potential, which accounts for species chemical potential and can be measured, and C, the concentrations of the reactants (C_X) and products (C_Y)[1].

1.1.1 Capacitance

Not all sources of measured current are due to chemical reactions. A given electrode-solution interface will have an electrochemical double-layer capacitance, typically just called double-layer capacitance within the electrocatalysis literature[5,6]. This is a result of a potential difference between the surface of the electrode compared to the electrolyte, causing the concentration of opposite-charge species near the surface of the electrode to increase. This leads to the formation of several layers of charged species[1,5]. The Helmholtz layer consists of ions or molecules that are specifically adsorbed. Solvated ions cannot get as close to the electrode and form the Outer-Helmholtz Plane (OHP) and diffuse layer[1,5]. The extent of the OHP depends on the difference in charge between the electrode and electrolyte, with greater differences in charge generally leading to more extensive OHP and therefore capacitance[1]. This relationship is not always linear however, and extensive charging can lead to ion crowding, which reduces the charge gained for a given potential change[1].

1.2 The Hydrogen evolution reaction (HER)

Of interest in this thesis is the hydrogen evolution reaction. Hydrogen sees extensive use as a chemical feedstock, seeing use in oil refining, ammonia production for fertiliser and as a reducing gas in metallurgy[8]. Hydrogen also has potential as a portable fuel source, with the highest chemical specific energy of any material, at 140 MJ kg^{-1} [9]. This gives it great potential for the transport industry, which as of 2010 accounted for 19% of the world's energy[10], aided by the fact that it releases energy easily and cleanly, either via fuel cells, or via combustion[10]. Hydrogen also has the potential to be used as an admixture in domestic and industrial natural gas supply, with both studies and small-scale trials having been conducted to test its use in this role[8].

Hydrogen is currently produced via fossil fuels, using natural gas and coal, responsible for CO_2 emissions of up to 830 Mt/year[11]. These emissions drive research to produce hydrogen via cleaner means.

One such method is the clean production of hydrogen by splitting water via electrolysis[12]. This proceeds via two reactions; the oxygen evolution reaction, which takes place at the anode, and the hydrogen evolution reaction, which takes place at the cathode[13]. These reactions are inefficient, with an overpotential of 0.7-1.0 V required in simple industrial electrolysers (typically under alkaline conditions)[13]. Consequently, catalysts are required to reduce these inefficiencies, lowering the required overpotentials. The hydrogen evolution reaction also serves as an ideal "model" electrocatalysis reaction, with limited mass transport issues[14] and simple, easily modelled experimental descriptors, namely the energy of adsorption of hydrogen onto the catalyst surface[15]. Understanding the HER on a given surface can allow for the deconvolution of factors contributing to more complex electrochemical reactions.

The catalytic HER may take place under acid or alkaline conditions. This thesis is interested in the HER under acidic conditions, which proceeds via one of two mechanisms, the Volmer-Heyrovsky or Volmer-Tafel mechanism[16], outlined in Figure 1 below. Each mechanism has a characteristic Tafel slope. These are 30 mV/dec for Volmer-Tafel mechanism, 40 mV/dec for the Volmer-Heyrovsky mechanism, and 120 mV/dec if limited by the Volmer step[16]. This in turn provides information about the characteristics of the catalyst. This information can be convoluted with other effects but provides useful information about the performance of a catalyst[17].

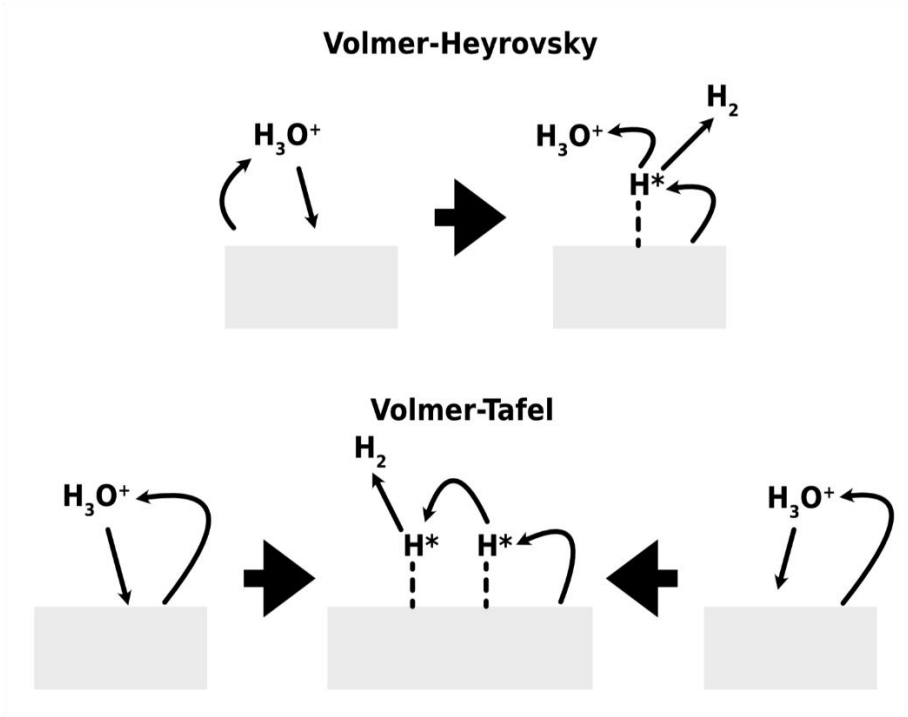


Figure 1. The two mechanisms for the hydrogen evolution reaction in an acidic medium. In the Volmer-Heyrovsky mechanism, a hydrogen atom is adsorbed (Volmer step). Subsequently, the adsorbed hydrogen bonds with an incident hydrogen to form hydrogen gas. In the Volmer-Tafel mechanism, two hydrogens are adsorbed near each other. The adsorbed hydrogen atoms react with each other to form hydrogen gas.

1.3 References

(1) Bard, A. J.; Faulkner, L. R.; White, H. S. *Electrochemical Methods: Fundamentals and Applications*; John Wiley & Sons, 2022.

(2) Jones, T. E.; Teschner, D.; Piccinin, S. Toward Realistic Models of the Electrocatalytic Oxygen Evolution Reaction. *Chem. Rev.* **2024**, *124* (15), 9136–9223. https://doi.org/10.1021/acs.chemrev.4c00171.

(3) van der Heijden, O.; Park, S.; Vos, R. E.; Eggebeen, J. J. J.; Koper, M. T. M. Tafel Slope Plot as a Tool to Analyze Electrocatalytic Reactions. *ACS Energy Lett.* **2024**, *9* (4), 1871–1879. https://doi.org/10.1021/acsenergylett.4c00266.

(4) Yang, T. T.; Patil, R. B.; McKone, J. R.; Saidi, W. A. Revisiting Trends in the Exchange Current for Hydrogen Evolution. *Catal. Sci. Technol.* **2021**, *11* (20), 6832–6838. https://doi.org/10.1039/D1CY01170G.

(5) Wu, J. Understanding the Electric Double-Layer Structure, Capacitance, and Charging Dynamics. *Chemical Reviews* **2022**, *122* (12), 10821–10859. https://doi.org/10.1021/acs.chemrev.2c00097.

(6) Wei, Z.; Elliott, J. D.; Papaderakis, A. A.; Dryfe, R. A. W.; Carbone, P. Relation between Double Layer Structure, Capacitance, and Surface Tension in Electrowetting of Graphene and Aqueous Electrolytes. *J Am Chem Soc* **2024**, *146* (1), 760–772. https://doi.org/10.1021/jacs.3c10814.

(7) Nørskov, J. K.; Bligaard, T.; Logadottir, A.; Kitchin, J. R.; Chen, J. G.; Pandelov, S.; Stimming, U. Trends in the Exchange Current for Hydrogen Evolution. *J. Electrochem. Soc.* **2005**, *152* (3), J23. https://doi.org/10.1149/1.1856988.

(8) Bullock, M.; More, K. *Basic Energy Sciences Roundtable: Foundational Science for Carbon-Neutral Hydrogen Technologies*; 1834317; 2021; 1834317. https://doi.org/10.2172/1834317.

(9) Fu, Q.; Han, J.; Wang, X.; Xu, P.; Yao, T.; Zhong, J.; Zhong, W.; Liu, S.; Gao, T.; Zhang, Z.; Xu, L.; Song, B. 2D Transition Metal Dichalcogenides: Design, Modulation, and Challenges in Electrocatalysis. *Advanced Materials* **2021**, *33* (6). https://doi.org/10.1002/adma.201907818.

(10) Seh, Z. W.; Kibsgaard, J.; Dickens, C. F.; Chorkendorff, I.; Nørskov, J. K.; Jaramillo, T. F. Combining Theory and Experiment in Electrocatalysis: Insights into Materials Design. *Science* **2017**, *355* (6321). https://doi.org/10.1126/science.aad4998.

(11) Fu, X.; Shi, R.; Jiao, S.; Li, M.; Li, Q. Structural Design for Electrocatalytic Water Splitting to Realize Industrial-Scale Deployment: Strategies, Advances, and Perspectives. *Journal of Energy Chemistry* **2022**, *70*, 129–153. https://doi.org/10.1016/j.jechem.2022.02.010.

(12) Chen, X.; Yang, J.; Cao, Y.; Kong, L.; Huang, J. Design Principles for Tungsten Oxide Electrocatalysts for Water Splitting. *ChemElectroChem* **2021**, *8* (23), 4427–4440. https://doi.org/10.1002/celc.202101094.

(13) Xiang, C.; Papadantonakis, K. M.; Lewis, N. S. Principles and Implementations of Electrolysis Systems for Water Splitting. *Materials Horizons* **2016**, *3* (3), 169–173. https://doi.org/10.1039/c6mh00016a.

(14) Anantharaj, S.; Noda, S.; Driess, M.; Menezes, P. W. The Pitfalls of Using Potentiodynamic Polarization Curves for Tafel Analysis in Electrocatalytic Water Splitting. *ACS Energy Letters* **2021**, *6* (4), 1607–1611.

(15) Dubouis, N.; Grimaud, A. The Hydrogen Evolution Reaction: From Material to Interfacial Descriptors. *Chemical Science* **2019**, *10* (40), 9165–9181. https://doi.org/10.1039/C9SC03831K.

(16) Cao, Y. Roadmap and Direction toward High-Performance MoS2 Hydrogen Evolution Catalysts. *ACS Nano* **2021**, *15* (7), 11014–11039. https://doi.org/10.1021/acsnano.1c01879.

(17) Shinagawa, T.; Garcia-Esparza, A. T.; Takanabe, K. Insight on Tafel Slopes from a Microkinetic Analysis of Aqueous Electrocatalysis for Energy Conversion. *Sci Rep* **2015**, *5* (1), 13801. https://doi.org/10.1038/srep13801.

Chapter 2. Background

2.0 Abstract

This chapter introduces the transition metal dichalcogenides (TMDCs) as a class of materials, setting them briefly in their context as catalysts. The chapter then turns to discussing the necessity and application of rational design and descriptors to TMDCs.

The group V TMDCs are introduced and placed in context as a set of materials particularly promising in a catalytic context, as well as being amenable to the construction of descriptors. Lacunae in the current understanding of the catalytic behaviour of group V TMDCs are briefly introduced, after which a thesis outline is provided.

2.1 Transition Metal Dichalcogenides (TMDCs)

Transition Metal Dichalcogenides (TMC/TMD/TMDC), are layered materials whose empirical formula is MX_2, where M is a transition metal and X represents group 16 elements, excluding oxygen. Transition metal dichalcogenides were known of throughout the 20th century, but rose to prominence with the discovery of graphene, and the subsequent exploration of other few- and mono-layered materials[1]. The first few-layer TMDC to be reported was MoS_2, which rose to prominence around 2010[1,2]. While the basal plane of MoS_2 was not found to be reactive, catalytic activity for the MoS_2 edge site with respect to the hydrogen evolution reaction was predicted by Hinnemann et al[3] in 2005 and proven by Jaramillo et al[4] in 2007. Since then, a wide variety of TMDCs have been explored for their catalytic potential towards the hydrogen evolution reaction. These have proven to be of high interest due to various factors. TMDCs can be easily tuned via modification to their electronic structures, such as by alloying[5], intercalation[6] and polymorph selection[7–9]. TMDCs are also easily synthesised in the lab via a variety of methods, such as CVD, CVT, hydrothermal synthesis and high temperature reaction of elements. Some TMDCs (metal sulfides) are also of interest due to their low elemental

component cost[10], as they can be synthesised using inexpensive transition metals and relatively common sulfur and selenium. TMDCs are particularly interesting for electrocatalysis as they maintain chemical stability and good activity towards the HER, comparable at their best to platinum, even at high current densities, enabling their future use in commercial reactors[9,11].

TMDCs can adopt several crystal phases, polymorphs and polytypes. In ideal MX_2 compositions, where M is the metal and X the chalcogenide, the two most common polymorphs are the 1T octahedral and 2H trigonal prismatic[12]. Additionally, there exist distorted versions of these structures, such as the 3R phase, a polytype of the 2H phase (Figure 1) and the 1T' and $1T_d$ polymorphs, which are distorted 1T derived phases[12]. Stoichiometry is not necessarily consistent between polymorphs, often resulting from self-intercalation[13], and intralayer structure may remain the same even while layer stacking changes. Consequently, this thesis uses the term "phase" as a broad descriptor to refer to these different structures. TMDCs can also be split primarily into metallic, semi-metallic and semiconducting materials, of which the 1T and 1T-derived phases often exhibit metallic behaviour[12]. TMDCs have also seen utility in batteries[14], capacitors[15], superconductivity research[16], sensing[17], spin- and opto-electronics[17].

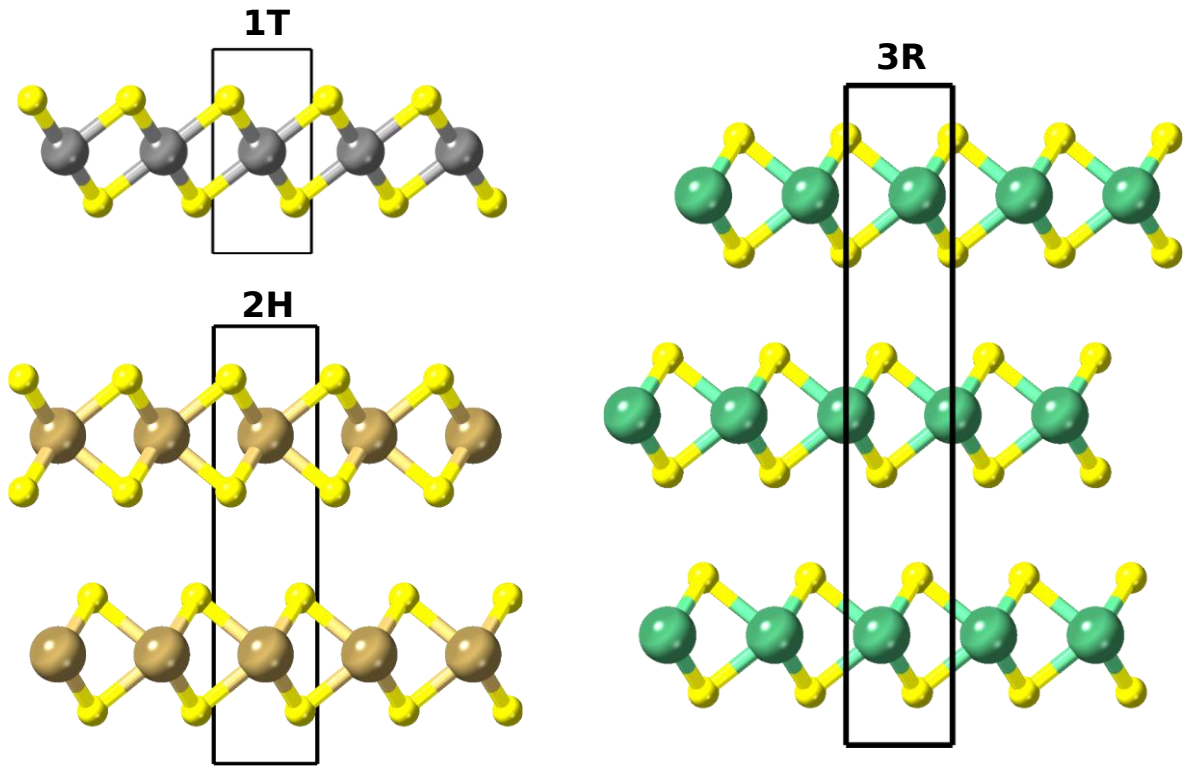


Figure 1. The 1T (shown as 1T-VS_2), 2H (shown as 2H-TaS_2) and 3R (shown as 3R-NbS_2) structures of TMDCs. Structures are viewed along the a axis of the cell, with the primitive unit cell highlighted by a black box. This serves to illustrate the differences between the structures. The 1T primitive unit cell consists of a single octahedral layer, while the 2H trigonal prismatic primitive unit cell is two-layer. The 3R structure is a polytype of the 2H structure, and the primitive unit cell consists of three trigonal prismatic layers. Additional unit cells (un-highlighted) are shown for the reader's benefit. Images were generated using CrystalMaker® from calculated structures (Chapter 4).

In electrocatalysis, TMDCs have shown utility in a variety of reactions. TMDCs have been explored for the carbon dioxide reduction reaction[18] (CO_2RR), the oxygen reduction reaction[19], the nitrate reduction reaction[20] (NO_3RR) and most commonly the hydrogen evolution reaction (HER)[21].

2.2 Design of TMDCs

2.2.1 Improving TMDC activity for electrocatalysis

Throughout the literature exploring the catalytic properties of TMDCs, an ongoing theme is their modification to improve their active site performance[22], permit greater selectivity, such as selectivity towards carbon for the carbon dioxide reduction reaction (CO_2RR)[23], or activate additional sites, such as the basal plane[24]. All of these require the modification of the TMDC electronic structure, and a variety of methods exist to tune the electronic structure of TMDCs. These methods can be divided into a few overarching groups. One option is intercalating the TMDC, where atoms are inserted between the layers of the TMDC[25] to modify its electronic structure. This intercalation may be either a metal[26] or chalcogenide[27].

The electronic structures of TMDCs can also be modified by defect creation[22]. There are a large variety of possible defects, including missing atoms, and atoms added onto the surface of the catalyst (adatoms). It should be noted that not all defect types are stable. Defects can allow for the activation of basal planes and permit for increases in activity[28].

Structure engineering is another method by which catalysts can be modified. TMDCs can exist in several metastable phases, with the electronic structure and activity shifting. Structure change, such as from 2H to 1T, typically takes place via intercalation, which changes the relative stabilities of the phases[7].

Heterostructures are another method to tune the electronic structure. Heterostructures are constructs consisting of layers of different materials. Each layer modifies the electronic structure of its surrounding layers to a lesser or greater extent, permitting for very precise tuning of the surface[22].

Some modification methods do not necessarily change the electronic structure but rather increase the number of active sites. One such method is to reduce the size of the catalytic particles to improve the edge-basal plane ratio[29]. For catalysts and reactions that are only reactive on the edges, such as pristine MoS_2 for the HER, this increases the number of active sites. Similarly, growing complex structures, such as nanoflowers[17], can increase both edge active sites and basal plane active sites. While complex structures are difficult to model, simpler structures can act as analogues, allowing modifications found to be successful on analogue systems to be effective for more complex systems.

Testing each possible modification empirically is impractical, due to the wide range of TMDCs, possible modifications and combinations thereof. Since the search space for high activity TMDCs is so broad, computational and experimental descriptors that connect experimental performance to electronic behaviour are necessary to allow for the identification of which modifications are most likely to improve catalytic behaviour, reducing the search space and allowing for the empirical testing of a small number of promising candidates.

2.2.2 Rational design

The principle of rational design argues for the modification of catalysts in an intentional manner, to reduce the time and effort required for improvement. Catalysts have a variety of measures by which the utility of a catalyst might be measured. These are primarily activity[30], stability[30], efficiency[31], selectivity[32], and cost of synthesis[32,33]. Rational design seeks to improve all or some of these factors. Rational design can be executed by exploring a variety of materials with computational methods, such as DFT, followed by synthesis of selected materials, and finally testing and study of the catalyst to validate and inform theoretical predictions.

There exist a large variety of transition metal dichalcogenides, and a wide variety of methods of modifying the reactivity of these materials. Consequently, it is useful to be able to construct

descriptors to be able to better understand which materials are amenable to modification, and which modifications to make to improve catalytic properties.

2.2.3 Catalytic Descriptors

Catalytic descriptors are parameters which can be used to evaluate the potential performance of a catalyst. Descriptors can be broadly divided into two categories. The first category is extrinsic descriptors, which describe the performance of a catalyst without providing insight into the basis of the performance[34]. Intrinsic descriptors provide an indication of the performance of the catalyst, while also providing an understanding of that performance[34].

Extrinsic descriptors primarily take the form of the adsorption energies of the reactant to the surface of the heterogeneous catalyst. For the hydrogen evolution reaction in TMDCs, this takes the form of the relatively simple adsorption energy of the hydrogen atom onto the surface of the catalyst. This was described by Nørskov in 2005[35,36] and has been used in a variety of research. For the CO_2RR, the adsorption of CHO and COOH are excellent extrinsic descriptors of the reaction[37]. This allows extrinsic descriptors to act as screening parameters, allowing the rapid determination of the potential catalytic activity of a material via computational means. The use of extrinsic descriptors allows for the rapid determination of catalyst effectiveness but does not reduce the number of materials in the catalyst parameter space.

Intrinsic descriptors by contrast provide both a screening parameter and a theoretical explanation for the activity of the material, allowing the deliberate design of catalysts and therefore significantly reducing the number of possible catalysts that need be examined. A classic example of the intrinsic parameter is d-band theory, constructed by Hammer and Nørskov[38,39], first used to explain the nobility of gold, and later used to describe the catalytic activity of transition metals and transition metal alloys[40]. The theory establishes a relationship between the position of the d-band centre of the transition metal, and the adsorbate antibonding

states. As an adsorbate nears the catalytic surface, its valence bands form bonding and antibonding states. The adsorbate antibonding states are always higher than the d-band states and weaken the adsorption bond. Consequently, the higher the d-band centre, the higher the antibonding states and the less occupied they are, and consequently the stronger the bond[39]. In line with the Sabatier principle, the ideal catalyst ΔG of adsorption (for the HER, hydrogen adsorption to the catalyst) is 0[36].

Similar intrinsic descriptors have been constructed for the TMDCs. The Nørskov group[37] argue that the d-band centre determines the strength of the metal-sulfur bond, which is inversely correlated with the strength of the sulfur-hydrogen bond. Zhang *et al*[41]. constructed a model based off the Fermi softness model of Huang *et al.*[42] where a weighting function is applied to the occupied states to construct a descriptor of the material's bonding. Liu *et al.*[43] argue that the density of states (DOS) remains largely unchanged, and that the dominant contribution of the hydrogen is effectively electron transfer, occupying the previously lowest unoccupied orbitals. The lower in energy the lowest unoccupied orbitals are, the stronger the bond.

2.3 Group V TMDCs

Group V TMDCs consist of materials with the formula MX_2, where X is a chalcogenide, and the metal is one of vanadium, niobium or tantalum. Of particular interest are the group V disulfides, which are unique in that they are metallic across the group[44], with all phases of VS_2, NbS_2 and TaS_2 demonstrating electronic metallicity in the basal plane. This is due to the d-shell electron counts, which result in a partial occupation of the valence band of the 2H TMDs. Consequently, these materials exhibit metallic behaviour. In contrast, other groups of TMDCs have a filled valence band separated from the conduction band by a band gap, giving rise to semiconducting behaviour. Another advantage is the easy synthetic access to multiple phases

for NbS_2 and TaS_2[44], allowing for direct comparison between different metallic phases of the same material.

Group V TMDCs therefore present an ideal set of materials for rational design as they are basal-plane active across all available phases[43,45]. The basal plane provides a large, well-defined area for spectroscopy of electrocatalysis, such as Raman or XPS. Additionally, the well-defined area of the basal plane permits for better estimations of electrochemical surface area (Chapter 6). The pre-activation of the basal plane also eliminates basal plane activation as a potential cause of catalytic activity improvement, such as occurs in MoS_2[46,47], where effects on catalytic activity from the activation of sites in the basal plane are difficult to deconvolute from improvements to intrinsic activity[48], as they both appear as increases of current density.

Due to their basal plane activity, as well as other properties, the group V TMDCs have been targets of study, both as catalysts and for other scientific applications. This section briefly introduces each of the group V TMDCs and discusses prior work to construct descriptors for TMDCs.

2.3.1 Vanadium Disulfide

VS_2 is one of the more extensively studied of the group V TMDCs. It is reliably reported in only one phase, namely the 1T phase (Figure 1). This phase is well reported, with substantial evidence of its synthesis[49]. 1T-VS_2 is reported to have been synthesised both via hydrothermal synthesis[50] and APCVD[51]. Despite these reported syntheses, literature data on VS_2 synthesis can be somewhat contradictory, with inconsistent reports of the Raman spectra obtained from the synthesised materials[51–54]. Additionally, reported APCVD syntheses take place at temperatures thought to be too high for the synthesis of VS_2 at ambient pressure[55]. The origins of the reported Raman spectra and the nature of the APCVD syntheses are discussed further in the appendix (section A.2).

The 2H phase has been studied in the computational literature[56], and multiple reports of its synthesis have emerged[57,58]. Despite these reports, reliable evidence for the successful synthesis of 2H-VS_2 remains scarce.

VS_2 catalytic activity was first and remains primarily reported for the HER[59], with subsequent applications focused on improving its performance via a variety of methods, such as doping[60] or by increasing the surface area using hydrothermal synthesis[53]. VS_2 has also been studied for a variety of other catalytic applications, such as the CO_2RR[60] and NO_3RR[61].

2.3.2 Niobium Disulfide

NbS_2 is synthesised in two primary phases, the 2H and 3R phase[62]. The phases have similar structures, with 3R phase also a trigonal phase, albeit with the positions of the basal planes shifted relative to each other along the in-plane axis (Figure 1). These phases have been known in bulk form since at least 1969[63], and their spectroscopy and synthesis is well studied. The 3R phase is stable at room temperature, while the 2H phase is metastable, requiring quenching at a minimum of 800 °C to form[13]. There has also been an experimental report of a 1T phase[64], although evidence for it is limited.

Both the 3R phase and the 2H phase have been extensively studied for catalysis. Of particular interest has been their behaviour under negative potentials, which after sufficient cathodic cyclic voltammetry (~20,000 cycles) these materials see a very substantial increase in catalytic activity. This is thought to be due to the breaking of basal planes by emerging hydrogen bubbles, and subsequent improvements in conductivity and surface area[43]. Additional reports have explored the increase in catalytic activity via improving conductivity via intercalation[6] and improvements in activity via the reaction of intercalated lithium with water, producing hydrogen to rapidly achieve a similar effect to cycling[9].

2.3.3 Tantalum Disulfide

As with NbS_2, TaS_2 is synthesised in two primary phases, the 2H and 1T phases, although a 6R phase has also been reported[65]. As with NbS_2, there are reports of increases in catalytic activity for the 2H-TaS_2 phase after cathodic cycling[43,66], with fewer cycles required to achieve maximum performance (~4000) than for NbS_2[43]. TaS_2 has seen a great deal of non-catalytic interest in the literature, as the formation of charge density waves (CDWs) in 1T-TaS_2[67] has attracted great interest. TaS_2 still attracts fundamental work, and recent analyses of the XPS of 2H-TaS_2[68] and nanoscale inhomogeneities of 1T-TaS_2[69] have been published.

2.3.4 Constructing descriptors for group V TMDCs

As a consequence of their basal plane activation, group V TMDCs have been the subject of investigation for the construction of descriptors. Nørskov *et al*. examined their descriptors computationally, testing their modified d-band theory against hydrogen adsorption energy to establish its utility for a large set of TMDCs, including the group V TMDCs[35]. Experimental tests of descriptors are relatively rare; however, Liu *et al*.[43] proposed a descriptor which linked the hydrogen adsorption energy to the energy of the lowest unoccupied state. They tested this experimentally for TaS_2, NbS_2 and 1T-MoS_2, finding 2H-NbS_2 and 2H-TaS_2 to have high catalytic activity for the HER[43]. Despite this, experimental confirmation and comparison of the effectiveness of these descriptors remains sparse.

While the group V TMDCs have been extensively studied experimentally, they remain poorly understood. Studies by Najafi *et al.*[9,66] have indicated the importance of understanding the edges, with higher-than-expected performance of TaS_2 crystal edges[66] despite computational studies predicting similar or poorer performance[35]. Additionally, the handling of the catalysts is important, since HER catalysts are invariably exposed to air, understanding their reaction to

oxygen is essential to adequate understanding of catalytic activity, as TMDCs have been reported to rapidly form surface oxides on contact with air[70].

Additionally, while the performance of the group V TMDCs has been well-studied at standard HER potentials, the paucity of reports of the behaviour of these materials at higher potentials means their suitability for reactions requiring higher reducing potentials, such as the CO_2RR remains largely unknown.

Furthermore, the specific capacitance of the group V TMDCs is unknown. The specific capacitance (capacitance per unit area) is essential for establishing the catalytic activity per unit area of the catalyst, which is in turn necessary to establish the intrinsic activity of the material. The specific capacitance of these materials remains wholly unreported. This is exacerbated by poor reporting of catalyst area across the group V TMDC literature and is discussed further in Chapter 6.

To compensate for issues around surface area, results demonstrating an improved catalyst are often reported in terms of the Tafel slope obtained with the material[43,59], which provides insight into the kinetics of the reaction. For the HER, a lower Tafel slope is typically better, as it implies a higher reaction rate for a given overpotential[71]. However, as demonstrated by Liu *et al.*[43] and others[6,66], the Tafel slope of group V TMDCs does not accurately reflect the intrinsic catalytic activity, making it a poor measure of descriptor effectiveness.

To enable the effective rational design of transition metal dichalcogenides for electrocatalysis, a greater understanding of the properties of these materials must be achieved. A proper understanding of the crystal domains (edge vs basal plane) allows us to explore their different behaviours and deconvolute their contributions to catalytic activity. Once we have the catalytic activity of a sample, the intrinsic empirical performance must be extracted to allow for comparison to the chosen descriptor. To do so, the material performance must be corrected for

surface area, so that the material intrinsic performance, which the descriptor predicts, can be compared to other materials. Finally, the limits of the material, in terms of current density or applied potential must be understood, and the origins of any failures clarified.

2.4 Thesis aims

This thesis seeks to understand certain behaviours of TMDCs which are prerequisites for the construction and testing of effective TMDC electronic descriptors. As such, this thesis explores the oxidation properties of group V TMDCs, as well as the effect of correct electrochemical surface area (ECSA) determination on performance. These properties are necessary for accurate construction of descriptors. This thesis also examines the behaviour of these materials under extreme potentials.

Chapter 5 asks if the group V TMDCs oxidise in the same way in all domains of a TMDC crystal. This aims to permit for the extension of the results found there to the behaviour of typical catalytic powders, which are used to establish the performance of catalysts. Chapter 6 seeks to allow for the effective construction and comparison of future descriptors by examining the hypothesis that the correct unit-area measurement of these materials has a meaningful effect on the measured performance of the materials. This allows for empirical activity comparisons between different materials and samples which may have different surface areas. Chapter 6 also hypothesises that specific capacitance (by area) and exchange current density can be used as empirical descriptors of intrinsic performance, which can then be compared to theoretical descriptors. Chapter 7 theorises that the cause of colour and consistency changes of some group V TMDCs at extreme negative potentials is due to interlayer bubble formation. This chapter seeks to provide insight into the preparation and use of basal-plane active materials at high current densities.

2.5 References

(1) Mak, K. F.; Lee, C.; Hone, J.; Shan, J.; Heinz, T. F. Atomically Thin MoS2: A New Direct-Gap Semiconductor. *Physical Review Letters* **2010**, *105* (13), 2–5. https://doi.org/10.1103/PhysRevLett.105.136805.

(2) Splendiani, A.; Sun, L.; Zhang, Y.; Li, T.; Kim, J.; Chim, C. Y.; Galli, G.; Wang, F. Emerging Photoluminescence in Monolayer MoS2. *Nano Letters* **2010**, *10* (4), 1271–1275. https://doi.org/10.1021/nl903868w.

(3) Hinnemann, B.; Moses, P. G.; Bonde, J.; Jørgensen, K. P.; Nielsen, J. H.; Horch, S.; Chorkendorff, I.; Nørskov, J. K. Biomimetic Hydrogen Evolution: MoS2 Nanoparticles as Catalyst for Hydrogen Evolution. *Journal of the American Chemical Society* **2005**, *127* (15), 5308–5309.

(4) Jaramillo, T. F.; Jørgensen, K. P.; Bonde, J.; Nielsen, J. H.; Horch, S.; Chorkendorff, I. Identification of Active Edge Sites for Electrochemical H2 Evolution from MoS2 Nanocatalysts. *Science* **2007**, *317* (5834), 100–102. https://doi.org/10.1126/science.1141483.

(5) Kwon, I. S.; Kwak, I. H.; Zewdie, G. M.; Lee, S. J.; Kim, J. Y.; Yoo, S. J.; Kim, J.; Park, J.; Kang, H. S. $MoSe_2$–VSe_2–$NbSe_2$ Ternary Alloy Nanosheets to Boost Electrocatalytic Hydrogen Evolution Reaction. *Advanced Materials* **2022**, *34* (41). https://doi.org/10.1002/adma.202205524.

(6) Yang, J.; Mohmad, A. R.; Wang, Y.; Fullon, R.; Song, X.; Zhao, F.; Bozkurt, I.; Augustin, M.; Santos, E. J. G.; Shin, H. S.; Zhang, W.; Voiry, D.; Jeong, H. Y.; Chhowalla, M. Ultrahigh-Current-Density Niobium Disulfide Catalysts for Hydrogen Evolution. *Nat. Mater.* **2019**, *18* (12), 1309–1314. https://doi.org/10.1038/s41563-019-0463-8.

(7) Chang, L.; Sun, Z.; Hu, Y. H. 1T Phase Transition Metal Dichalcogenides for Hydrogen Evolution Reaction. *Electrochemical Energy Reviews* **2021**, *4* (2), 194–218. https://doi.org/10.1007/s41918-020-00087-y.

(8) Gan, X.; Lee, L. Y. S.; Wong, K.; Lo, T. W.; Ho, K. H.; Lei, D. Y.; Zhao, H. 2H/1T Phase Transition of Multilayer MoS2 by Electrochemical Incorporation of S Vacancies. *ACS Appl. Energy Mater.* **2018**, *1* (9), 4754–4765. https://doi.org/10.1021/acsaem.8b00875.

(9) Najafi, L.; Bellani, S.; Oropesa-Nuñez, R.; Martín-García, B.; Prato, M.; Mazánek, V.; Debellis, D.; Lauciello, S.; Brescia, R.; Sofer, Z.; Bonaccorso, F. Niobium Disulphide (NbS2)-Based (Heterogeneous) Electrocatalysts for an Efficient Hydrogen Evolution Reaction. *J. Mater. Chem. A* **2019**, *7* (44), 25593–25608. https://doi.org/10.1039/C9TA07210A.

(10) Li, Z.; Attanayake, N. H.; Blackburn, J. L.; Miller, E. M. Carbon Dioxide and Nitrogen Reduction Reactions Using 2D Transition Metal Dichalcogenide (TMDC) and Carbide/Nitride (MXene) Catalysts. *Energy and Environmental Science* **2021**, *14* (12), 6242–6286. https://doi.org/10.1039/d1ee03211a.

(11) Yang, X.; Guo, R.; Cai, R.; Shi, W.; Liu, W.; Guo, J.; Xiao, J. Engineering Transition Metal Catalysts for Large-Current-Density Water Splitting. *Dalton Transactions* **2022**, *51* (12), 4590–4607. https://doi.org/10.1039/d2dt00037g.

(12) Zhao, B.; Shen, D.; Zhang, Z.; Lu, P.; Hossain, M.; Li, J.; Li, B.; Duan, X. 2D Metallic Transition-Metal Dichalcogenides: Structures, Synthesis, Properties, and Applications. *Advanced Functional Materials* **2021**, *2105132*, 1–36. https://doi.org/10.1002/adfm.202105132.

(13) Witteveen, C.; Górnicka, K.; Chang, J.; Månsson, M.; Klimczuk, T.; Rohr, F. O. von. Polytypism and Superconductivity in the NbS2 System. *Dalton Transactions* **2021**, *50* (9), 3216–3223. https://doi.org/10.1039/D0DT03636F.

(14) Li, W.; Kheimeh Sari, H. M.; Li, X. Emerging Layered Metallic Vanadium Disulfide for Rechargeable Metal-Ion Batteries: Progress and Opportunities. *ChemSusChem* **2020**, *13* (6), 1172–1202. https://doi.org/10.1002/cssc.201903081.

(15) Sofer, Z.; Sedmidubský, D.; Luxa, J.; Bouša, D.; Huber, Š.; Lazar, P.; Veselý, M.; Pumera, M. Universal Method for Large-Scale Synthesis of Layered Transition Metal Dichalcogenides. *Chemistry - A European Journal* **2017**, *23* (42), 10177–10186. https://doi.org/10.1002/chem.201701628.

(16) Song, L.; Li, H.; Zhang, Y.; Shi, J. Recent Progress of Two-Dimensional Metallic Transition Metal Dichalcogenides: Syntheses, Physical Properties, and Applications. *Journal of Applied Physics* **2022**, *131* (6). https://doi.org/10.1063/5.0083929.

(17) Samal, R.; Rout, C. S. Recent Developments on Emerging Properties, Growth Approaches, and Advanced Applications of Metallic 2D Layered Vanadium Dichalcogenides. *Advanced Materials Interfaces* **2020**, *7* (8), 1–24. https://doi.org/10.1002/admi.201901682.

(18) Zhai, W.; Li, Z.; Wang, Y.; Zhai, L.; Yao, Y.; Li, S.; Wang, L.; Yang, H.; Chi, B.; Liang, J.; Shi, Z.; Ge, Y.; Lai, Z.; Yun, Q.; Zhang, A.; Wu, Z.; He, Q.; Chen, B.; Huang, Z.; Zhang, H. Phase Engineering of Nanomaterials: Transition Metal Dichalcogenides. *Chem. Rev.* **2024**, *124* (7), 4479–4539. https://doi.org/10.1021/acs.chemrev.3c00931.

(19) Karmodak, N.; Bursi, L.; Andreussi, O. Oxygen Evolution and Reduction on Two-Dimensional Transition Metal Dichalcogenides. *J. Phys. Chem. Lett.* **2022**, *13* (1), 58–65. https://doi.org/10.1021/acs.jpclett.1c03431.

(20) Luo, Y.; Chen, K.; Wang, G.; Zhang, G.; Zhang, N.; Chu, K. Ce-Doped MoS2−x Nanoflower Arrays for Electrocatalytic Nitrate Reduction to Ammonia. *Inorg. Chem. Front.* **2023**, *10* (5), 1543–1551. https://doi.org/10.1039/D2QI01798A.

(21) Roy, S.; Joseph, A.; Zhang, X.; Bhattacharyya, S.; Puthirath, A. B.; Biswas, A.; Tiwary, C. S.; Vajtai, R.; Ajayan, P. M. Engineered Two-Dimensional Transition Metal Dichalcogenides for Energy Conversion and Storage. *Chem. Rev.* **2024**, *124* (16), 9376–9456. https://doi.org/10.1021/acs.chemrev.3c00937.

(22) Sun, J.; Meng, X. Modulating the Electronic Properties of MoS2 Nanosheets for Electrochemical Hydrogen Production: A Review. *ACS Applied Nano Materials* **2021**, *4* (11), 11413–11427. https://doi.org/10.1021/acsanm.1c02832.

(23) Shao, X.; Zhang, X.; Liu, Y.; Qiao, J.; Zhou, X. D.; Xu, N.; Malcombe, J. L.; Yi, J.; Zhang, J. Metal Chalcogenide-Associated Catalysts Enabling CO2 electroreduction to Produce Low-Carbon Fuels for Energy Storage and Emission Reduction: Catalyst Structure, Morphology, Performance, and Mechanism. *Journal of Materials Chemistry A* **2021**, *9* (5), 2526–2559. https://doi.org/10.1039/d0ta09232k.

(24) Li, Q.; Guo, Y.; Tian, Y.; Liu, W.; Chu, K. Activating VS2 basal Planes for Enhanced NRR Electrocatalysis: The Synergistic Role of S-Vacancies and B Dopants. *Journal of Materials Chemistry A* **2020**, *8* (32), 16195–16202. https://doi.org/10.1039/d0ta05282e.

(25) Cao, Y. Roadmap and Direction toward High-Performance MoS2 Hydrogen Evolution Catalysts. *ACS Nano* **2021**, *15* (7), 11014–11039. https://doi.org/10.1021/acsnano.1c01879.

(26) Luo, R.; Luo, M.; Wang, Z.; Liu, P.; Song, S.; Wang, X.; Chen, M. The Atomic Origin of Nickel-Doping-Induced Catalytic Enhancement in MoS2 for Electrochemical Hydrogen Production. *Nanoscale* **2019**, *11* (15), 7123–7128. https://doi.org/10.1039/c8nr10023c.

(27) Liu, P.; Zhu, J.; Zhang, J.; Xi, P.; Tao, K.; Gao, D.; Xue, D. P Dopants Triggered New Basal Plane Active Sites and Enlarged Interlayer Spacing in MoS2 Nanosheets toward Electrocatalytic Hydrogen Evolution. *ACS Energy Letters* **2017**, *2* (4), 745–752. https://doi.org/10.1021/acsenergylett.7b00111.

(28) Xie, J.; Yang, X.; Xie, Y. Defect Engineering in Two-Dimensional Electrocatalysts for Hydrogen Evolution. *Nanoscale* **2020**, *12* (7), 4283–4294. https://doi.org/10.1039/c9nr09753h.

(29) Wang, T.; Gao, D.; Zhuo, J.; Zhu, Z.; Papakonstantinou, P.; Li, Y.; Li, M. Size-Dependent Enhancement of Electrocatalytic Oxygen-Reduction and Hydrogen-Evolution Performance of MoS2 Particles. *Chemistry - A European Journal* **2013**, *19* (36), 11939–11948. https://doi.org/10.1002/chem.201301406.

(30) He, W.; Zheng, X.; Peng, J.; Dong, H.; Wang, J.; Zhao, W. Mo-Dopant-Strengthened Basal-Plane Activity in VS2 for Accelerating Hydrogen Evolution Reaction. *Chemical Engineering Journal* **2020**, *396* (February), 125227. https://doi.org/10.1016/j.cej.2020.125227.

(31) Lv, K.; Suo, W.; Shao, M.; Zhu, Y.; Wang, X.; Feng, J.; Fang, M. Nitrogen Doped MoS2 and Nitrogen Doped Carbon Dots Composite Catalyst for Electroreduction CO2 to CO with High Faradaic Efficiency. *Nano Energy* **2019**, *63* (May), 103834. https://doi.org/10.1016/j.nanoen.2019.06.030.

(32) Pang, Y.; Su, C.; Jia, G.; Xu, L.; Shao, Z. Emerging Two-Dimensional Nanomaterials for Electrochemical Nitrogen Reduction. *Chemical Society Reviews* **2021**, *50* (22), 12744–12787. https://doi.org/10.1039/d1cs00120e.

(33) Fu, Q.; Han, J.; Wang, X.; Xu, P.; Yao, T.; Zhong, J.; Zhong, W.; Liu, S.; Gao, T.; Zhang, Z.; Xu, L.; Song, B. 2D Transition Metal Dichalcogenides: Design, Modulation, and Challenges in Electrocatalysis. *Advanced Materials* **2021**, *33* (6). https://doi.org/10.1002/adma.201907818.

(34) Wang, B.; Zhang, F. Main Descriptors To Correlate Structures with the Performances of Electrocatalysts. *Angewandte Chemie - International Edition* **2022**, *61* (4). https://doi.org/10.1002/anie.202111026.

(35) Tsai, C.; Chan, K.; Nørskov, J. K.; Abild-Pedersen, F. Theoretical Insights into the Hydrogen Evolution Activity of Layered Transition Metal Dichalcogenides. *Surface Science* **2015**, *640*, 133–140. https://doi.org/10.1016/j.susc.2015.01.019.

(36) Nørskov, J. K.; Bligaard, T.; Logadottir, A.; Kitchin, J. R.; Chen, J. G.; Pandelov, S.; Stimming, U. Trends in the Exchange Current for Hydrogen Evolution. *J. Electrochem. Soc.* **2005**, *152* (3), J23. https://doi.org/10.1149/1.1856988.

(37) Tsai, C.; Chan, K.; Nørskov, J. K.; Abild-Pedersen, F. Understanding the Reactivity of Layered Transition-Metal Sulfides: A Single Electronic Descriptor for Structure and Adsorption. *J. Phys. Chem. Lett.* **2014**, *5* (21), 3884–3889. https://doi.org/10.1021/jz5020532.

(38) Zhao, Z. J.; Liu, S.; Zha, S.; Cheng, D.; Studt, F.; Henkelman, G.; Gong, J. Theory-Guided Design of Catalytic Materials Using Scaling Relationships and Reactivity Descriptors. *Nature Reviews Materials* **2019**, *4* (12), 792–804. https://doi.org/10.1038/s41578-019-0152-x.

(39) Hammer, B.; Norskov, J. K. Why Gold Is the Noblest of All the Metals. *Nature* **1995**, *376* (6537), 238–240. https://doi.org/10.1038/376238a0.

(40) Liu, M.; Hybertsen, M. S.; Wu, Q. A Physical Model for Understanding the Activation of MoS2 Basal-Plane Sulfur Atoms for the Hydrogen Evolution Reaction. *Angewandte Chemie - International Edition* **2020**, *59* (35), 14835–14841. https://doi.org/10.1002/anie.202003091.

(41) Zhang, Y.; Chen, X.; Huang, Y.; Zhang, C.; Li, F.; Shu, H. The Role of Intrinsic Defects in Electrocatalytic Activity of Monolayer VS2 Basal Planes for the Hydrogen Evolution Reaction. *Journal of Physical Chemistry C* **2017**, *121* (3), 1530–1536. https://doi.org/10.1021/acs.jpcc.6b11987.

(42) Huang, B.; Xiao, L.; Lu, J.; Zhuang, L. Spatially Resolved Quantification of the Surface Reactivity of Solid Catalysts. *Angewandte Chemie International Edition* **2016**, *55* (21), 6239–6243. https://doi.org/10.1002/anie.201601824.

(43) Liu, Y.; Wu, J.; Hackenberg, K. P.; Zhang, J.; Wang, Y. M.; Yang, Y.; Keyshar, K.; Gu, J.; Ogitsu, T.; Vajtai, R.; Lou, J.; Ajayan, P. M.; Wood, B. C.; Yakobson, B. I. Self-Optimizing, Highly Surface-Active Layered Metal Dichalcogenide Catalysts for Hydrogen Evolution. *Nat Energy* **2017**, *2* (9), 1–7. https://doi.org/10.1038/nenergy.2017.127.

(44) Sim, Y.; Chae, Y.; Kwon, S.-Y. Recent Advances in Metallic Transition Metal Dichalcogenides as Electrocatalysts for Hydrogen Evolution Reaction. *iScience* **2022**, *25* (10). https://doi.org/10.1016/j.isci.2022.105098.

(45) Zhang, J.; Wu, J.; Zou, X.; Hackenberg, K.; Zhou, W.; Chen, W.; Yuan, J.; Keyshar, K.; Gupta, G.; Mohite, A.; Ajayan, P. M.; Lou, J. Discovering Superior Basal Plane Active Two-Dimensional Catalysts for Hydrogen Evolution. *Materials Today* **2019**, *25*, 28–34. https://doi.org/10.1016/j.mattod.2019.02.014.

(46) Zhu, J.; Wang, Z.-C.; Dai, H.; Wang, Q.; Yang, R.; Yu, H.; Liao, M.; Zhang, J.; Chen, W.; Wei, Z.; Li, N.; Du, L.; Shi, D.; Wang, W.; Zhang, L.; Jiang, Y.; Zhang, G. Boundary Activated Hydrogen Evolution Reaction on Monolayer MoS2. *Nat Commun* **2019**, *10* (1), 1348. https://doi.org/10.1038/s41467-019-09269-9.

(47) Park, S.; Park, J.; Abroshan, H.; Zhang, L.; Kim, J. K.; Zhang, J.; Guo, J.; Siahrostami, S.; Zheng, X. Enhancing Catalytic Activity of MoS2 Basal Plane S-Vacancy by Co Cluster Addition. *ACS Energy Lett.* **2018**, *3* (11), 2685–2693. https://doi.org/10.1021/acsenergylett.8b01567.

(48) Wu, L.; Hofmann, J. P. Comparing the Intrinsic HER Activity of Transition Metal Dichalcogenides: Pitfalls and Suggestions. *ACS Energy Lett.* **2021**, *6* (7), 2619–2625. https://doi.org/10.1021/acsenergylett.1c00912.

(49) Hossain, M.; Zhang, H.; Huangfu, Y.; Saeed, M. Z.; Qin, B.; Bloos, D.; Duan, X. 2D Metallic Vanadium Dichalcogenides and Related Heterostructures. *Materials Today Advances* **2024**, *21*, 100451. https://doi.org/10.1016/j.mtadv.2023.100451.

(50) Mandal, A.; Yadav, A. K.; Pandey, S. K.; Chakrabarti, S. Fabrication of 1T VS2 Electrode-Based In-Plane Micro-Supercapacitor Using a Cost-Effective Mask-Assisted Printing Technique. *physica status solidi (a)* **2023**, *220* (20), 2300274. https://doi.org/10.1002/pssa.202300274.

(51) Hossain, M.; Wu, J.; Wen, W.; Liu, H.; Wang, X.; Xie, L. Chemical Vapor Deposition of 2D Vanadium Disulfide and Diselenide and Raman Characterization of the Phase Transitions. *Advanced Materials Interfaces* **2018**, *5* (16), 1800528. https://doi.org/10.1002/admi.201800528.

(52) Ji, Q.; Li, C.; Wang, J.; Niu, J.; Gong, Y.; Zhang, Z.; Fang, Q.; Zhang, Y.; Shi, J.; Liao, L.; Wu, X.; Gu, L.; Liu, Z.; Zhang, Y. Metallic Vanadium Disulfide Nanosheets as a Platform Material for Multifunctional Electrode Applications. *Nano Lett.* **2017**, *17* (8), 4908–4916. https://doi.org/10.1021/acs.nanolett.7b01914.

(53) Qu, Y.; Shao, M.; Shao, Y.; Yang, M.; Xu, J.; Kwok, C. T.; Shi, X.; Lu, Z.; Pan, H. Ultra-High Electrocatalytic Activity of VS2 Nanoflowers for Efficient Hydrogen Evolution Reaction. *J. Mater. Chem. A* **2017**, *5* (29), 15080–15086. https://doi.org/10.1039/C7TA03172F.

(54) Avilés, M. O.; Jelken, J.; Lagugné-Labarthet, F. Periodic Spiral Ripples on VS_2 Flakes: A Tip-Enhanced Raman Investigation. *J. Phys. Chem. Lett.* **2022**, *13* (41), 9771–9776. https://doi.org/10.1021/acs.jpclett.2c02555.

(55) Moutaabbid, H.; Le Godec, Y.; Taverna, D.; Baptiste, B.; Klein, Y.; Loupias, G.; Gauzzi, A. High-Pressure Control of Vanadium Self-Intercalation and Enhanced Metallic Properties in 1T-V1+xS2 Single Crystals. *Inorg. Chem.* **2016**, *55* (13), 6481–6486. https://doi.org/10.1021/acs.inorgchem.6b00532.

(56) Liu, M.; Zhao, Z.; Zhang, W.; Zheng, W. Perspective of Vanadium Disulfide: A Rising Star Finds Plenty of Room in Single and Multielectron Energy Storage. *Energy Fuels* **2022**, *36* (23), 13931–13955. https://doi.org/10.1021/acs.energyfuels.2c02642.

(57) Karthick, K.; Bijoy, T. K.; Sivakumaran, A.; Mansoor Basha, A. B.; Murugan, P.; Kundu, S. Enhancing Hydrogen Evolution Reaction Activities of 2H-Phase VS2 Layers with Palladium Nanoparticles. *Inorg. Chem.* **2020**, *59* (14), 10197–10207. https://doi.org/10.1021/acs.inorgchem.0c01339.

(58) Dai, J.-Q.; Liu, Y.-Z.; Yuan, J. Modifying the Magnetic and Electronic Properties of Monolayer 2H-VS2 via Ferroelectric Substrate with Different Surface Terminations. *physica status solidi (b)* **2022**, *259* (11), 2200087. https://doi.org/10.1002/pssb.202200087.

(59) Yuan, J.; Wu, J.; Hardy, W. J.; Loya, P.; Lou, M.; Yang, Y.; Najmaei, S.; Jiang, M.; Qin, F.; Keyshar, K.; Ji, H.; Gao, W.; Bao, J.; Kono, J.; Natelson, D.; Ajayan, P. M.; Lou, J. Facile Synthesis of Single Crystal Vanadium Disulfide Nanosheets by Chemical Vapor Deposition for Efficient Hydrogen Evolution Reaction. *Advanced Materials* **2015**, *27* (37), 5605–5609. https://doi.org/10.1002/adma.201502075.

(60) Wang, P.; Wang, X.; Zhang, J.; Wu, C.; Zhang, A.; Chen, N.; Sheng, T.; Wu, Z. Modulating the Active Sites of VS2 by Mn Doping for Highly Selective CO2 Electroreduction to Methanol in a Flow Cell. *ACS Appl. Mater. Interfaces* **2024**, *16* (28), 36453–36461. https://doi.org/10.1021/acsami.4c06789.

(61) Wang, G.; Shen, P.; Chen, K.; Guo, Y.; Zhao, X.; Chu, K. Rare-Earth La-Doped VS2−x for Electrochemical Nitrate Reduction to Ammonia. *Inorg. Chem. Front.* **2023**, *10* (7), 2014–2021. https://doi.org/10.1039/D2QI02757G.

(62) McMullan, W. G.; Irwin, J. C. Raman Scattering from 2H and 3R–NbS2. *Solid State Communications* **1983**, *45* (7), 557–560. https://doi.org/10.1016/0038-1098(83)90426-X.

(63) Wilson, J. A.; Yoffe, A. D. The Transition Metal Dichalcogenides Discussion and Interpretation of the Observed Optical, Electrical and Structural Properties. *Advances in Physics* **1969**, *18* (73), 193–335. https://doi.org/10.1080/00018736900101307.

(64) Carmalt, C. J.; Manning, T. D.; Parkin, I. P.; Peters, E. S.; Hector, A. L. Formation of a New (1T) Trigonal NbS2 Polytype via Atmospheric Pressure Chemical Vapour Deposition. *J. Mater. Chem.* **2004**, *14* (3), 290–291. https://doi.org/10.1039/B315782M.

(65) Achari, A.; Bekaert, J.; Sreepal, V.; Orekhov, A.; Kumaravadivel, P.; Kim, M.; Gauquelin, N.; Balakrishna Pillai, P.; Verbeeck, J.; Peeters, F. M.; Geim, A. K.; Milošević, M. V.; Nair, R. R. Alternating Superconducting and Charge Density Wave Monolayers within Bulk 6R-TaS2. *Nano Lett.* **2022**, *22* (15), 6268–6275. https://doi.org/10.1021/acs.nanolett.2c01851.

(66) Najafi, L.; Bellani, S.; Oropesa-Nuñez, R.; Martín-García, B.; Prato, M.; Pasquale, L.; Panda, J.-K.; Marvan, P.; Sofer, Z.; Bonaccorso, F. TaS2, TaSe2, and Their Heterogeneous Films as Catalysts for the Hydrogen Evolution Reaction. *ACS Catal.* **2020**, *10* (5), 3313–3325. https://doi.org/10.1021/acscatal.9b03184.

(67) Lacinska, E. M.; Furman, M.; Binder, J.; Lutsyk, I.; Kowalczyk, P. J.; Stepniewski, R.; Wysmolek, A. Raman Optical Activity of 1T-TaS2. *Nano Lett.* **2022**, *22* (7), 2835–2842. https://doi.org/10.1021/acs.nanolett.1c04990.

(68) Drivas, C.; Catlow, C. R. A.; Isaacs, M. A.; Kyriakou, G. Considerations on the XPS Analysis of 2H-TaS2 (0001). *Surface and Interface Analysis* **2025**, *57* (10), 802–808. https://doi.org/10.1002/sia.70013.

(69) Campbell, B.; Riffle, J. V.; De La Torre, A.; Wang, Q.; Plumb, K. W.; Hollen, S. M. Nanoscale Electronic Inhomogeneities in 1T-TaS 2. *Phys. Rev. Materials* **2024**, *8* (3), 034002. https://doi.org/10.1103/PhysRevMaterials.8.034002.

(70) Jones, L. X-Ray Photoemission Spectroscopy of the Mo, Re and W Dichalcogenides. Ph.D. Thesis, University of Liverpool, 2022

(71) Bard, A. J.; Faulkner, L. R.; White, H. S. *Electrochemical Methods: Fundamentals and Applications*; John Wiley & Sons, 2022.

Chapter 3. Experimental Methods

3.1 Spectroscopies and XRD

3.1.1 X-ray photoelectron spectroscopy

X-ray photoelectron spectroscopy (XPS) arises from the photoelectric effect, whereby an incident photon, typically in the X-ray range, causes the emission of a photoelectron from a sample. This photoemission occurs when the incident photon of energy hv has sufficient energy to overcome the binding energy (E_b) of the electron. The binding energy is directly equivalent to the ionisation energy for that electron. Additionally, a certain amount of energy is required to release the electron from the surface of the material, which is known as the work function, ϕ. When emitted, the electron will have a defined kinetic energy E_k, for which the total of the binding energy, work function and kinetic energy must equal the energy of the incoming photon for the maximum probability of emission[1].

$$E_k = hv - E_b - \phi \qquad (3-1)$$

The emitted photoelectrons are translated through a series of electron optics and then captured by a hemispherical analyser (Figure 1), which consists of two concentric hemispheres to which voltage is applied. The photoelectrons enter the analyser, and the analyser selects for electrons with a specific kinetic energy. Since the original incident photon has a known energy, the binding energies of the core electrons can be calculated from the kinetic energy of the emitted electron. The binding energy of the electrons at the Fermi level is 0 eV[1,2].

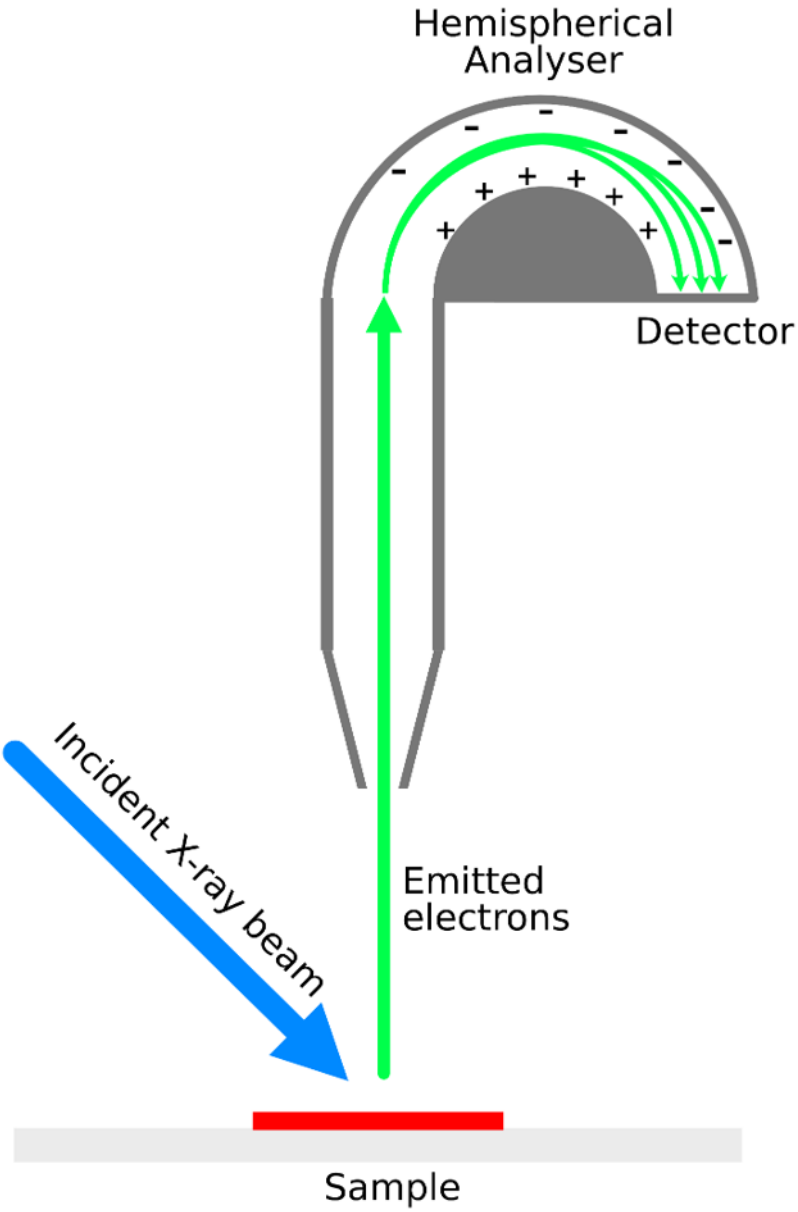


Figure 1. A diagram of an X-ray photoelectron spectroscopy system. X-rays interacting with the sample cause emission of photoelectrons, some of which are captured by electron optics and sent through the hemispherical analyser. The charged hemispheres of the analyser allow for the detection of electrons with specific kinetic energies, which can in turn be converted into binding energy.

Each element has a unique set of binding energies for its core (non-valence) electrons. Those binding energies are sensitive to the chemical environment of the atom from which the

photoelectron is emitted. This sensitivity leads to “shifts”, or changes in the binding energies of the resulting peaks from their elemental values. More electronegative atoms can be expected to have higher binding energies. Binding energies also often correlate with oxidation states, with more oxidised atoms having fewer electrons and therefore higher binding energies, and vice versa[1,2].

XPS is highly surface-sensitive. While the typical XPS X-rays have penetration on the order of micrometres, the photoelectrons generated have a high probability of interaction with matter. Many of those interactions are inelastic, leading to losses in energy and increases in apparent binding energy. At sufficient depths (~1-10 nm), the photoelectrons are exponentially more unlikely to escape the material before their energy is lost to the material. This is described by Beer’s law, where:

$$I = I_0 \exp\left(-\frac{d}{\lambda}\right) \qquad (3-2)$$

I is the intensity of detected photoelectrons, I_0 the intensity of photoelectrons generated, d is the depth of the emitted electrons, and λ is the attenuation length. Varying the energy of the incoming photons can vary the maximum detection depth. Another consequence of these interactions is the necessity to maintain low pressure in XPS systems to minimise electron scattering in air on the way to the analyser[1,2].

Energy resolution in XPS devices is typically affected by source linewidth, that is how narrow the range of X-ray energies emitted by the source is; analyser radius, with larger radii providing better resolution; and pass energy, that is the energy to which the electrons are retarded to pass through the initial electron optics. Higher pass energies provide lower resolution[2].

Additional effects can make acquired XPS spectra more complex. Many XPS core levels, such as the sulfur 2p (Figure 2), give multiple peaks on the acquired spectrum. This is due to spin-

orbit coupling, where the electron spin and angular momentum vector of the orbital can be parallel or anti-parallel. These have different binding energies, due to differences in the energies of the two states and have known relative intensities and relative binding energies[1].

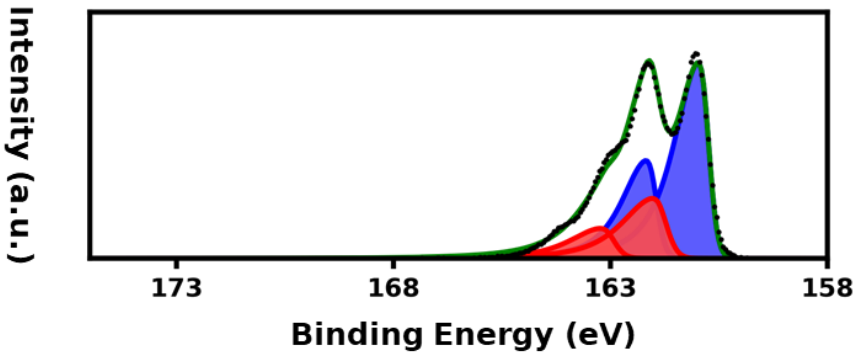


Figure 2. An example XPS spectrum, in this case the sulfur 2p region of 3R-NbS_2 (data from Chapter 5). The peaks are asymmetric, and fitted as such, with two distinct environments.

Peak shape is also important. XPS peaks are typically symmetric, with the contributing factors to peak width including core-hole lifetime and material in/homogeneity. This can also be affected by the system energy resolution. Peak asymmetry arises in metallic materials, namely materials that are electrically conductive. In a multi-electron understanding of XPS, the emission of a photoelectron creates a core hole which in turn creates a potential between it and the remaining electrons. In metallic materials, due to the availability of states near the Fermi level, low-energy excitations are possible, reducing the energy of the photoelectron and therefore its kinetic energy. The lower kinetic energy is observed as higher intensity on the high-binding energy side of the peak and therefore peak asymmetry[3,4].

To derive greater insight into the results of XPS spectra, peaks can be fit with modelled peaks. This can allow for the deconvolution of the different atomic environments that contribute to an XPS peak. Symmetric XPS peaks can often be fit with a combination of Gaussian and

Lorentzian broadening, where the Gaussian broadening is due to the contributions of the spectrometer system while the Lorentzian accounts for broadening from the material[5]. For asymmetric peaks, an additional factor or factors can be added to model the asymmetry. In this work, the LA(*α, β, m*) line shape (CasaXPS[6]) is used, where *α* and *β* specify the Lorentzian width at lower and higher binding energies respectively either side of the peak and m defines the Gaussian broadening.

XPS was conducted using a PHI 5000 VersaProbe III using a monochromatic Al Kα X-ray source under UHV. Typical analysis chamber vacuum was in the range of 10^{-8}-10^{-9} mbar. Spectra were processed using CasaXPS with Shirley type background subtractions. Survey spectra were acquired from 0 to 1100 eV, with an acquisition time of 20 minutes. Charge neutralisation was not used. Spin-orbit splitting and area ratios were constrained to literature/theoretical values for S 2p, Nb 3d and Ta 4f doublets. FWHM values were constrained to be equal within chemically related doublets. Binding energies were referenced to adventitious carbon at 284.8 eV.

Powdered samples were deposited onto carbon tape, and excess un-adhered powder was removed by gentle tapping of the sample holder. Powdered samples were ground further using a ceramic mortar and pestle to improve homogeneity. Crystal samples were placed directly on carbon tape. Inert transfer was achieved via an inert transfer device from the glovebox. Inertly transferred materials were exfoliated/cleaved in the glovebox while on carbon tape.

Exfoliation/cleaving was achieved via an additional piece of carbon tape applied to the crystal and then removed. This is referred to in a dual manner (exfoliated/cleaving) due to required product being either of the crystals removed or left behind, and the technique being a classic exfoliation technique while producing cleaved products. The sample was then immediately transferred into the sealed transfer device. Materials exposed to air were exfoliated/cleaved

using carbon tape while adhered to carbon tape under air and allowed to remain in air for up to ten minutes, then placed into the sealed transfer device and transferred to the vacuum of the XPS system.

XPS was acquired with a beam power of 25 W, and a beam diameter of 50 μm. S 2p, Nb 3d, Nb 3p and Ta 4f typical acquisition times were 20, 40, 16 and 16 minutes respectively, with a step size of 0.1 eV and pass energy of 26 eV.

3.1.2 X-ray absorption spectroscopy

X-ray absorption spectroscopy (XAS) is a technique which measures the interaction of X-rays of varying energy with the electron states of the material. A typical XAS interaction involves the transition of an electron from a lower (ground) energy state to a higher (excited) energy state or its emission as a photoelectron. The various interactions arising from that base interaction give rise to a variety of X-ray absorption techniques[7,8].

As with XPS, the core electron levels of different elements have characteristic values. When the energy of the X-ray incident photon is equal to that of the characteristic transition absorption significantly increases, and at photon energies greater than the transition energy the probability of absorption remains significantly higher than at energies lower than the transition, leading to a defined edge[7,8] (Figure 3).

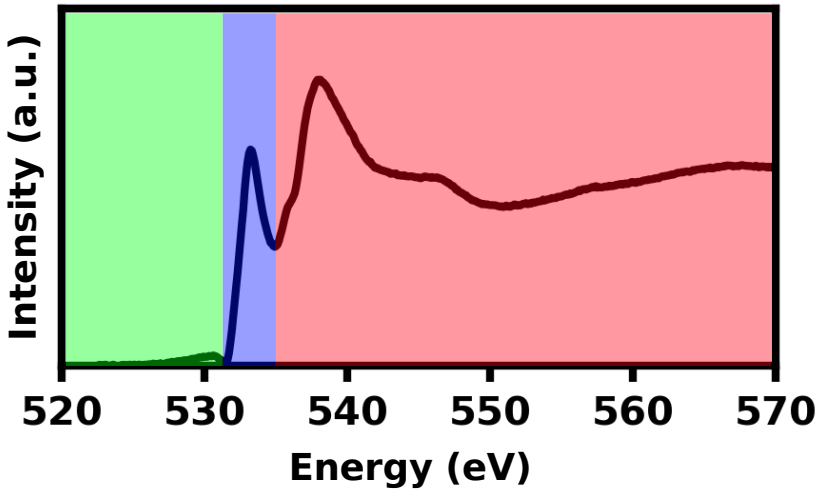


Figure 3. The oxygen NEXAFS spectrum for 3R-NbS_2 (data from Chapter 7). Shown in green is the pre-edge region, the edge is shown in blue, while the post-edge region is shown in red.

XAS techniques are typically divided into hard and soft X-ray techniques. Hard X-ray data is typically discussed in terms of the X-ray absorption near-edge structure (XANES) region, which measures the position and shape of the edge, and the extended X-ray absorption fine structure (EXAFS) region, which studies the post-edge region to obtain structural information. These techniques take place at higher photon energies. Soft X-ray studies take place at lower photon energies. The most common soft XAS technique is near edge X-ray absorption fine structure, or NEXAFS[7,8]. Due to the lower photon energies, NEXAFS is typically more surface-sensitive than hard-XAS. XANES and NEXAFS permit the identification of the element and element oxidation state, while EXAFS gives information about the local coordination environment, such as neighbouring-atom identification, bond distances and coordination number[7].

NEXAFS spectra are typically collected via two means. The first is fluorescent yield (FY), which detects the photons emitted as a result of relaxation from the excited state caused by the absorption of the incident X-ray. This technique is constrained by the mean free path of the photons in the material[8]. Total electron yield, or TEY functions via the detection of electrons

emitted from the sample, either photoelectrons or Auger electrons. The emission of these electrons is proportional to the X-ray absorption. This technique is more surface sensitive, being constrained by the mean free path of electrons in the material[8].

For XAS data, materials were transferred in air to end-station ES-2 at B07B in Diamond and examined using both FY (fluorescent yield) and TEY (total electron yield) modes. FY signals were invariably poor, so only TEY data is present in this thesis. Energies were calibrated to the O-K edge of silicon oxide. Spectra were normalised to the incident photon flux, measured from the current of the final refocusing mirror. Steps in the spectra related to ring-top ups were removed from the spectra manually.

Samples were prepared in air and were mounted on carbon tape with an aluminium core. Powder samples were spread on the carbon tape using a steel spatula and excess loose powder was removed via gentle tapping of the samples. Powdered samples were ground further using a ceramic mortar and pestle to improve homogeneity. Crystal samples were placed directly on carbon tape, exfoliated/cleaved using additional carbon tape and pumped down to vacuum (approximately 1×10^{-3} mbar) within ten minutes.

3.1.3 X-Ray Diffraction

X-ray diffraction is a technique that measures the physical spacing between atoms. Since X-ray wavelengths are close to that of atomic bond lengths, when X-rays scatter off the electrons in atoms, the photons can interfere constructively. This is described by Bragg's law[9] (eq. 3-3, Figure 4):

$$2d\sin\theta = n\lambda \qquad (3-3)$$

Where λ is the wavelength of the X-ray, θ is the glancing angle between the beam and the lattice planes, and d the inter-plane distance. Constructive interference is observed when $2dsin\theta$ is an

integer (n) multiple of λ [9]. That constructive interference gives rise to intensity peaks on XRD patterns (Figure 5).

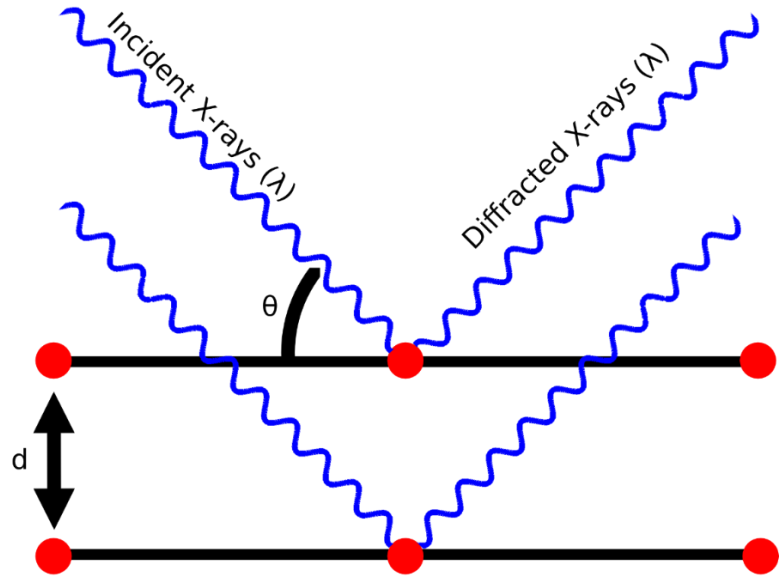


Figure 4. A diagram of the XRD process. X-rays scatter off atoms, and the photons interfere constructively at specific angles. The result of this process is shown in Figure 5.

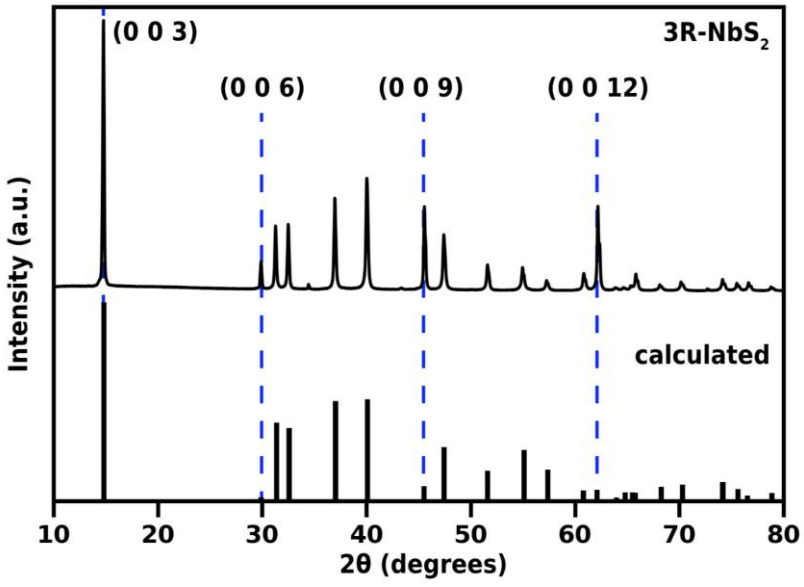


Figure 5. Example PXRD pattern. Above is the acquired pattern of 3R-NbS_2 (figure from Chapter 5), while below is shown the pattern calculated from a model of the material unit cell. The (0 0 l), where l = 3,6,9 and 12 are marked.

Of relevance to this thesis is powder X-ray diffraction, or PXRD. In PXRD the sample is a powder consisting of many small crystallites. The ideal powder XRD sample has a flat surface, aligned to the detector with random crystallite orientation. Surface irregularity can cause additional peaks to appear on the acquired pattern. Peak sharpness is dependent on crystallinity, with lower crystallinity leading to broader peaks, while crystallite size can also affect peak broadness, with small crystallites (<200 nm) leading to widened peaks. Peak intensity can be affected by the number of symmetrically equivalent reflections, the geometry of diffraction, absorption of the X-rays by the material and porosity of the sample[9].

The preferred orientation effect is of particular relevance to TMDCs, whose layered structure ensures that the resulting crystallites typically prefer to orient themselves in the out-of-plane direction. As a result, the peaks resulting from the (0 0 *l*) reflections, where *l* is an integer number, often have greatly increased intensities[9].

X-ray diffraction patterns were obtained using Rigaku SmartLab X-ray diffractometers with either a 3 kW or 9 kW X-ray Cu Kα source, using a glass sample holder. Patterns were also acquired using a Rigaku Miniflex diffractometer in a nitrogen glovebox with a 600 W Cu Kα source, typically using a low background silicon sample holder or an aluminium sample holder (where indicated). Samples were prepared in air, with both crystal samples and powdered samples ground using a ceramic mortar and pestle to either render them into a powder or to improve powder homogeneity. Powders were subsequently agitated with a steel spatula and placed inside a sample holder. Excess material was removed with a glass slide. Acquisition length was 40 minutes unless indicated otherwise.

3.1.4 Raman spectroscopy

Raman spectroscopy measures the inelastic scattering of visible and near-visible light on materials. In the classical understanding of Raman scattering, the electric field of incident

photons, *E,* interact with the electrons of a material. The irradiation produces an electric dipole moment, $P = \alpha E$, where α is the polarisability of the vibrational mode. The molecule is excited to a virtual state and then emits a photon to return to a lower energy state. This emission produces three types of scattering[10,11]. The first type of scattering is Rayleigh scattering, which is elastic. Anti-Stokes is the first type of inelastic scattering and occurs via the interaction of a vibrationally excited molecule with an incident photon, after which the molecule returns to ground state. The photon produced has a value of v_i+v_m, where v_i is the wavenumber of the incident photon and v_m the wavenumber of the vibrational state. By contrast, Stokes scattering is a result of the excitation of a ground state molecule which relaxes into an excited vibrational state, producing a photon of wavenumber v_i-v_m. Since the population of molecules at the ground state is much higher than the population of the molecules in an excited state, Stokes scattering is more probable and therefore produces lines of higher intensity than anti-Stokes (Figure 6)[10,11].

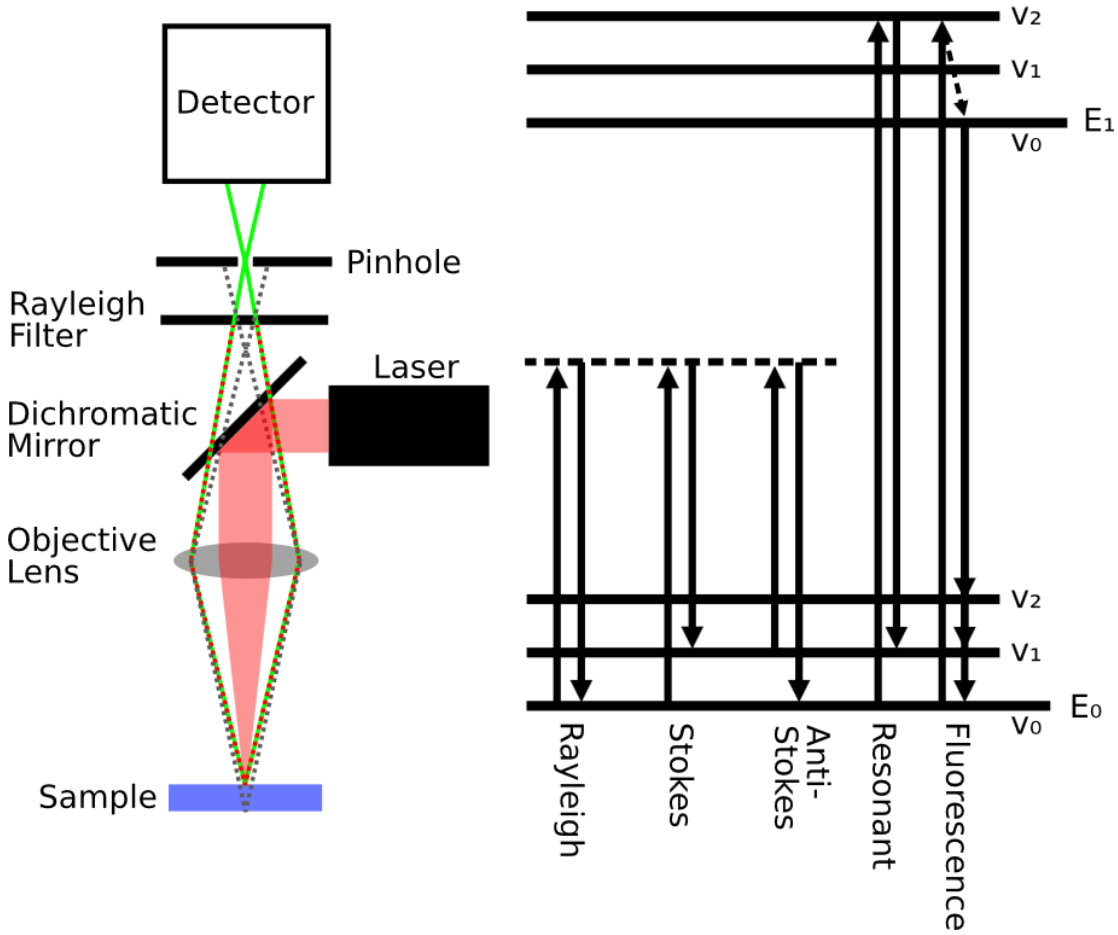


Figure 6. On the left is shown a diagram of a confocal Raman microscope. This uses a laser to emit monochromatic light onto a sample, which is then filtered through a Rayleigh filter to remove the elastically scattered light, and passed through a pinhole to remove out-of-focus light. The detector detects the changed wavelengths of the inelastically scattered light. On the right is shown the typical modes of light scattering, where E_1 is an electronically excited state, while v_x are the various vibrationally excited states.

In a practical Raman experiment, the intensity and wavelength of the Stokes scattered light is detected. The Raman shift of the emitted light is reported as:

$$\Delta\nu = \nu_i - \nu_e \qquad (3-4)$$

where ν_i is the wavenumber of the incident light, and ν_e the wavenumber of the emitted light, in units of cm^{-1} [10,11].

Two other categories of scattering can contribute to a Raman spectrum. The first is resonant Raman, by which the incident photon excites the molecule via an electronic transition. This transition is significantly more probable than to a virtual state and consequently leads to strong peaks. The second is fluorescence, which is a result of electronic excitation from the ground state, after which various radiation-free transitions take place before radiation is emitted in a return to the electronic ground state[10,11] (Figure 6).

Raman peak resolution, or bandwidth, is determined by a number of factors. For a standard sample, frequency is determined by the local chemical environment. This affects the force constant of the chemical bond and therefore the molecular vibrations. Typically, more amorphous or less crystalline materials with less well-defined bonds will have broader peaks, rendering Raman sensitive to crystallinity. Similarly, higher temperatures can affect the peak width[10,11].

Raman spectroscopy can be used to analyse both small molecules and crystals. In crystals, the vibrations of the crystal are best expressed through phonons, which are quasiparticles representing the quantised vibrational modes of the crystal lattice. Raman peaks then correlate to the frequencies of the phonon modes, whose frequencies are also reported in units of cm^{-1} [10,11].

Determination of Raman active modes can be achieved via group theory. Crystal group theory is somewhat more complex than that for molecules and can be analysed via nuclear site group analysis. This method examines the site symmetry of individual atoms within the unit cell, allowing assignment of the individual atoms to appropriate symmetries and consequently irreducible representations via analysis of the available symmetric sites in the unit cell space group. From those individual symmetries the sum total of atomic vibrations can be derived,

and their contributions to the unit cell vibrational modes determined. The derived vibrational modes can then be tested against Raman and IR selection rules[12].

For the materials of interest in this thesis, vibrational modes are denoted as either an "A" type, which are non-degenerate modes that are symmetric with respect to the axis of symmetry, and "E" type, which are doubly degenerate[12].

The Raman technique used in this thesis is confocal Raman microscopy. In confocal microscopy, out-of-focus light is eliminated by use of a pinhole, ensuring that it does not contribute to the signal. For Raman, this is achieved by placing a pinhole aperture between the dichroic mirror and the spectrometer (Figure 6). This permits excellent spatial resolution for the Raman signals[13].

Raman spectra (example Figure 7) were acquired using a Renishaw inVia confocal microscope primarily using a 785 nm 300 mW laser, as well as a 532 nm 50 mW laser and a 633 nm 20 mW laser. Raman spectra were typically gathered at 0.01% power (calibrated to ensure no burning of the samples) for ten minutes (20 accumulations of 30 seconds) at 50x microscope magnification. The Raman microscope was calibrated to silicon at 520 cm^{-1}. Spectra were primarily gathered under an air atmosphere; however, some spectra were acquired under argon in a Raman-compatible cell sealed in a glovebox. Both crystals and powders were mounted on carbon tape, however the laser was positioned entirely on the sample surface. Cosmic rays were removed as needed.

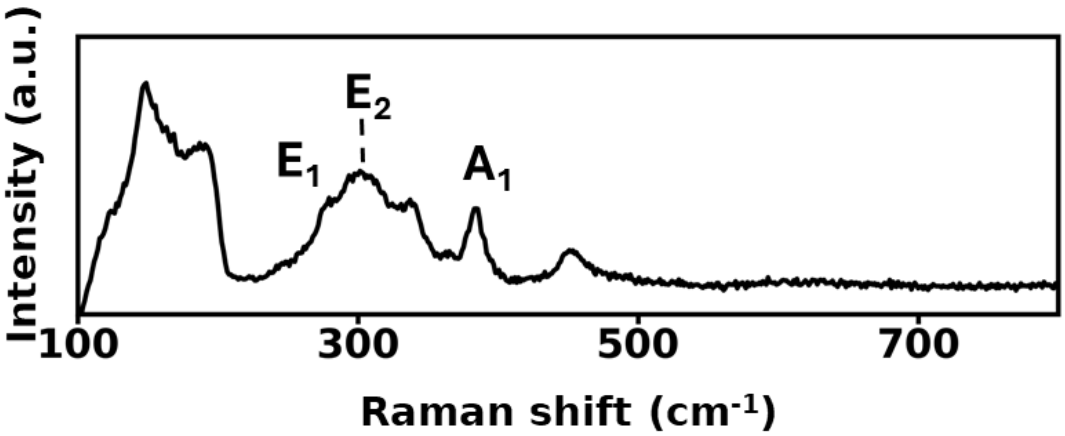


Figure 7. Raman spectrum arising from 3R-NbS_2 (data from Chapter 5). The peaks known to arise from the E and A vibration modes are shown, while other peaks arise from two-phonon effects[14] or the Rayleigh filter cutoff.

3.2 Electrochemical methods

3.2.1 The electrochemical cell

A two-electrode cell consists of a working electrode and a counter electrode. The cell is typically used to examine the response of the working electrode, where the reaction of interest occurs. However, because the measured potential is the potential difference between the working and counter electrodes, the potential of the working electrode cannot be independently controlled or measured[15]. If the counter electrode also serves as the reference electrode, any appreciable current passing through it can polarise its surface and shift its potential. As a result, the applied cell voltage no longer corresponds directly to a well-defined working-electrode potential[15].

Consequently, the three-electrode electrochemical cell is commonly used for the examination of catalytic electrochemical systems. The cell consists of a working, reference and counter electrode (Figure 8). This cell is constructed to examine the response of the working electrode, on which the reaction of interest takes place. In this cell, the current primarily passes through

the working electrode and the counter electrode. The reference electrode is connected via a high impedance circuit, which minimises the current flow between the working and reference electrode[15] thereby avoiding polarisation of the reference electrode. This prevents reference-electrode polarisation from causing shifts in the measured potential.

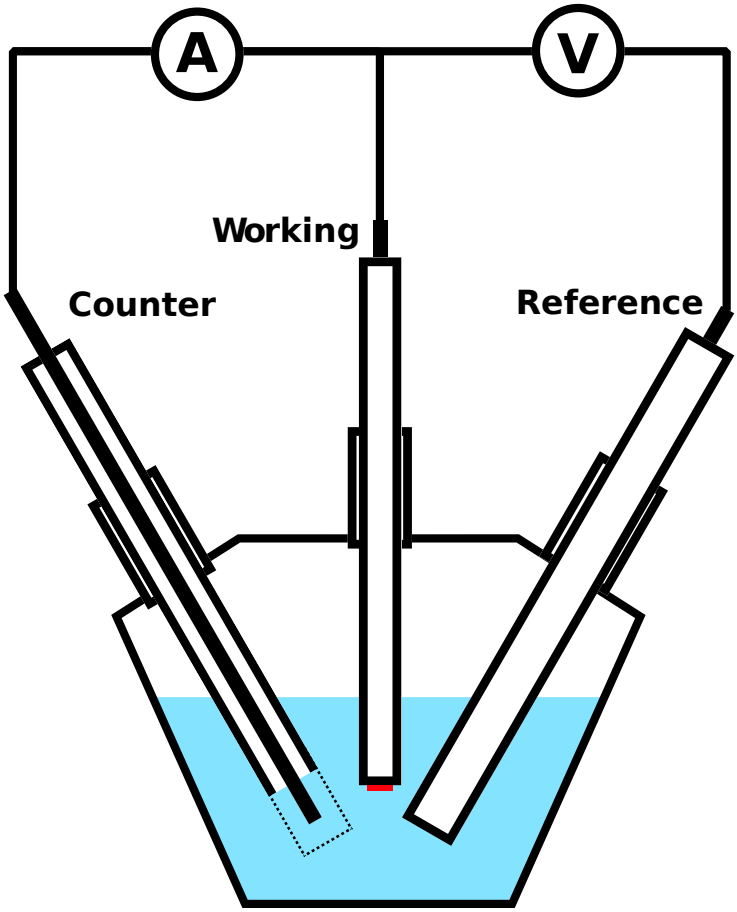


Figure 8. Example three-electrode electrochemical cell. The current flow is measured for the working electrode, while the potential is measured between the working electrode and the reference electrode. The glass frit isolating the counter electrode from the electrolyte is shown by the dotted lines around the counter electrode (black solid line).

When examining hydrogen evolution reaction catalysts, the working electrode is a cathode. Glassy carbon is often used as an electrode substrate due to its poor catalytic activity for the hydrogen evolution reaction and low reactivity to common electrolytes[16]. Historically,

platinum was commonly used as a counter electrode for the hydrogen evolution reaction. However, recent work brought to light the tendency of platinum to dissolve when used in acidic electrolytes, causing the small-scale deposition of platinum onto the working electrode and increasing catalytic activity[17]. Consequently, other counter electrodes such as carbon or ITO (indium tin oxide), typically placed behind a glass frit (finely porous glass, Figure 8), are used[18].

The choice of reference electrode varies. Typical reference electrode systems are placed behind a glass frit to minimise solvent exchange with the main cell while maintaining conductivity. However, some leakage does still occur, which makes solvent compatibility between the cell and reference electrode important. Ideally, the reference electrode filling solution should be maximally similar to the electrolyte, such as mercury-mercury sulfate (Hg/Hg_2SO_4) for sulfuric acid solutions and silver-silver chloride (Ag/AgCl) for hydrochloric acid solutions. This minimises reference potential drift due to changes in the reference electrode solution due to solution slowly leaking through the frit. Care should also be taken to select a reference electrode whose chemistry does not interfere with the chemistry being studied, such as chloride sensitive processes for Ag/AgCl. Recently, a new class of leakless electrodes have been designed. These leakless electrodes can maintain electrical conductivity while preventing solvent exchange between the cell and reference cell solutions[19].

3.2.2 Linear sweep voltammetry, cyclic voltammetry and series chronoamperometry

Two primary methods are used to examine the response of electrocatalytic systems to the application of a potential[15]. Voltammetry measures the change in current, I, as a function of the applied potential, E. Linear sweep voltammetry measures the change in current between an initial potential, E_i and a final potential, E_f by changing the potential at a linear rate between those two potentials. Cyclic voltammetry examines the response of a system when sweeping between E_i and E_f, then sweeps back, reversing the rate of potential change.

Linear sweep voltammetry is commonly used in catalysis to evaluate irreversible reactions, such as the hydrogen and oxygen evolution reactions. Cyclic voltammetry by contrast is typically used to evaluate reversible reactions, such as reversible redox reactions or non-Faradaic processes. The polarisation curves derived from these methods can be used to calculate the kinetic and thermodynamic properties of an electrochemical process[15].

Recently, doubts have been raised in the literature with respect to the use of polarisation curves derived from LSV and CV methods for Tafel analysis of the reactions at the working electrode. This is due to the steady-state assumption inherent to Tafel analyses, and the lack of a true steady state in even slow-rate sweeps. To correct for this, Tafel analyses are executed using polarisation curves derived from series chronoamperometry. In a chronoamperometry experiment, current is measured as a function of time at a set potential (Figure 9).

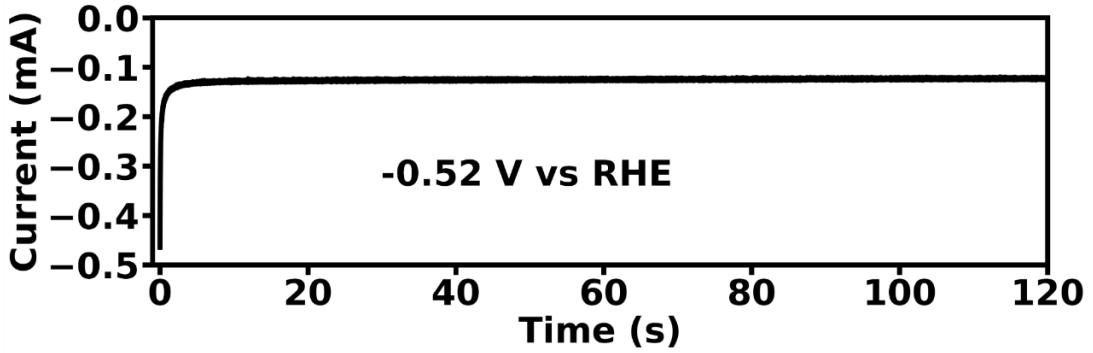


Figure 9: Example chronoamperometry plot (data from a single point in the Chapter 6 series chronoamperometry plot, Figure 4), plotting the current vs time at a set potential (-0.52 V vs RHE). The current at the beginning of the experiment starts off at -0.46 mA and over time its magnitude decreases to a steady state current of approximately -0.13 mA.

Series chronoamperometry (Figure 10) runs a series of chronoamperometry experiments at a potential that varies between E_i and E_f, then selects a specific time in that experiment where all the experiments appear to be in a steady state. The acquired data is a series of current values as

a function of potential and can be analysed in much the same fashion as linear sweep voltammetry[20].

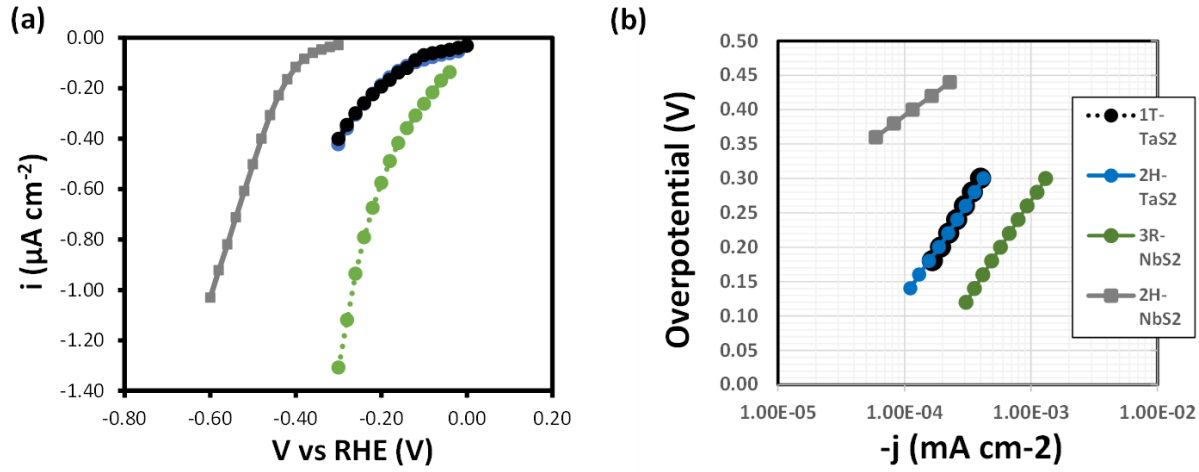


Figure 10. A series chronoamperometry plot (a), plotting the steady state current of a series of chronoamperometry experiments against the potential of the experiments in 0.5 M H_2SO_4 (Chapter 6). Derived Tafel slopes (b) of the series chronoamperometry of various group V transition metal dichalcogenides. Figure replicated from Chapter 6.

The use of series chronoamperometry allows for the evaluation of steady state systems. It is limited by mass-transport concerns; however, this can be mitigated by evaluating at lower current-densities or improving mass transport via various means such as rotating disc electrodes and flow cells. Additionally, the HER and OER reactions are less sensitive to mass transport limitations[20].

3.2.3 Electrochemical Impedance spectroscopy

Understanding the contributions of impedance to cell behaviour is critical to the analysis of essential cell and catalyst properties. While series resistance arising from the impedance of the electrolyte, as well as wire, contact and internal resistances can be easily compensated for either in real time or after the fact, other forms of impedance also arise within the cell, such as

capacitive, inductive and other forms of non-ohmic behaviours. Electrochemical impedance spectroscopy, or EIS, can give us insight into these other processes.

Electrochemical impedance spectroscopy applies a sinusoidal alternating potential to an electrochemical cell (3-5), measuring the current response. The current response takes the form of a sinusoidal wave that has been phase shifted relative to the input wave[15] (3-6).

$$E_t = E_0 \sin(\omega t) \qquad (3-5)$$

$$I_t = I_0 \sin(\omega t - \phi) \qquad (3-6)$$

Where E_t and I_t represent the input potential and current response, I_0 the expected current response at potential E_0, ω the angular frequency, t as time and ϕ as the phase-shift. By keeping the amplitude of the potential input wave small, the system is pseudo-linear, that is in a sufficiently small range of potentials the current appears to change linearly with applied potential[15]. It therefore obeys the law:

$$I = kE \qquad (3-7)$$

Where I is current, E is potential, and k is a constant. This is necessary for equation (3-6) to hold true[15]. This then allows the evaluation of the impedance, Z via the expression:

$$Z = \frac{E_t}{I_t} = Z_0 \frac{\sin(\omega t)}{\sin(\omega t - \phi)} \qquad (3-8)$$

Z_o is defined as E_o/I_o and is a constant scaling factor for impedance. Euler's relationship can be used to express the input potential and response current as complex numbers, which allows the expression of the impedance, Z, as a complex number, which can then be plotted on either a Nyquist plot or a Bode plot[15].

$$Z(\omega) = \frac{E}{I} = Z_0\big(\cos(\phi) + j\sin(\phi)\big) \qquad (3-9)$$

In a Bode plot, the frequency of the sine wave in Hz is plotted against both the absolute values of the impedance ($|Z|$, ohm) and the phase-shift (ϕ, °). More commonly used is the Nyquist plot, which plots the real (Z') and imaginary (Z'') components of the impedance against each other[15,21].

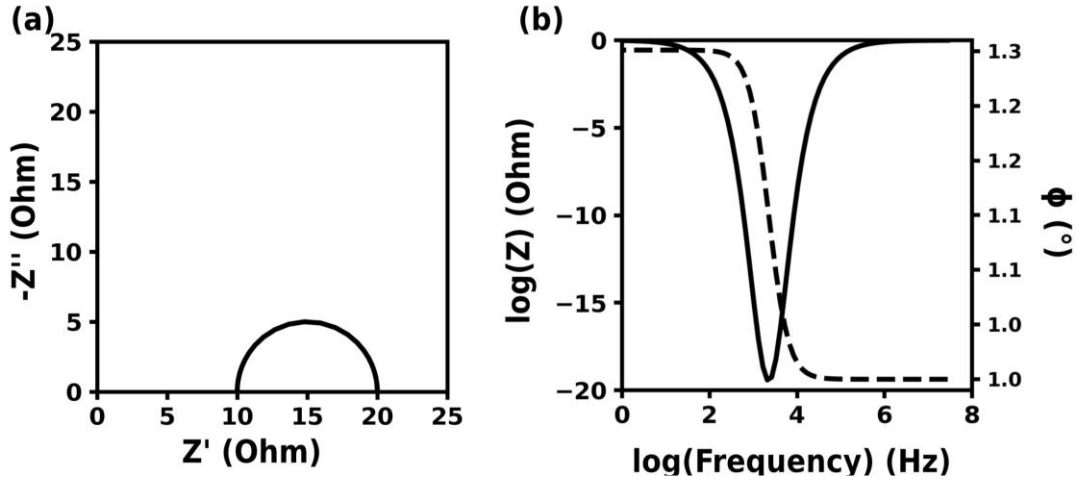


Figure 11. Simulated (via EC-Lab[22]) Nyquist (a) and Bode (b) plots of a Randles cell. The Nyquist plot axes are shown at the same scale, as is typical in the literature. The Bode plot plots the log of the negative impedance (Z) against the log of the frequency (solid line); and the phase angle(ϕ) against the log of the frequency (dashed line).

The impedance behaviour of the system can be modelled by constructing an equivalent circuit. Each element of the equivalent circuit models the behaviour of a proposed element of the cell. By refining the parameters of the model, the data obtained can be replicated and the system understood. EIS fitting therefore requires some understanding of the nature of the cell being analysed to enable a correct model to be constructed and avoid overfitting[15,21].

The classic model for a catalytic cell is the Randles circuit[23] (Figure 11, 12(e)). This incorporates solution resistance (R_s, Figure 12(e)) as an ohmic element in series with a component consisting of a capacitor (C_{dl}) modelling the Helmholtz double-layer capacitive behaviour of the catalyst; in parallel with a resistor modelling the charge transfer resistance of

the sample. The solution resistance can be estimated from the high frequency intercept of the Nyquist plot and can in turn be used to calculate the voltage loss due to resistance, or iR drop.

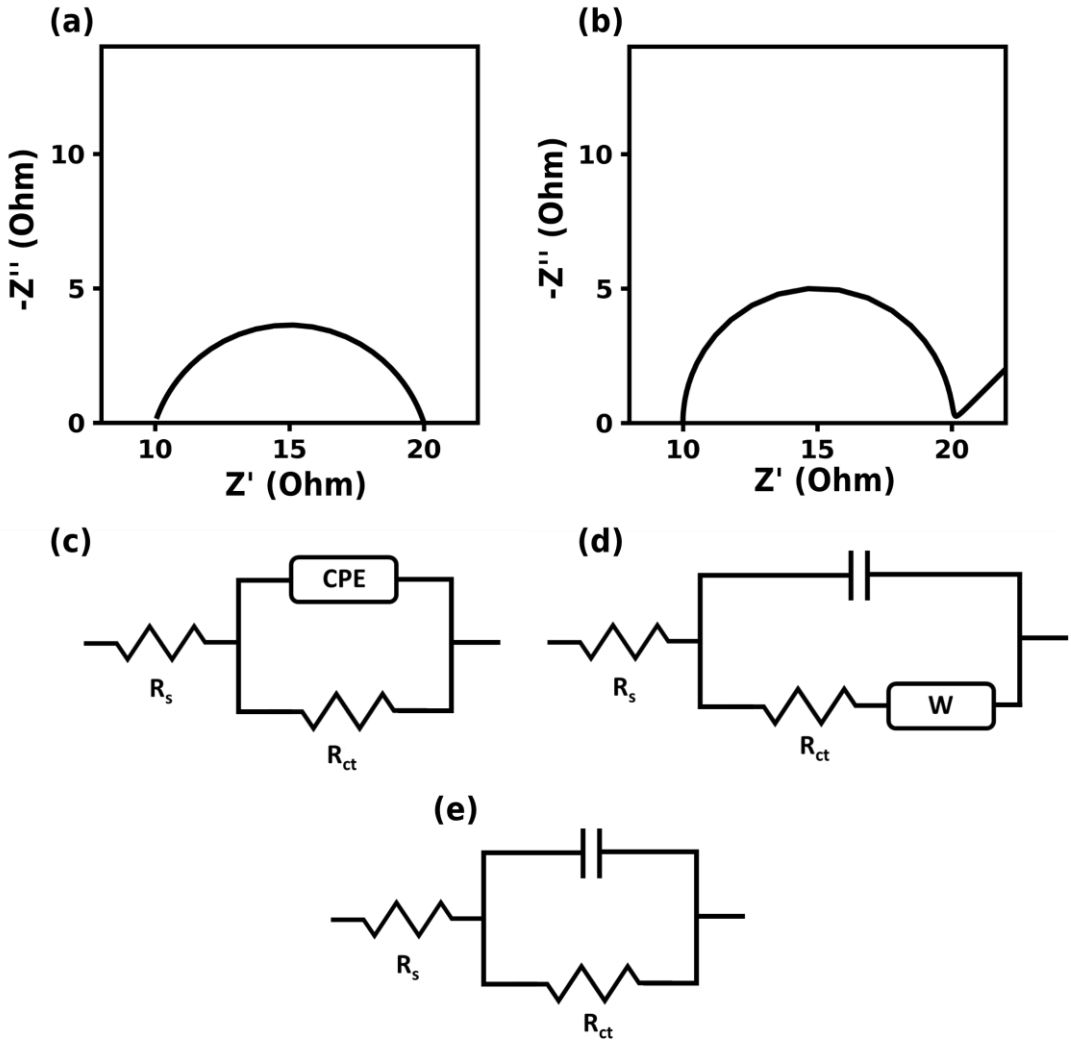


Figure 12. Simulated (via EC-Lab[22]) Nyquist plots of various systems. (a) shows the Nyquist plot of a Randles cell (e) modified with a CPE element replacing the capacitor (c). (b) shows the Nyquist plot of a Randles cell with an additional Warburg component (d). The elements R_{ct} and R_s represent the charge transfer and solution resistance respectively.

The Randles circuit can often be insufficient to describe the behaviour of an electrochemical catalytic system. To describe a more complex system, additional components may have to be added or modified, and the model itself may have to be extended (Figure 12(d)). The Warburg element[21] is one such component used to describe the diffusion layer of a system. The simplest

form, the unbounded Warburg, appears on a Nyquist plot as a 45° line in the low frequency region of the plot and models an infinite diffusion layer. Modifications to the Warburg component include the finite or bounded Warburg for the more likely case of a limited diffusion layer, which in turn is split into the Warburg short (W_s), which models a transmissive (permeable) boundary, and Warburg open (W_o), which models a reflective (impermeable) boundary[21].

The capacitive element describes the impedance of an ideally polarisable electrode, without any reactions taking place at the surface. Many electrodes do not conform to this behaviour, so the capacitive element is often replaced with the constant phase element, or CPE (Figure 12(c)), which takes the form:

$$Z = \frac{1}{Y_o(j\omega)^n} \qquad (3-10)$$

Where Y_o is a parameter containing capacitance information and n defines the extent to which the CPE behaves as an ideal capacitor[21]. At values of n=1, the CPE behaves identically to a double-layer capacitor. The CPE permits for the modelling of more complex capacitors but makes the estimation of the double layer capacitance non-trivial, since the CPE, unlike the capacitive element does not directly describe the double-layer capacitance, instead using Y_o[24–26]. A variety of relations have been proposed to convert the Y_o into double layer capacitance, but the most commonly used are the Brug[27] (3-11) and Hsu-Mansfeld[28] (3-12) equations:

$$C_{dl} = Y_o^{1/n}\left(\frac{1}{R_u} + \frac{1}{R_{ct}}\right)^{\frac{n-1}{n}} \qquad (3-11)$$

$$C_{dl} = Y_o^{1/n}\left(\frac{1}{R_f}\right)^{\frac{n-1}{n}} = Y_o\omega_{z''_{max}}{}^{n-1} \qquad (3-12)$$

Where R_u is the solution resistance, R_{ct} the charge transfer resistance and R_f the film resistance (equivalent to R_{ct} in a Randles cell). $\omega_{Z''_{max}}$ represents the angular frequency at which the imaginary component of the impedance (-Z'') reaches its maximum. The Brug equation (3-11), was derived for a standard Randles cell while under reaction conditions, while the Hsu-Mansfeld equations (3-12) were constructed more generally for films in electrochemical cells. Both the Brug and Hsu-Mansfeld equations are not-uncommonly used outside of their immediate use cases, where they are considered to estimate less accurately the capacitance of the electrode[24].

3.2.4 Electrochemical procedure

Electrochemical data was gathered using a glass three-electrode electrochemical cell and a Gamry 1010E potentiostat. Samples were analysed in a 0.5 molar solution of H_2SO_4 prepared using Milli-Q ultrapure water and sparged with argon. A 99.9995% purity graphite rod from Alfa Aesar inside a glass frit of porosity 4-8 μm was used as the counter electrode. A Gamry mercury-mercury sulfate reference electrode was used, calibrated to a master silver-silver chloride reference electrode. Platinum was excluded from use with the glassware to avoid contamination. EIS data was acquired at 0 V vs RHE between an initial frequency of 1×10^5 Hz and a final frequency of 0.1 Hz at 10 points per decade with an AC voltage amplitude of 10 mV rms. Crystal samples were typically either solid crystals mounted in specialised holders (Chapter 6) or mounted between glassy carbon plates (Chapter 7). Powder samples were drop-cast in isopropanol on a 1x1 cm polished glassy carbon plate using 0.5 wt% Nafion, briefly sonicated, to immobilise the samples. Potentials reported from chronoamperometry, CV and LSV measurements were corrected for iR drop during acquisition. Series chronoamperometry was run for five minutes per point, and reported current values were averaged from the last 30 s of data.

3.3 Synthesis methods

3.3.1 Introduction to Chemical vapour transport

Chemical vapour transport is a synthesis technique used to synthesise pure crystalline solids. The earliest experiments were carried out by Van Arkel and de Boer[29,30] using the hot-wire method, via which a metal iodide in a sealed tube was decomposed on a hot wire to form the pure metal. In general, CVT reactions deposit the most thermodynamically favourable product at the sink, which is typically the cooler zone[30] (Figure 13).

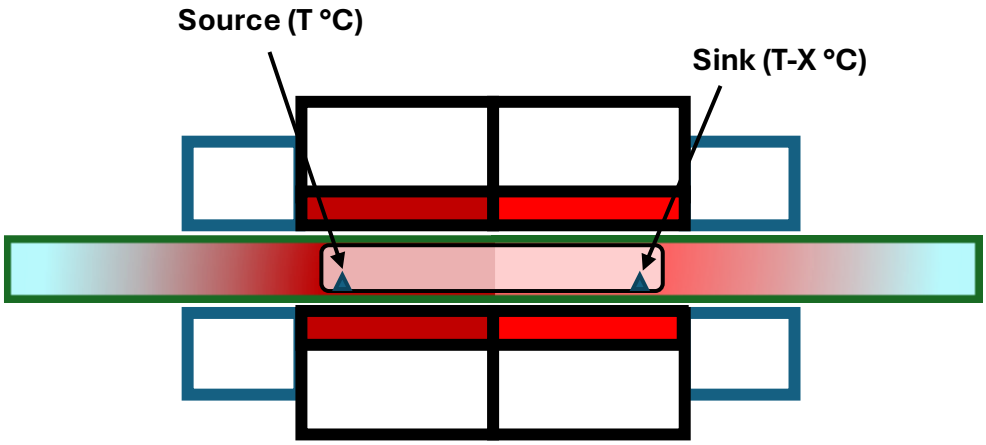


Figure 13. A diagram of a typical CVT setup. A sealed quartz ampoule contains the synthesis material and a transport agent. The tube is differentially heated by a multi-zone tube furnace. A work tube is between the furnace and the ampoule and protects the furnace from damage in case of ampoule failure.

CVT reactions rely on two reactions, which typically occur in a sealed quartz glass vessel. The first reaction is dissolution, where the substance at the source reacts with a volatile species known as the transport agent. The product of the reaction of the transport agent and the source material forms a volatile species that migrates via diffusion to the sink, which is at a different temperature from the source. At the sink, the volatile transport-reactant species either nucleates or reacts with a seed crystal, forming a crystal of the desired product and freeing the transport

agent. In the production of metal chalcogenides, it is common to use as the source materials the precursor powders, namely the metal and sulfur. For these materials, iodine is typically used as the transport agent[30].

In CVT, there are a variety of relevant parameters. Most important are the source and sink temperatures, for which T_{source} controls the rate of dissolution into the transport agent, T_{sink} controls the phase produced and rate of formation, and T_{source}-T_{sink} controls the rate of diffusion. The rate of material formation at the sink is of critical importance – too high a rate can cause the synthesis of polycrystals rather than the typically preferred single crystal. The diameter of the tube and the distance between the source and the sink also contribute to the rate of material formation[30].

3.3.2 Solid-state (powder) synthesis methods

The experimental methods for materials synthesis are as follows. Materials used were vanadium powder, 99.5% (metals basis), tantalum powder, 99.9% (metals basis), sulfur powder, 99.5%, all from Alfa Aesar. Niobium powder, 99.8% was obtained from Merck.

Initial powders of the metal sulfide are produced via a mixture of metal and sulfur in either a 1:2.05 or a 1:2.01 molar ratio. This excess ensures the formation of the layered material and reduces intercalation[30]. Metal powders are hand-ground for 10 minutes in a glovebox, then mixed and ground with sulfur for a further five minutes. In an argon glovebox, iodine (used as a mineralising agent, sufficient for 1 bar of pressure as calculated using the ideal gas equation at the source temperature) is added to a clean quartz tube, followed by the powder mixture, typically 1 g.

The bottom of the tube is cooled with liquid nitrogen for five minutes, then the tube interior is placed under vacuum. Any condensed argon is permitted to boil off, typically via a 5-minute

delay. The tube is then flame sealed under vacuum. The sealed tube is placed in a box furnace, and, dependent on material and desired phase, heated.

3R-NbS_2 and 2H-TaS_2 are heated to 975 °C for 200 hours, then cooled over 48 hours to 700 °C and allowed to stand at that temperature for an additional 48 hours. For 2H-NbS_2 and 1T-TaS_2, the ampoule is heated to 950 °C, removed from the furnace and quenched whole in water.

Inside a glovebox, the ampoule is broken from the top, the powders retrieved and optionally cleaned in dimethyl carbonate to remove any remaining iodine. Little or no deposition elsewhere is seen, as the heating is even across the ampoule, and the powders are retrieved from the bottom of the ampoule.

3.3.3 CVT methods

A quartz tube of length 20 cm was prepared as outlined for the solid-state synthesis. Sufficient iodine is added for one bar of pressure (as calculated using the ideal gas equation) at source temperatures. The powders are placed in the source end of the tube, and care is taken to ensure powders are not elsewhere in the tube. The tube is then sealed, as outlined above, and added to a two- or three-zone tube furnace. The source and sinks are heated differently, depending on desired material, phase and size of crystal (Figure 13). The CVT source and sink temperatures are outlined in the table below:

Table 1. Table of source and sink temperatures for TMD synthesis via CVT

Material	Source temperature (°C)	Sink temperature (°C)
3R-NbS_2	800	700
2H-NbS_2	950	850
2H-TaS_2	750	700
1T-TaS_2	950	850

After growth, the ampoule is allowed to cool, or for 2H-NbS_2 and 1T-TaS_2, is quenched in water. After cooling, the ampoule is broken in the centre. The un-transported powders are retrieved from the source, and separately, the transported crystals are retrieved from the sink and optionally cleaned in dimethyl carbonate to remove any remaining iodine. Dimethyl carbonate solution turns orange when iodine is dissolved within it. Alternatively, the crystals are heated to 80°C in vacuum to remove the iodine.

3.3.4 Hydrothermal synthesis

Hydrothermal synthesis is a method by which precursor materials are dissolved in water then placed inside a reaction vessel. The solution is then heated to temperatures greater than water's boiling point, at which point the materials react. Hydrothermal synthesis is often used to produce nanoparticles, and the morphology and size of those particles is highly sensitive to reaction conditions such as temperature, pH and reactant concentration[31].

Hydrothermal reactions were carried out using Hastelloy-C276 and stainless-steel hydrothermal reactors. In a typical reaction, 5 mmol of ammonium metavanadate (NH_4VO_3) and 25 mmol of thioacetamide were added to 24 ml of water and 6 ml of 30% $NH_{3(aq)}$ and

stirred using a Teflon stirrer bar for one hour. The subsequent solution was transferred to the reactor and heated to 160 °C for twelve hours. In the C276 reactor, reactions were conducted with and without NH_3 as an addition to the synthesis solution, while in the stainless-steel reactor, reactions were conducted both with and without cetyltrimethylammonium chloride (CTAC, 6 ml of 25 wt% in H_2O) as a co-catalyst. All reactions in the stainless-steel reactor were conducted using a Teflon liner, while some reactions in the C276 reactor were conducted with bare walls, and others with a borosilicate liner. All reactions were carried out in air.

3.4 References

(1) Moulder, J. F.; Stickle, W. F.; Sobol, P. E.; Bomben, K. D. *Handbook of X-ray Photoelectron Spectroscopy: A Reference Book of Standard Spectra for Identification and Interpretation of XPS Data*; Perkin-Elmer Corporation, 1992.

(2) Stevie, F. A.; Donley, C. L. Introduction to X-Ray Photoelectron Spectroscopy. *Journal of Vacuum Science & Technology A* **2020**, *38* (6).

(3) Morgan, D. J. XPS Insights: Asymmetric Peak Shapes in XPS. *Surface and Interface Analysis* **2023**, *55* (8), 567–571.

(4) Hüfner, S. *Photoelectron Spectroscopy: Principles and Applications*; Springer Science & Business Media, 2013.

(5) Briggs, D. *Surface Analysis of Polymers by XPS and Static SIMS*; Cambridge University Press, 1998.

(6) Fairley, N.; Fernandez, V.; Richard-Plouet, M.; Guillot-Deudon, C.; Walton, J.; Smith, E.; Flahaut, D.; Greiner, M.; Biesinger, M.; Tougaard, S.; et al; Systematic and Collaborative Approach to Problem Solving Using X-Ray Photoelectron Spectroscopy. *Applied Surface Science Advances* **2021**, *5*, 100112.

(7) George, G. N.; Pickering, I. J. *X-Ray Absorption Spectroscopy*; De Gruyter: Berlin, Boston, 2025. https://doi.org/doi:10.1515/9783110570441.

(8) Smith, J. W.; Saykally, R. J. Soft X-Ray Absorption Spectroscopy of Liquids and Solutions. *Chemical reviews* **2017**, *117* (23), 13909–13934.

(9) Pecharsky, V. K.; Zavalij, P. Y. *Fundamentals of Powder Diffraction and Structural Characterization of Materials*; Springer, 2003.

(10) Ferraro, J. R. *Introductory Raman Spectroscopy*; Elsevier, 2003.

(11) Vandenabeele, P. *Practical Raman Spectroscopy: An Introduction*; John Wiley & Sons, 2013.

(12) Rousseau, D. L.; Bauman, R. P.; Porto, S. P. S. Normal Mode Determination in Crystals. *Journal of Raman Spectroscopy* **1981**, *10* (1), 253–290. https://doi.org/10.1002/jrs.1250100152.

(13) Giridhar, G.; Manepalli, R.; Apparao, G. Confocal Raman Spectroscopy. In *Spectroscopic methods for nanomaterials characterization*; Elsevier, 2017; pp 141–161.

(14) McMullan, W. G.; Irwin, J. C. Raman Scattering from 2H and 3R–NbS2. *Solid State Communications* **1983**, *45* (7), 557–560. https://doi.org/10.1016/0038-1098(83)90426-X.

(15) Bard, A. J.; Faulkner, L. R.; White, H. S. *Electrochemical Methods: Fundamentals and Applications*; John Wiley & Sons, 2022.

(16) Benck, J. D.; Pinaud, B. A.; Gorlin, Y.; Jaramillo, T. F. Substrate Selection for Fundamental Studies of Electrocatalysts and Photoelectrodes: Inert Potential Windows in Acidic, Neutral, and Basic Electrolyte. *PLoS ONE* **2014**, *9* (10), e107942. https://doi.org/10.1371/journal.pone.0107942.

(17) Chen, R.; Yang, C.; Cai, W.; Wang, H.-Y.; Miao, J.; Zhang, L.; Chen, S.; Liu, B. Use of Platinum as the Counter Electrode to Study the Activity of Nonprecious Metal Catalysts for the Hydrogen Evolution Reaction. *ACS energy letters* **2017**, *2* (5), 1070–1075.

(18) Bird, M. A.; Goodwin, S. E.; Walsh, D. A. Best Practice for Evaluating Electrocatalysts for Hydrogen Economy. *ACS Applied Materials & Interfaces* **2020**, *12* (18), 20500–20506.

(19) Walker, N. L.; Dick, J. E. Leakless, Bipolar Reference Electrodes: Fabrication, Performance, and Miniaturization. *Analytical chemistry* **2021**, *93* (29), 10065–10074.

(20) Anantharaj, S.; Noda, S.; Driess, M.; Menezes, P. W. The Pitfalls of Using Potentiodynamic Polarization Curves for Tafel Analysis in Electrocatalytic Water Splitting. *ACS Energy Letters* **2021**, *6* (4), 1607–1611.

(21) Macdonald, J. R.; Johnson, W. B.; Raistrick, I.; Franceschetti, D.; Wagner, N.; McKubre, M.; Macdonald, D.; Sayers, B.; Bonanos, N.; Steele, B.; et al. *Impedance Spectroscopy: Theory, Experiment, and Applications*; John Wiley & Sons, 2018.

(22) *EC-Lab Software*, Version 11.62, BioLogic Science Instruments, 2025

(23) Randles, J. E. B. Kinetics of Rapid Electrode Reactions. *Discuss. Faraday Soc.* **1947**, *1* (0), 11–19. https://doi.org/10.1039/DF9470100011.

(24) Chang, B.-Y. Conversion of a Constant Phase Element to an Equivalent Capacitor. *J. Electrochem. Sci. Technol* **2020**, *11* (3), 318–321. https://doi.org/10.33961/jecst.2020.00815.

(25) Gateman, S. M.; Gharbi, O.; Gomes de Melo, H.; Ngo, K.; Turmine, M.; Vivier, V. On the Use of a Constant Phase Element (CPE) in Electrochemistry. *Current Opinion in Electrochemistry* **2022**, *36*, 101133. https://doi.org/10.1016/j.coelec.2022.101133.

(26) Lasia, A. The Origin of the Constant Phase Element. *The journal of physical chemistry letters* **2022**, *13* (2), 580–589.

(27) Brug, G.; van den Eeden, A. L.; Sluyters-Rehbach, M.; Sluyters, J. H. The Analysis of Electrode Impedances Complicated by the Presence of a Constant Phase Element. *Journal of electroanalytical chemistry and interfacial electrochemistry* **1984**, *176* (1–2), 275–295.

(28) Hsu, C.; Mansfeld, F. Concerning the Conversion of the Constant Phase Element Parameter Y into a Capacitance. *Corrosion* **2001**, *57* (9), 747–748.

(29) Van Arkel, A.; de Boer, J. H. Darstellung von Reinem Titanium-, Zirkonium-, Hafnium- Und Thoriummetall. *Zeitschrift für anorganische und allgemeine Chemie* **1925**, *148* (1), 345–350.

(30) Binnewies, M.; Glaum, R.; Schmidt, M.; Schmidt, P. *Chemical Vapor Transport Reactions:* DE GRUYTER, 2012. https://doi.org/10.1515/9783110254655.

(31) Li, J.; Wu, Q.; Wu, J. Synthesis of Nanoparticles via Solvothermal and Hydrothermal Methods. In *Handbook of nanoparticles*; Springer, 2016; pp 295–328.

Chapter 4. Computational Methods

4.0 Introduction

This chapter discusses the computational techniques used to model the behaviour of TMDCs. This modelling is essential to many applications. Specific to this thesis is modelling the structure and electronic structure of the TMDs, (Chapter 6) as well as the calculation of phonon modes to attempt to elucidate the VS_2 Raman spectrum (Chapter 7 & Appendix, section A.2).

4.1 Methodology

4.1.1 The Schrödinger equation and atomic systems

At the heart of theoretical chemistry is the solution to the Schrödinger equation:

$$\hat{H}\Psi = E\Psi \tag{4-1}$$

Here, $\hat{H}$ is the Hamiltonian operator, E the corresponding eigenvalue representing the system energy and Ψ is the eigenfunction and the system's wavefunction. This operator describes the various interactions of the system components:

$$\hat{H}_{elec} = -\frac{1}{2}\sum_{i}^{N}\nabla_i^2 - \sum_{i}^{N}\sum_{A}^{M}\frac{Z_A}{r_{iA}} + \frac{1}{2}\sum_{i}^{N}\sum_{j\neq i}^{N}\frac{1}{r_{ij}} = \hat{T} + \hat{V}_{Ne} + \hat{V}_{ee} \tag{4-2}$$

Where the terms describe in order the kinetic energy of the electrons ($\hat{T}$), nucleus-electron interactions ($\hat{V}_{Ne}$) and electron-electron interactions ($\hat{V}_{ee}$). The equation assumes the Born-Oppenheimer approximation, where the nuclei are fixed in space, thereby eliminating the nuclear kinetic energy and interaction terms. The equation above (eq. 4-2) and all subsequent equations in this chapter are constructed using atomic units[1,2].

No method to exactly solve the Schrödinger equation for multi-electron systems is known. This is due to the electron-electron interactions, which are a many-body problem. The variational

principle states that a lower energy wave-function is always a more correct description of the ground state than a higher energy wave function. By using an averaged value for the electron-electron repulsion, the equation can be solved iteratively using the self-consistent field, or SCF method, where an initial configuration of electron orbitals is guessed, solved for, and then iterated upon until reaching a suitable convergence. The Hartree-Fock method uses these approximations and techniques to approximate the system wavefunction using a Slater determinant constructed from one-electron orbitals, which is then solved iteratively using the SCF method. Despite these solutions, solving computational chemistry problems using the Hartree-Fock method is extremely computationally expensive for systems with more than a trivial number of electrons[1,2].

4.1.2 Density Functional Theory

Density functional theory (DFT) relies on replacing the complex N-electron wave function (eq. 4-2) with electron density. This relies on two theorems, proven by Hohenberg and Kohn in 1964[3]. First, that the external potential of a system of interacting electrons is uniquely determined by $\rho(r)$ up to a given constant, where $\rho(r)$ represents the electron density of the system, expressed as a three-coordinate system. The second theorem is that the variational principle applies to the electron density, such that the density that minimises the total energy functional corresponds to the true ground state of the system[1,2].

Kohn and Sham used these theorems to construct a system of non-interacting single electron orbitals (ϕ_i). The sum of the square modulus of the occupied orbitals is equal to the overall electron density of the system ($\rho(\boldsymbol{r})$).

$$\rho(\boldsymbol{r}) = \sum_{i}^{N} |\phi_i(\boldsymbol{r})|^2 \qquad (4\text{-}3)$$

These single electron orbitals satisfy the Kohn-Sham equations:

$$\hat{f}^{KS}\phi_i(\boldsymbol{r}) = \epsilon_i\phi_i(\boldsymbol{r}) \tag{4-4}$$

$$\hat{f}^{KS} = -\frac{1}{2}\nabla^2 + v(\boldsymbol{r}) + v_H(\boldsymbol{r}) + v_{XC}(\boldsymbol{r}) \tag{4-5}$$

Where $\hat{f}^{KS}$ is the one-electron Kohn-Sham operator, ϵ_i is the orbital eigenvalue (used as energy when calculating orbital energies, e.g. in density of states calculations), and ϕ_i is the one-electron orbital, analogous to the equivalent Hartree-Fock equations. In eq. 4-5, ∇^2 represents the Laplacian, while $v(\boldsymbol{r})$, $v_H(\boldsymbol{r})$, and $v_{XC}(\boldsymbol{r})$ represent different potentials, with $v(\boldsymbol{r})$ representing the sum of the contributions from the electron-nucleus Coulomb interactions, $v_H(\boldsymbol{r})$ describing the Coulomb repulsion between the electron i and the total electron density and $v_{xc}(\boldsymbol{r})$ representing the exchange-correlation potential, which corrects for interactions neglected elsewhere. These neglected interactions include the depletion of density due to Pauli exclusion of other electrons as well as corrections to kinetic energy from the assumption of non-interaction of electron orbitals[1,2].

The electron-nucleus interactions are given by the potential:

$$v(\boldsymbol{r}) = -\sum_A \frac{Z_A}{|\boldsymbol{r} - \boldsymbol{R}_A|} \tag{4-6}$$

Where Z_A is the charge of the nucleus A, and R_A the position of the same. The Hartree potential is:

$$v_H(\boldsymbol{r}) = \int \frac{\rho(\boldsymbol{r}')}{|\boldsymbol{r} - \boldsymbol{r}'|}\, d^3\, r' \tag{4-7}$$

Finally, the exchange-correlation potential is a functional derivative which takes the form:

$$v_{XC}(\boldsymbol{r}) = \frac{\delta E_{XC}[\rho(\boldsymbol{r})]}{\delta \rho(\boldsymbol{r})} \tag{4-8}$$

The correct functional E_{XC} to allow for evaluation of the exchange-correlation potential is not known, so various alternatives have been proposed. Kohn and Sham initially proposed the local density approximation, or LDA, where the potential is equal to the E_{XC} of a theoretical uniform electron gas. The LDA suffers from overbinding, as the assumption of a uniform electron gas does not hold for atomic systems. Consequently, the LDA can deviate from experimental atomisation energies by as much as 1.5 eV[2]. More complex exchange-correlation functionals have been constructed which allow for greater accuracy. This is known as the "Jacob's ladder" of functionals, where each rung represents a more accurate class of functionals. Of interest in this thesis are the GGA and meta-GGA functionals. GGA incorporates the gradient of the electron density, thereby reducing the calculated strength of the bonds and providing more accurate estimations of the bond-energy. However, the estimation of the d-band orbital energies remains poor, causing notoriously poor estimation of bandgaps[4,5]. Meta-GGA functionals such as SCAN are the next rung up the ladder, and function by explicitly including second-order gradient (Laplacian) of the electron density or kinetic energy density[1]. These functionals are regarded as more accurate than GGAs for metal solids, but typically, although not universally, perform worse at modelling unit cell parameters such as bond length and cell dimensions[6,7].

In practice, in DFT the electron density and energy of an atomic system is calculated via the SCF method. An initial electron density is constructed and the Kohn-Sham Hamiltonian constructed ($\hat{f}_0^{KS}$) using a chosen functional to allow for the description of the exchange potential. A new set of wavefunctions are then obtained by solving the Kohn-Sham equations using $\hat{f}_0^{KS}$ to obtain $\phi_{1,i}$, where $\phi_{1,i}$ is the set of one-electron wavefunctions resulting from the first iteration, and subsequently the resulting electron density ρ_1. This begins a series of iterative

cycles where the density acquired in the current cycle is mixed with the density acquired in the last cycle to obtain new $\hat{f}_n^{KS}$. The obtained electron densities ρ_n are compared with the previous cycle's density ρ_{n-1} until the new density is sufficiently similar. The system properties can then be obtained from the resulting electron densities and orbitals[1,2].

4.1.3 Dispersion interactions

Dispersion interactions, also known as London forces, are of particular importance for layered compounds. Dispersion forces arise from the formation of instantaneous temporary dipoles due to perturbations originating in electron correlation affecting the charge distributions in nearby atoms. Classical dispersion interactions take the general form

$$V_{dispersion} = -\frac{C}{r^6} \tag{4-9}$$

Where r is the distance between the atoms and C represents various physical constants. GGA functionals are unable to effectively model dispersion forces, and even meta-GGA are unable to consistently model these forces. Consequently, it is often necessary to add an empirical or semi-empirical correction to the energy of the final state to compensate. Early corrections include the Grimme 2006 D2 method (G06)[8] as well as the Tkatchenko and Scheffler (TS) model[9]. A later modification to the TS correction is known as the many-body dispersion or MBD correction, which corrects TS overestimation of dispersion energy[10].

4.1.4 Plane-wave cutoff and k-point spacing.

DFT calculations in crystals are typically conducted in reciprocal space. As a consequence of the Bloch theorem, the wavefunction of an infinite crystal can be represented as a finite number of occupied electronic states per point in reciprocal space (k-space), sampled at infinite points. Since the wavefunction smoothly varies within the reciprocal space primitive unit cell (the first Brillouin zone), a sufficiently dense sampling of points in k-space (k-points) can adequately

reproduce the wavefunction of the infinite lattice. Denser sampling can more accurately reproduce the wavefunction at the cost of greater computational expense[11].

Bloch's theorem allows us to express the wavefunction as a sum of plane waves. In principle, an infinite number of plane waves is required, however only plane waves with a small kinetic energy contribute significantly to the wavefunction. This allows the user to choose an energy at which to cut-off the basis set[12]. Smaller basis sets are computationally cheaper[11].

4.1.5 Pseudopotentials

Each electronic orbital has an associated computational cost. To reduce this computational burden, it is possible to separate out the valence electrons, which are actively involved in bonding, from the core electrons, which are not. The core electron's wavefunctions remain broadly similar regardless of the structure of the system and hence are approximated by pre-constructed pseudopotentials, which smooths/slows the variation of the wavefunction near the core, reducing the number of planewaves needed to approximate it. This is known as the frozen core approximation. In norm-conserving pseudopotentials, the total charge of the pseudo wave function is equal to the charge of the all-electron wave function for an equivalent atom. By contrast, ultrasoft pseudopotentials relax the norm conservation. Ultrasoft pseudopotentials do not need to incorporate as many plane waves but are more complex and consequently more difficult to implement for the calculations of certain properties, like phonon and NMR calculations[13].

4.1.6 Density functional perturbation theory

As described in Chapter 3, the frequency of phonons corresponds to the frequency of the Raman and infra-red peaks in materials. Phonon modes are also essential to understanding charge- and heat-transport properties. Additionally, phonons are essential for predicting material stability,

as structure with phonons with calculated negative (imaginary) modes are typically unstable. As such, the calculation of phonons is an important task.

Calculating phonon modes can be computationally expensive. One approach to this problem is the finite-displacement method, where the system's atoms are perturbed, and the resulting changes in energies and forces used to calculate the vibrational modes. This is however extremely expensive computationally, necessitating the use of supercells to obtain accurate results[14].

One alternative to this is density functional perturbation theory, DFPT. DFPT constructs equations from the linearisation of the Kohn-Sham equations, that is the construction of equations that evaluate the linear response of a system to perturbations. This system of equations permits the decoupling of the perturbations of different wavelengths, eliminating the need to use supercells and greatly reducing computational complexity[15].

4.2 Calculations

The materials NbS_2, TaS_2 and VS_2 were modelled in all experimentally available phases (2H-NbS_2, 3R-NbS_2, 2H-TaS_2, 1T-TaS_2, 1T-VS_2). All calculations were conducted with the CASTEP[3,11,16–19] DFT code. Initial cells were obtained from the ICSD[20]. Plane wave energy cutoff and k-point spacing were converged for single point energy, where convergence was achieved once the changes in total energy dropped below ca. 1×10^{-5} eV. The choice in single point convergence was set arbitrarily to permit for purposeful convergence in later calculations. Cell geometry was subsequently optimised using both the PBE[21] and rSCAN[4] functionals, and converged to cell parameters, where cell parameters were converged to 0.01 Å. For rSCAN calculations, the effect of the fine grid scale was also checked. All PBE and rSCAN calculations used the CASTEP default pseudopotentials generated on the fly, unless specified otherwise.

4.2.1 1T-VS_2

For the single point convergence, a k-point spacing[17] of 0.025 $Å^{-1}$ and a plane-wave energy cut-off of 900 eV were found to be sufficient to converge phonon calculations to within a single wavenumber. rSCAN cells were converged at a coarser k-point spacing of 0.027 $Å^{-1}$, with the same plane-wave energy cut-off of 900 eV (Figure 1). The fine grid scale was varied between 1.0 and 3.0 at intervals of 0.2, and was found to be converged, with the changes in energy much reduced with denser k-point spacing and energy cutoff. Single point and geometry optimisation convergence was also conducted with the NCP19 norm-conserving pseudopotential for use in phonon calculations.

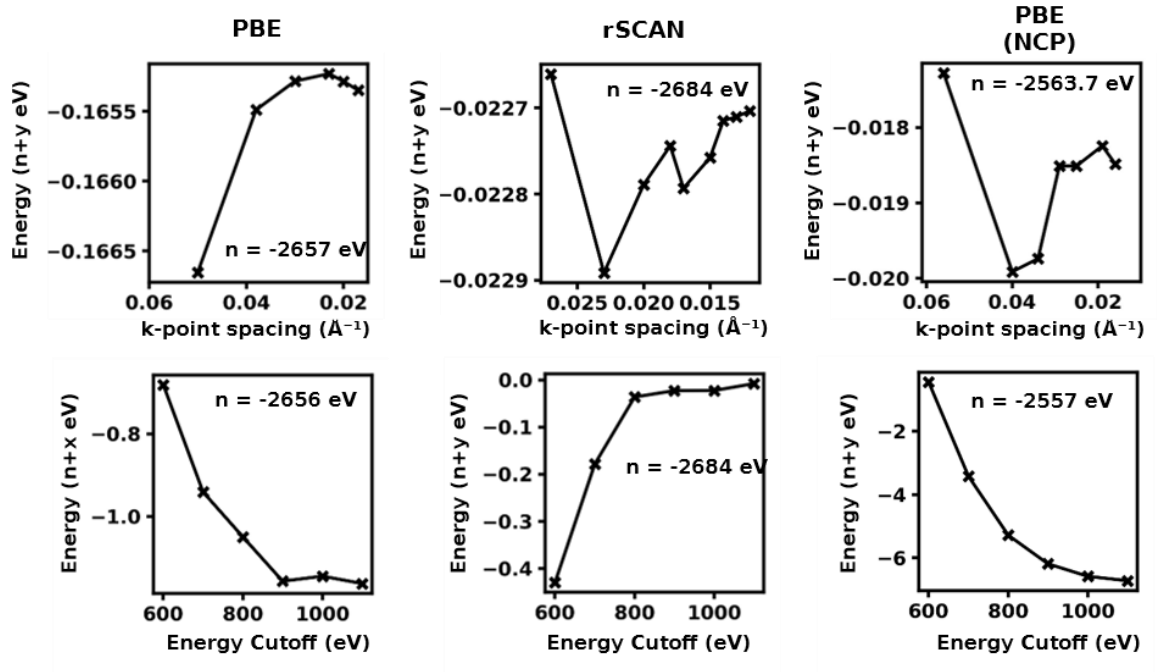


Figure 1: Convergence of the k-point spacing (above) and energy cutoff parameters (below). The k-point spacing was converged at an energy cutoff of 900 eV, while the energy cutoff was converged at a k-point spacing of 0.025 $Å^{-1}$ and 0.027 $Å^{-1}$ for PBE and rSCAN respectively.

Geometry optimisation for 1T-VS_2 was conducted using an ICSD cell (collection code 651361 [22]) for the initial configuration. Geometry optimisation was run with and without dispersion

corrections using the settings from the single point energy convergence. For the PBE optimised cell, the G06 [8] and TS [9] dispersion corrections were used. For the rSCAN functional, the MBD [23] dispersion correction was used. Geometry optimisations were tested for convergence by increasing plane wave energy cut-off and k-point spacing and confirming no change to the resultant cell dimensions. Cell vectors *a* and *b* (Figure 2) were constrained to be equal to each other, while cell vector *c* was constrained to equal the ICSD experimental value where dispersion corrections were not used. For all geometry optimisations in all materials, cell angles were constrained to equal the initial values.

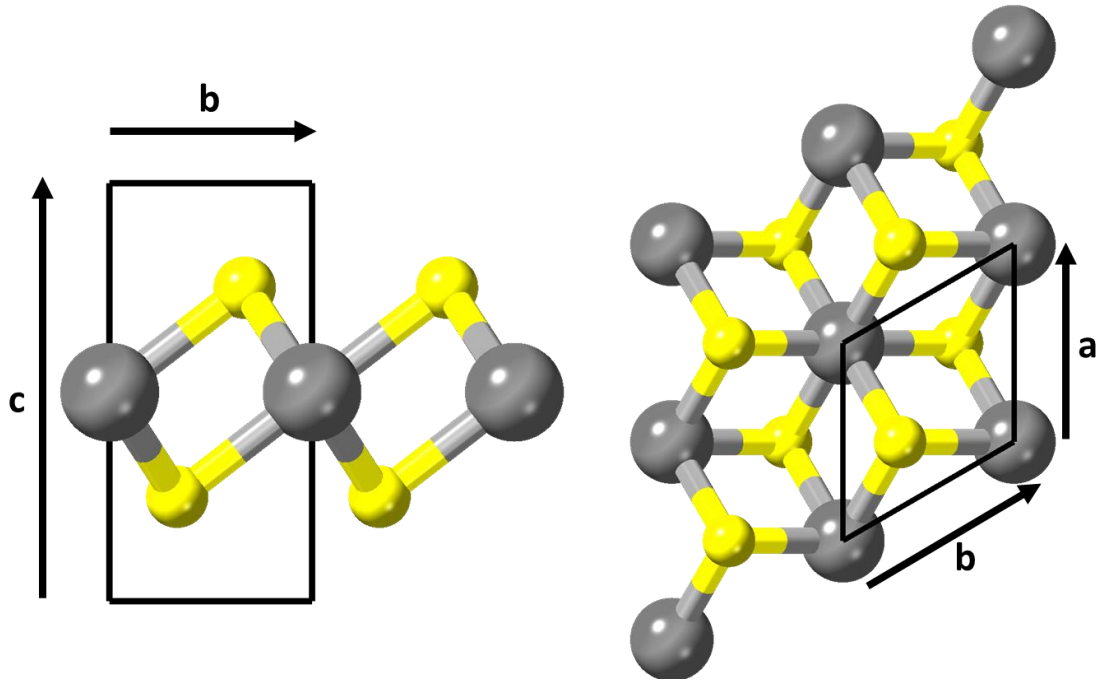


Figure 2: Structure of VS_2. Cell axis a, b and c are shown. Cell axes a and b were constrained to be equal, while the c axis was constrained where dispersion corrections were not used. Images were generated using CrystalMaker® from calculated structures.

Geometry optimisation (results in Table 1) indicates that PBE with dispersion corrections was effectively equivalent to rSCAN with respect to the cell vectors *a* and *b* (Figure 2), and the sulfur-vanadium bond length, with a difference of less than 1 picometre between the

functionals. The *c* axis (out-of-plane) was the differentiating factor, with PBE-G06 overestimating the *c* axis by 0.074 Å, while the TS correction underestimates the value of the *c* axis by a larger 0.275 Å. The rSCAN functional with the MBD dispersion correction comes closest, with a *c* axis underestimation of 0.063 Å (Table 1).

Geometry optimisations for the rSCAN and PBE functionals with the *c* axis not fixed were also run. The *c* axis was found to expand greatly, and the process stopped once obviously unphysical.

Table 1: Cell geometry after optimisation of the VS_2 cells and the ICSD experimental values for the same cells. The differences to the ICSD values are shown in brackets. The column labelled a,b denotes the cell lengths parallel to the basal plane, as shown in Figure 2, while c is the axis perpendicular to the basal plane. During the geometry optimisation, a and b are constrained to equal one another, and the angles of the ICSD cell are also maintained. Entries with a dash (-) denote that the axis was frozen at the ICSD value.

	Cell axis (*a,b*) length (Å)	**Cell axis (*c*) length (Å)**	**S-V bond length (Å)**
PBE	3.259 (+0.042)	-	2.363 (+0.014)
PBE-G06	3.241 (+0.024)	5.830 (+0.074)	2.359 (+0.010)
PBE-TS	3.225 (+0.008)	5.480 (-0.275)	2.351 (+0.002)
rSCAN	3.251 (+0.034)	-	2.358 (+0.009)
rSCAN-MBD	3.242 (+0.025)	5.692 (-0.063)	2.350 (+0.001)
ICSD (experimental)	3.217	5.755	2.349

The densities of state (DOS) of the converged, geometry optimised cells were obtained using the PBE, rSCAN and rSCAN-MBD corrected functionals. Plane wave energy cut-off was 900 eV for all configurations. A k-point and spectral k-point spacing of 0.027 $Å^{-1}$ was used for the PBE electronic structure calculations, while the rSCAN calculations used a k-point spacing of 0.025 $Å^{-1}$ with a spectral k-point spacing of 0.023 $Å^{-1}$. The electronic structures obtained for VS_2 are shown in Figure 3 below. All three functionals find the material to be metallic, while

the projected density of states shows a large density of states directly above and below the Fermi level.

The rSCAN functional with the MBD dispersion correction was used for electronic structure calculations due to its better ability to accurately reproduce the d-band in transition metal electronic structures[6].

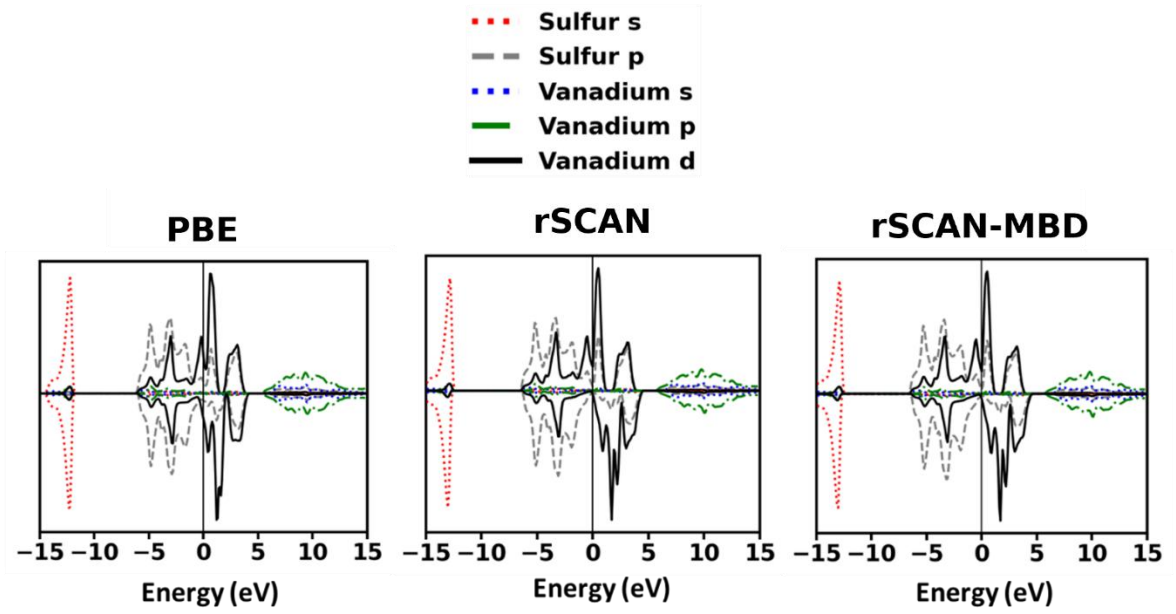


Figure 3: Calculated (CASTEP) PDOS of 1T-VS2 for the PBE and rSCAN functionals as well as the rSCAN functional with the MBD dispersion correction. The Fermi level in all plots is at 0 eV.

Single-point phonon calculations[24] for VS_2 were conducted using the DFPT method as implemented in CASTEP[18]. A higher precision for geometry optimisation is necessary for optimal phonon calculations and the NCP19 pseudopotentials were used. A k-point spacing of 0.02 $Å^{-1}$ and a plane-wave energy cut-off of 1200 eV was found to be sufficient, and the PBE functional with the G06 dispersion correction was used for reasons of compatibility in the software. The phonon calculation was converged via plane-wave energy cut-off and k-point spacing, and was converged to phonon mode frequencies, with a convergence criterion of 1

cm^{-1}. Small (magnitude less than 0.1 cm^{-1}) negative acoustic phonon modes were observed which were caused by numerical errors.

4.2.2 NbS_2

Only the rSCAN functional was used to evaluate the NbS_2 system. For the single point convergence, a k-point spacing of 0.03 $Å^{-1}$ and a plane-wave energy cut-off of 900 eV were found to be sufficient (Figure 4). Geometry optimisations for both 2H-NbS_2 and 3R-NbS_2 were run with and without the MBD dispersion corrections, using the single-point energy convergence parameters. Modelled structural parameters for these cells can be seen in Table 2. Electronic structure calculations were found to be converged by comparison of the modelled densities of state at a plane wave cut-off of 900 eV and a k-point spacing of 0.025 $Å^{-1}$ with a spectral k-point spacing of 0.013 $Å^{-1}$.

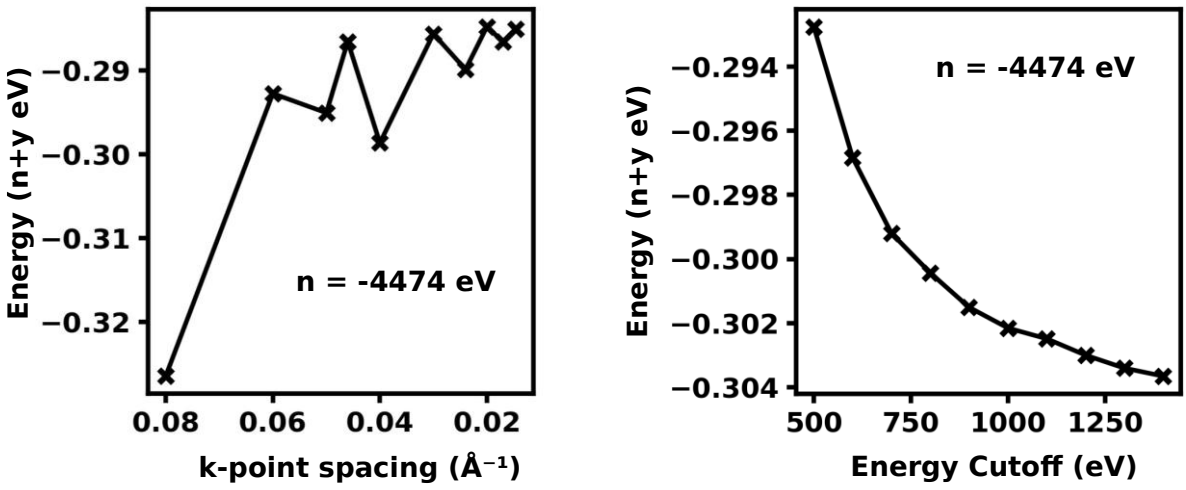


Figure 4. Convergence of the k-point spacing and energy cutoff parameters. The system was determined to be converged at an energy cutoff of 900 eV, while k-point spacing was determined to be converged at 0.03 $Å^{-1}$.

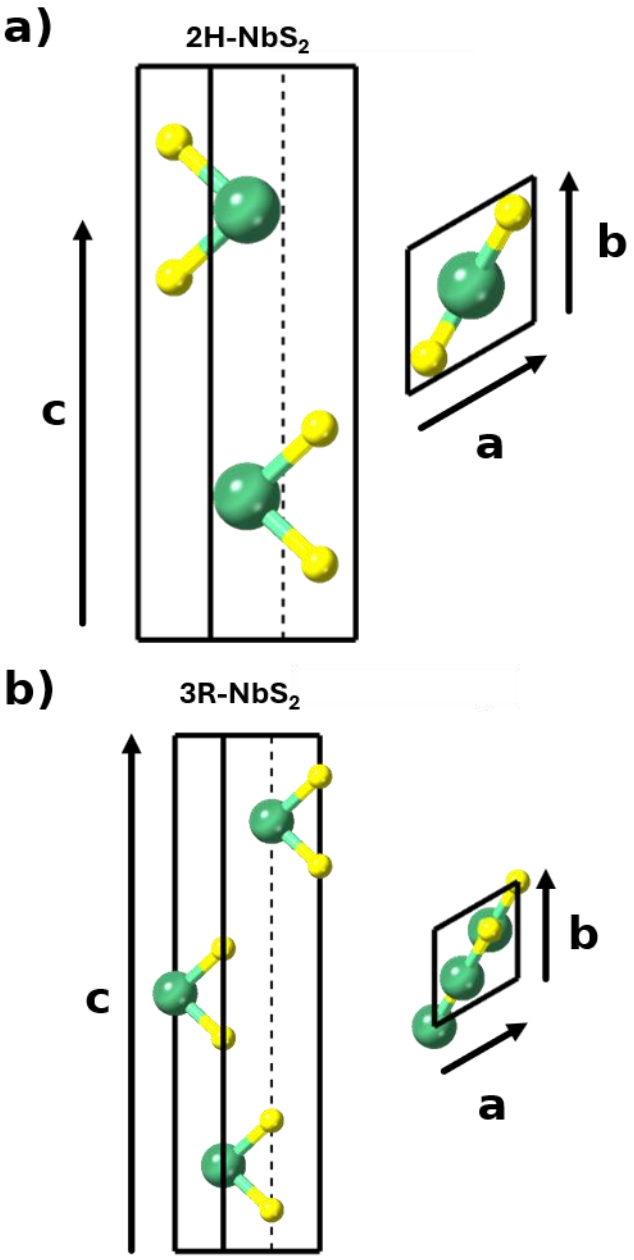


Figure 5. *Structures of NbS_2. Cell axis a, b and c are shown. Shown in (a) is the structure for* 2H-NbS_2*, while (b) shows the* 3R-NbS_2 *structure. Scale is maintained within sub-figures, but not between them. Images were generated using CrystalMaker® from calculated structures.*

Table 2. Cell geometry after optimisation of the NbS_2 cells and the ICSD experimental values for the same cells. The column labelled a,b denotes the cell lengths parallel to the basal plane, as shown in Figure 5, while c is the axis perpendicular to the basal plane. During the geometry optimisation, a and b are constrained to equal one another, and the angles of the ICSD cell are also maintained.

	Cell axis (*a,b*) length (Å)	**Cell axis (*c*) length (Å)**	**S-Nb bond length (Å)**
2H-NbS_2 rSCAN-MBD	3.326	12.09	2.470
2H-NbS_2 ICSD (experimental)	3.324	11.95	2.562
3R-NbS_2 rSCAN-MBD	3.330	18.10	2.470
3R-NbS_2 ICSD (experimental)	3.330	17.91	2.475

4.2.3 TaS_2

Only the rSCAN functional was used to evaluate the TaS_2 system. For the single point convergence, a k-point spacing of 0.025 $Å^{-1}$ and a plane-wave energy cut-off of 900 eV were

found to be sufficient (Figure 6). Geometry optimisations for both 2H-TaS_2 and 1T-TaS_2 were run with and without the MBD dispersion corrections, using the single-point energy convergence parameters. Modelled structural parameters for these cells can be seen in Table 3. Electronic structure calculations were found to be converged by comparison of the modelled densities of state at a plane wave cut-off of 900 eV and a k-point spacing of 0.025 $Å^{-1}$ with a spectral k-point spacing of 0.013 $Å^{-1}$.

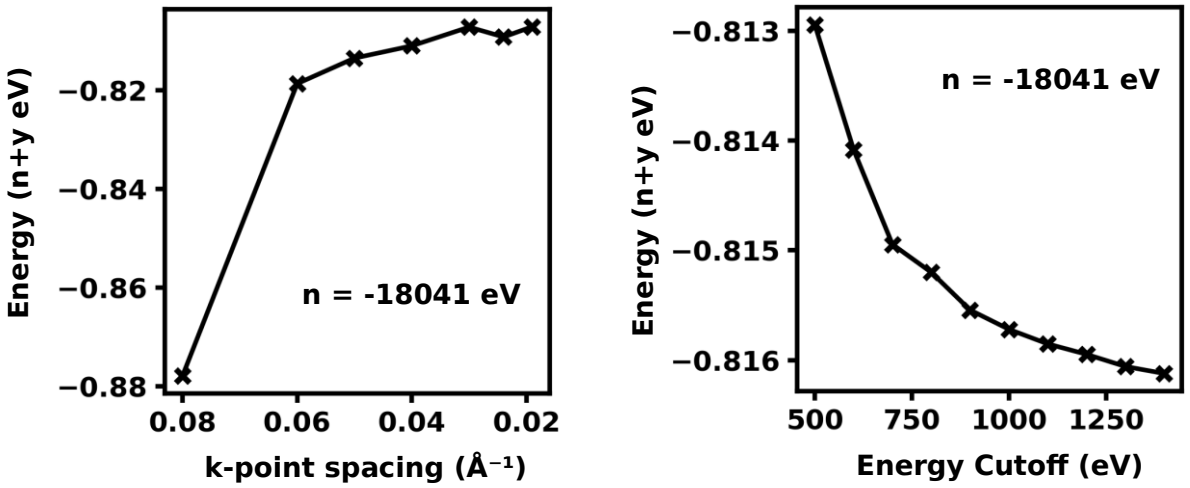


Figure 6. Convergence of the k-point spacing and energy cutoff parameters. The system was determined to be converged at an energy cutoff of 900 eV, while k-point spacing was determined to be converged at 0.025 $Å^{-1}$.

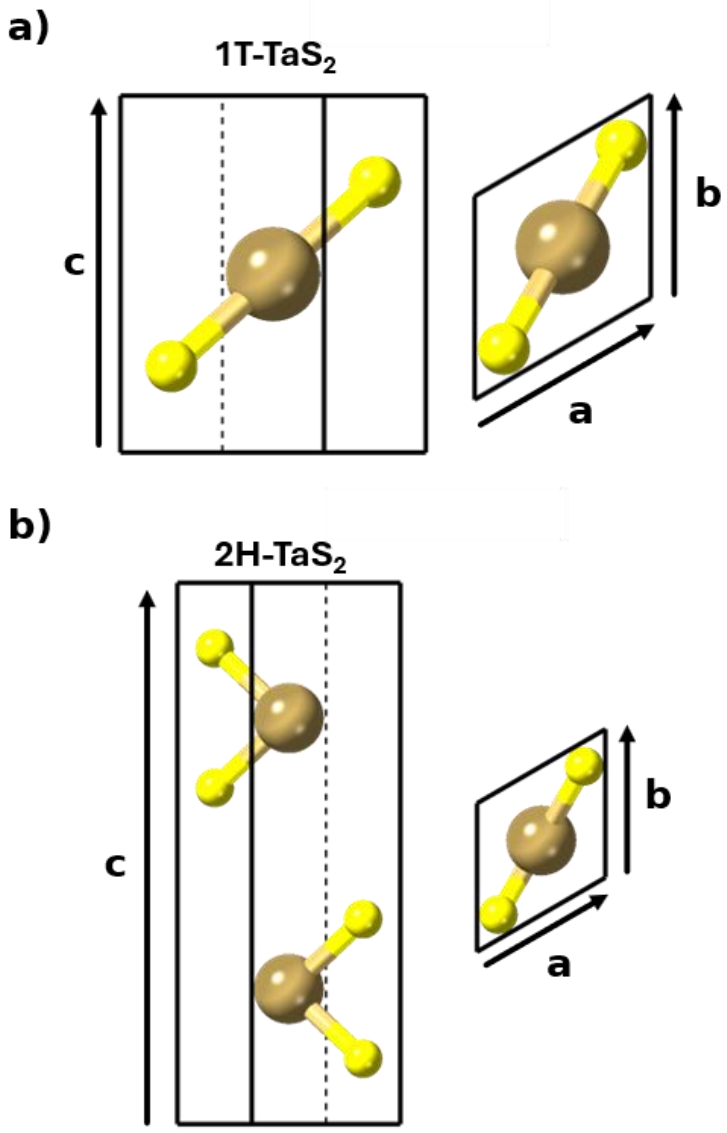


Figure 7. Structures of TaS_2. Cell axis a, b and c are shown. Shown in (a) is the structure for 1T-TaS_2, while (b) shows the 2H-TaS_2 structure. Scale is maintained within sub-figures, but not between them. Images were generated using CrystalMaker® from calculated structures.

Table 3. Cell geometry after optimisation of the TaS_2 cells and the ICSD experimental values for the same cells. The column labelled a,b denotes the cell lengths parallel to the basal plane, as shown in Figure 7, while c is the axis perpendicular to the basal plane. During the geometry optimisation, a and b are constrained to equal one another, and the angles of the ICSD cell are also maintained.

	Cell axis (*a,b*) length (Å)	**Cell axis (c) length (Å)**	**S-Ta bond length (Å)**
2H-TaS_2 rSCAN-MBD	3.32	12.07	2.47
2H-TaS_2 ICSD (experimental)	3.31	12.10	2.47
1T-TaS_2 rSCAN-MBD	3.35	5.91	2.46
1T-TaS_2 ICSD (experimental)	3.36	5.90	2.47

4.3 References

(1) Sholl, D. S.; Steckel, J. A. *Density Functional Theory: A Practical Introduction*; John Wiley & Sons, 2022.

(2) Koch, W.; Holthausen, M. C. *A Chemist's Guide to Density Functional Theory*; John Wiley & Sons, 2015.

(3) Hohenberg, P.; Kohn, W. Inhomogeneous Electron Gas. *Phys. Rev.* **1964**, *136* (3B), B864–B871. https://doi.org/10.1103/PhysRev.136.B864.

(4) Furness, J. W.; Kaplan, A. D.; Ning, J.; Perdew, J. P.; Sun, J. Construction of Meta-GGA Functionals through Restoration of Exact Constraint Adherence to Regularized SCAN Functionals. *The Journal of Chemical Physics* **2022**, *156* (3), 034109. https://doi.org/10.1063/5.0073623.

(5) Sun, J.; Remsing, R. C.; Zhang, Y.; Sun, Z.; Ruzsinszky, A.; Peng, H.; Yang, Z.; Paul, A.; Waghmare, U.; Wu, X.; et al. SCAN: An Efficient Density Functional Yielding Accurate Structures and Energies of Diversely-Bonded Materials. *arXiv preprint arXiv:1511.01089* **2015**.

(6) Zhang, I. Y.; Xu, X. On the Top Rung of Jacob's Ladder of Density Functional Theory: Toward Resolving the Dilemma of SIE and NCE. *WIREs Computational Molecular Science* **2021**, *11* (1), e1490. https://doi.org/10.1002/wcms.1490.

(7) Perdew, J. P.; Schmidt, K. Jacob's Ladder of Density Functional Approximations for the Exchange-Correlation Energy. In *AIP conference proceedings*; American Institute of Physics, 2001; Vol. 577, pp 1–20.

(8) Grimme, S. Semiempirical GGA-Type Density Functional Constructed with a Long-Range Dispersion Correction. *Journal of computational chemistry* **2006**, *27* (15), 1787–1799.

(9) Tkatchenko, A.; Scheffler, M. Accurate Molecular van Der Waals Interactions from Ground-State Electron Density and Free-Atom Reference Data. *Physical review letters* **2009**, *102* (7), 073005.

(10) Grimme, S.; Hansen, A.; Brandenburg, J. G.; Bannwarth, C. Dispersion-Corrected Mean-Field Electronic Structure Methods. *Chemical reviews* **2016**, *116* (9), 5105–5154.

(11) Payne, M. C.; Teter, M. P.; Allan, D. C.; Arias, T. A.; Joannopoulos, J. D. Iterative Minimization Techniques for Ab Initio Total-Energy Calculations: Molecular Dynamics and Conjugate Gradients. *Rev. Mod. Phys.* **1992**, *64* (4), 1045–1097. https://doi.org/10.1103/RevModPhys.64.1045.

(12) *CUT_OFF_ENERGY*. https://www.tcm.phy.cam.ac.uk/castep/documentation/WebHelp/content/modules/castep/keywords/k_cut_off_energy_castep.htm (accessed 2025-10-21).

(13) *Setting Up Pseudopotentials*. https://www.tcm.phy.cam.ac.uk/castep/documentation/WebHelp/content/modules/castep/tskcastepsetelecpotentials.htm (accessed 2025-10-21).

(14) Lee, H.; Hegde, V. I.; Wolverton, C.; Xia, Y. Accelerating High-Throughput Phonon Calculations via Machine Learning Universal Potentials. *Materials Today Physics* **2025**, *53*, 101688.

(15) Baroni, S.; De Gironcoli, S.; Dal Corso, A.; Giannozzi, P. Phonons and Related Crystal Properties from Density-Functional Perturbation Theory. *Reviews of modern Physics* **2001**, *73* (2), 515.

(16) Kohn, W.; Sham, L. J. Self-Consistent Equations Including Exchange and Correlation Effects. *Phys. Rev.* **1965**, *140* (4A), A1133–A1138. https://doi.org/10.1103/PhysRev.140.A1133.

(17) Monkhorst, H. J.; Pack, J. D. Special Points for Brillouin-Zone Integrations. *Phys. Rev. B* **1976**, *13* (12), 5188–5192. https://doi.org/10.1103/PhysRevB.13.5188.

(18) Clark, S. J.; Segall, M. D.; Pickard, C. J.; Hasnip, P. J.; Probert, M. I. J.; Refson, K.; Payne, M. C. First Principles Methods Using CASTEP. *Zeitschrift für Kristallographie - Crystalline Materials* **2005**, *220* (5–6), 567–570. https://doi.org/10.1524/zkri.220.5.567.65075.

(19) McNellis, E. R.; Meyer, J.; Reuter, K. Azobenzene at Coinage Metal Surfaces: Role of Dispersive van Der Waals Interactions. *Phys. Rev. B* **2009**, *80* (20), 205414. https://doi.org/10.1103/PhysRevB.80.205414.

(20) Zagorac, D.; Müller, H.; Ruehl, S.; Zagorac, J.; Rehme, S. Recent Developments in the Inorganic Crystal Structure Database: Theoretical Crystal Structure Data and Related Features. *Journal of Applied Crystallography* **2019**, *52* (5), 918–925. https://doi.org/10.1107/S160057671900997X.

(21) Perdew, J. P.; Burke, K.; Ernzerhof, M. Generalized Gradient Approximation Made Simple. *Phys. Rev. Lett.* **1996**, *77* (18), 3865–3868. https://doi.org/10.1103/PhysRevLett.77.3865.

(22) Murphy, D. W.; Cros, C.; Di Salvo, F. J.; Waszczak, J. V. Preparation and Properties of LixVS2. *Inorg. Chem.* **1977**, *16* (12), 3027–3031. https://doi.org/10.1021/ic50178a008.

(23) Ambrosetti, A.; Reilly, A. M.; DiStasio, R. A.; Tkatchenko, A. Long-Range Correlation Energy Calculated from Coupled Atomic Response Functions. *J Chem Phys* **2014**, *140* (18), 18A508. https://doi.org/10.1063/1.4865104.

(24) Refson, K.; Tulip, P. R.; Clark, S. J. Variational Density-Functional Perturbation Theory for Dielectrics and Lattice Dynamics. *Phys. Rev. B* **2006**, *73*, 155114.

Chapter 5. Synthesis and characterisation of large crystal group V TMDCs

5.0 Abstract

In order to experimentally probe the behaviour and structure of the group V TMDCs, large poly- and single crystals were synthesised. The large size of these crystals enables separation of the basal plane and edge regions for these materials which can then be extended to the more common powder electrodes. This chapter examines the large single- and poly-crystal growth of NbS_2 and TaS_2, their phases and polymorphs and the properties of their edge and basal plane regions. This chapter also provides insight into the oxidation behaviour of these materials.

5.1 Introduction

Transition metal dichalcogenide synthesis methods can be divided broadly into methods which produce well-ordered crystalline materials (high order) and methods which produce primarily nano-structured poorly crystalline materials (low order). Preferred methods of synthesis vary based on their ultimate application. High order methods typically utilised in the literature are chemical vapour transport (CVT)[1], melt growth[2] and atmospheric pressure chemical vapour deposition (APCVD)[3]. CVT and melt growth are used to grow single crystals, more commonly used to study the electronic properties of materials, while CVD is used to grow thin film more commonly used for studying catalysis[3]. A common low order synthesis method is hydrothermal synthesis, which is used in the literature for synthesising high surface area nanoparticles of the desired materials for use as catalysts[4] and batteries[5].

Single- and large poly-crystals of group V TMDCs have not been extensively studied in the context of catalysis, yet understanding the behaviour of large crystals can provide essential insight into their behaviour as catalysts in powder form. One such example exists for group V TMDCs, where a study by Zhang *et al*.[6] of APCVD grown single crystals showed that the 3R-NbS_2 crystal edges contribute notably to the overall performance of the material. Consequently,

understanding the nature of those edges is essential to accurately reporting the overall material performance. To gain that understanding, the growth of large crystals of these materials is necessary to allow for separate spectroscopy measurements of the edge-free domains and edge regions.

To this end, baseline Raman spectra for the samples must be established. Raman is a good tool to separately investigate basal planes and edges, as it is a rapid, low cost, sensitive to chemistry, structure, and purity[7], and can be focused to small beam sizes (<1 μm) suitable for investigations of small areas. On large crystals, facets of sufficient size can be isolated where basal plane edges dominate over the basal plane itself. Different behaviours of these domains, such as unequal extents of oxidation can therefore be detected. This is straightforward for 2H-TaS_2 and NbS_2, where the Raman spectra are well documented in the literature[8,9]. Similarly, 1T-TaS_2, which, due to an intermediate charge density wave state possesses a complex Raman spectrum that has attracted investigation in the literature, has a fairly well-established Raman spectrum[10].

This chapter therefore examines the large single- and poly-crystal growth of NbS_2 and TaS_2, their phases and domain properties. This chapter also provides insight into the chemical behaviour of the edges of these materials under realistic conditions.

5.2. Synthesis of large group V transition metal chalcogenide crystals

Solid-state synthesis and CVT were chosen for NbS_2 and TaS_2 over available hydrothermal syntheses[11,12] to permit for the synthesis of large single crystals and to access crystals of multiple phases without the use of intercalants.

As discussed in Chapter 2, the stoichiometry of these materials can shift slightly when their structure changes, or they may retain their layer structure but the interlayer structure changes.

Consequently, the term phase is used to describe the variety of different structures resulting from the metal-sulfur system.

5.2.1 3R-NbS_2 synthesis and characterisation

3R-NbS_2 CVT synthesis (Chapter 3) formed small black symmetrical triangular crystals of ~5 mm in average diameter with fine hair-like crystalline growths on the edges and corners of the crystal. The solid-state synthesis produced a fine black powder. The crystals produced were difficult to exfoliate/cleave and grind. The crystals grew with basal planes parallel to the walls of the quartz growth tube and adhered to glass strongly (Figure 1).



Figure 1. Amorphous quartz tube (19 mm diameter) containing 3R-NbS_2 crystals. The crystals are triangular with distinct hair-like crystal growths at the corners and edges. The crystals shown are smaller than typically grown.

Raman of the crystal basal planes showed peaks in line with literature[8,13] at 150, 301, 337 and 384 cm^{-1} and a distinct shoulder at 187 cm^{-1} (Figure 2).

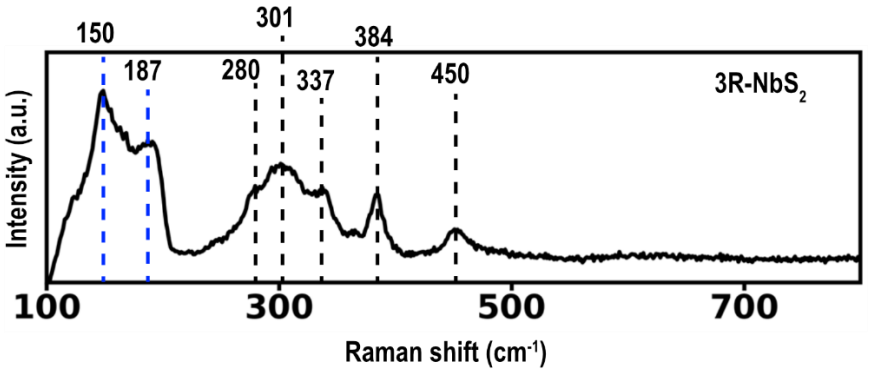


Figure 2. Basal plane Raman spectrum of a 3R-NbS_2 crystal, with characteristic peaks at 150, 301, 337, 384 and 450 cm^{-1} and distinct shoulders at 187 and 280 cm-1. Raman peak positions are labelled above the dashed lines. The units, cm^{-1} are omitted for space. Dashed lines in blue denote peaks not arising from single phonon vibration modes.

XRD of both the powder and the ground up crystals showed characteristic reflections, whose positions were as predicted by material models and reported in the literature[14,15] (Figure 3). The relative intensities of the peaks are not in alignment with the calculations due to the preferred orientation effect, which is discussed further later in the chapter.

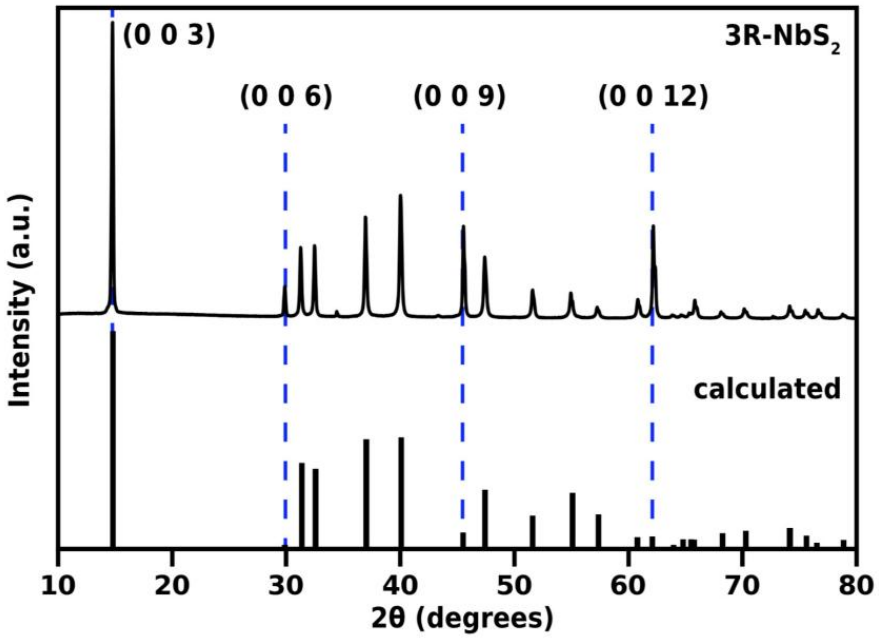


Figure 3. Experimental XRD of 3R-NbS_2 (above), while the calculated XRD for 3R-NbS_2 is shown below. The relative intensities of the peaks are not in alignment with the calculations due to the preferred orientation effect, which is discussed further later in the chapter. The (0 0 l) peaks are highlighted with blue dashed lines.

XPS of the crystal exfoliated/cleaved under argon showed the presence of niobium and sulfur as well as adventitious oxygen, carbon and silicon (Figure 4). The silicon peaks likely arise from contamination by glass from the opening of the quartz ampoule after synthesis. XPS spectra both in the Nb 3d region and in the S 2p region show asymmetric peaks. This asymmetry is expected for materials with a metallic electronic structure, where the emission of a photoelectron causes a potential to form between the hole created and remaining electrons. This permits the low-energy excitation of electrons to empty orbitals near the Fermi level, which causes the reduction in energy of photoelectrons (Chapter 3), resulting in an asymmetric peak. This asymmetry is present in both the oxidised and unoxidised materials.

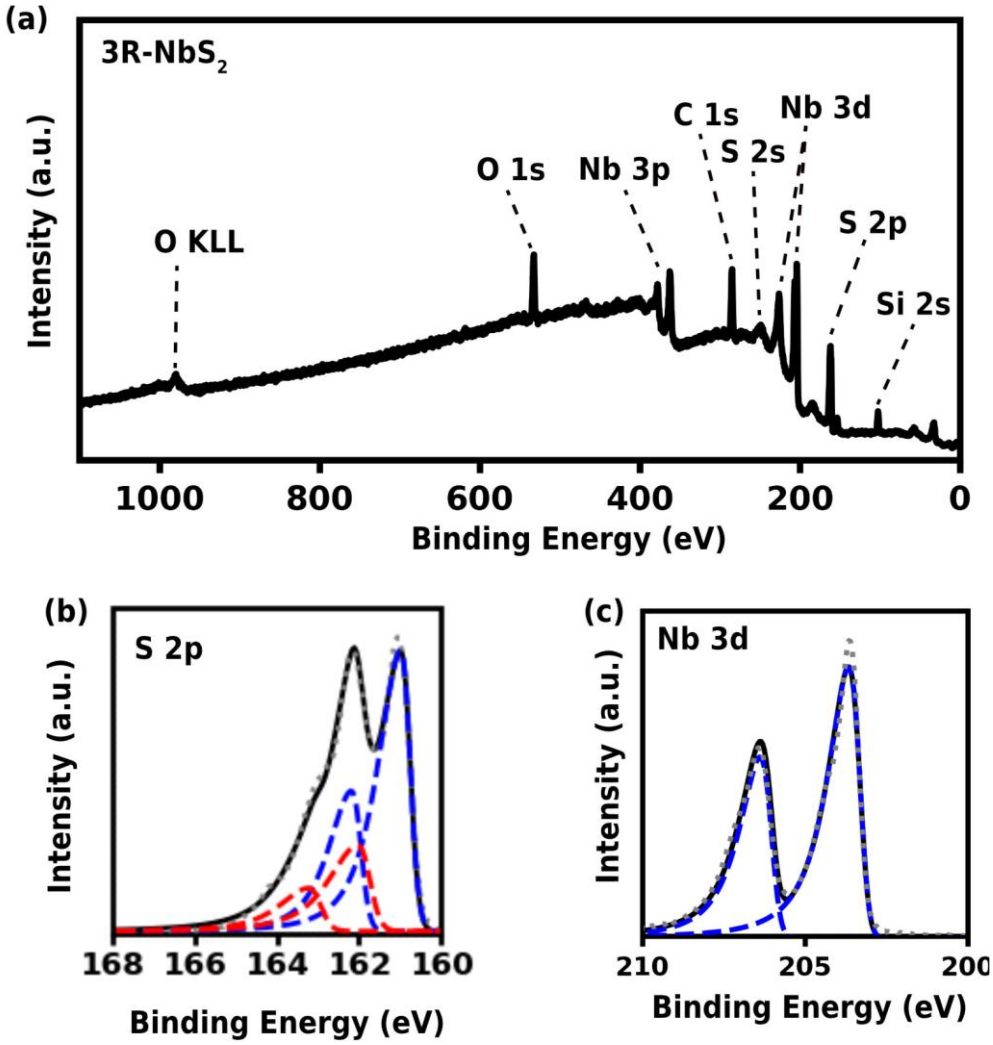


Figure 4. XPS of 3R-NbS_2. A survey spectrum is shown in (a), with peaks annotated. Silicon is present due to contamination from the synthesis ampoule, while the sulfur 2p and niobium 3d regions with their accompanying fits are shown in (b) and (c) respectively.

The presence of at least two 3R-NbS_2 sulfur environments is clear from the XPS, showing shoulders at 163 eV and 164 eV consistent with a second set of peaks. These two components are thought to arise from different phases within the niobium sulfide[16], however there is little evidence from the XRD or Raman of the co-existence of phases. Instead, these likely arise from sub-surface niobium self-intercalation, while the surface layer of sulfur, with lower coordination to niobium is oxidised relative to the sub-surface sulfur. Component fitting for the NbS_2 S 2p region is further discussed in Chapter 7.

5.2.2 2H-TaS_2 synthesis and characterisation

2H-TaS_2 formed long dark-grey asymmetrical hexagonal polycrystals ~10 mm in average length, while the solid-state synthesis produced a black powder. The crystals produced were easily exfoliated/cleaved and somewhat flexible, albeit brittle. Crystals grew with basal planes approximately perpendicular to the walls of the quartz growth tube, adhering to the glass lightly (Figure 5).



Figure 5. Amorphous quartz tube (12 mm diameter) containing 2H-TaS_2 crystals.

Raman of the crystal basal planes showed peaks at 170, 290 and 400 cm^{-1} (Figure 6), in line with literature reports[17,18].

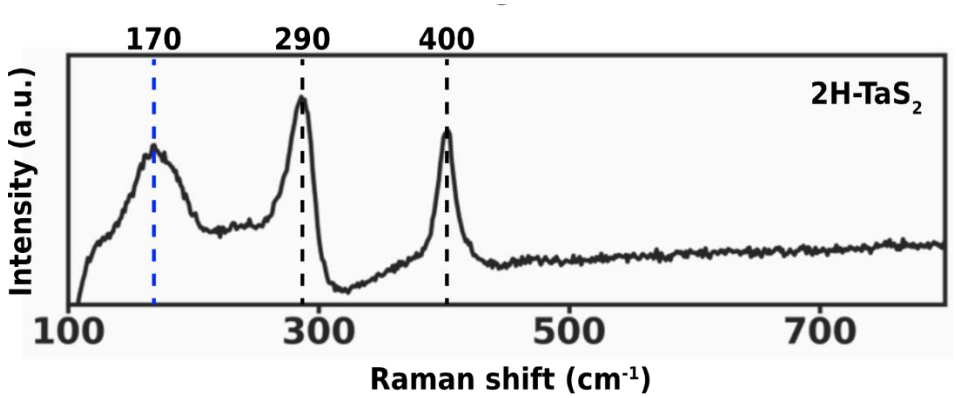


Figure 6. Basal plane Raman spectrum of a 2H-TaS_2 crystal, with characteristic peaks at 170, 290 and 400 cm-1. Raman peak positions are labelled above the dashed lines. The units, cm^{-1} are omitted for space. Dashed lines in blue denote peaks not arising from single phonon vibration modes.

XRD of both the powder and the ground up crystals showed characteristic reflection positions as predicted by material models and reported in the literature[15,19]. The (0 0 *l*) reflection intensities were much stronger than predicted (Figure 7).

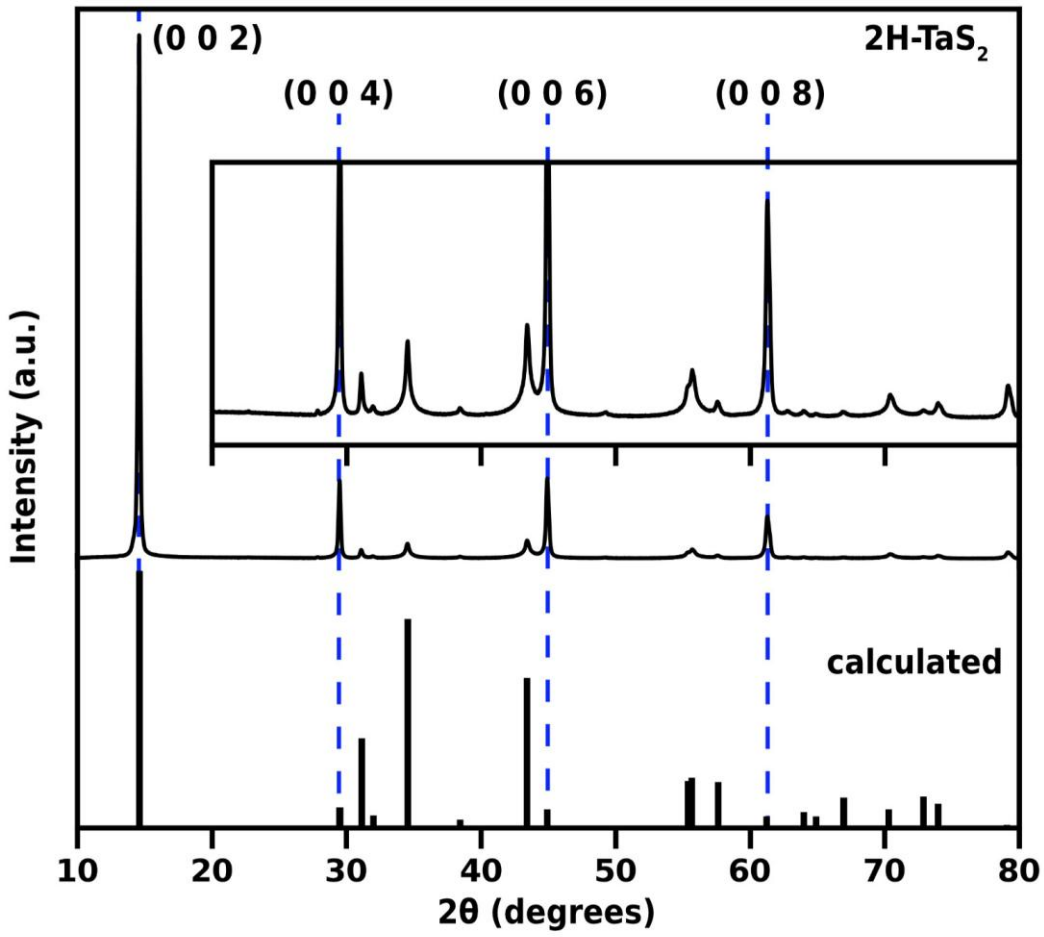


Figure 7. Experimental XRD of 2H-TaS_2 (above) and calculated XRD pattern (below). The inset shows the XRD data from 10-80° 2θ with the y-axis zoomed in to better display that region. The relative intensities of the peaks are not in alignment with the calculations due to the preferred orientation effect, which is discussed further later in the chapter. The (0 0 l) peaks are highlighted with blue dashed lines.

XPS of the crystal exfoliated/cleaved under argon showed asymmetric peaks as expected for the metallic electronic structure of 2H-TaS_2, with a single asymmetric peak shape sufficient to fit both pristine 2H-TaS_2 and 1T-TaS_2 (Figure 8). Component fitting for the TaS_2 S 2p region is likewise discussed in Chapter 7.

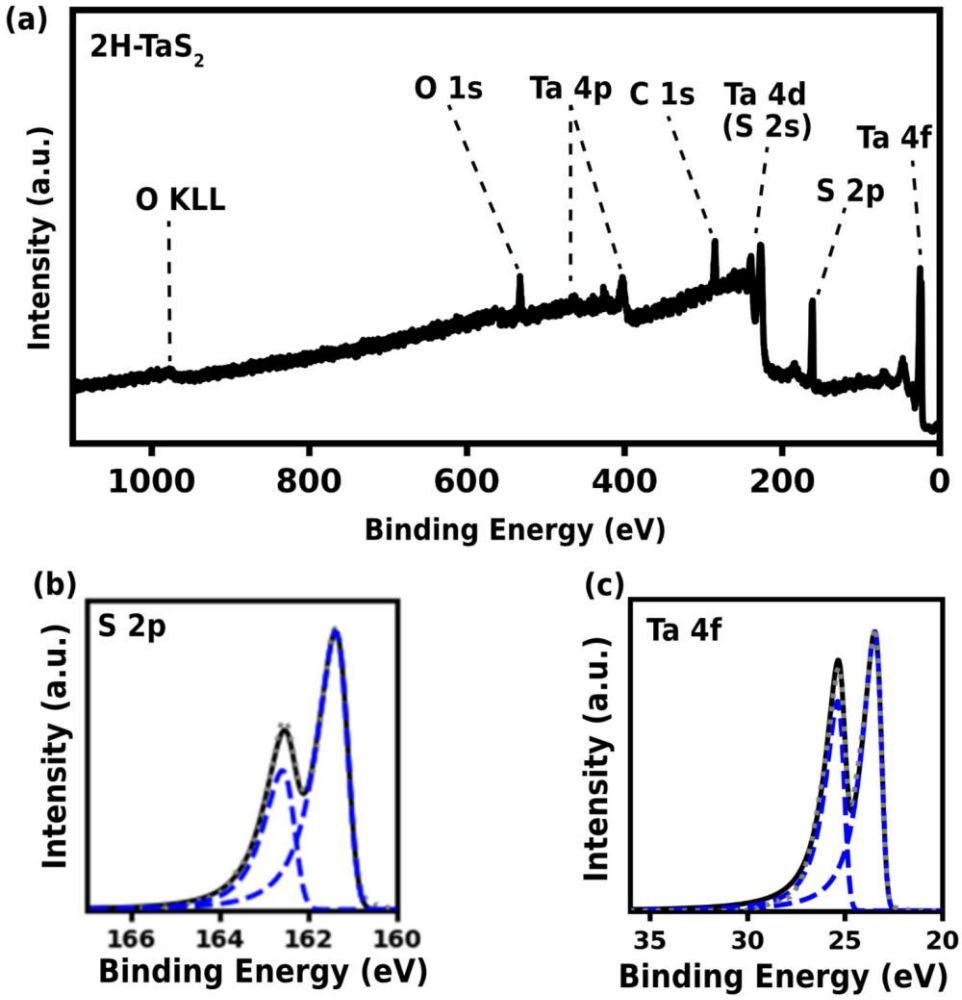


Figure 8. XPS of 2H-TaS_2. The survey spectrum is shown in (a) with annotated peaks, while the sulfur 2p and tantalum 4f regions and their accompanying fits are shown in (b) and (c) respectively.

5.2.3 2H-NbS_2 synthesis and characterisation

2H-NbS_2 formed large black near-symmetrical hexagonal polycrystals (Figure 9) ~10 mm diameter on average, while solid-state synthesis produced a black powder. Produced crystals were easy to exfoliate/cleave and grind and single crystals could be isolated. Crystals adhered lightly to the interior of the quartz growth tube and grew with basal planes parallel to the glass walls.



Figure 9. 2H-NbS_2 crystals. They are black, shiny and near-hexagonal. Many crystals grow as pairs or large polycrystals.

Raman of the crystal basal planes showed peaks at 240, 290 and 385 cm^{-1} in line with literature reports[8,20] (Figure 10).

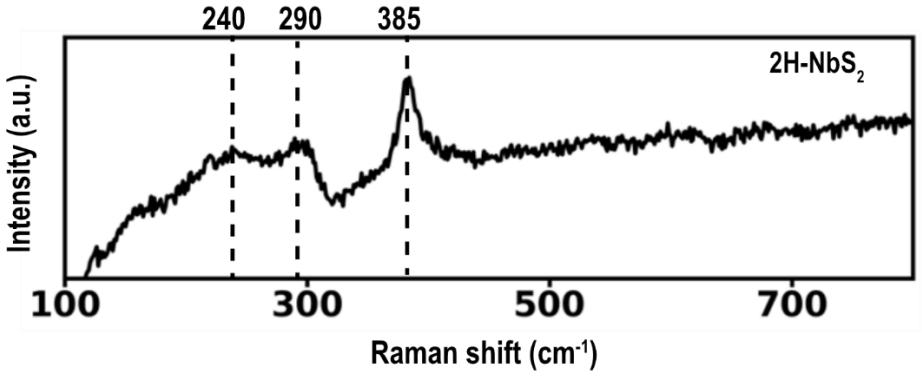


Figure 10. Basal plane Raman spectrum of 2H-NbS_2 crystal, with characteristic peaks 290 and 385 cm^{-1} and a shoulder at 240 cm^{-1}. Raman peak positions are labelled above the dashed lines. The units, cm^{-1} are omitted for space.

XRD of both the powder and the ground up crystals showed characteristic reflections as predicted by material models and reported in the literature (Figure 11)[15,21,22]. Certain reflections

in the 2H-NbS_2, such as those at ~35° and 45° are broadened. This has been observed elsewhere[23] and is thought to arise from stacking faults or turbostratic disorder (random orientation of stacked plates about the stacking direction).

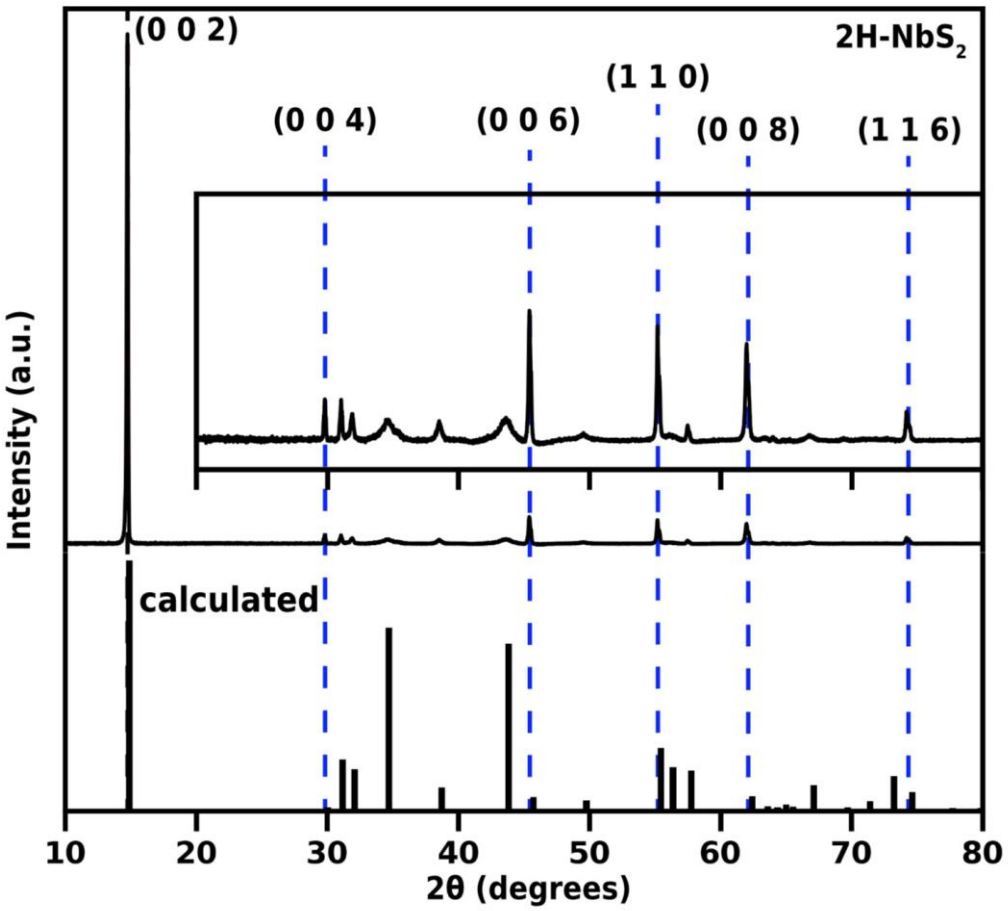


Figure 11. The obtained experimental XRD of 2H-NbS_2 (above) and the calculated XRD for 2H-NbS_2 (below). The inset shows the XRD data from 10-80° 2θ with the y-axis zoomed in. A substantial preferred-orientation effect is observed, so that the peaks resulting from out-of-plane reflections ((0 0 l) where l=2,4,6,8, marked with blue dashed lines) have higher intensity than predicted. Additionally, the (1 1 x), x=0,6 appear to also be stronger than predicted, indicating that the preferred orientation is not strictly out-of-plane.

XPS of both the Nb 3d and S 2p show asymmetric peaks (Figure 12). The peak asymmetry parameter for 3R-NbS_2 transfers well, and a good fit is obtained using a single environment in the 2H-NbS_2. Both the single environment and asymmetric peaks are as expected for the phase.

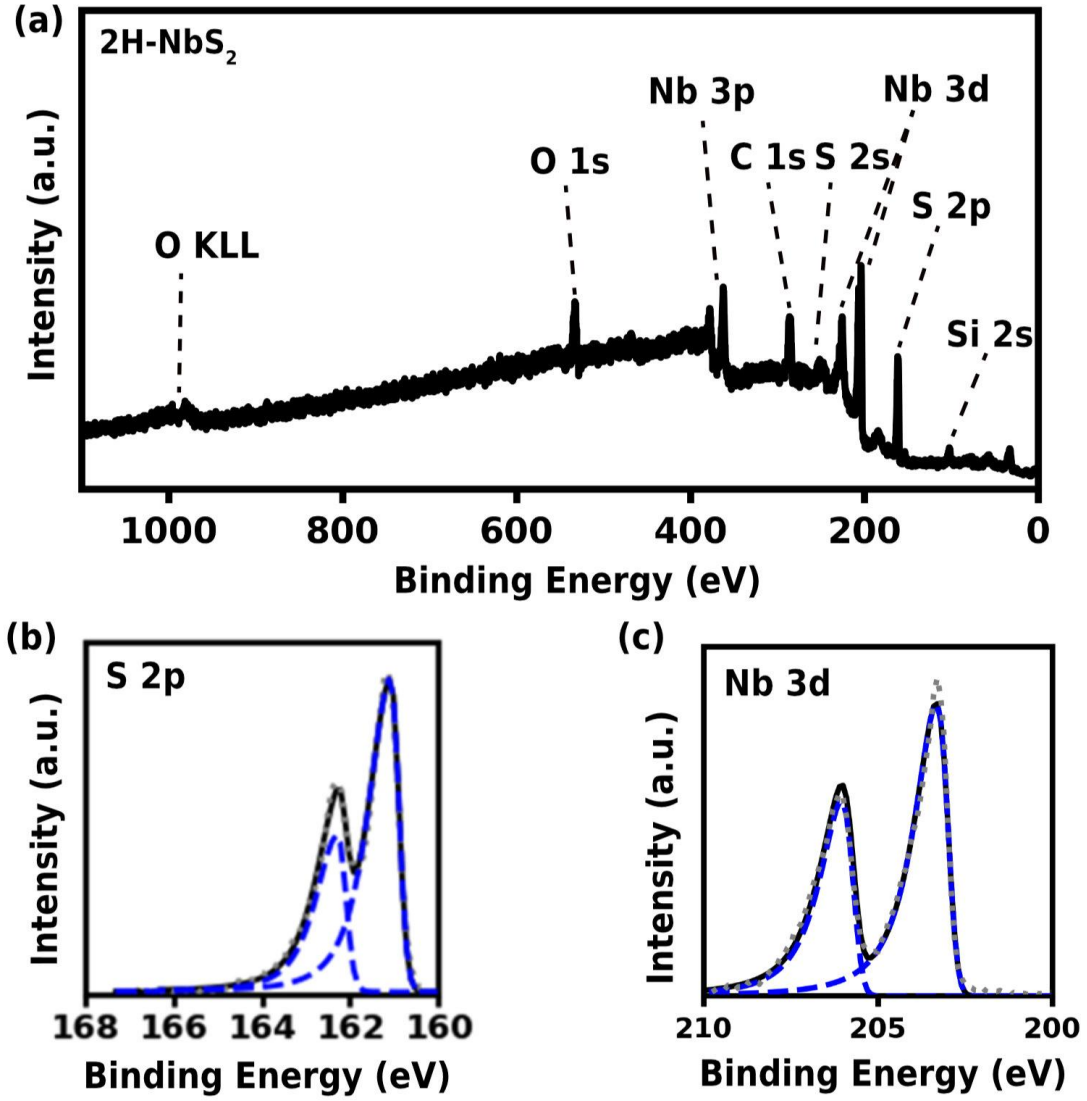


Figure 12. XPS of 2H-NbS_2. The survey spectrum is shown in (a) with annotated peaks. Silicon is present due to contamination from the synthesis ampoule. The sulfur 2p region, niobium 3d region and their accompanying fits are shown in (b) and (c) respectively.

5.2.4 1T-TaS_2 synthesis and characterisation

1T-TaS_2 formed gold-coloured asymmetrical hexagonal crystals approximately 5 mm in diameter (Figure 13), while the solid-state synthesis produced a characteristic dark gold powder. Produced crystals were easy to exfoliate/cleave and grind. Crystals adhered lightly to the interior of the quartz growth tube and grew with basal planes perpendicular to the glass walls.

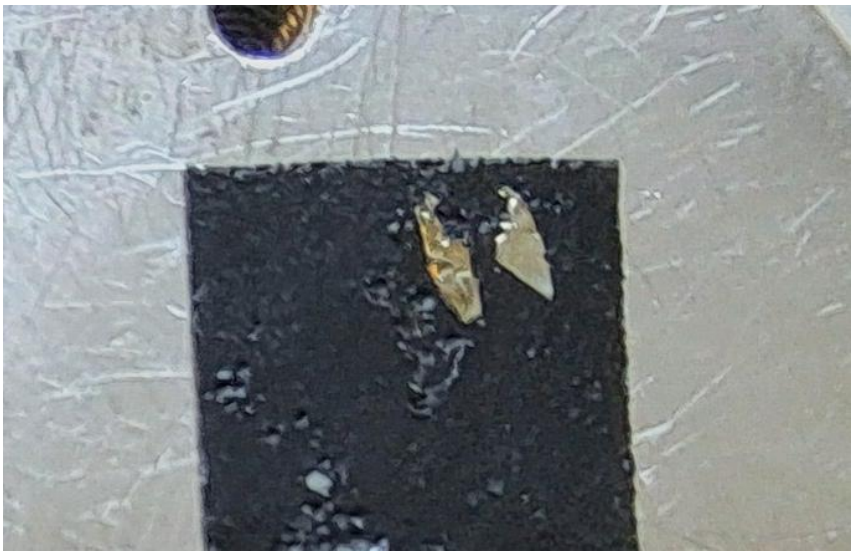


Figure 13. 1T-TaS_2 crystals (gold) mounted on glassy carbon. The crystals have been freshly cleaved and are therefore somewhat damaged.

Raman of the crystal basal planes showed peaks at 240, 300 and 380 cm^{-1} in line with literature reports of 1T-TaS_2 at room temperature[10,24] (Figure 14).

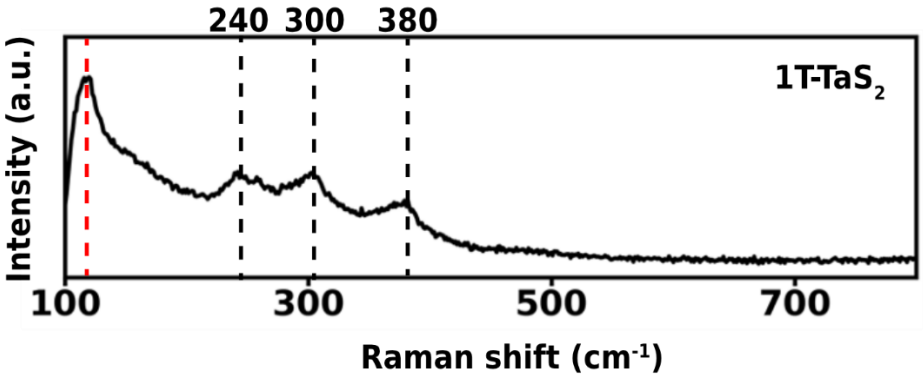


Figure 14. Basal plane Raman spectrum of a 1T-TaS_2 crystal, with characteristic peaks at 240, 300 and 380 cm^{-1}. The red line marks a false peak created by the Rayleigh filter cutoff. Raman peak positions are labelled above the dashed lines. The units, cm^{-1} are omitted for space.

XRD of both the powder and the ground crystals showed characteristic reflections as predicted by material models and reported in the literature (Figure 15)[15,25,26].

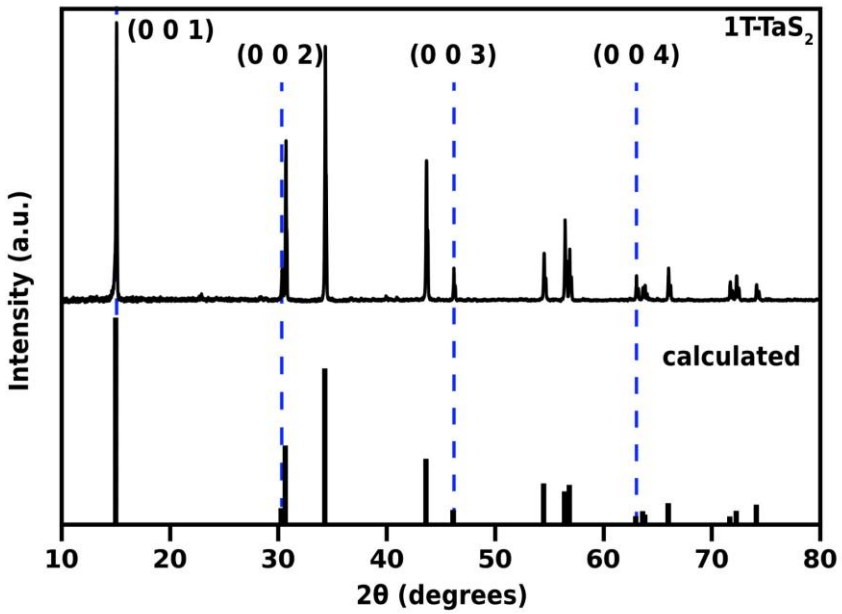


Figure 15. Experimental XRD of 1T-TaS_2 (above) and calculated XRD pattern (below). The relative intensities of the peaks are not in alignment with the calculations due to the preferred orientation effect, which is discussed further later in the chapter. The (0 0 l) peaks are highlighted with blue dashed lines.

XPS of the crystal exfoliated/cleaved under argon showed the presence of sulfur and tantalum, with adventitious carbon and oxygen. The Ta and S peaks were asymmetric as expected for the metallic electronic structure of 1T-TaS_2 (Figure 16).

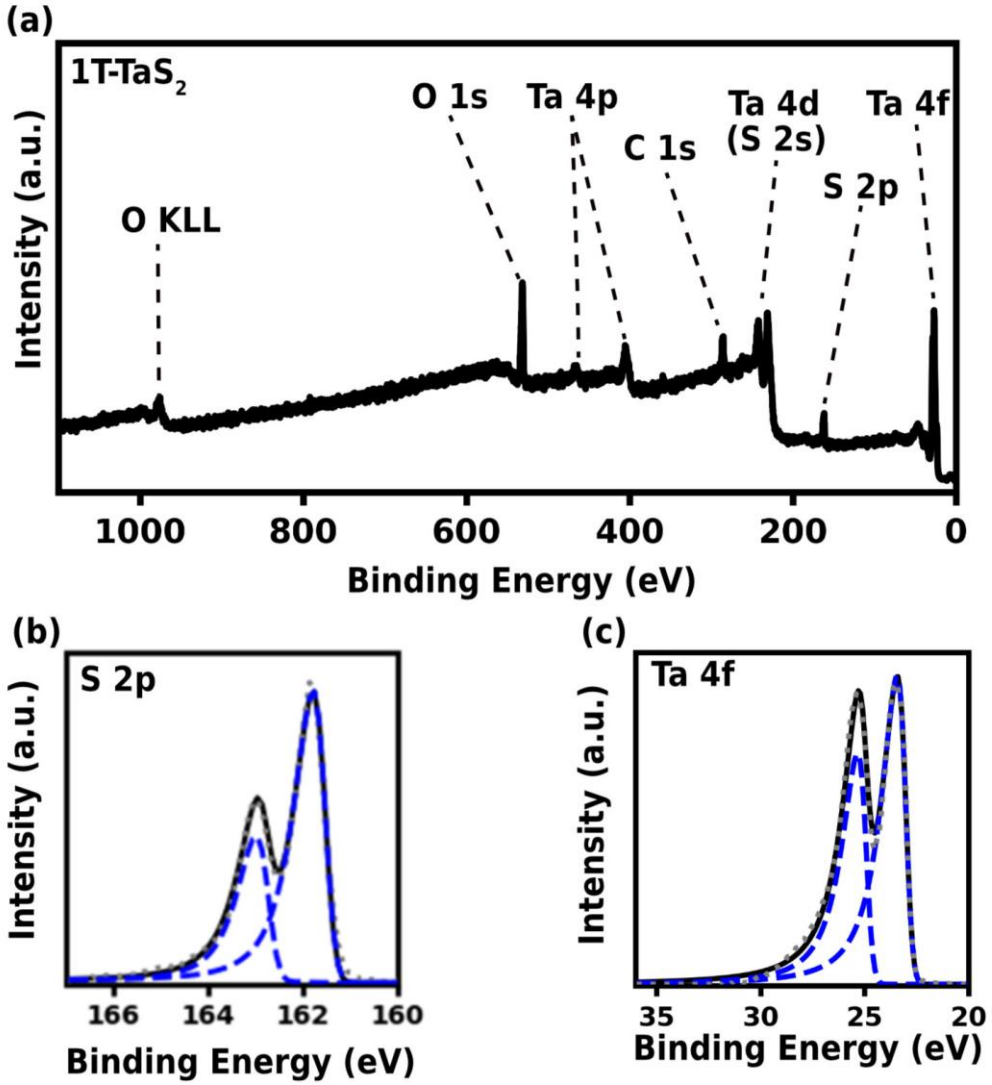


Figure 16. XPS of 1T-TaS_2. The survey spectrum is shown in (a) with annotated peaks, while the sulfur 2p and tantalum 4f regions and their accompanying fits are shown in (b) and (c) respectively.

Overall, XRD of all produced materials showed a distinct preferred orientation effect, albeit somewhat limited for 1T-TaS_2, whereby certain reflections on the obtained pattern were substantially stronger than predicted by theory, while others were weaker[27]. This can be

attributed to the preferred in-plane growth of the material during synthesis, which causes the resulting crystallites to have larger in-plane than out-of-plane dimensions. This asymmetry causes the crystallites to prefer to orient themselves in similar directions within the powder. Similarly, crystals when ground up prefer to break along the basal plane due to the weak inter-planar forces rather than within the plane, so that individual grains within the resultant powder tend to settle along similar orientations as with the powder synthesised via solid-state synthesis. For 2H-NbS_2, the additional preferred orientation effect for the (1 1 0) and (1 1 6) indices may result from preferred orientations within the turbostratic disorder, with certain orientations being favoured over others.

For XPS across all materials, the S 2p peaks of the materials were fitted well with empirically derived asymmetric peaks, as discussed further in Chapter 7. The metal peaks (Nb 3d, Ta 4f) are more difficult to fit, since metals can take a variety of oxidation states, of which some may overlap substantially with the metal sulfide component and can contribute in an unknown fashion to the peak shape. Due to this factor, well constrained line shapes cannot be constructed for these peaks. Consequently, this thesis does not consider the Nb 3d and Ta 4f peak fits further, and the fits thus far obtained should not be considered as definitive.

5.3. Understanding the spectroscopy of group V TMDC crystals

For large crystals of the group V TMDCs, the Raman spectra acquired vary with position on the crystal. For both NbS_2 and TaS_2, differences in the Raman can be seen when the spectrum of the basal plane is collected as compared to the spectrum collected from the edge of the crystals.

2H-TaS_2 spectra collected at the edges (Figure 17 (ii)) show a new peak at 232 cm^{-1}, as well as the beginning of a peak towards 100 cm^{-1} as compared to the Raman from the basal plane.

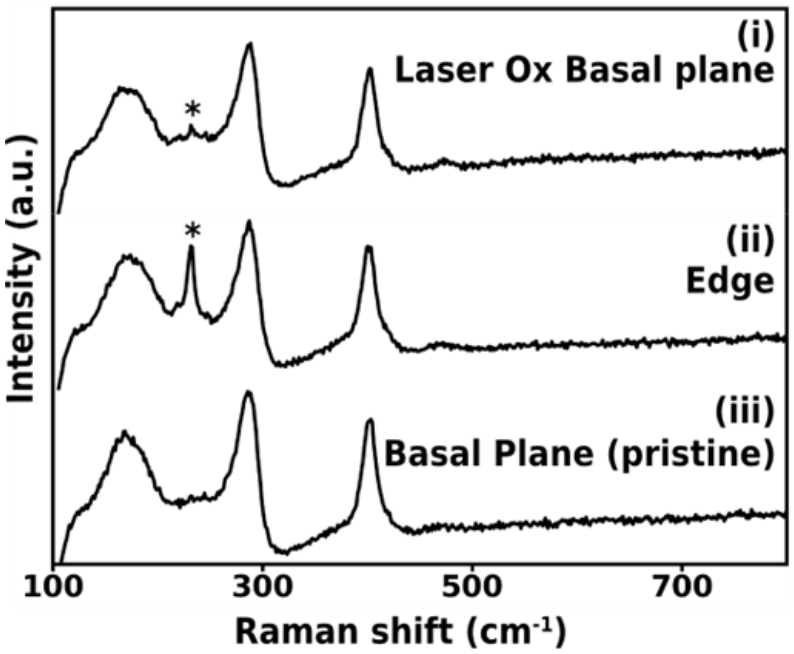


*Figure 17. Changes in Raman spectra of 2H-TaS_2. (i) shows the spectrum obtained from the laser-oxidised basal plane, while (ii) and (iii) show the spectrum obtained from edges and unoxidised basal plane respectively. Oxide peaks are marked with a *.*

Similar peaks arise at the edges of 1T-TaS_2 crystals (Figure 18 (ii)), with additional peaks seen at 150 and 471 cm^{-1}, oxide peaks which are likely suppressed by the sulfide signal in 2H-TaS_2.

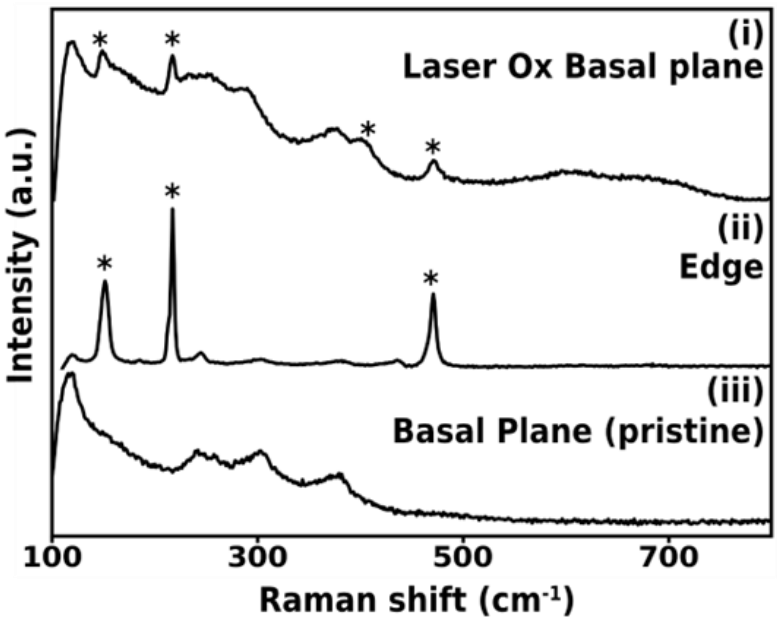


*Figure 18. Changes in Raman spectra of 1T-TaS_2. (i) shows the spectrum obtained from the laser-oxidised basal plane of 1T-TaS_2, while (ii) and (iii) show the spectrum obtained from edges and unoxidised basal plane respectively. (ii) shows near-total oxidation of the material. Oxide peaks are marked with a *.*

For the tantalum disulfides, changes on the edges of the crystal are attributable to the differential oxidation rates of the edges and basal plane, with the crystal edges substantially more vulnerable to oxidation. This is evidenced by induced oxidation of the basal plane and spectroscopy of freshly formed crystal edges. Oxidation via laser heating of the crystal basal plane induces visible changes to the crystal surface (Figure 19).

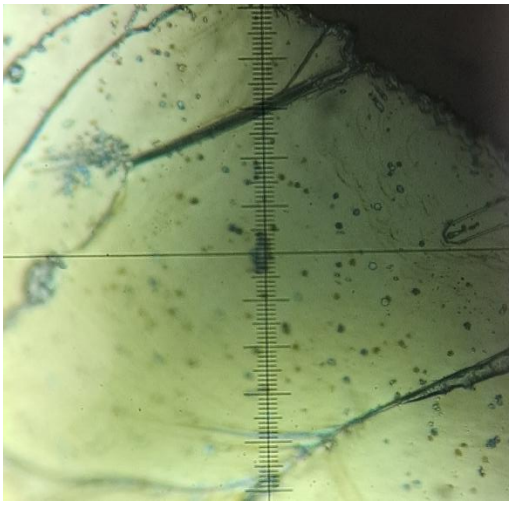


Figure 19. Microscope view of a burned 2H-TaS_2 crystal (image centre under crosshairs). Other flaws can be seen in the dark striations, which are cracks in the crystal, while the bubble-shaped objects are microscope artefacts.

Resultant Raman spectroscopy shows a mix of both the oxide and sulfide (Figure 17). Raman spectroscopy of crystal edges formed by breaking the crystals shows no evidence of edge oxidation. The observed peaks correlate to the Raman of crystalline Ta_2O_5, particularly the weak peaks at 600-700 cm^{-1} (Figure 17 (ii)), resulting from TaO_6 octahedra[28], while missing peaks at 250 and 150 cm^{-1} are easily explained by strong sulfide peaks concealing the oxide signal.

The story for the niobium disulfides is somewhat more complex. 2H-NbS_2 shows clear evidence of edge oxidation, with a crystal edge Raman peak at 220 cm^{-1} consistent with a basal plane spot heated and oxidised via laser heating (Figure 20(ii)). Laser exposure of the basal plane shows formation of the 220 cm^{-1} peak, increasing in intensity with increasing oxidation. After extended exposure, additional peaks appear at 125, 230, 300 cm^{-1} and a strong peak at 690 cm^{-1} corresponding well to niobium oxide[29] (Figure 20(i)). The peak at 690 cm^{-1} is understood to arise from NbO_6 octahedra[29], evidencing early formation of Nb-O defects,

without corresponding O-O bonds that form part of an extended oxide, followed by eventual reorganisation into Nb_2O_5. This indicates a light oxidation of the edges of 2H-NbS_2.

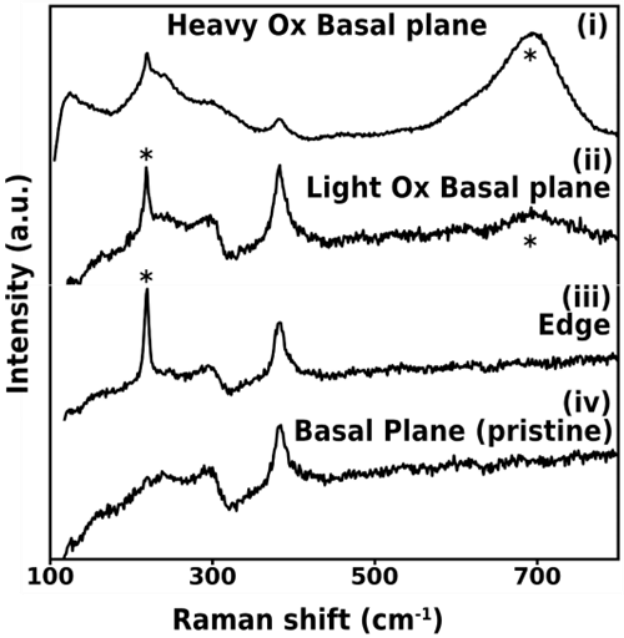


Figure 20. Changes in Raman spectra of the niobium disulfides. (i) shows the spectrum obtained from the heavily laser-oxidised basal plane of 2H-NbS_2, while (ii) shows the lightly oxidised version of the same. (iii) and (iv) show the spectrum obtained from edges and unoxidised basal plane respectively.

3R-NbS_2 has three distinct regions on the formed triangular crystal. The basal plane shows the standard peaks at 150, 301, 337 and 384 cm^{-1} (Figure 21(iii)). Distinctions in the Raman spectra between edge, basal plane and hair-like growths on the edges of the crystals are limited. Basal plane peaks are broader, while peaks recorded from the edges are sharper and more distinct. Additional peaks appear in the Raman spectrum at the edges at 224 and at 245 cm^{-1}. The first peak can be reasonably attributed to minor oxide formation, as seen in 2H-NbS_2. The second peak is more difficult to attribute but may be due to the formation of a Nb-O bond in a non-octahedral environment (Figure 21(ii)).

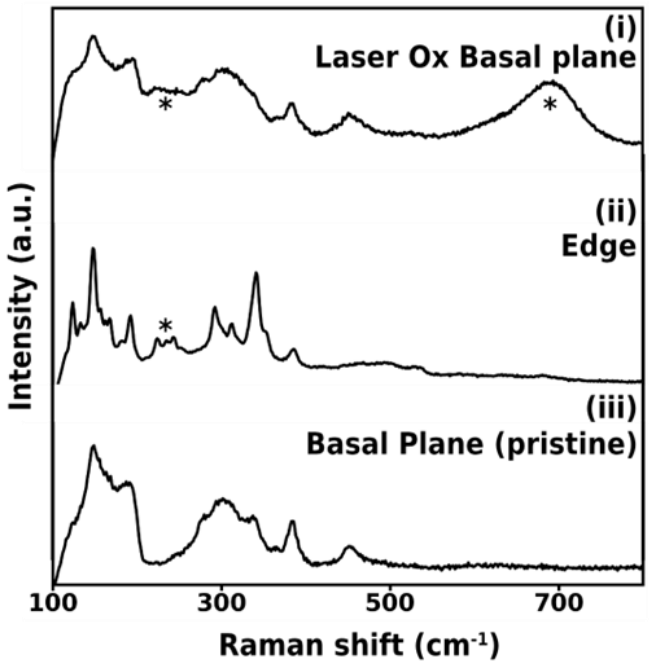


*Figure 21. Changes in Raman spectra of 3R-NbS_2. (i) shows the spectrum obtained from the laser-oxidised basal plane of 3R-NbS_2, while (ii) and (iii) show the spectrum obtained from edges and unoxidised basal plane respectively. Oxide peaks are marked with a *.*

The 3R-NbS_2 basal plane is highly sensitive to laser-induced oxidation, and the intermediate state with a distinct Nb-O peak at 220 cm^{-1} is not observed. Raman spectroscopy from burned sites evidences the formation of Nb_2O_5, with the formation of a shoulder at ~126 cm^{-1} and a substantial peak at 685 cm^{-1} indicating the presence of NbO_6 octahedra as in oxidised 2H-NbS_2 (Figure 21(i)). The expected peak at 310 cm^{-1} is not visible but is expected to be weak and thus could be concealed within the sulfide peaks. As with 2H-NbS_2, the lack of the broad peak at 685 cm^{-1} in the Raman spectrum of the edge indicates that edge oxide formation is limited and consists of primarily Nb-O defects rather than fully developed niobium oxides.

Further evidence as to the nature of TMDC oxidation was gathered with XPS. XPS was conducted on samples exfoliated/cleaved in air then rapidly (< 5 minutes) transferred into an argon atmosphere. XPS of NbS_2 shows additional oxide peaks at higher binding energies

(~207.5, 210.5 eV) than the sulfide peaks (~202.5, 205.5 eV) (Figure 22), explained well by the higher oxidation state of the metals.

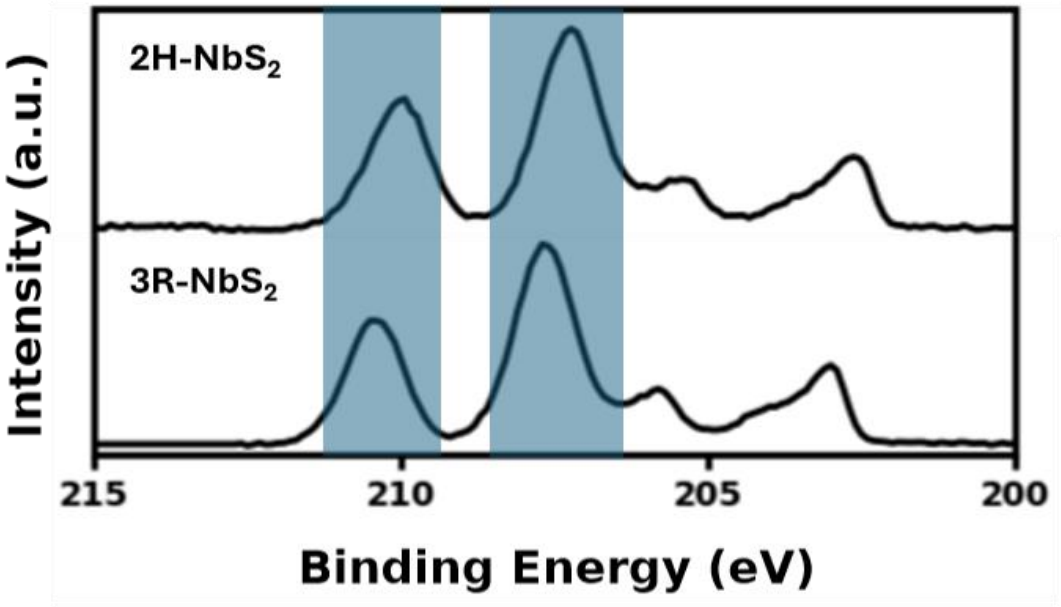


Figure 22. XPS (Nb 3d) spectra of NbS_2 crystals exfoliated/cleaved under air. Surface oxidation is evident, with oxide peaks appearing at higher binding energies than their sulfide counterparts due to the higher oxidation states of the metals (Nb_2O_5). The Nb 3d oxide peaks (marked in blue) are observed at 207.5 and 210.5 eV. The degree of oxidation varies between samples, as indicated by the relative intensities of sulfide and oxide peaks.

Similarly, TaS_2 also shows oxide peaks at higher binding energies (26.5, 28.5 eV) than the sulfide peaks (23, 25 eV) (Figure 23).

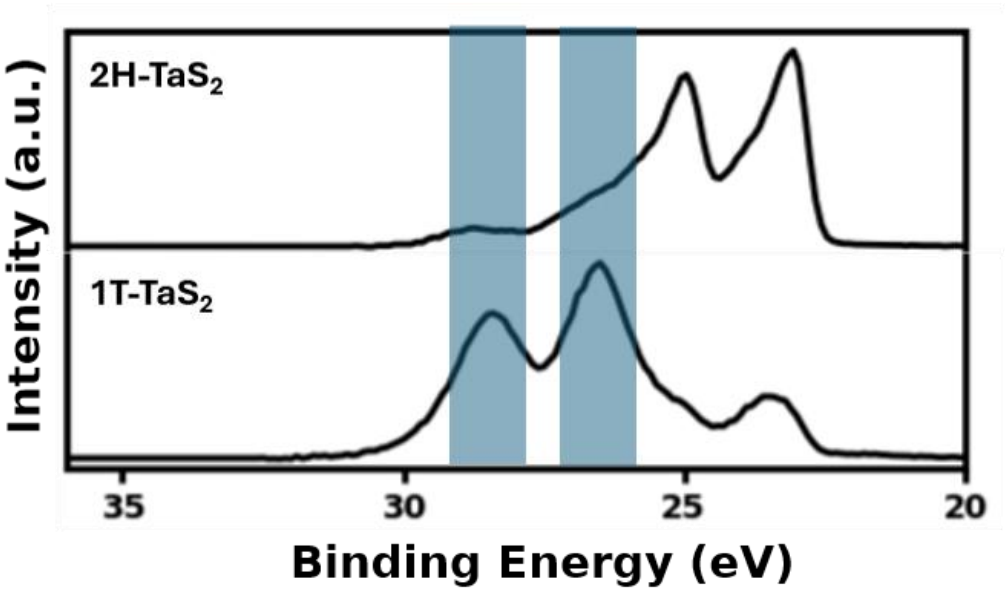


Figure 23. XPS (Ta 4f) spectra of TaS_2 crystals exfoliated/cleaved under air. Surface oxidation is evident, with oxide peaks appearing at higher binding energies than their sulfide counterparts due to the higher oxidation states of the metals (Ta_2O_5). The Ta 4f oxide peaks (marked in blue) appear at 26.5 and 28.5 eV and are evident as either peaks or shoulders. The degree of oxidation varies between samples, as indicated by the relative intensities of sulfide and oxide peaks.

With the larger XPS spot size, it is difficult to distinguish between metal-oxide signals arising from the edges and metal-oxide signals arising from the basal planes. The continued presence of metal-sulfide is explained by the protection of the sub-surface by the outer oxidised basal plane, ensuring the sub-surface layers do not react with the air. Since this basal plane oxidation takes place primarily on the outer layer, the Raman, which probes much deeper (~1 μm) does not detect it.

The consequences of these observations on the electrocatalytic behaviour of the materials can now be considered. Theoretical calculations show that both edges and planes may have an effect on the performance of 2H-NbS_2 and 1T/2H-TaS_2 [3,30], with experimental evidence for 3R-

NbS_2 evidencing some contribution of the edges to overall performance[6]. The nature of these basal planes and edges is therefore essential for a proper understanding of the materials.

TMDCs are being extensively examined for use as electrocatalysts, and with group V TMDCs of particular interest because of their basal plane activity, the oxidation characteristics of these materials are important to understand. It has been shown from the XPS (Figure 22, 23) that the basal planes of the materials are oxidised after brief exposure to air and while these oxidised planes might contribute to the activity, they are expected to be removed fairly rapidly with electrochemical cycling between 0 and -0.6 V vs RHE[16]. In contrast, the oxidised edge domains evidenced by the Raman spectra of these materials are expected to be more stable and can persist throughout electrochemical operation, meaning their influence on catalytic performance may be long-lived.

Additionally, standard preparation of TMDC catalytic electrodes requires grinding or sonicating[16] the source material before creating an ink with a suspending fluid and binder. The material is then drop or spin cast and dried to form the electrode, which is then added to a cell and the experiments conducted. Since all these preparation steps typically take place in air, preparation can lead to the introduction of oxide edges and other oxygen-based defects which may modify performance. Detecting the oxidation of edges rather than basal planes once the powder is ground is difficult, as the oxidised facets are small and distributed throughout the powder.

Raman data also evidences that oxidation is not instantaneous, as freshly broken crystals do not show rapid oxidation. Consequently, although preparation of inks and electrodes in air is possible, rapid preparation from source is recommended for consistent results. Additionally, use of IR lamps to dry electrodes is contraindicated, as the increased heat may exacerbate

oxidation. Finally, initial cycling of the material is essential before any measurement can be relied upon.

5.4 Conclusion

Large crystal syntheses of the NbS_2 and TaS_2 materials were demonstrated, both for the 2H and 3R phases of NbS_2, and for the 1T and 2H phases of TaS_2. Examination of the edge domains of the crystals with Raman spectroscopy showed that the crystal edges were more easily oxidised than the basal planes, oxidising slowly in the presence of air while the basal planes remained apparently pristine, though some oxidation was visible under XPS spectroscopy. Oxidation of the materials was also induced by Raman laser heating, and when induced, initially formed M-O sites before eventually forming MO_6 octahedra after sufficient oxidation, as indicated by Raman spectroscopy. Since water splitting catalysts are typically exposed to air in testing and use, this chapter provides insight on the edge structure expected to exist for the materials when in use.

5.5 References

(1) Lian, H.; Wu, Y.; Xing, H.; Wang, S.; Liu, Y. Effect of Stoichiometry on the Superconducting Transition Temperature in Single Crystalline 2*H*-NbS2. *Physica C: Superconductivity and its Applications* **2017**, *538*, 27–31. https://doi.org/10.1016/j.physc.2017.05.003.

(2) Cheng, Z.; He, S.; Han, X.; Wang, M.; Zhang, S.; Liu, S.; Liang, G.; Zhang, S.; Xia, M. Interfaces Determine the Nucleation and Growth of Large NbS2 Single Crystals. *CrystEngComm* **2021**, *23* (5), 1312–1320. https://doi.org/10.1039/D0CE01393E.

(3) Shi, J.; Wang, X.; Zhang, S.; Xiao, L.; Huan, Y.; Gong, Y.; Zhang, Z.; Li, Y.; Zhou, X.; Hong, M.; Fang, Q.; Zhang, Q.; Liu, X.; Gu, L.; Liu, Z.; Zhang, Y. Two-Dimensional Metallic

Tantalum Disulfide as a Hydrogen Evolution Catalyst. *Nat Commun* **2017**, *8* (1), 958. https://doi.org/10.1038/s41467-017-01089-z.

(4) Jaramillo, T. F.; Jørgensen, K. P.; Bonde, J.; Nielsen, J. H.; Horch, S.; Chorkendorff, I. Identification of Active Edge Sites for Electrochemical H2 Evolution from MoS2 Nanocatalysts. *Science* **2007**, *317* (5834), 100–102. https://doi.org/10.1126/science.1141483.

(5) Wu, L.; Sun, R.; Xiong, F.; Pei, C.; Han, K.; Peng, C.; Fan, Y.; Yang, W.; An, Q.; Mai, L. A Rechargeable Aluminum-Ion Battery Based on a VS2 Nanosheet Cathode. *Phys. Chem. Chem. Phys.* **2018**, *20* (35), 22563–22568. https://doi.org/10.1039/C8CP04772C.

(6) Zhang, J.; Wu, J.; Zou, X.; Hackenberg, K.; Zhou, W.; Chen, W.; Yuan, J.; Keyshar, K.; Gupta, G.; Mohite, A.; Ajayan, P. M.; Lou, J. Discovering Superior Basal Plane Active Two-Dimensional Catalysts for Hydrogen Evolution. *Materials Today* **2019**, *25*, 28–34. https://doi.org/10.1016/j.mattod.2019.02.014.

(7) Jones, L. X-Ray Photoemission Spectroscopy of the Mo, Re and W Dichalcogenides. Ph.D. Thesis, University of Liverpool, 2022

(8) McMullan, W. G.; Irwin, J. C. Raman Scattering from 2H and 3R–NbS2. *Solid State Communications* **1983**, *45* (7), 557–560. https://doi.org/10.1016/0038-1098(83)90426-X.

(9) Sugai, S.; Murase, K.; Uchida, S.; Tanaka, S. Studies of Lattice Dynamics in 2H TaS2 by Raman Scattering. *Solid State Communications* **1981**, *40* (4), 399–401. https://doi.org/10.1016/0038-1098(81)90847-4.

(10) Lacinska, E. M.; Furman, M.; Binder, J.; Lutsyk, I.; Kowalczyk, P. J.; Stepniewski, R.; Wysmolek, A. Raman Optical Activity of 1T-TaS2. *Nano Lett.* **2022**, *22* (7), 2835–2842. https://doi.org/10.1021/acs.nanolett.1c04990.

(11) Mandal, A.; Yadav, A. K.; Pandey, S. K.; Chakrabarti, S. Fabrication of 1T VS2 Electrode-Based In-Plane Micro-Supercapacitor Using a Cost-Effective Mask-Assisted Printing Technique. *physica status solidi (a)* **2023**, *220* (20), 2300274. https://doi.org/10.1002/pssa.202300274.

(12) Liang, H.; Shi, H.; Zhang, D.; Ming, F.; Wang, R.; Zhuo, J.; Wang, Z. Solution Growth of Vertical VS2 Nanoplate Arrays for Electrocatalytic Hydrogen Evolution. *Chem. Mater.* **2016**, *28* (16), 5587–5591. https://doi.org/10.1021/acs.chemmater.6b01963.

(13) Yang, J.; Mohmad, A. R.; Wang, Y.; Fullon, R.; Song, X.; Zhao, F.; Bozkurt, I.; Augustin, M.; Santos, E. J. G.; Shin, H. S.; Zhang, W.; Voiry, D.; Jeong, H. Y.; Chhowalla, M. Ultrahigh-Current-Density Niobium Disulfide Catalysts for Hydrogen Evolution. *Nat. Mater.* **2019**, *18* (12), 1309–1314. https://doi.org/10.1038/s41563-019-0463-8.

(14) Morosin, B. Structure Refinement on NbS2. *Acta Crystallographica Section B* **1974**, *30* (2), 551–552. https://doi.org/10.1107/S0567740874003220.

(15) Zagorac, D.; Müller, H.; Ruehl, S.; Zagorac, J.; Rehme, S. Recent Developments in the Inorganic Crystal Structure Database: Theoretical Crystal Structure Data and Related Features. *Journal of Applied Crystallography* **2019**, *52* (5), 918–925. https://doi.org/10.1107/S160057671900997X.

(16) Najafi, L.; Bellani, S.; Oropesa-Nuñez, R.; Martín-García, B.; Prato, M.; Mazánek, V.; Debellis, D.; Lauciello, S.; Brescia, R.; Sofer, Z.; Bonaccorso, F. Niobium Disulphide (NbS2)-Based (Heterogeneous) Electrocatalysts for an Efficient Hydrogen Evolution Reaction. *Journal of Materials Chemistry A* **2019**, *7* (44), 25593–25608. https://doi.org/10.1039/C9TA07210A.

(17) Island, J. Quantum Transport in Superconducting Hybrids: Molecular Devices and Layered Materials, Ph.D. Thesis, Delft University of Technology, 2016.

(18) Zhang, D.; Wu, Y.; Su, Y.-H.; Hsu, M.-C.; Ó Coileáin, C.; Cho, J.; Choi, M.; Chun, B. S.; Guo, Y.; Chang, C.-R.; Wu, H.-C. Charge Density Waves and Degenerate Modes in Exfoliated Monolayer 2H-TaS_2. *IUCrJ* **2020**, *7* (5), 913–919. https://doi.org/10.1107/S2052252520011021.

(19) Meetsma, A.; Wiegers, G. A.; Haange, R. J.; De Boer, J. L. Structure of 2H-TaS2. *Acta Crystallogr C Cryst Struct Commun* **1990**, *46* (9), 1598–1599. https://doi.org/10.1107/S0108270190000014.

(20) Peng, Y.; Zhu, L.; Li, C.; Hu, J.; Lu, Y.; Fu, J.; Cui, F.; Wang, X.; Cao, A.; Ji, Q.; Huan, Y.; Zhang, Y. Highly Stable Vertically Oriented 2H-NbS2 Nanosheets on Carbon Nanotube Films toward Superior Electrocatalytic Activity. *Advanced Energy Materials* **2024**, *14* (3), 2302510. https://doi.org/10.1002/aenm.202302510.

(21) Pfalzgraf, B. W.; Spreckels, H.; Paulus, W.; Schollhorn, R. Order-Disorder Phase Transition in Layered Cu1/2NbS2 Observed by Electrical Resistivity Measurements. *J. Phys. F: Met. Phys.* **1987**, *17* (4), 857. https://doi.org/10.1088/0305-4608/17/4/013.

(22) Fisher, W. G.; Sienko, M. J. Stoichiometry, Structure, and Physical Properties of Niobium Disulfide. *Inorg. Chem.* **1980**, *19* (1), 39–43. https://doi.org/10.1021/ic50203a009.

(23) Witteveen, C.; Górnicka, K.; Chang, J.; Månsson, M.; Klimczuk, T.; Rohr, F. O. von. Polytypism and Superconductivity in the NbS2 System. *Dalton Transactions* **2021**, *50* (9), 3216–3223. https://doi.org/10.1039/D0DT03636F.

(24) Duffey, J. R.; Kirby, R. D.; Coleman, R. V. Raman Scattering from 1T-TaS2. *Solid State Communications* **1976**, *20* (6), 617–621. https://doi.org/10.1016/0038-1098(76)91073-5.

(25) Jellinek, F. The System Tantalum-Sulfur. *Journal of the Less Common Metals* **1962**, *4* (1), 9–15. https://doi.org/10.1016/0022-5088(62)90053-X.

(26) Spijkerman, A.; de Boer, J. L.; Meetsma, A.; Wiegers, G. A.; van Smaalen, S. X-Ray Crystal-Structure Refinement of the Nearly Commensurate Phase of 1T-TaS2 in (3+2)-Dimensional Superspace. *Phys. Rev. B* **1997**, *56* (21), 13757–13767. https://doi.org/10.1103/PhysRevB.56.13757.

(27) Holder, C. F.; Schaak, R. E. Tutorial on Powder X-Ray Diffraction for Characterizing Nanoscale Materials. *ACS Nano* **2019**, *13* (7), 7359–7365. https://doi.org/10.1021/acsnano.9b05157.

(28) Joseph, C.; Bourson, P.; Fontana, M. D. Amorphous to Crystalline Transformation in Ta2O5 Studied by Raman Spectroscopy. *Journal of Raman Spectroscopy* **2012**, *43* (8), 1146–1150. https://doi.org/10.1002/jrs.3142.

(29) Hossain, N.; Günes, O.; Zhang, C.; Koughia, C.; Li, Y.; Wen, S.-J.; Wong, R.; Kasap, S.; Yang, Q. Structural and Physical Properties of NbO2 and Nb2O5 Thin Films Prepared by Magnetron Sputtering. *J Mater Sci: Mater Electron* **2019**, *30* (10), 9822–9835. https://doi.org/10.1007/s10854-019-01319-8.

(30) Tsai, C.; Chan, K.; Nørskov, J. K.; Abild-Pedersen, F. Theoretical Insights into the Hydrogen Evolution Activity of Layered Transition Metal Dichalcogenides. *Surface Science* **2015**, *640*, 133–140. https://doi.org/10.1016/j.susc.2015.01.019.

Chapter 6. Capacitance, catalysis and electronic structure of the group V TMDCs

6.0 Abstract

The group V transition metal dichalcogenides have basal planes which are active as electrocatalysts. This enables much greater catalytic surface areas compared to edge-active materials, and as such are of great interest, particularly for the hydrogen evolution reaction (HER). The wide space of possible materials, phases and dopants makes catalytic descriptors necessary, while the substantial differences in performance across different morphologies and long preparation time make experimental descriptors for intrinsic performance important. To accomplish this task, adequate methods of evaluating performance are necessary. To this end, the electronic structure of four group-V transition metal dichalcogenides, 1T-TaS_2, 2H-TaS_2, 2H-NbS_2 and 3R-NbS_2 were simulated and large single- and poly-crystals of these materials synthesised from which the performance of the pristine materials and their specific capacitance was obtained. Resulting evidence shows a substantial change of catalytic activity when performance is corrected for each material's specific capacitance, while the specific capacitance itself appears to align well with the expected catalytic performance from theory and provides a useful experimental descriptor of the thermodynamics of hydrogen adsorption onto the metal surface.

6.1 Introduction

TMDCs have a large range of potential materials and modifications, such as alloying[1], doping[2,3], material phase[4] and dimension control[5,6] which can allow for improvements in catalytic performance. Effective exploration of these options necessitates descriptors, both theoretical and experimental. This is particularly essential for the group V TMDCs, which may require thousands of cycles to induce improved conductivity across basal planes[7,8]. This cycling

is needed as the intrinsic catalytic performance of these materials is suppressed by comparatively low out-of-plane material conductivity[8].

For many TMDC studies, of both basal plane active and basal plane inactive materials, examination of material performance has centred on measuring and improving the intrinsic performance of these materials[9,10]. To this end, a consensus has developed in the HER catalytic community to report the intrinsic activity of these materials[11]. The performance is often reported using polarisation curves, which plot the current density against voltage; overpotential, which reports the voltage required to get to given current density (typically 10 mA/cm^2); and Tafel plots, which plot the logarithm of the polarisation plots to give insight into catalyst kinetics and performance[11–13].

Standard electrochemical techniques such as cyclic voltammetry, chronoamperometry and linear sweep voltammetry[14] measure the total current flow through the working electrode. Sample surface area can vary and therefore leads to different measured performances for each sample, necessitating correction and compensation[10,11,15]. This surface area variation can be independent of sample mass due to changes in particle size or roughness, modifying the specific surface area (cm^2/g). To measure sample surface area, a variety of methods are used such as SEM[8,16] and gas sorption analysis (BET)[17]. These methods are effective but suffer from being unable to directly measure the surface area accessible to the electrolyte and are unable to distinguish which areas are electrochemically active[13]. In TMDCs, this is a particular concern, as the basal planes of many TMDCs are semiconducting, and consequently will be measured as surface area by these techniques while not contributing to the electrocatalytic activity. This is because these techniques measure all surfaces regardless of whether they are conductive/metallic, and consequently catalytically active. Therefore, measurement of the electrochemically active surface area (ECSA) is necessary, and is typically achieved indirectly by measuring the capacitance, either via electrochemical impedance spectroscopy (EIS), or

variable rate cyclic voltammetry (see methods)[11,18]. Underpotential deposition methods can also be used, although those can contaminate the sample and are therefore single-use under certain circumstances[13]. The ECSA can be calculated from the capacitance via the following equation:

$$ECSA = \frac{C}{C_s} \qquad (6-1)$$

Where the sample capacitance (C, μF) is divided by the specific capacitance (C_s, μF cm^{-2}). It is therefore necessary to obtain an accurate value of C_s in order to obtain an accurate understanding of the catalyst performance.

A common assumption across the literature is to use a value of 40 μF cm^{-2} for the specific capacitance[18,19]. However, this has been challenged, with demonstrated material capacitances varying from 15 to 80 μF cm^{-2} [15,20] in aqueous electrolytes, with some materials showing specific capacitances of up to 257 μF cm^{-2} [18]. The obtained values vary greatly even for rigorously studied materials such as platinum, with reports finding values of 17 and 20 μF cm^{-2} for single crystal facets[21–23] and 52 μF cm^{-2} for polycrystalline samples[24].

The assumption of a single specific capacitance across different materials is made in the TMDC literature too, with seminal papers such as Yang et al.[7] not reporting the utilised C_s value, or using a specific capacitance of approximately 40 μF cm^{-2}, [12,25–27] or in other cases relying on area estimates from techniques that are prone to significant error, such as SEM.[8] Other reports use a specific capacitance of 60 μF cm^{-2} [11,28] which is derived from a theoretical atomically smooth MoS_2 system[29]. These difficulties have led to some reports neglecting accurate reporting of intrinsic performance altogether, relying on ECSA as a rough guide to surface area[26,30] and preferring to report performance based on geometric surface area[31,32]. These inaccuracies in measuring surface area potentially affect the accuracy of the performance

reported by these papers, and consequently the ability to extract intrinsic performance, descriptors and therefore rationally design material improvements to catalytic activity.

The use of cyclic voltammetry to obtain capacitance also relies on a non-trivial assumption, specifically assuming the electrode is a perfect capacitor[33], and use of CV or EIS is inconsistent in the literature, with little justification given for the choice of method[18,33]. While the extent of the error from CV can be small with only slightly imperfect capacitors, many pseudocapacitive materials are highly imperfect.

For an adequate understanding of the intrinsic performance of a material a value for the specific capacitance of the material must be obtained. For TMDCs, both EIS[16] and CV[7,8,34,35] are used to establish surface area, including for the group V dichalcogenides. This chapter examines the effectiveness of these ECSA methods and assumptions, understanding their utility and effects. This is done by obtaining and understanding the specific capacitance of the group V TMDCs NbS_2 and TaS_2. This permits for an accurate understanding of the performance of the pristine materials.

6.2 Theoretical Work

Construction of computational descriptors of intrinsic catalytic activity was achieved by modelling of the electronic structure of the materials. Cells of 2H-NbS_2, 3R-NbS_2, 2H-TaS_2 and 1T-TaS_2 were modelled using CASTEP[36], utilising the rSCAN[37] functional with the MBD[38] correction for the dispersion forces. rSCAN was used due to its superior replication of the material's unit cells (Chapter 4) and an expected superior[39] modelling of the material electronic structure as compared to non-meta-GGA functionals such as PBE. The obtained densities of state are shown in Figure 1. For all materials, as expected, the d-band contributes the most to the density of states around the Fermi level, with substantial p-contributions throughout. Sulfur p contributions are much more important below the Fermi level than above. The 2H-NbS_2 and

3R-NbS_2 electronic structures are very similar, with the primary difference between them being the position of the Fermi level. This is expected, as the primary difference in structure between the materials is in the positions of the layers relative to each other. Interlayer interactions therefore take place predominantly via London dispersion forces, with minimal hybridisation of orbitals, and do not meaningfully affect the band structure.

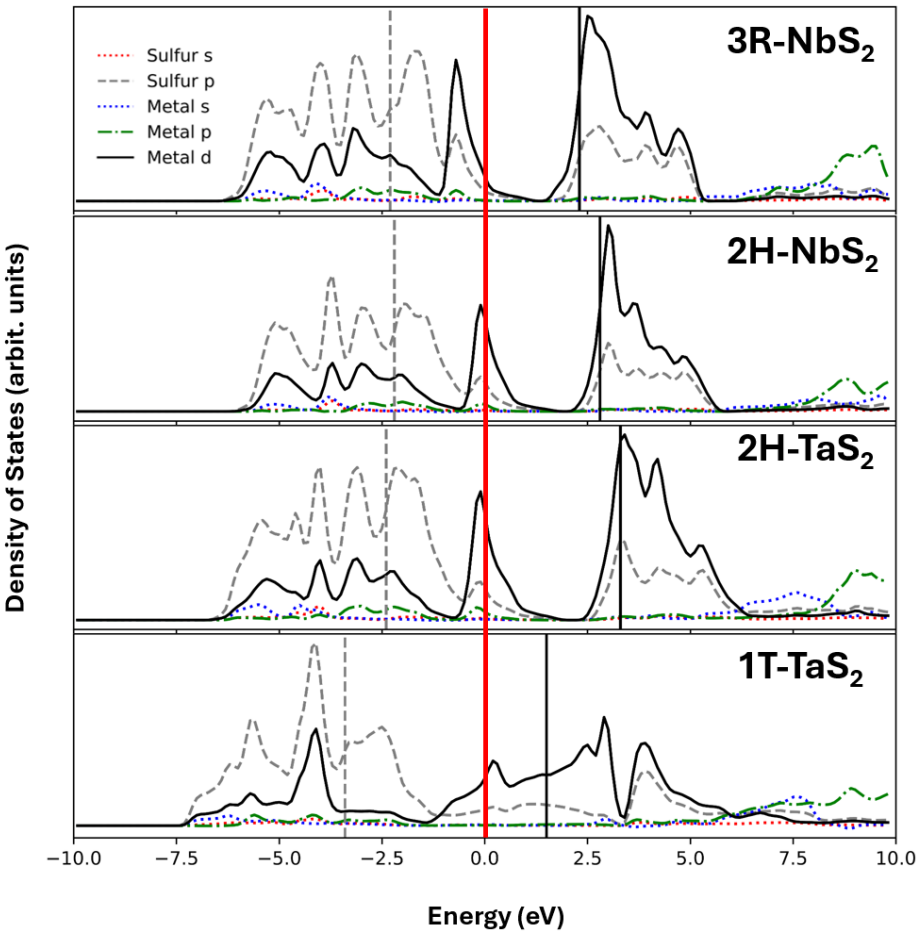


Figure 1: Plots of the projected densities of state (pDOS) of the group V metal disulfides. The 2H and 3R phases show substantial similarities, with high d-band densities of states at higher energies. The broad similarities in electronic structure can be seen in the 2H and 3R materials, which all have similar structures, while 1T-TaS_2 stands out as having a distinctly different electronic structure. The Fermi level is represented by the red vertical line, while the d-band centre and p-band centre are solid black and dashed grey respectively.

Averaged d- and p-band centre energies are shown in Table 1. D-band and p-band centres were calculated as the first moment of the projected densities of state as per equation (6-2)[40].

$$\epsilon_n = \frac{\int_{-\infty}^{\infty} \rho(\epsilon)\epsilon \, d\epsilon}{\int_{-\infty}^{\infty} \rho(\epsilon) \, d\epsilon} \qquad (6-2)$$

Where ϵ_n is the band centre, ρ the densities of state and ϵ the energy. The lower average energy of the 1T-TaS_2 d- and p- band centres indicate an expected performance different from the otherwise similar 2H-NbS_2, 3R-NbS_2 and 2H-TaS_2 (Table 1). D-band and p-band centre positions do not correlate well, but the large difference between the 1T and other structures exists in both p-band and d-band centre positions.

Table 1: calculated d-band and p-band centres of the group V disulfides. Band centres are calculated in eV relative to the Fermi centre of the material. D-band theory for transition metals predicts the performance of the material correlates to the position of the d-band centres, whose effect on the sulfur atoms can be seen in the p-band centre.

Material	**d-band centre (eV)**	**p-band centre (eV)**
3R-NbS_2	2.3	-2.3
2H-NbS_2	2.8	-2.2
1T-TaS_2	1.5	-3.4
2H-TaS_2	3.3	-2.4

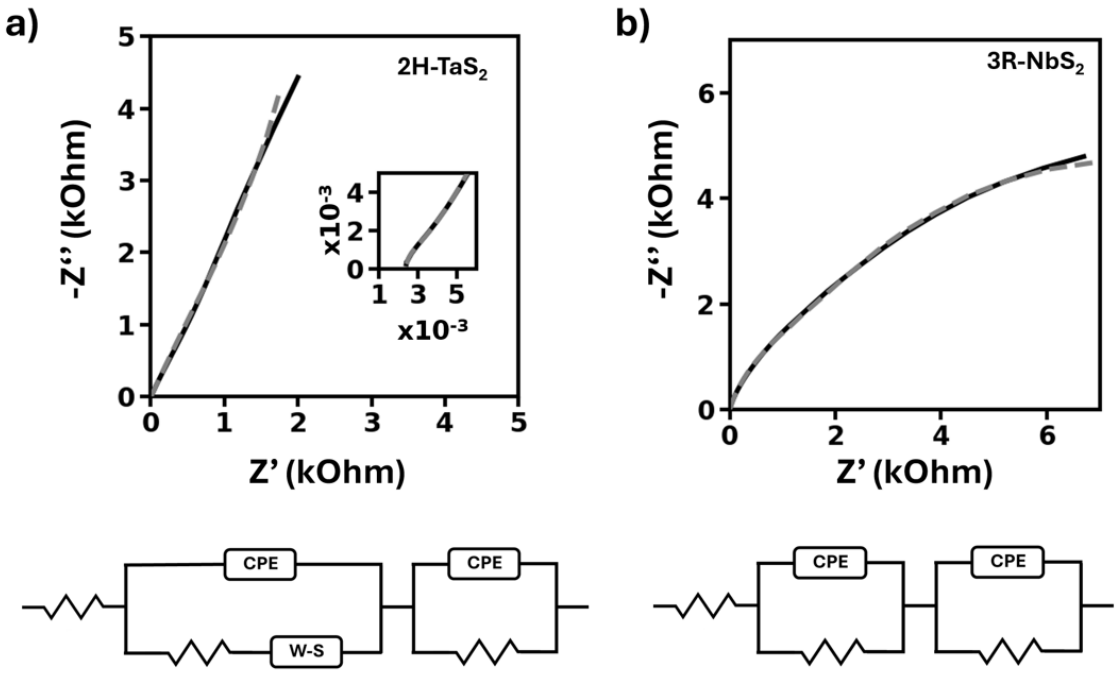
6.3 Understanding the performance of pristine materials

6.3.1 Obtaining the surface area of powdered samples

At a given voltage, the observed current from a sample is dependent on the catalytic performance of the material and the sample surface area. To adequately understand the performance of a given material, sample surface area must be obtained and corrected for.

The electrochemically active surface area of each sample was obtained using eq. 6-1, which calculates the surface area from the experimentally obtained capacitance. For this section, a commonly used[18] literature value of 40 μF cm^{-2} is used as the specific capacitance (C_s). Sample capacitances were obtained both via EIS and rapid cyclic voltammetry.

A surface-bulk model (Figure 2c) and resulting model circuit was chosen due to clear presence of two time-constants in the resulting EIS and the expected infiltration of electrolyte into the bulk of the crystal between layers, as shown by Liu et al.[8], thus causing delamination of the powder crystals forming pore-like flaws in between the layers. The expected formation of these flaws is due to the processing of the powders, which involves mechanical grinding and high energy ultrasound. The voids in these flaws would not have the same electrolytic makeup as the main solution and consequently require another time constant.


a)
2H-TaS2
-Z'' (kOhm)
Z' (kOhm)
x10-3
x10-3
CPE
CPE
W-S
b)
3R-NbS2
-Z'' (kOhm)
Z' (kOhm)
CPE
CPE

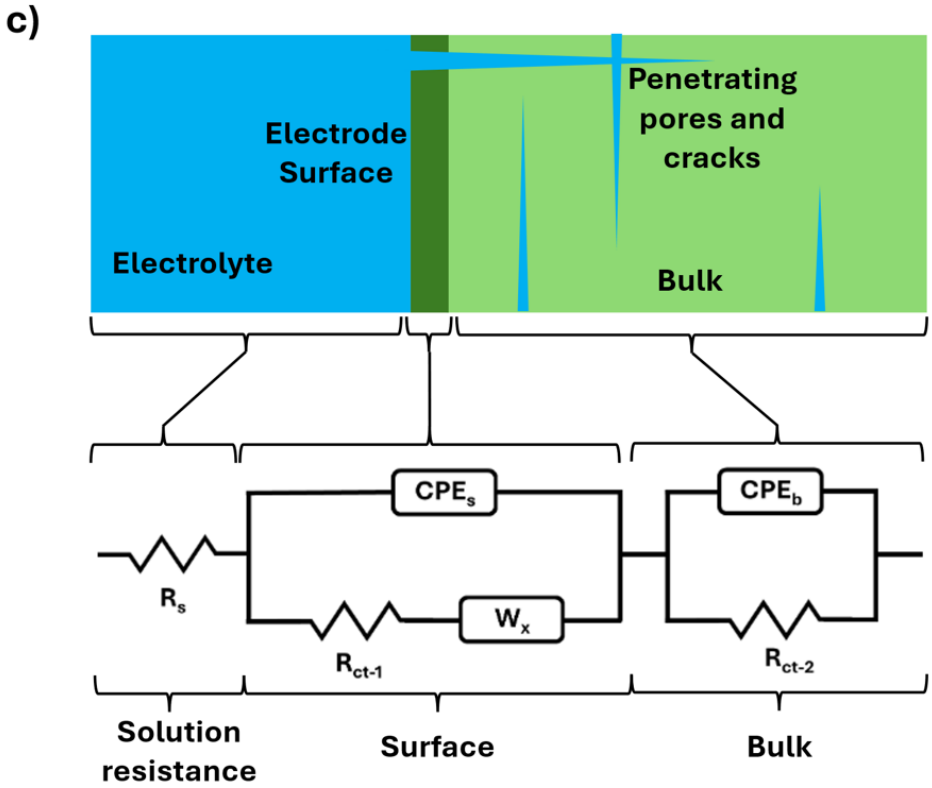

c)
Electrode Surface
Electrolyte
Penetrating pores and cracks
Bulk
CPEs
CPEb
Rs
Wx
Rct-1
Rct-2
Solution resistance
Surface
Bulk

Figure 2. Illustrative EIS of the group V metal disulfide powders. (a)-(b) show the Nyquist plots of the EIS of 2H-TaS_2 and 3R-NbS_2 respectively. Inset is a zoomed in section of the high-frequency region, showing the first time-constant region, while below each plot is the equivalent circuit used to model the spectrum. The observed data is shown in black, while the modelled data is represented by the dashed grey lines. (c) shows the expected structure of the electrode with the sections of the equivalent circuit modelling that structure. The model shows both cracks and delaminated sections, which are expected to have a different electrolyte environment from the solvent bulk, necessitating a second time constant. In the overarching model CPE_s represent the high frequency element responsible for surface capacitance, while CPE_b describes the low frequency bulk section. R_s represents the solution resistance, while R_{ct-1} and R_{ct-2} represent the charge transfer resistances. W_x represents the various possible Warburg elements that describe diffusion near the surface.

EIS spectra were fitted using an ensemble of models derived from the basic surface bulk model. In this model, the surface is dominant in the high frequency regions of the EIS plot while the bulk dominates the low frequency regions. Warburg elements, infinite (*W*), finite transmissive (*W-S*) or finite reflective (*W-PB*) are added as necessary to the surface section of the model to describe the impedance due to diffusion both at and near the surface. The necessity of using CPEs is an indicator for the presence of pseudocapacitive adsorption mechanisms throughout the crystal. These pseudocapacitive mechanisms are expected to take place primarily on the surface, while the use of CPEs for the bulk section of the model is a result of the expected complex and varying structure of bulk flaws. Nevertheless, it was found that not all samples required CPEs for modelling the capacitive element, and capacitors were substituted where appropriate.

EIS spectra (Figure 2) showed high impedance in line with expectations for uncycled materials. All EIS spectra showed multiple time constants on inspection.

Capacitance cannot be obtained from a CPE element directly. Multiple formulae for extracting the capacitance of a CPE element have been proposed[41,42]. The surface-bulk model indicates that the TMDC electrodes are not blocking electrodes, and consequently the capacitance parameter was extracted using the equations for a CPE in parallel with a resistor, as proposed by Hsu and Mansfeld[43,44].

The necessity of constructing a surface-bulk model for these materials also calls into question the use of techniques such as SEM to establish material surface area by direct observation[8,45]. The existence and extent of the bulk, as evidenced by this data and other findings in the literature, as well as potential changes to the structure of the bulk during cycling[8], which cannot be observed by SEM, renders the use of this technique dubious in the context of TMDCs. These techniques are either insufficiently selective, as they include catalytically inactive surface area, or unable to capture the extended surface area from the bulk, or both. The resulting surface areas can then lead to incorrect estimations of intrinsic catalytic activity.

Rapid cyclic voltammetry was also used to obtain capacitance data. An example set of rapid (10-300 mV/s) cyclic voltammetry is shown (Figure 3). Plots of the current vs scan rate showed deviations from the ideal straight line (Figure 3c, d), while the slow charge and discharge in the cycles (Figure 3) strongly evidences pseudocapacitive mechanisms at play. The slow charge and discharge are evidenced by the shape of the CV curve, which deviates strongly from the ideal square shape. In practice, the resulting capacitances can differ substantially from those obtained via EIS data (Table 2) and are fundamentally theoretically flawed. The effect of these pseudocapacitive and other mechanisms on capacitance values, and the resulting theoretical flaws are discussed further in section 6.6. Due to these effects, capacitance data from cycling is not used for surface area calculations, and the EIS data is used to establish intrinsic performance.

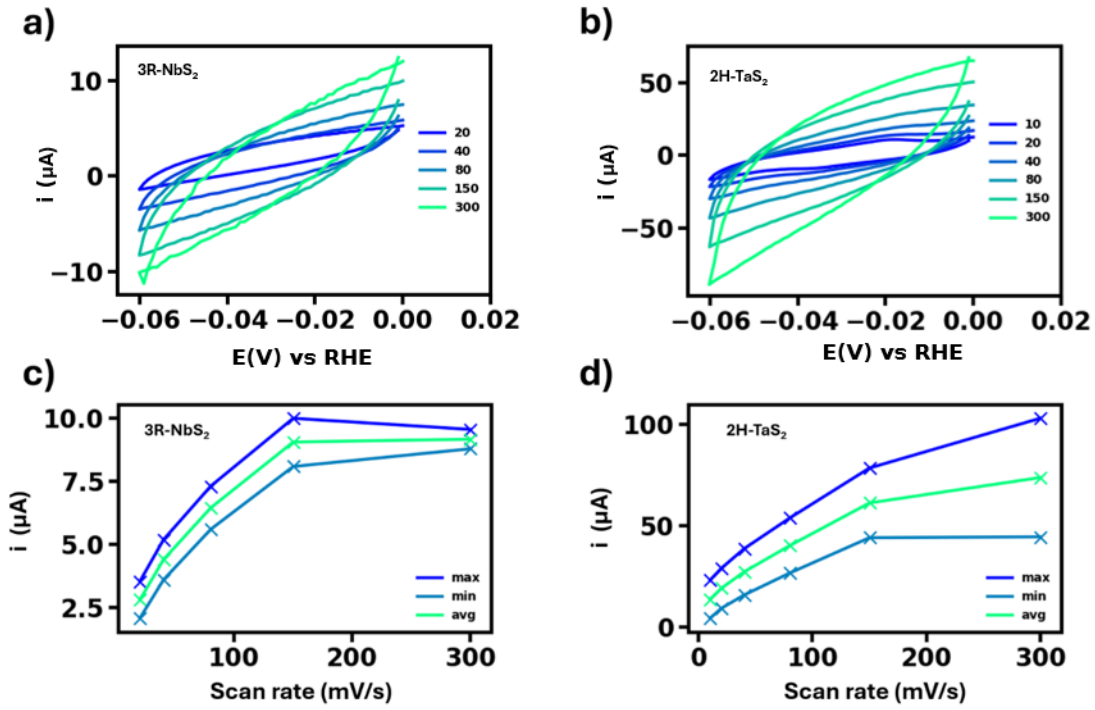


Figure 3. An example set of high-speed (10-300 mV/s) CV plots on some powder samples. a and b show the plots of 3R-NbS_2 and 2H-TaS_2 respectively, while c and d show the derived plot of scan rate against current, from whose slope the capacitance is derived. The CV plots show non-ideal behaviour, with the curve of the CV indicating that the samples are non-ideal capacitors. This can be further seen in the scan rate plots, where the deviation from a straight line means that the value of the calculated capacitance changes substantially with choice of scan rates.

Table 2. Selected sample capacitances using both the rapid cyclic voltammetry and EIS methods. The sample capacitance for CV is taken from the slope of a linear fit of all points in the current-scan speed plot. The linear fit is poor, due to the curved nature of the plot, and hence the acquired capacitance is poorly defined.

Material	**Sample capacitance (EIS, μF)**	**Sample capacitance (CV, μF)**
2H-TaS_2	0.34	0.11
1T-TaS_2	0.47	0.28
3R-NbS_2	0.075	0.08
2H-NbS_2	0.11	0.31

6.3.2 Catalytic performance

Material catalytic performance was evaluated using series chronoamperometry, from which both overpotentials and Tafel slopes were obtained (Figure 4, Figure 5 (area corrected)). The overpotential allows for direct comparison of material performance, while Tafel plots provide both the Tafel slope and the exchange current density (j_0), which provide insight into reaction mechanism and material performance respectively. All units of area are reported as the catalyst electrochemically active surface area, as obtained via EIS.

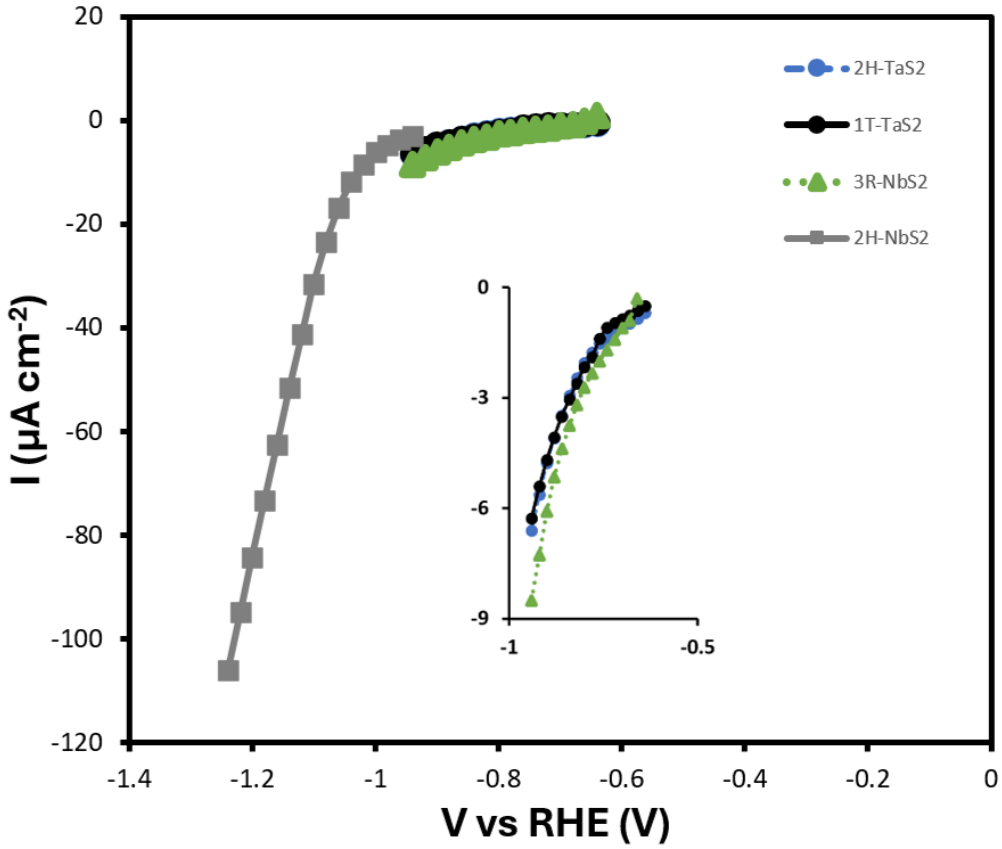


Figure 4. Polarisation plot of the TaS_2 and NbS_2 materials, showing the current passing through the catalyst as the voltage changes. These plots are constructed from a series of chronoamperometry experiments, where each point on the graph is the stabilised value of a chronoamperometry experiment, and are not corrected for sample surface area. The inset shows the performance of 2H-TaS_2, 1T-TaS_2 and 3R-NbS_2 more clearly. Samples were measured on a 1x1 cm glassy carbon piece.

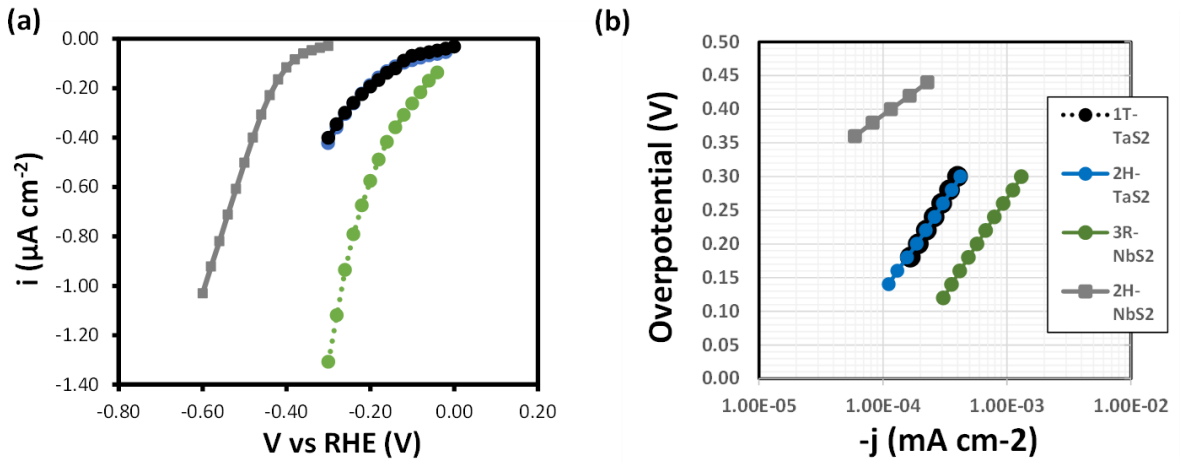


Figure 5. Plots of the performance of the group V disulfides, as corrected for ECSA. (a) Polarisation plot of the materials, showing the current passing through the material as the voltage changes. These plots are corrected for catalytic ECSA using a specific capacitance of 40 µF cm^{-2}. (b) Tafel slope plot of the materials. Both figures show near equivalent performance for the TaS_2 materials, while 2H-NbS_2 shows inferior performance to 3R-NbS_2.

Overpotentials are typically reported as the required voltage to obtain 10 mA cm^{-2}, however this was not possible for these materials, as voltages damaging to the materials are reached before the necessary current density could be obtained. Nevertheless, the series chronoamperometry plot demonstrates the expected material performance, showing the best performance for 3R-NbS_2, while both TaS_2 phases have similar but ultimately worse performance. 2H-NbS_2 shows as a distinctly worse performer than the other three. The poor performances are reflected in the Tafel slope and material exchange current densities (Table 3). The Tafel slope values for most of the phases are very high, with all phases showing Tafel slopes greater than 120 mV decade^{-1}, indicating that the system is a Volmer-limited process[46], although the extent to which the slope is above 120 mV decade^{-1} indicates other processes at play as well. The generally low exchange current densities are also in line with literature expectations[8].

Table 3. Tafel slope and exchange current densities of the group V metal disulfides 2H-NbS_2, 3R-NbS_2, 1T-TaS_2 and 2H-TaS_2 as calculated using a specific capacitance of 40 μF cm^{-2}

Material	**Tafel Slope (mV dec^{-1})**	**Exchange Current Density (mA cm^{-2})**
2H-TaS_2	307	4.20×10^{-8}
1T-TaS_2	305	4.21×10^{-9}
3R-NbS_2	286	4.84×10^{-8}
2H-NbS_2	135	1.33×10^{-10}

Interestingly, the performance of the samples does not correlate with the expected performance derived from computational data. The data shows substantially poorer performance, but crucially, the materials do not perform as expected relative to each other (Figure 5).

When corrected for surface area, the TaS_2 phases perform similarly to each other, while the NbS_2 phases have substantial differences in performance. This poor performance can be partially explained by the poor conductivity between basal planes, which is thought to increase charge transfer resistance and is not accounted for by d-band theory. It should be noted that due to this, the Tafel slopes of the materials are expected to shift with differences in morphology[8]. However, as is shown below, a major cause of this unexpected behaviour is the assumption of a single value, in this case 40 μF cm^{-2} for the specific capacitance of multiple materials.

6.4 Obtaining Specific Capacitance using large crystals

The use of a single value for the specific capacitance distorts the expected performance by distorting the value of the ECSA obtained via either EIS or capacitive cyclic voltammetry. This

distortion therefore carries over to reported overpotentials and the value of the exchange current density, while the Tafel slope is area independent. Specific capacitance is known to vary heavily across different materials, up to multiple orders of magnitude[18], and accurate material specific C_s is necessary to fully characterise a material's performance. This can be achieved by experimentally determining the capacitance of a known surface area, essentially reversing equation 6-1.

To obtain the specific capacitance, electrodes with a known surface area were constructed (Figure 6). Large (>5 mm) crystals of both phases of TaS_2 and NbS_2 were obtained via CVT. Crystals were exfoliated/cleaved and attached to copper plates with silver adhesive and all but a small (ca. 10,000 μm^2) area covered with epoxy (Loctite EA9492). The exposed area was examined under optical microscope for flaws in the crystal, and the assembly was permitted to harden, then baked at 80 °C under vacuum to prevent crystal oxidation. The baking procedure was found necessary to prevent the degradation of the epoxy in sulfuric acid. This degradation is likely to be caused by sulfuric acid etching epoxy that is not fully cured, which the baking process minimises.

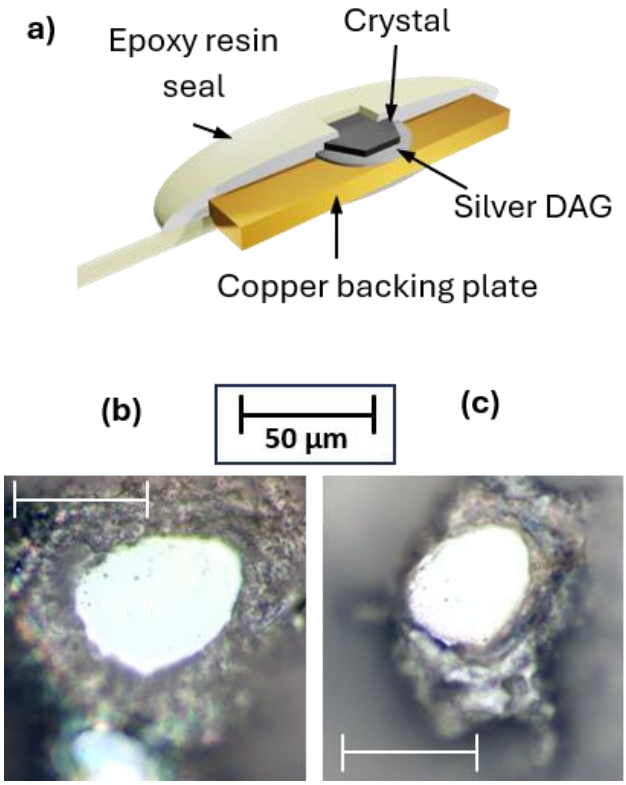


Figure 6. (a) shows the structure of the electrode used to obtain the data, while (b) and (c) shows the view under the microscope of the electrode, with the crystal seen in the centre. (b) is the crystal while pristine, while (c) is the crystal after use.

The group V TMDCs are particularly suited to this approach as they have a conductive basal plane, permitting for the determination of the ECSA from measurement of the exposed surface on the electrode.

The constructed electrode was then used as the working electrode in a standard three electrode cell (outlined in methods) and permitted to stabilise for approximately an hour at the open circuit potential (OCP), then cycled 100 times between 0 and -0.2 V vs RHE at a rate of 100 mV/s in 0.5 M H_2SO_4, after which EIS (at 0 V vs RHE) and variable scan rate capacitive cyclic voltammetry measurements were conducted. The reference electrode was a mercury-mercury sulfate electrode (Gamry, calibrated against an Ag/AgCl master reference electrode). The capacitance measurement potential was chosen to minimise the quantity of hydrogen produced,

as hydrogen production modifies the morphology of the surface and bulk[8] via delamination, increasing surface area. This delamination was visible to the naked eye at higher potentials (ca. -1 V vs RHE). Additionally, the potential production of microbubbles, which would obscure the surface is eliminated via this approach. Multiple samples were measured for each material except for 3R-NbS_2, and multiple measurements were obtained from each sample.

As with the powders, the crystal electrode capacitance was measured with EIS (Figure 7) and capacitive cyclic voltammetry (section 6.6). Across all phases and samples, EIS showed two time-constants. The exfoliation and surface selection minimise the number of edges by removing the rough grown crystal face, while exposing a smooth, unoxidised surface. Geometrically, powders are expected to have a higher edge-to-basal plane ratio due to the change in surface area to edge ratio as size changes. As expected, high impedance is observed for the large crystal samples, likely a combination of the crystals being thicker as well as the high impedance of the silver adhesive.

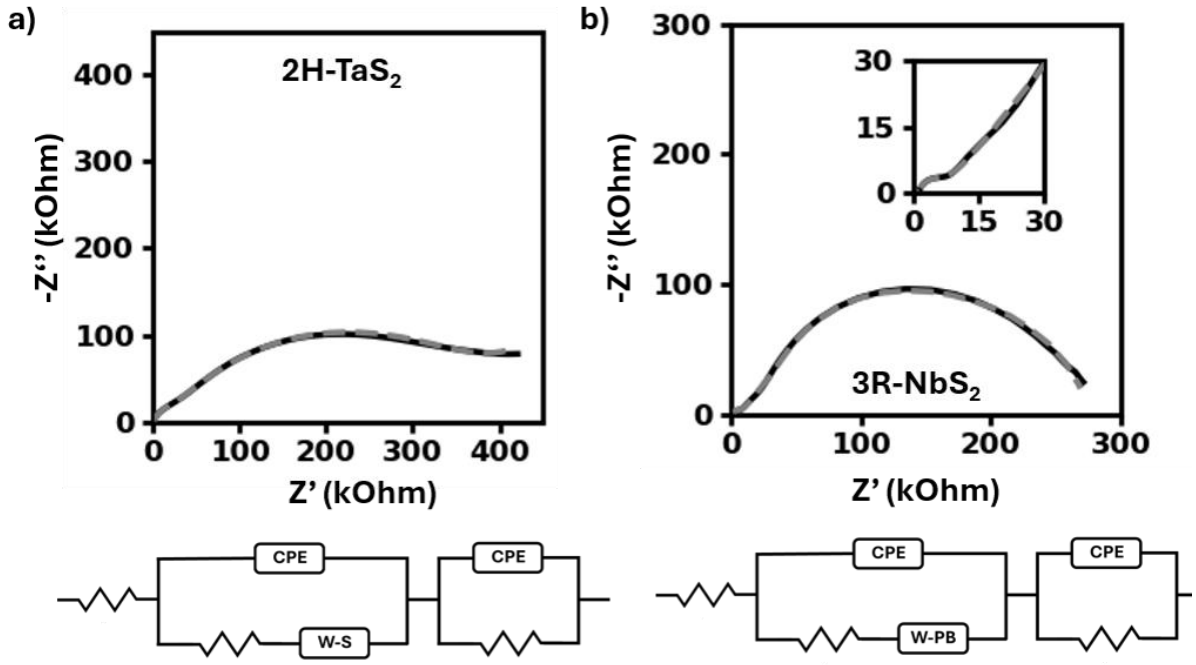


Figure 7. EIS of the group V metal disulfide crystals. (a) and (b) show the Nyquist plots of the EIS of 2H-TaS_2 and 3R-NbS_2 respectively. Inset are zoomed in sections of the high-frequency region, while below each plot is the equivalent circuit used to model the spectrum. The observed data is shown in black, while the modelled data is in grey. The presence of two time-constants in the Nyquist plots for the crystals is particularly clear, with the characteristic double hump showing well in 3R-NbS_2, while being also necessary to fit the other materials.

The presence of the two time-constants for these crystals is of interest, as similarly to the powder this indicates the necessity of a surface-bulk model, where the bulk is in the low-frequency region and has a high surface area relative to the rest of the material. The presence of the bulk in the crystal can be explained by flaws in the surface of the crystal caused by damage during the exfoliation process. These flaws will have different electrolyte environments. Another set of possible contributors to the second time-constant are voids known to be caused by microbubbles[8] forming between the layers of the material. These voids will have a different electrolyte environment, contributing to the second time constant. While these

flaws likely also exist in the powder, the voids and flaws are necessary to explain the penetration of solution into the crystal.

The surface-bulk model and the consequent separation of the surface from the bulk in EIS permits for the separate evaluation of the surface and bulk capacitance. To evaluate the specific capacitance of the material, the equivalent circuit is modelled as a whole, while only the capacitance arising from the surface/high frequency part of the model, which correlates closely to the geometric surface area, is used to evaluate surface area for specific capacitance.

Specific capacitances of the materials were obtained from multiple samples and averaged, with standard deviations recorded (Table 4). The sources of error likely arise from a combination of two factors, surface roughness and EIS model error. While the samples were selected for minimal roughness, some variation of surface roughness is expected, and this is likely reflected in the error. The EIS model error is particularly relevant. Due to high impedance and sample complexity, it is difficult to fully model the spectrum without overfitting the model. Consequently, some model inaccuracy is expected. For these samples, the standard deviations are approximately an order of magnitude lower than the obtained values.

Table 4. Obtained specific capacitances of the group V metal disulfides 2H-NbS_2, 3R-NbS_2, 1T-TaS_2 and 2H-TaS_2.

Material	Specific Capacitance ($\mu F\ cm^{-2}$)
2H-TaS_2	15.5±2.3
1T-TaS_2	7.9±0.6
3R-NbS_2	13.5±0.9
2H-NbS_2	15.3±1.6

Of the three structure types in the crystals examined, 2H, 3R and 1T, both 2H and 3R crystals have an identical intralayer structure (structure within a single layer), while the 1T intralayer structure is different. This is reflected in the data, with 2H-TaS_2, 2H-NbS_2 and 3R-NbS_2 showing similar specific capacitances at approximately 13-16 $\mu F\ cm^{-2}$, while 1T-TaS_2 shows a distinctly lower specific capacitance of ca. 8 $\mu F\ cm^{-2}$ and is the only material to have a deviation in specific capacitance beyond the error, indicating a less extensive capacitive double layer. The consistency between the structure types is expected for 2H-NbS_2 and 3R, which display identical surfaces to the electrolyte, but interestingly also remains similar across different transition metals, specifically 2H-NbS_2 and 2H-TaS_2, whose surfaces are structurally similar but chemically different.

Rapid cyclic voltammetry was also employed to obtain specific capacitances of the crystals. The resulting specific capacitances (Table 5) differ substantially from those obtained from the EIS data, and from the reasonable range of values observed in the literature. This is primarily

due to the inability of rapid cyclic voltammetry to distinguish between bulk and surface, and partially due to the prior-mentioned (section 6.3.1) effect of pseudocapacitive and other mechanisms on the capacitance values (section 6.6). If the CV-derived specific capacitance is used, these effects can lead to a large underestimation of surface areas from obtained sample capacitances. Consequently, the EIS-derived specific capacitance is preferred.

Table 5. Obtained specific capacitances from cyclic voltammetry capacitance measurements of the group V metal disulfides 2H-NbS_2, 3R-NbS_2, 1T-TaS_2 and 2H-TaS_2.

Material	**Specific Capacitance (CV derived, µF cm^{-2})**
2H-TaS_2	1392
1T-TaS_2	578
3R-NbS_2	1840
2H-NbS_2	1246

6.5 Capacitance and material performance

6.5.1 Specific capacitance and activity

The specific capacitance is sensitive to both physical structure and electronic structure. This can be understood by adapting the work of Sani et al.[47] as well as Le et al.[48], applying them in the case of negative potentials. Here, water networks form via the chemisorption of the hydrogen moiety in water, which forms a hydrophobic adlayer. This adlayer creates cavity sites for ions in the solvent between it and an adjacent water/air-like layer, with greater bonding to the hydrogen moiety increasing the capacity for those ions, whose presence increases the size of the capacitive double layer (Figure 8). Consequently, C_s can be related to the hydrogen

adsorption energy. Since hydrogen adsorption energy functions as a descriptor for the HER, C_s can also arguably function as a descriptor for the HER.

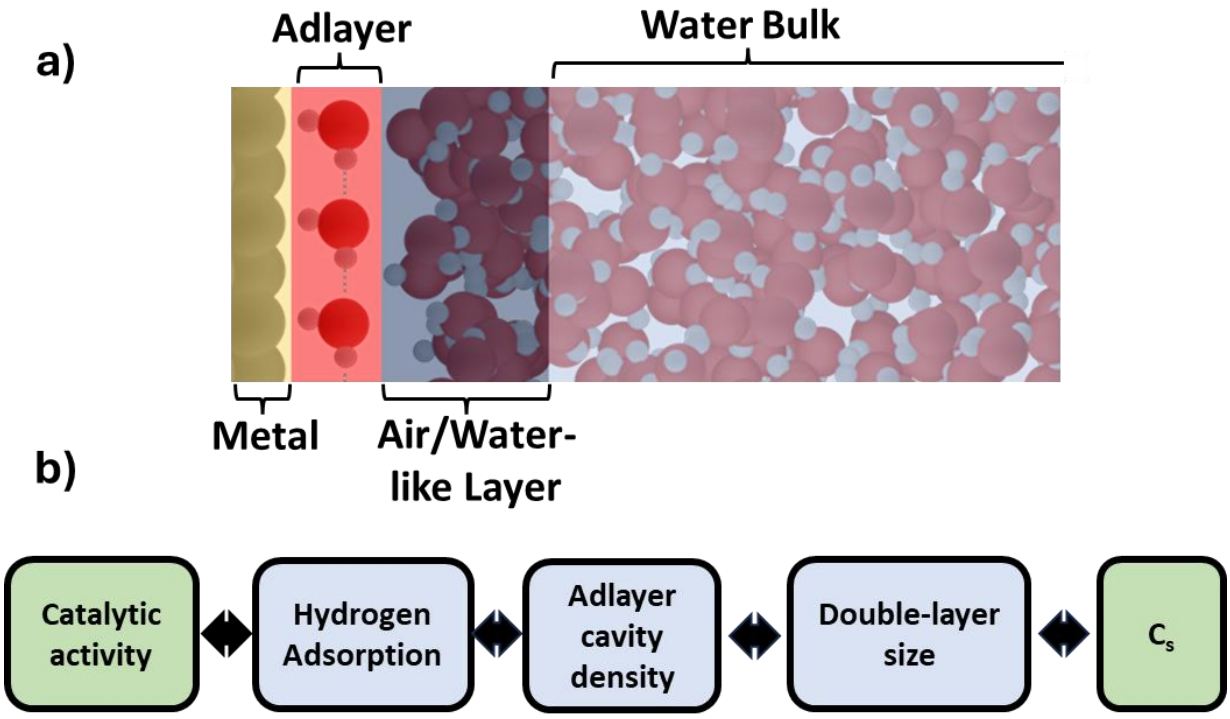


Figure 8. Section (a) shows a model of the water-metal interface. The binding of hydrogen atoms causes a hydrophobic adlayer to form, which in turn causes the formation of an air/water-like layer. Cavities between the layer and hydrophobic adlayer can accept ions, which in turn correlate to the extent of the capacitance. Section (b) summarises how catalytic activity provides information on the specific capacitance, and vice versa. Subfigure (a) was made using the Blender 3D modelling software.

This understanding of the specific capacitance arises from an assumption that the primary mechanism for the observed capacitance is double-layer capacitance. While there is good reason to believe that the TMDCs are highly pseudocapacitive, in this case it is reasonable to neglect that effect. This is because contributing pseudo-capacitance can be expected to arise from H^+ adsorption[23], either via contributions from H_3O^+ or H_2O, and therefore is expected to still act in line with its descriptive properties. Nevertheless, a specific capacitance of <20 μF

cm^{-2} is well within expected range for a purely double layer-capacitive system[23], and the EIS can be expected to minimise the pseudocapacitive behaviour of the systems, with the high value of n (>0.8, see Chapter 3) in the CPE models indicating a behaviour quite close to a capacitor.

A deeper examination of the specific capacitance values and d-bands provides further insight into the nature of the hydrogen adsorption-capacitance correlation. Basal plane adsorption of hydrogen (H_{ads}) on NbS_2 and TaS_2 is a slightly ΔG positive process[40]. The Sabatier principle predicts better performance for the hydrogen evolution reaction the closer the hydrogen adsorption energy is to 0 eV. D-band theory predicts stronger bonds (more negative ΔG) for electronic structures with higher energy antibonding states. While d-band theory as modified for TMDCs[40] predicts a negative correlation between the position of the d-band and the strength of hydrogen adsorption, this may not hold true across different phase types, such as 2H to 1T. By extending d-band theory to the p-band, we can maintain our understanding of the system. In the calculated pDOS for the materials, 1T-TaS_2 has by far the lowest energy p-band. The calculated electronic structures therefore predict weaker bonding for 1T-TaS_2 in a set of systems already suffering from too-weak bonds and consequently predicts weaker performance.

This predicted weaker performance is borne out by the literature, which consistently finds[8,49] poorer performance for 1T-TaS_2, while often finding the performance of the cycled (and therefore unaffected by poor conductivity) 2H-NbS_2, 3R-NbS_2 and 2H-TaS_2 to be roughly equivalent[8,16]. By contrast, platinum is often seen as an ideal HER catalyst, with an energy of hydrogen adsorption near 0 eV. While an early and commonly reported value for the platinum specific capacitance is 40 μF cm^{-2}, both contemporaneous and modern measurements find the value to be much closer to 20 μF cm^{-2}, which fits well with the expected trend. 1T-TaS_2 as the poorest of the catalysts has a specific capacitance of 7.9 μF cm^{-2}, while catalytic ability then continues to rise as specific capacitance does. It is likely that platinum represents an ideal value

for specific capacitance, and materials with higher specific capacitances would have their performance reduced.

This descriptor is of particular interest for TMDCs. Standard transition metal catalysts are more conductive than TMDCs, and do not suffer from significant charge transfer issues in the catalyst. TMDCs however conduct poorly between their basal planes and charge transfer issues reduce their catalytic activity, increasing both the Tafel slope value and the overpotential for the HER. Processing these TMDCs can take thousands of cycles and finalising a working recipe can be difficult. C_s is therefore a useful descriptor as its mechanism is not reliant on bulk electron transport, allowing for the indirect measurement of intrinsic catalytic activity and therefore permitting rapid experimental verification of TMDC HER catalysts. Critically, this descriptor may provide vital experimental insight into the thermodynamics of adsorption, indicating whether the material has a too-negative or too-positive ΔG of H_{ads}.

6.5.2 Pristine material performance with specific capacitance

By correcting for material area with the specific capacitance of our materials, substantial changes to the overpotentials, polarisation plots, exchange current density and Tafel plots can be observed. Since the value of the Tafel plot slopes is area independent, no change is observed (Figure 9). For the corrected exchange current densities, 3R-NbS_2 and 2H-NbS_2 have broadly similar values and 2H-TaS_2 has a lower value, while 1T-TaS_2 has a notably lower value than the other three (Table 6). The polarisation plot (Figure 9) shows a large overestimation of catalytic performance when using the value of 40 μF cm^{-2}. This demonstrates the high importance of obtaining material specific C_s to report true catalytic activity.

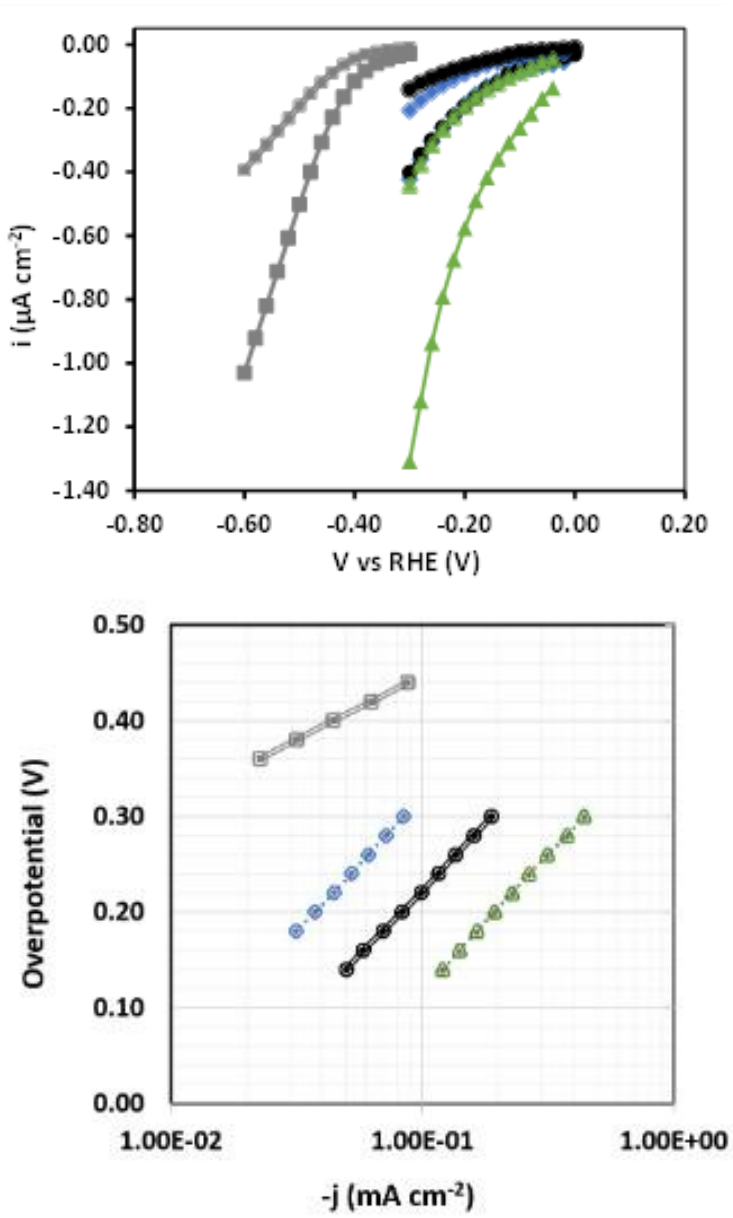


Figure 9. Polarisation plots (upper) and Tafel plots (lower) of the group V metal disulfides 2H-NbS_2, 3R-NbS_2, 1T-TaS_2 and 2H-TaS_2. The polarisation plots contrast the changes to current per unit area with previous data (Figure 5, replotted), and therefore intrinsic performance when using correct specific capacitance for the area correction. The Tafel slopes show only the calculated plots for the correct specific capacitances. While the Tafel slope does not change with different calculated surface area, the exchange current density, the intercept of the plots, does change. Data without legend entries are reproduced from Figure 5 with the same colour scheme.

Table 6. Contrasting the exchange current densities as obtained from a single C_s value as compared to the correct C_s values

Material	Tafel Slope (mV/dec)	Exchange Current Density [single C_s] (mA/cm^2)	Exchange Current Density [obtained C_s] (mA/cm^2)
2H-TaS_2	307	4.20×10^{-8}	1.87×10^{-5}
1T-TaS_2	305	4.21×10^{-9}	8.44×10^{-6}
3R-NbS_2	286	4.84×10^{-8}	3.90×10^{-5}
2H-NbS_2	135	1.33×10^{-10}	5.07×10^{-5}

This is particularly relevant for sections of the literature that seek to extract evidence for catalytic effectiveness. The similarity of reported Tafel slopes in these papers makes the Tafel slope a poor measure for understanding the performance of the material, while the data obtained here demonstrates an accurate C_s value is indispensable for accurate extraction of material performance as compared to materials such as platinum. Similarly, comparisons to chemically different TMDCs, such as MoS_2 must be treated with significant caution. Nevertheless, the close similarity in C_s between the 2H and 3R materials indicates that comparisons between those materials are accurate relative to each other.

Also, of interest as a measure of intrinsic catalytic activity is the exchange current density. Nørskov *et al*.[50] related the exchange current density to the energy of hydrogen adsorption for

the HER. With a single C_s value, the exchange current density does not reflect the electronic structure calculations and reported results in the literature[7,8,35] of apparent intrinsic catalytic activity. With material specific C_s, calculated exchange current densities reflect the expected intrinsic catalytic performance substantially better, with 1T-TaS_2 possessing a distinctly lower exchange current density than the other materials. Similarly, the performance of 2H-NbS_2 and 3R-NbS_2 are closer to each other than to 2H-TaS_2, reflecting the similarity in structures and electronic structures of the NbS_2 phases. In the absence of C_s proving a reliable experimental descriptor of the activity of HER catalysts, a properly area-calibrated exchange current density may be an effective alternative.

6.6 Use of scan rate cyclic voltammetry for determination of ECSA

Obtaining material capacitance via varying scan rate of cyclic voltammetry is a common[15] technique. However, this technique has weaknesses when significant pseudo-capacitance is present alongside double-layer capacitance. This is typically demonstrated by a curve in the CV plot at the vertices, as the change in charge leads to rapid changes in charging or discharging of the double layer, but slower charging and discharging of charge arising from pseudo-capacitance (Figure 10). This can have a pronounced effect on the accuracy of this technique, as it relies on change in current against the CV rate being linear:

$$i_c = vC \qquad (6-3)$$

Where v is the rate of change of voltage, C the capacitance and i_c the observed current. Where pseudo-capacitance is enough to cause significant changes to the value of Δi, the linearity of that relationship is affected. This effect is particularly pronounced for the group V TMDCs, where it leads to extreme changes in the capacitance value calculated from the slope of the plot, making evaluations of capacitance at any cycling speed unreliable (Figure 10, 11).

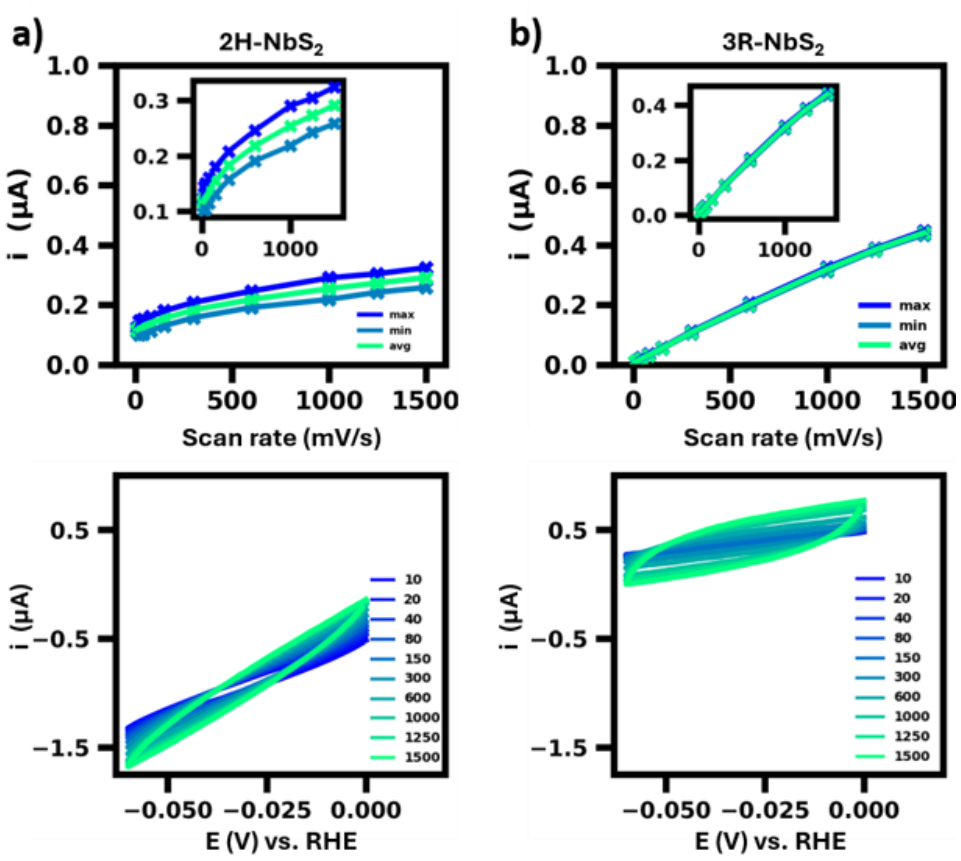


Figure 10. Shown are the high-speed (10-1500 mV/s) CV plots and rate-current plots of the group V metal disulfides 2H-NbS_2 (a) and 3R-NbS_2 (b). Insets show areas of interest zoomed in. The CV plots show highly non-ideal capacitance behaviour, while the rate-current plots, from whose slopes the capacitance can be derived, are clearly non-linear, making the derivation of an accurate capacitance difficult. The basis of this deviation from ideal behaviour is thought to be due to pseudocapacitive behaviour and indicates that the CV method for obtaining capacitance is unsuitable for these materials.

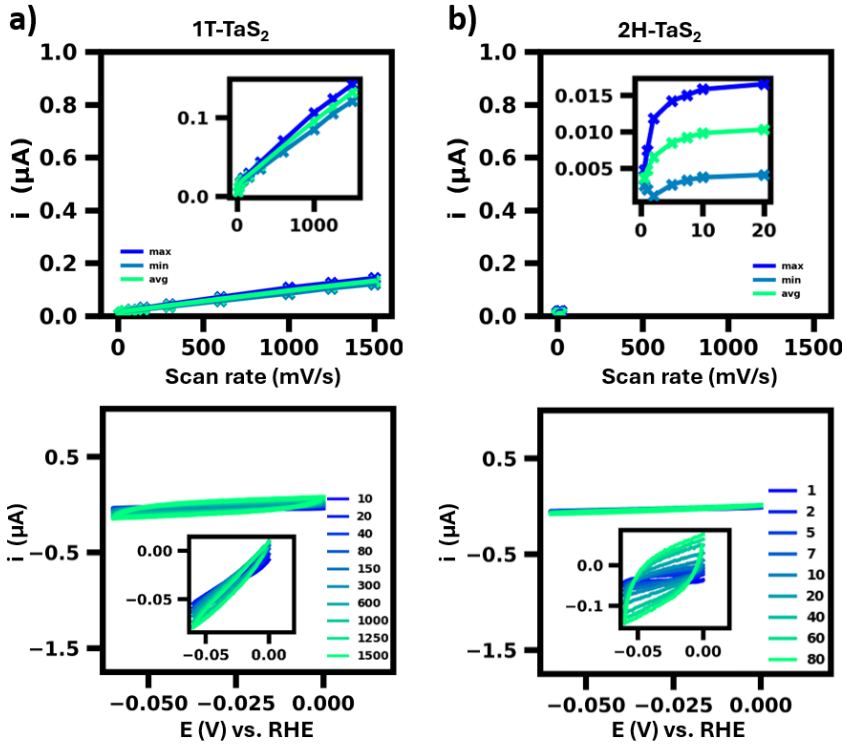


Figure 11. Shown are the high-speed (10-1500 mV/s) CV plots and rate-current plots of the group V metal disulfides 1T-TaS_2 (a) and 2H-TaS_2 (b). Insets show areas of interest zoomed in. The CV plots show highly non-ideal capacitance behaviour, while the rate-current plots, from whose slopes the capacitance can be derived, are clearly non-linear, making the derivation of an accurate capacitance difficult. The basis of this deviation from ideal behaviour is thought to be due to pseudocapacitive behaviour and indicates that the CV method for obtaining capacitance is unsuitable for these materials.

While this effect is very pronounced for scan rate, the effect on EIS capacitance estimation appears to be less notable. As discussed in section 6.5.1, the CPE components appear to be minimally pseudocapacitive. This difference in behaviour of the CVs and EIS may be attributable to slow pseudocapacitive adsorption processes, which are substantial and observable in the large amplitude slower CV scans, but not present in the small amplitude and substantially more rapid EIS[51]. Consequently, it is strongly recommended to use EIS over scan rate cyclic voltammetry for electrochemical surface area determination in group V TMDCs.

6.7 Conclusion

This chapter demonstrates the necessity of using EIS for the effective acquisition of group V TMDC surface area, and shows the fundamental issues encountered when using variable scan rate cyclic voltammetry to obtain capacitance or SEM to obtain surface area. Additionally, a surface-bulk model ensemble was constructed for EIS evaluation of these materials. The use of EIS over scan rate or SEM is therefore strongly recommended for determination of the ECSA of these materials.

The performance of the uncycled materials 2H-NbS_2, 3R-NbS_2, 2H-TaS_2 and 1T-TaS_2 was obtained, and corrected for specific capacitance, which itself was obtained via construction of a working electrode consisting of larger crystals encased in epoxy of known surface area. The C_s of the materials were found to be 15.5, 7.9, 13.5 and 15.3 μF cm^{-2} for 2H-TaS_2, 1T-TaS_2, 3R-NbS_2, 2H-NbS_2, with standard deviations of 2.3, 0.6, 0.9 and 1.6 respectively, indicating that 1T-TaS_2 had a substantially different specific capacitance than the rest of the materials, which were broadly similar.

Comparison of the material performances corrected with the obtained specific capacitance to the use of the standard value of 40 μF cm^{-2} evidenced substantial changes in apparent performance. While the behaviour of these materials relative to each other was found to be mostly invariant due to the similar C_s of the 2H and 3R materials, substantial changes to the relative performance of the 1T materials were observed. The correct use of C_s is therefore shown to be important for adequate comparison of these materials to platinum and other materials, and therefore the construction of adequate descriptors of material performance.

The electronic structures of 2H-NbS_2, 3R-NbS_2, 2H-TaS_2 and 1T-TaS_2 were simulated, and d-band theory applied and modified to understand the apparent correlation between material pDOS, specific capacitance and material performance. Applying the theories of Sani et al.[47]

and Le et al.[48] provides insight into the mechanism of this correlation, namely that electronic structure correlates well to hydrogen adsorption, which causes changes in the solvent adlayer on the metal surface, correlating to ion adsorption and consequently double layer size and finally specific capacitance. By reversing this, we realise that specific capacitance provides experimental insight into the thermodynamics of material adsorption and could permit specific capacitance to act as a descriptor for the intrinsic electrocatalytic activity of a material, unconstrained by sample impedance. Similarly, the reflection of the energy of hydrogen adsorption in the exchange current densities when used with the correct C_s may provide an additional descriptor of the intrinsic catalytic activity.

6.8 References

(1) Kwon, I. S.; Kwak, I. H.; Zewdie, G. M.; Lee, S. J.; Kim, J. Y.; Yoo, S. J.; Kim, J.; Park, J.; Kang, H. S. $MoSe_2$–VSe_2–$NbSe_2$ Ternary Alloy Nanosheets to Boost Electrocatalytic Hydrogen Evolution Reaction. *Advanced Materials* **2022**, *34* (41). https://doi.org/10.1002/adma.202205524.

(2) Luo, R.; Luo, M.; Wang, Z.; Liu, P.; Song, S.; Wang, X.; Chen, M. The Atomic Origin of Nickel-Doping-Induced Catalytic Enhancement in MoS 2 for Electrochemical Hydrogen Production. *Nanoscale* **2019**, *11* (15), 7123–7128. https://doi.org/10.1039/C8NR10023C.

(3) Liu, P.; Zhu, J.; Zhang, J.; Xi, P.; Tao, K.; Gao, D.; Xue, D. P Dopants Triggered New Basal Plane Active Sites and Enlarged Interlayer Spacing in MoS2 Nanosheets toward Electrocatalytic Hydrogen Evolution. *ACS Energy Lett.* **2017**, *2* (4), 745–752. https://doi.org/10.1021/acsenergylett.7b00111.

(4) Chang, L.; Sun, Z.; Hu, Y. H. 1T Phase Transition Metal Dichalcogenides for Hydrogen Evolution Reaction. *Electrochem. Energ. Rev.* **2021**, *4* (2), 194–218. https://doi.org/10.1007/s41918-020-00087-y.

(5) Wang, T.; Gao, D.; Zhuo, J.; Zhu, Z.; Papakonstantinou, P.; Li, Y.; Li, M. Size-Dependent Enhancement of Electrocatalytic Oxygen-Reduction and Hydrogen-Evolution Performance of MoS2 Particles. *Chemistry – A European Journal* **2013**, *19* (36), 11939–11948. https://doi.org/10.1002/chem.201301406.

(6) He, Q.; Chen, X.; Chen, S.; Liu, L.; Zhou, F.; Li, X.-B.; Wang, G. Electrochemical Hydrogen Evolution at the Interface of Monolayer VS_2 and Water from First-Principles Calculations. *ACS Appl. Mater. Interfaces* **2019**, *11* (3), 2944–2949. https://doi.org/10.1021/acsami.8b17075.

(7) Yang, J.; Mohmad, A. R.; Wang, Y.; Fullon, R.; Song, X.; Zhao, F.; Bozkurt, I.; Augustin, M.; Santos, E. J. G.; Shin, H. S.; Zhang, W.; Voiry, D.; Jeong, H. Y.; Chhowalla, M. Ultrahigh-Current-Density Niobium Disulfide Catalysts for Hydrogen Evolution. *Nat. Mater.* **2019**, *18* (12), 1309–1314. https://doi.org/10.1038/s41563-019-0463-8.

(8) Liu, Y.; Wu, J.; Hackenberg, K. P.; Zhang, J.; Wang, Y. M.; Yang, Y.; Keyshar, K.; Gu, J.; Ogitsu, T.; Vajtai, R.; Lou, J.; Ajayan, P. M.; Wood, B. C.; Yakobson, B. I. Self-Optimizing, Highly Surface-Active Layered Metal Dichalcogenide Catalysts for Hydrogen Evolution. *Nat Energy* **2017**, *2* (9), 1–7. https://doi.org/10.1038/nenergy.2017.127.

(9) Yu, Q.; Luo, Y.; Qiu, S.; Li, Q.; Cai, Z.; Zhang, Z.; Liu, J.; Sun, C.; Liu, B. Tuning the Hydrogen Evolution Performance of Metallic 2D Tantalum Disulfide by Interfacial Engineering. *ACS Nano* **2019**, *13* (10), 11874–11881. https://doi.org/10.1021/acsnano.9b05933.

(10) Anantharaj, S.; Kundu, S. Do the Evaluation Parameters Reflect Intrinsic Activity of Electrocatalysts in Electrochemical Water Splitting? *ACS Energy Lett.* **2019**, *4* (6), 1260–1264. https://doi.org/10.1021/acsenergylett.9b00686.

(11) Wu, L.; Hofmann, J. P. Comparing the Intrinsic HER Activity of Transition Metal Dichalcogenides: Pitfalls and Suggestions. *ACS Energy Lett.* **2021**, *6* (7), 2619–2625. https://doi.org/10.1021/acsenergylett.1c00912.

(12) McCrory, C. C. L.; Jung, S.; Peters, J. C.; Jaramillo, T. F. Benchmarking Heterogeneous Electrocatalysts for the Oxygen Evolution Reaction. *J. Am. Chem. Soc.* **2013**, *135* (45), 16977–16987. https://doi.org/10.1021/ja407115p.

(13) Wei, C.; Rao, R. R.; Peng, J.; Huang, B.; Stephens, I. E. L.; Risch, M.; Xu, Z. J.; Shao-Horn, Y. Recommended Practices and Benchmark Activity for Hydrogen and Oxygen Electrocatalysis in Water Splitting and Fuel Cells. *Advanced Materials* **2019**, *31* (31). https://doi.org/10.1002/adma.201806296.

(14) Bard, A. J.; Faulkner, L. R.; White, H. S. *Electrochemical Methods: Fundamentals and Applications*; John Wiley & Sons, 2022.

(15) Trasatti, S.; Petrii, O. A. Real Surface Area Measurements in Electrochemistry. *Pure and Applied Chemistry* **1991**, *63* (5), 711–734. https://doi.org/10.1351/pac199163050711.

(16) Zhang, J.; Wu, J.; Zou, X.; Hackenberg, K.; Zhou, W.; Chen, W.; Yuan, J.; Keyshar, K.; Gupta, G.; Mohite, A.; Ajayan, P. M.; Lou, J. Discovering Superior Basal Plane Active Two-Dimensional Catalysts for Hydrogen Evolution. *Materials Today* **2019**, *25*, 28–34. https://doi.org/10.1016/j.mattod.2019.02.014.

(17) Crane, M. J.; Lim, M. B.; Zhou, X.; Pauzauskie, P. J. Rapid Synthesis of Transition Metal Dichalcogenide–Carbon Aerogel Composites for Supercapacitor Electrodes. *Microsyst Nanoeng* **2017**, *3* (1), 1–9. https://doi.org/10.1038/micronano.2017.32.

(18) Connor, P.; Schuch, J.; Kaiser, B.; Jaegermann, W. The Determination of Electrochemical Active Surface Area and Specific Capacity Revisited for the System MnOx as

an Oxygen Evolution Catalyst. *Zeitschrift für Physikalische Chemie* **2020**, *234* (5), 979–994. https://doi.org/10.1515/zpch-2019-1514.

(19) Liang, H.; Gandi, A. N.; Anjum, D. H.; Wang, X.; Schwingenschlögl, U.; Alshareef, H. N. Plasma-Assisted Synthesis of NiCoP for Efficient Overall Water Splitting. *Nano Lett.* **2016**, *16* (12), 7718–7725. https://doi.org/10.1021/acs.nanolett.6b03803.

(20) Boggio, R.; Carugati, A.; Trasatti, S. Electrochemical Surface Properties of Co3O4 Electrodes. *J Appl Electrochem* **1987**, *17* (4), 828–840. https://doi.org/10.1007/bf01007821.

(21) Rosen, M.; Flinn, D. R.; Schuldiner, S. Double Layer Capacitance on Platinum in 1 M H2SO4 from the Reversible Hydrogen Potential to the Oxygen Formation Region. *J. Electrochem. Soc.* **1969**, *116* (8), 1112. https://doi.org/10.1149/1.2412227.

(22) Pajkossy, T.; Kolb, D. M. Double Layer Capacitance of the Platinum Group Metals in the Double Layer Region. *Electrochemistry Communications* **2007**, *9* (5), 1171–1174. https://doi.org/10.1016/j.elecom.2007.01.002.

(23) Pajkossy, T.; Kolb, D. M. Double Layer Capacitance of Pt(111) Single Crystal Electrodes. *Electrochimica Acta* **2001**, *46* (20), 3063–3071. https://doi.org/10.1016/S0013-4686(01)00597-7.

(24) Chen, D.; Tao, Q.; Liao, L. W.; Liu, S. X.; Chen, Y. X.; Ye, S. Determining the Active Surface Area for Various Platinum Electrodes. *Electrocatal* **2011**, *2* (3), 207–219. https://doi.org/10.1007/s12678-011-0054-1.

(25) Kumar, M.; Nagaiah, T. C. A NiCu–MoS 2 Electrocatalyst for pH-Universal Hydrogen Evolution Reaction and Zn–Air Batteries Driven Self-Power Water Splitting. *Journal of Materials Chemistry A* **2023**, *11* (34), 18336–18348.

(26) Yue, H.; Guo, Z.; Zhou, Z.; Zhang, X.; Guo, W.; Zhen, S.; Wang, P.; Wang, K.; Yuan, W. S−S Bond Strategy at Sulfide Heterointerface: Reversing Charge Transfer and Constructing Hydrogen Spillover for Boosted Hydrogen Evolution. *Angew Chem Int Ed* **2024**, *63* (48). https://doi.org/10.1002/anie.202409465.

(27) Park, J.; Cho, I.; Jeon, H.; Lee, Y.; Zhang, J.; Lee, D.; Cho, M. K.; Preston, D. J.; Shong, B.; Kim, I. S.; Lee, W. Conversion of Layered WS_2 Crystals into Mixed-Domain Electrochemical Catalysts by Plasma-Assisted Surface Reconstruction. *Advanced Materials* **2024**, *36* (25). https://doi.org/10.1002/adma.202314031.

(28) Benson, J.; Li, M.; Wang, S.; Wang, P.; Papakonstantinou, P. Electrocatalytic Hydrogen Evolution Reaction on Edges of a Few Layer Molybdenum Disulfide Nanodots. *ACS Appl. Mater. Interfaces* **2015**, *7* (25), 14113–14122. https://doi.org/10.1021/acsami.5b03399.

(29) Benck, J. D.; Chen, Z.; Kuritzky, L. Y.; Forman, A. J.; Jaramillo, T. F. Amorphous Molybdenum Sulfide Catalysts for Electrochemical Hydrogen Production: Insights into the Origin of Their Catalytic Activity. *ACS Catal.* **2012**, *2* (9), 1916–1923. https://doi.org/10.1021/cs300451q.

(30) Si, J.; Zheng, Q.; Chen, H.; Lei, C.; Suo, Y.; Yang, B.; Zhang, Z.; Li, Z.; Lei, L.; Hou, Y.; Ostrikov, K. (Ken). Scalable Production of Few-Layer Niobium Disulfide Nanosheets via Electrochemical Exfoliation for Energy-Efficient Hydrogen Evolution Reaction. *ACS Appl. Mater. Interfaces* **2019**, *11* (14), 13205–13213. https://doi.org/10.1021/acsami.8b22052.

(31) Yu, Q.; Zhang, Z.; Qiu, S.; Luo, Y.; Liu, Z.; Yang, F.; Liu, H.; Ge, S.; Zou, X.; Ding, B.; Ren, W.; Cheng, H.-M.; Sun, C.; Liu, B. A Ta-TaS2 Monolith Catalyst with Robust and Metallic Interface for Superior Hydrogen Evolution. *Nat Commun* **2021**, *12* (1), 6051. https://doi.org/10.1038/s41467-021-26315-7.

(32) Jaramillo, T. F.; Jørgensen, K. P.; Bonde, J.; Nielsen, J. H.; Horch, S.; Chorkendorff, I. Identification of Active Edge Sites for Electrochemical H2 Evolution from MoS2 Nanocatalysts. *Science* **2007**, *317* (5834), 100–102. https://doi.org/10.1126/science.1141483.

(33) Gharbi, O.; Tran, M. T.; Tribollet, B.; Turmine, M.; Vivier, V. Revisiting Cyclic Voltammetry and Electrochemical Impedance Spectroscopy Analysis for Capacitance Measurements. *Electrochimica Acta* **2020**, *343*, 136109.

(34) Najafi, L.; Bellani, S.; Oropesa-Nuñez, R.; Martín-García, B.; Prato, M.; Mazánek, V.; Debellis, D.; Lauciello, S.; Brescia, R.; Sofer, Z.; Bonaccorso, F. Niobium Disulphide (NbS2)-Based (Heterogeneous) Electrocatalysts for an Efficient Hydrogen Evolution Reaction. *J. Mater. Chem. A* **2019**, *7* (44), 25593–25608. https://doi.org/10.1039/C9TA07210A.

(35) Najafi, L.; Bellani, S.; Oropesa-Nuñez, R.; Martín-García, B.; Prato, M.; Pasquale, L.; Panda, J.-K.; Marvan, P.; Sofer, Z.; Bonaccorso, F. TaS2, TaSe2, and Their Heterogeneous Films as Catalysts for the Hydrogen Evolution Reaction. *ACS Catal.* **2020**, *10* (5), 3313–3325. https://doi.org/10.1021/acscatal.9b03184.

(36) Clark, S. J.; Segall, M. D.; Pickard, C. J.; Hasnip, P. J.; Probert, M. I. J.; Refson, K.; Payne, M. C. First Principles Methods Using CASTEP. *Zeitschrift für Kristallographie - Crystalline Materials* **2005**, *220* (5–6), 567–570. https://doi.org/10.1524/zkri.220.5.567.65075.

(37) Furness, J. W.; Kaplan, A. D.; Ning, J.; Perdew, J. P.; Sun, J. Construction of Meta-GGA Functionals through Restoration of Exact Constraint Adherence to Regularized SCAN Functionals. *The Journal of Chemical Physics* **2022**, *156* (3), 034109. https://doi.org/10.1063/5.0073623.

(38) Ambrosetti, A.; Reilly, A. M.; DiStasio, R. A.; Tkatchenko, A. Long-Range Correlation Energy Calculated from Coupled Atomic Response Functions. *J Chem Phys* **2014**, *140* (18), 18A508. https://doi.org/10.1063/1.4865104.

(39) Zhang, I. Y.; Xu, X. On the Top Rung of Jacob's Ladder of Density Functional Theory: Toward Resolving the Dilemma of SIE and NCE. *WIREs Computational Molecular Science* **2021**, *11* (1), e1490. https://doi.org/10.1002/wcms.1490.

(40) Tsai, C.; Chan, K.; Nørskov, J. K.; Abild-Pedersen, F. Understanding the Reactivity of Layered Transition-Metal Sulfides: A Single Electronic Descriptor for Structure and Adsorption. *J. Phys. Chem. Lett.* **2014**, *5* (21), 3884–3889. https://doi.org/10.1021/jz5020532.

(41) Hsu, C.; Mansfeld, F. Concerning the Conversion of the Constant Phase Element Parameter Y into a Capacitance. *Corrosion* **2001**, *57* (9), 747–748.

(42) Brug, G.; van den Eeden, A. L.; Sluyters-Rehbach, M.; Sluyters, J. H. The Analysis of Electrode Impedances Complicated by the Presence of a Constant Phase Element. *Journal of electroanalytical chemistry and interfacial electrochemistry* **1984**, *176* (1–2), 275–295.

(43) Chang, B.-Y. Conversion of a Constant Phase Element to an Equivalent Capacitor. *J. Electrochem. Sci. Technol* **2020**, *11* (3), 318–321. https://doi.org/10.33961/jecst.2020.00815.

(44) Lasia, A. The Origin of the Constant Phase Element. *The journal of physical chemistry letters* **2022**, *13* (2), 580–589.

(45) Kibsgaard, J.; Jaramillo, T. F.; Besenbacher, F. Building an Appropriate Active-Site Motif into a Hydrogen-Evolution Catalyst with Thiomolybdate [Mo3S13] 2- Clusters. *Nature chemistry* **2014**, *6* (3), 248–253.

(46) Schalenbach, M.; Tesch, R.; M. Kowalski, P.; Eichel, R.-A. The Electrocatalytic Activity for the Hydrogen Evolution Reaction on Alloys Is Determined by Element-Specific Adsorption Sites Rather than d-Band Properties. *Physical Chemistry Chemical Physics* **2024**, *26* (19), 14171–14185. https://doi.org/10.1039/D4CP01084A.

(47) Azimzadeh Sani, M.; Pavlopoulos, N. G.; Pezzotti, S.; Serva, A.; Cignoni, P.; Linnemann, J.; Salanne, M.; Gaigeot, M.-P.; Tschulik, K. Unexpectedly High Capacitance of the Metal Nanoparticle/Water Interface: Molecular-Level Insights into the Electrical Double Layer. *Angewandte Chemie International Edition* **2022**, *61* (5), e202112679. https://doi.org/10.1002/anie.202112679.

(48) Le, J.-B.; Fan, Q.-Y.; Li, J.-Q.; Cheng, J. Molecular Origin of Negative Component of Helmholtz Capacitance at Electrified Pt(111)/Water Interface. *Science Advances* **2020**, *6* (41), eabb1219. https://doi.org/10.1126/sciadv.abb1219.

(49) Tsai, C.; Chan, K.; Nørskov, J. K.; Abild-Pedersen, F. Theoretical Insights into the Hydrogen Evolution Activity of Layered Transition Metal Dichalcogenides. *Surface Science* **2015**, *640*, 133–140. https://doi.org/10.1016/j.susc.2015.01.019.

(50) Nørskov, J. K.; Bligaard, T.; Logadottir, A.; Kitchin, J. R.; Chen, J. G.; Pandelov, S.; Stimming, U. Trends in the Exchange Current for Hydrogen Evolution. *J. Electrochem. Soc.* **2005**, *152* (3), J23. https://doi.org/10.1149/1.1856988.

(51) Gateman, S. M.; Gharbi, O.; Gomes de Melo, H.; Ngo, K.; Turmine, M.; Vivier, V. On the Use of a Constant Phase Element (CPE) in Electrochemistry. *Current Opinion in Electrochemistry* **2022**, *36*, 101133. https://doi.org/10.1016/j.coelec.2022.101133.

Chapter 7. The behaviour of group V TMDCs under extreme potentials

7.0. Abstract

An electrochemically induced transformation observed in group V transition metal dichalcogenide catalysts (2H-NbS_2, 2H-TaS_2, 1T-VS_2) at applied potentials below or equal to –0.7 V vs RHE is reported for the first time. The partner phases/polymorphs, 3R-NbS_2 and 1T-TaS_2 do not undergo transformation in the voltage range studied (0 to -1 V vs RHE). The transformation manifests in visible changes, including a shift in colouration, delamination, and softening of the material, together with changes in the observed Raman spectra. Structural analysis via XRD indicates an expansion of the *c*-axis by approximately 1% in VS_2, with 2H-TaS_2 displaying similar behaviour, albeit shrinking rather than expanding. In contrast, 2H-NbS_2 follows a distinct pathway, initially forming a population of expanded unit cells that subsequently degrade into a variety of structures. This transformation in 2H-NbS_2 occurs without the substitutional incorporation of other atoms or changes in metal oxidation state. Finally, the characteristic Raman signature identified in electrochemically modified 1T-VS_2 enables development of a protocol for confirming the phase where sample quantities are insufficient for XRD measurement.

7.1 Introduction

Applying a potential to a catalyst can modify the catalyst itself. In OER catalysts such as nickel oxyhydroxide this is commonly reported, typically in the form of oxidation of the catalyst material which can involve reconstruction, yielding a variety of phases[1,2].

Reconstruction at the cathode for the HER (hydrogen evolution reaction) is less frequently reported[3]. This is particularly true of the TMDCs, which typically do not undergo chemical changes in the HER region (0.0 to -0.6 V vs RHE). Other materials do undergo changes, such as MoS_3, which was observed by Jaramillo *et al.*[4] to undergo irreversible transformation to

MoS_2 under a reducing potential. TMDCs are also known to undergo structural modification under strongly reducing potentials, with MoS_2 losing surface sulfur to create vacant sites under strongly reducing potentials[5] (-1.24 V vs RHE), even inducing phase transitions from 2H to 1T.[6] Similar effects have been reported with other metal sulfides, although typically at potentials more reducing than -1 V vs RHE[7,8].

Group V TMDCs have been reported to undergo morphological changes under HER conditions. These changes are suggested to be a combination of perforation and exfoliation, leading to improvements in material conductivity and surface area, and hence catalytic performance. Liu et al.[9], Yang et al.[10] and Najafi et al.[11] have all reported these morphological changes. This was theorised to be due to hydrogen bubbles forming between layers, either from electrolysis or as a result of the reaction of water with intercalated lithium, resulting in increased surface area and conductivity.

At more highly reducing potentials, Si *et al*. claimed the formation of NbS_2 nanosheets from NbS_2 powder[12]. A colour change to brown/yellow resulted from the application of a negative potential, with the collected Raman and XRD data suggesting minimal changes to the structure of the material. Understanding of the material is limited by the poor quality of the data, with both Raman and XRD intensities substantially reduced after the claimed formation of nanosheets.

In this chapter, the different phases of the group V transition metal dichalcogenides were subjected to strongly reducing or highly negative potentials (HNP, $\leq$ -0.7 V vs RHE). A gold/yellow colour change was observed for some materials, while Raman spectroscopy of the materials showed additional peaks. A better grasp of these changes is essential to understand the behaviour of these materials at more negative potentials, such as for the CO_2RR. Therefore, this chapter seeks to understand the nature of these chemical changes.

7.2 Physical observations and Raman spectroscopy

7.2.1 Physical observations

Electrochemical testing was conducted in a three-electrode configuration using 0.5 M H_2SO_4 as the electrolyte, sparged with argon for 20 minutes prior to measurement. The materials were prepared in three forms: single crystals mounted in resin (as described in Chapter 6), crystals compressed between glassy carbon and polymer supports, and powder. Powders were immobilised using 0.5% Nafion in isopropanol to reduce detachment of material from the electrode.

At -0.6 V vs RHE no changes were observed for any materials, even after several days of cycling. At –0.7 V, however, significant transformations occurred after a 12-hour period, and at more reducing potentials (-1.0 V) the rate of change increased markedly. For 2H-NbS_2 and 2H-TaS_2 crystals, the most striking feature was the emergence of a bright gold colour (Figure 1), accompanied by a noticeable softening of the crystal consistency at the more strongly reducing potentials (-1.0 V) or longer durations. At –0.7 V the change appeared largely confined to the top of the crystal, and cleaving with carbon tape restored much of the original appearance, although surface deformation remained evident. At more negative potentials, changes were visible throughout, and large crystals auto-exfoliated/cleaved while producing large bubbles. For powders, colour changes were less apparent, but the alteration in consistency was retained; in the case of 2H-NbS_2 powders, a distinct gold colour became visible when the material was spread. 3R-NbS_2 and 1T-TaS_2 polymorphs did not exhibit comparable visual changes or increases in softness.



Figure 1. Materials after the application of high negative potentials (≤-0.7 V). Left is a series of powders and crystals (2H-NbS_2 crystals in the green box, 2H-TaS_2 powders in the red box and 2H-TaS_2 crystals in the blue box) which have had negative potentials applied. The softened crystals have not been able to maintain their shape through the mounting process. The extent of the colour change varies, with some powders and crystals more apparently golden than others. Right are shown 2H-NbS_2 crystals after application of high negative potentials ≤ -0.7 V), after which the crystals were washed in water and placed in isopropanol. The shape of the crystals is maintained, although auto-exfoliation/cleaving has occurred, producing a large number of flakes from the original crystal.

7.2.2 Raman spectroscopy

Raman spectroscopy was used to examine structural changes in the materials after electrochemical treatment. Spectra were collected following cycling between 0 and -0.6 V, defined here as low negative potentials (LNP) and application of voltages at potentials more negative than or equal to -0.7 V, or strongly reducing potentials (HNP). Samples were washed in water then isopropyl alcohol. Crystal samples were deposited intact by depositing them on

glass while in IPA. Powder samples were washed, dried, and then examined as is. Samples were dried under vacuum at room temperature and handled under air.

For all materials, Raman spectroscopy after application of low negative potential was identical to the pristine materials. For 3R-NbS_2 (Figure 2a) and 1T-TaS_2 (Figure 3a), observed Raman spectra remained unchanged after application of a strongly reducing potential. In contrast, the Raman spectra observed after the application of strongly reducing potentials to the materials 2H-NbS_2 (Figure 2), 2H-TaS_2 (Figure 3) and 1T-VS_2 (Figure 4) differed from the pristine samples. For 2H-NbS_2, additional peaks are seen, with a broad peak at 271 cm^{-1} (Figure 2(i), red), a strong, moderately broad peak at 156 cm^{-1} and a weak, moderately broad peak at 340 cm^{-1}(Figure 2d, green arrows). Additional broad, weak peaks at 240 cm^{-1} (Figure 2d, green arrow) and 423 cm^{-1} (Figure 2(i), red) are seen in some samples as well as a medium narrow peak at 225 cm^{-1} (Figure 2c *). The broad peak at 290 cm^{-1} (Figure 2(i)) and the narrow, strong peak at 379 cm^{-1} (Figure 2(ii)) are assigned to pristine 2H-NbS_2 (Chapter 5). The peak at 423 cm^{-1} is sufficiently weak that it can become indistinct relative to the background, while the peak at 240 cm^{-1} is both weak and can become subsumed into the neighbouring Nb-O peak at 220 cm^{-1} present in some samples. The Raman spectra indicate the presence of at least one additional phase of material, while the pristine 2H-NbS_2 appears to still be present within the sample.

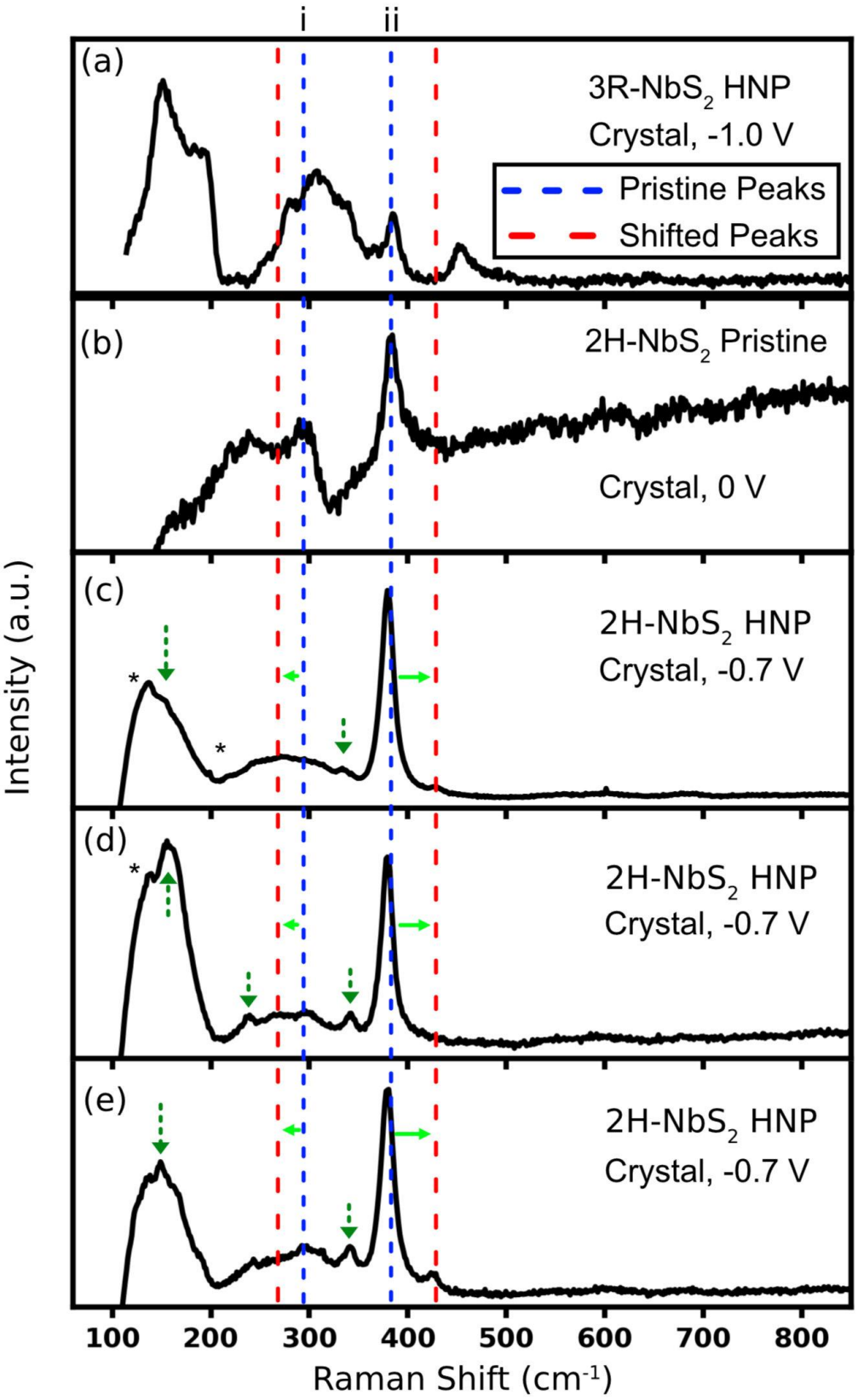

i
ii
(a)
3R-NbS2 HNP
Crystal, -1.0 V
Pristine Peaks
Shifted Peaks
(b)
2H-NbS2 Pristine
Crystal, 0 V
(c)
2H-NbS2 HNP
Crystal, -0.7 V
(d)
2H-NbS2 HNP
Crystal, -0.7 V
(e)
2H-NbS2 HNP
Crystal, -0.7 V
Intensity (a.u.)
100
200
300
400
500
600
700
800
Raman Shift (cm-1)

Figure 2. Raman of the various niobium disulfide samples. The 3R-NbS_2 spectrum (a) was collected after application of a strongly reducing potential. It is identical in all respects to the pristine Raman spectrum. 2H-NbS_2 (b) is shown pristine. Multiple spectra of NbS_2-HNP were taken at different positions, and are shown in (c), (d), and (e). Blue lines (i, ii) show peaks arising from pristine 2H-NbS_2, while red lines show weak peaks thought to arise from the strained 2H-NbS_2 caused by the application of a strongly reducing potential. Shifted peaks are designated in the text by the pristine peak from which they arise. Lime green horizontal arrows show the shift from pristine to strained, while dark green vertical arrows show peaks thought to arise from NbS_3. Peaks with a star have been discarded from consideration, either because they arise from post-potential application air exposure and oxidation (peaks around 220 cm^{-1}), or because they arise from the Rayleigh scattering filter cut-off. 2H-NbS_2 HNP spectra are spectra taken from different locations on a sample. The crystal designation indicates that the sample had a negative potential applied as a crystal and had its spectrum acquired in crystal form. Samples marked 0 V did not have potentials applied to them.

As with 3R-NbS_2, 1T-TaS_2 saw no changes to its Raman spectrum after the application of a strongly reducing potential. By contrast, Raman spectra of HNP 2H-TaS_2 (Figure 3) also showed a mixture of additional peaks and peaks from the pristine material. Additional strong, narrow peaks are seen on spectra collected from HNP samples at 308 and 326 cm^{-1} (Figure 3(i), red), with a broad peak at 780 cm^{-1} and a distinct additional shoulder at 375 cm^{-1} (Figure 3(ii), red). The pristine material peaks at 170 and 290 cm^{-1} (Figure 3(i)) are unaffected by the strongly reducing potential, but the peak at 400 cm^{-1} (Figure 3(ii)) appears to shift 9 cm^{-1} to 391 cm^{-1}. The Raman indicates that there exists a second phase, with the pristine phase also existing, albeit apparently slightly modified (Figure 3(ii), blue). Spectrum variation with position was minimal, and limited solely to relative intensities of peaks, indicating differences in the amount of pristine material as compared to voltage-modified material.

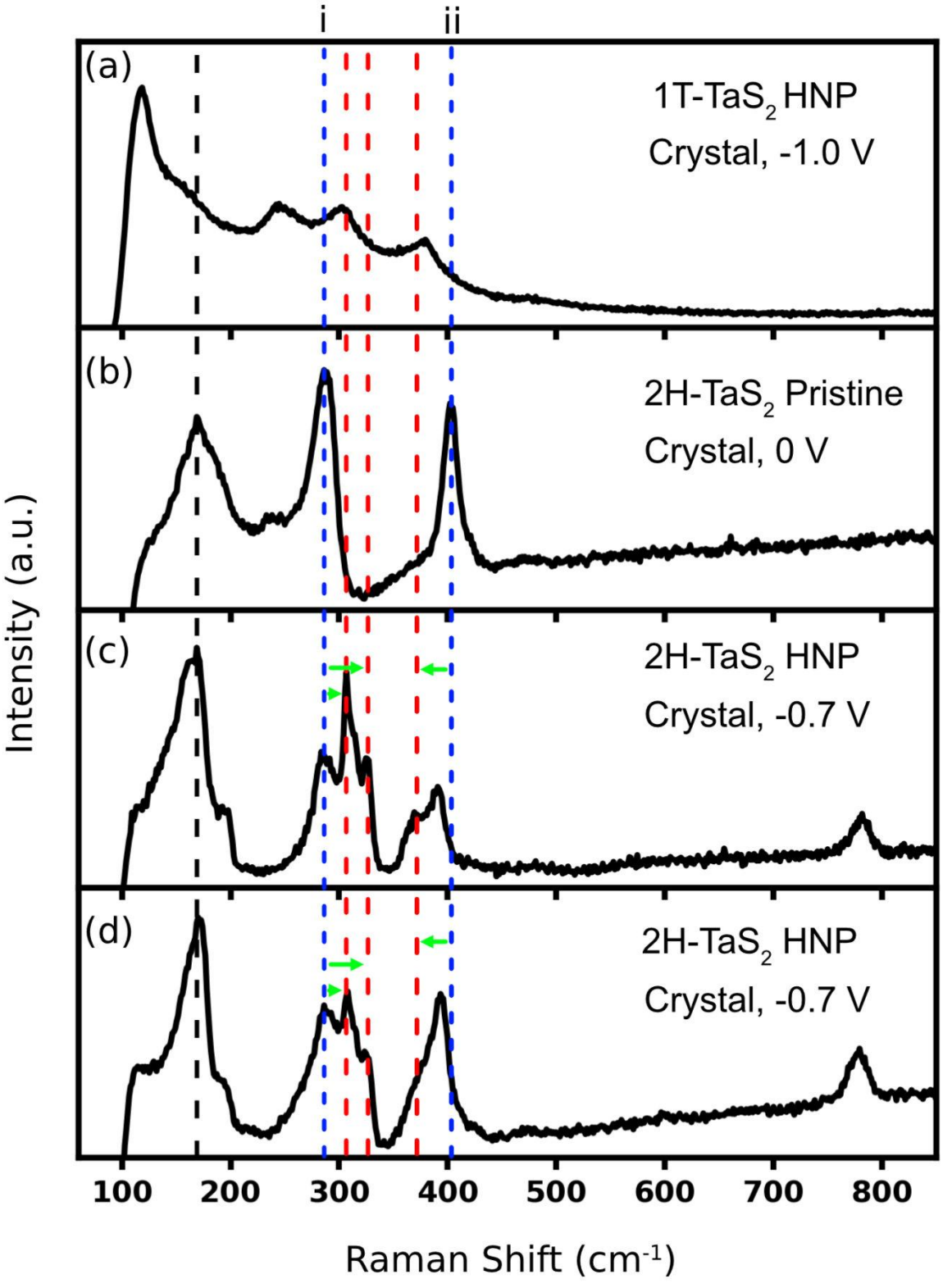

i
ii
(a)
1T-TaS2 HNP
Crystal, -1.0 V
(b)
2H-TaS2 Pristine
Crystal, 0 V
(c)
2H-TaS2 HNP
Crystal, -0.7 V
(d)
2H-TaS2 HNP
Crystal, -0.7 V
Intensity (a.u.)
100
200
300
400
500
600
700
800
Raman Shift (cm-1)

Figure 3. Raman of the various tantalum disulfide samples. The 1T-TaS_2 spectrum (a) was collected after application of a strongly reducing potential. Blue lines (i,ii) show peaks arising from pristine 2H-TaS_2, while red lines shifted from i and ii show peaks thought to arise from the strained 2H-TaS_2 arising from the application of a strongly reducing potential and are designated in the text by the pristine peak from which they arise. Lime green horizontal arrows show the shift from pristine to strained. The peak marked with a black dashed line is thought to arise from 2 phonon interactions[13], while the peak arising at 780 cm^{-1} has not been assigned. The multiple 2H-TaS_2 HNP spectra (b-d) are each taken from different sample positions. The crystal designation indicates that the material had a negative potential applied as a crystal and had its spectrum acquired in crystal form. Samples marked 0 V did not have potentials applied to them.

Raman spectra of HNP VS_2 (Figure 4) showed some variation with position. Throughout all samples, peaks were observed at 153-163 cm^{-1} (Figure 4(i), strong, sharp), 190 cm^{-1} (Figure 4(ii), strong, sharp) and 202 cm^{-1} (Figure 4(iii), strong, sharp). Additional sharp medium peaks were observed at 272 and 317 cm^{-1} (Figure 4 (iv, v)), as well as 373 and 402 cm^{-1} (Figure 4(vi), Figure 4 (vi) red). Small auxiliary peaks are of interest at 242 and 285 cm^{-1} (Figure 4 (iv) red, Figure 4 (v) red).

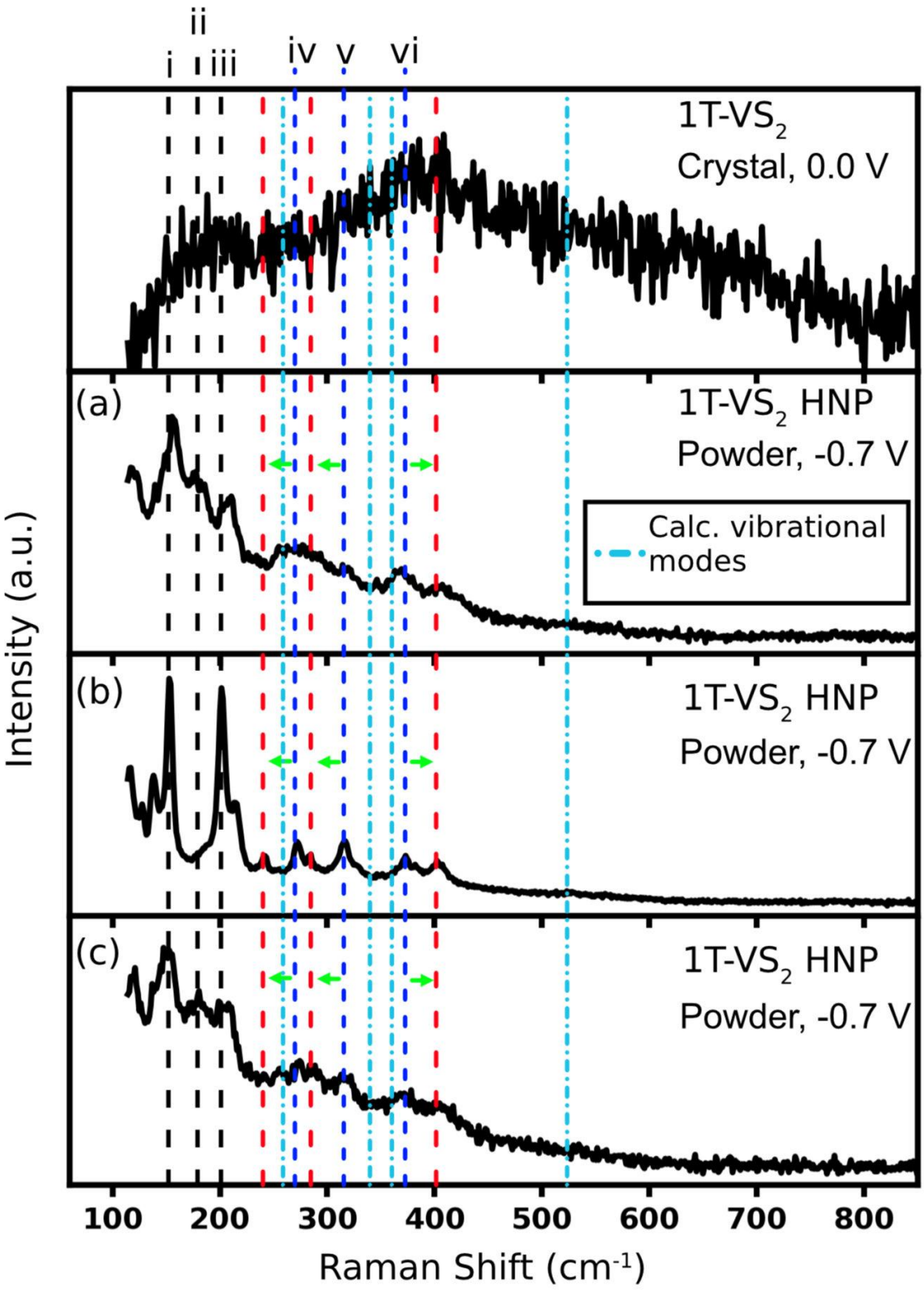

i
ii
iii
iv
v
vi
1T-VS2
Crystal, 0.0 V
(a)
1T-VS2 HNP
Powder, -0.7 V
Calc. vibrational modes
(b)
1T-VS2 HNP
Powder, -0.7 V
(c)
1T-VS2 HNP
Powder, -0.7 V
Intensity (a.u.)
100
200
300
400
500
600
700
800
Raman Shift (cm-1)

Figure 4. Raman of various HNP 1T-VS_2 samples. Blue lines (iv, v, vi) show peaks speculated to arise from pristine 1T-VS_2, while red lines show peaks thought to be from the strained 1T-VS_2 arising from the application of a strongly reducing potential, and are designated in the text by the pristine peak from which they arise. Due to noise and sample variation, both relative peak intensity and visibility change with different samples. Lime green horizontal arrows show the shift from pristine to strained. The peaks marked with dotted lines are thought to arise from 2 phonon interactions. The pristine VS_2 material has no known Raman spectrum (Appendix, section A.2). The powder designation indicates that the material had a negative potential applied and had its spectrum acquired in powdered form. The VS_2 crystal did not have a negative potential applied to it.

Peak height and width vary between spectra acquired at different positions, indicating the presence of more than one phase present in different amounts, with crystallinity also likely varying. This causes peaks to become indistinct or be subsumed into the background. This is consistent with the results from NbS_2 and TaS_2. HNP VS_2 was processed under air, with Raman spectrum acquisition also under air. Despite processing in air, there is no evidence of the presence of vanadium oxide, with characteristic peaks at 990 cm^{-1}, 700 cm^{-1} and 528 cm^{-1} not appearing, while peaks at 153, 272 and 317 cm^{-1} do not fit well with expected peaks at 145, 285, 701, 482, 528 and 996 cm^{-1} for V_2O_5.

7.3 X-ray spectroscopy of HNP materials

7.3.1 XPS of Ta and Nb in TaS_2 and NbS_2

Raman spectroscopy is able to distinguish the existence of different phases/polymorphs and their purities and crystallinities. The nature of those phases must still be elucidated. X-ray spectroscopies allow us to understand if other atoms have doped or alloyed the sample into a different phase, as well as determining the oxidation state of the atoms. To this end, both X-ray

photoelectron spectroscopy (XPS) and soft X-ray absorption spectroscopy (soft XAS) in total electron yield (TEY) mode were used. Both techniques are surface sensitive, with a depth of <10 nm as compared to the micrometre depth of Raman.

XPS was acquired from both phases/polymorphs of NbS_2 and TaS_2. VS_2 data quality was poor and has not been reproduced. Samples were crystals or powder and were prepared by application of strongly reducing potentials as outlined earlier (section 7.2.1). Crystal samples were ground lightly with a spatula into powder form and mounted on either glassy carbon or carbon tape, while powders were applied and measured directly on the working electrode (glassy carbon). Samples were washed in water and subsequently washed repeatedly in isopropyl alcohol, after which they were dried in vacuum overnight and transferred under air to the sample plate. In the HNP materials, no additional elements were detected in the XPS as compared to the pristine materials. Survey scans showed the presence of silicon oxide from glass of the synthesis ampoule as well as adventitious carbon, however notably no iodine, despite its use as a mineralising agent in the synthesis. XPS was aligned to adventitious carbon. XPS was acquired with an S 2p, Nb 3d, Nb 3p and Ta 4f typical acquisition time of 20, 40, 16 and 16 minutes respectively, with a step size of 0.1 eV and pass energy of 26 eV.

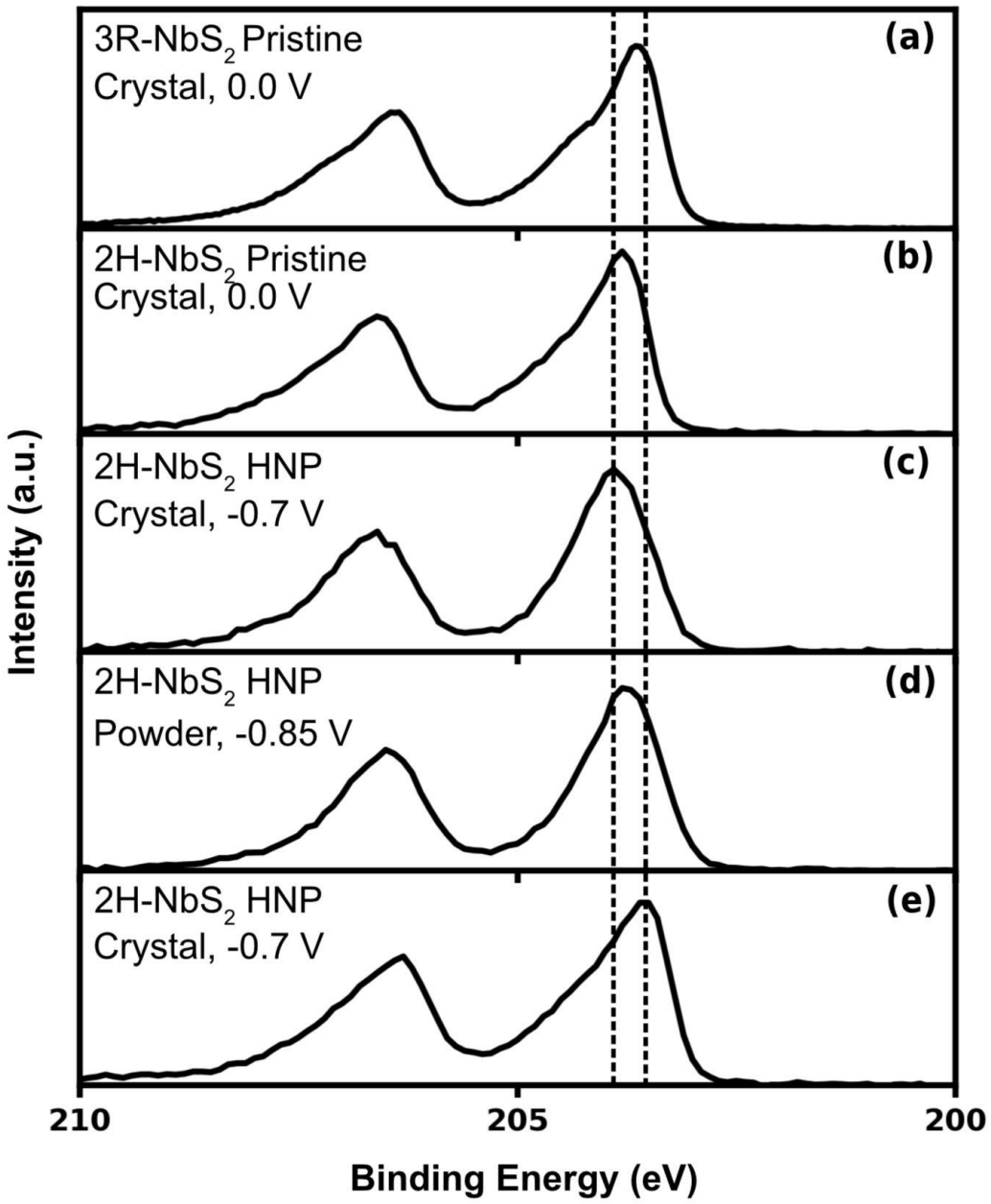


Figure 5. XPS of the Nb 3d region. Peaks are distinctly asymmetric as expected for a metallic material, while peak shape variation may be due to additional components arising from metal oxides. Peak position varies slightly, and the maximum extent of that variation is denoted by the dotted black lines. Peak shape varies slightly, particularly distinct in the 3R-NbS_2 peak, with a slight bump at 204.5 and 207.5 eV indicating an additional environment arising from Nb intercalation. Samples at 0.0 V were not subjected to a potential. Recorded potentials are against the RHE.

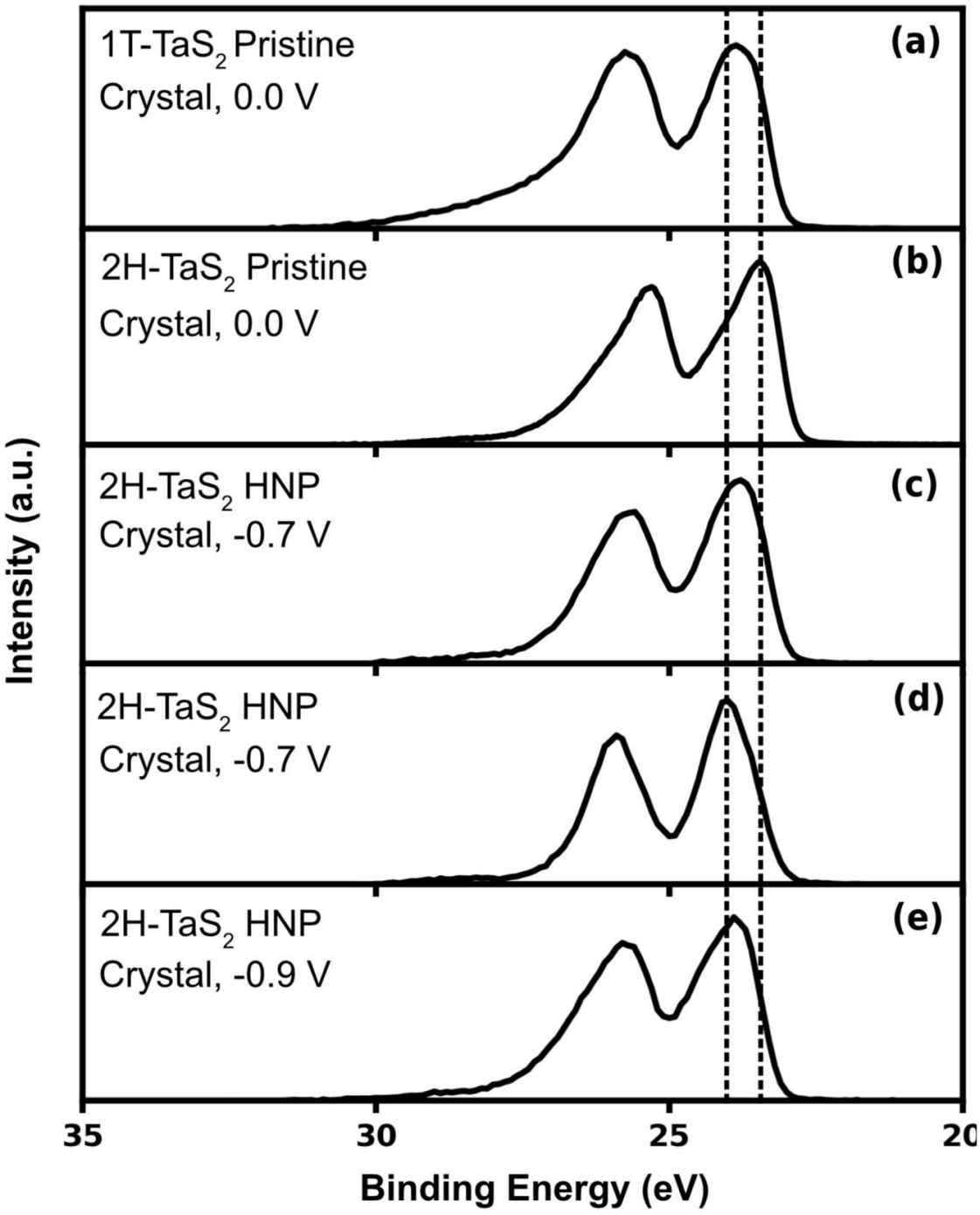


Figure 6. XPS of the Ta 4f region. Peaks are distinctly asymmetric as expected for a metallic material, while peak shape variation may be due to additional components arising from metal oxides. Peak position varies slightly, and the maximum extent of that variation is denoted by the dotted black lines. Peak shape varies slightly in the 2H-TaS_2, indicating possible slight oxidation of the material. Samples at 0.0 V were not subjected to a potential. Recorded potentials are against the RHE.

For the HNP samples, XPS spectra were obtained across multiple regions of sample crystals. Some variation in peak positions was observed between samples. The Nb 3d (Figure 5) and Ta 4f (Figure 6) peaks were found to be asymmetric, exhibiting metallic electronic character. The Nb $3d_{5/2}$ peak was found at 203.7 eV with a maximum deviation from the pristine material of 0.35 eV, while for TaS_2 $4f_{7/2}$ the peak position is found at 23.8 eV with a maximum deviation from pristine of 0.3 eV. While pristine samples processed identically showed evidence of oxidation (Chapter 5), HNP samples showed no evidence of large-scale metal oxidation, with the expected oxidation peaks from Nb_2O_5 at 207-207.5 and 210-210.5 eV not showing in the NbS_2 spectra, and similar oxidation peaks from Ta_2O_5 not showing at 26.5 and 28.5 eV in the TaS_2 spectra. This also indicates that there is no formal change in metal oxidation state, with the metal oxidation state remaining as +4.

3R-NbS_2 (Figure 5a) shows a slight bump at 204 eV, indicative of the intercalated niobium known to exist in 3R-NbS_2. Compared to the pristine 2H-NbS_2, the Nb peaks for the HNP materials may have additional components, evidenced by the different peak shape. These differences in peak shape may be due to differences in processing between pristine and HNP samples, with HNP samples being dried in air before introduction to the XPS vacuum chamber. The air-handling causes the formation of various oxides which increases the complexity of the peaks and reduces the insight into the chemical behaviour. Consequently, the metal peaks were not fitted, as discussed in Chapter 5. Ta (Figure 6) by contrast shows notable variation in peak shape between each of the samples, potentially evidencing greater sensitivity to the coordination environment, but likewise was not fitted.

7.3.2 XPS of Sulfur in TaS_2 and NbS_2

The S 2p region is significantly more amenable to analysis, as oxidised sulfur is present at distinctly different binding energies from reduced sulfides. To that end, all HNP samples showed evidence of sulfate contamination (Figure 7, Figure 8), with broad peaks present

consistently at 170 eV across all HNP samples despite cleaning. These sulfate signals were also observed in non-HNP samples from which spectra were collected at the same time on the same plate, indicating small amounts of sulfate evaporation and contamination under vacuum. Sulfate peaks were ill-defined, and varied between samples, likely due to a multitude of different oxidation states and coordination structures in the sulfate contaminants. Metallic sulfide peaks were observed between 160 and 165 eV and were notably asymmetric in character.

S 2p peak positions for the XPS samples shifted slightly and irregularly. For NbS_2 S $2p_{3/2}$ (Figure 7) all HNP peak positions were found at 161 eV, with variation of approximately 0.2 eV, while the TaS_2 HNP peaks were at approximately 161.5 eV with a maximum peak variation of 0.5 eV. Sample-specific changes in peak positions in the S 2p region varied, and the changes in position were not consistent with the position changes in the metal regions.

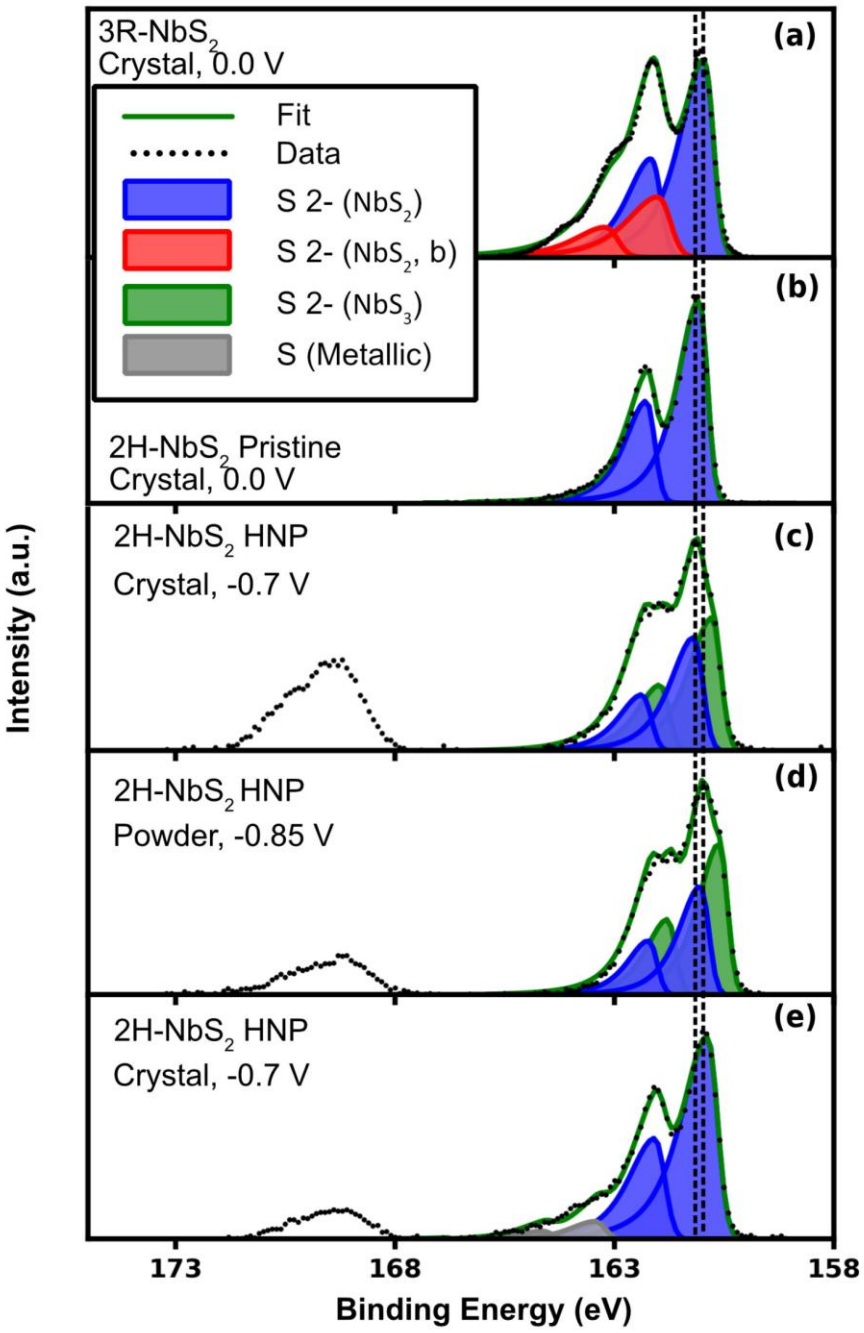


Figure 7. S 2p region of the niobium disulfide samples. The metal sulfide region is seen from 168 to 158 eV, while sulfate peaks are seen at binding energies higher than 168 eV. Both 3R-NbS_2 (a) and HNP 2H-NbS_2 (c-e) see additional sulfur environments as compared to pristine 2H-NbS_2 (b). Each 2H-NbS_2 HNP spectrum was acquired from a different sample. Potentials are recorded against the RHE. Crystals had negative potentials applied to them in crystal form, but were on the sample plate in powder/crushed crystal form.

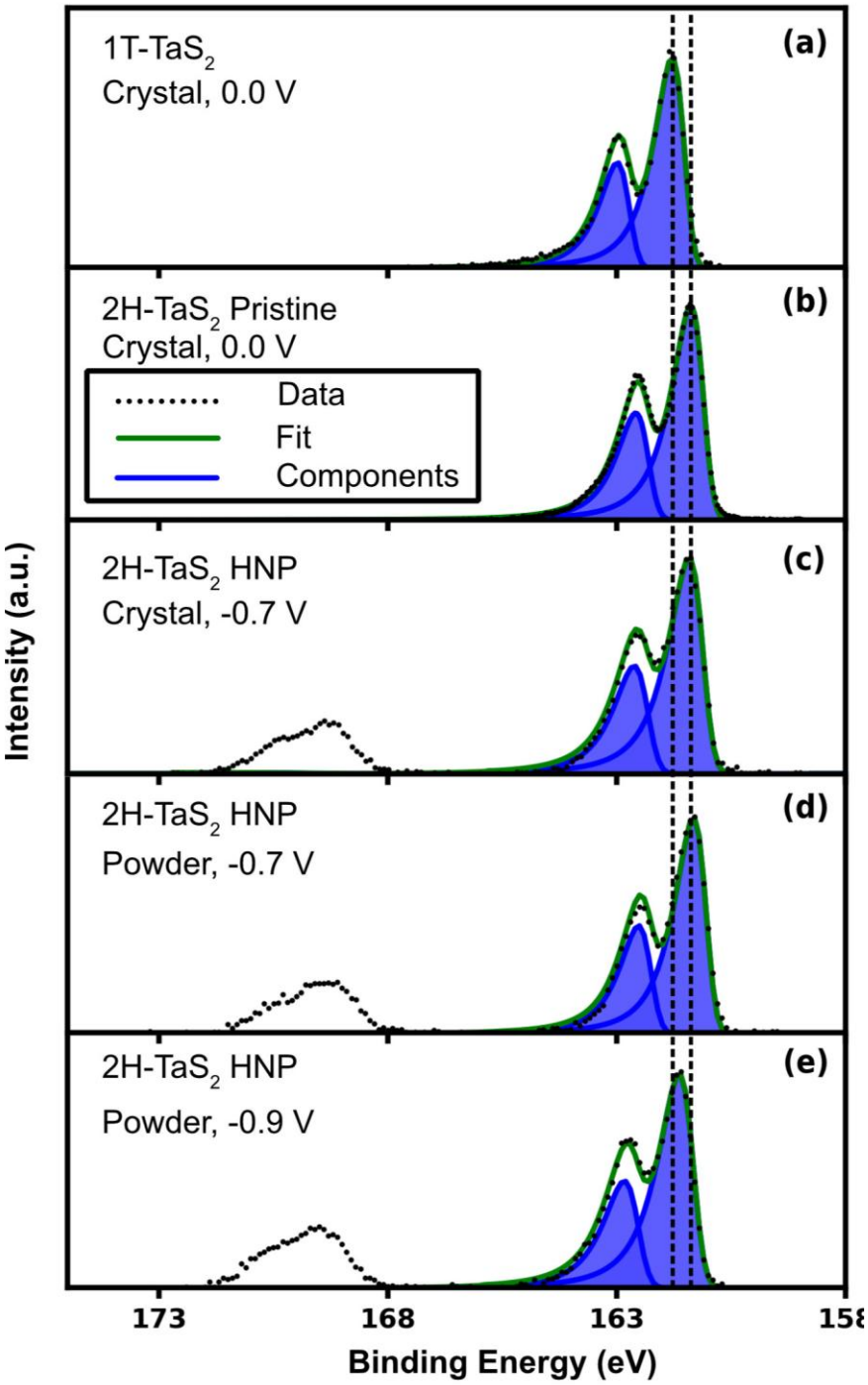


Figure 8. S 2p region of the tantalum disulfide 1T (a), 2H pristine (b) and multiple HNP (c-e) samples. The metal sulfide region is seen from 168 to 158 eV, while sulfate peaks are seen at binding energies higher than 168 eV. All samples can be effectively modelled by a single asymmetric peak. Potentials are recorded against the RHE. Crystals had negative potentials applied to them in crystal form but were on the sample plate in powder/crushed crystal form.

Sulfide S 2p peaks were fitted with asymmetric Lorentzian line shapes, as outlined in Chapter 3. For each of NbS_2 and TaS_2, asymmetry parameters were constructed by fitting the line shapes to one of the two pristine phases first, then tested for accurate fitting on the other. This assumes a surface structure similar to the known bulk structure but allowed for the accurate fitting of asymmetric lines in a metallic system. For NbS_2, two sets of components were fit onto the 3R-NbS_2 S 2p spectrum (Figure 7a), due to the shoulders at 163 and 164.2 eV. The first component at lower binding energies was assigned to the base 3R-NbS_2 sulfurs, while the component at higher binding energies was assigned to the sulfurs adjacent to intercalated niobium to be consistent with literature[14,15]. Although sulfur adjacent to intercalated niobium would be expected to be more reduced, and consequently at a lower binding energy than their non-intercalant adjacent equivalents, assignment of these peaks to intercalant adjacent sulfur is consistent with literature assignment for NbS_2[14,15] and other self-intercalated group V TMDCs[16].

The parameters for the asymmetric line shape were then transferred over to the pristine 2H-NbS_2 S 2p spectrum (Figure 7b), which successfully fit with a single component set as expected for the structure. For TaS_2 the procedure was repeated, with a single set of components used to fit 2H-TaS_2 (Figure 8b) and the parameters transferred to fit a similar single component set in 1T-TaS_2 (Figure 8a).

Parameters used to fit the pristine regions were also used to fit the HNP regions. For 2H-NbS_2 HNP (Figure 7c-e) samples, this results in two component sets, the first of which is a reduced environment which is similar to that of the pristine systems. The position of the second (oxidised) environment varies between samples. Evidence for these second environments does not just come from the fitting but is also visible in the data itself, with the relative heights in the S $2p_{3/2}$ and S $2p_{1/2}$ different than the 3R-NbS_2 and HNP 2H-NbS_2 samples (Figure 7a, c-d), while additional peaks are visible in the HNP 2H-NbS_2 peaks (Figure 7e)

For HNP 2H-TaS_2 (Figure 8c-e), the spectra are simpler, with a single environment being sufficient to successfully explain all samples. This environment does not change in position relative to the pristine peaks substantially, as outlined above.

7.3.3 XAS Data

X-Ray absorption spectroscopy, or XAS, is particularly sensitive to changes in oxidation states. While the XPS data provides detailed information on the metal oxidation states, with the +4 and +5 oxidation states very distinct, XAS provides further insight into the sulfur environment. While the XAS is surface sensitive, it penetrates deeper than XPS (approximately 5 nm) and provides additional insight into the surface and near-surface environments.

2H-NbS_2, HNP 2H-NbS_2 (Figure 9b), 2H-TaS_2 and HNP 2H-TaS_2 (Figure 9a) showed only the sulfide S^{2-} state at 164.4 and 165.3 eV. Edge positions are in line with expectations from the literature[17]. While an unchanged oxidation state is evident from the HNP 2H-TaS_2 XPS S 2p spectra, the XAS confirms that the peak shifts in the XPS of HNP 2H-NbS_2 are not due to a change in the integer oxidation state but rather due to smaller changes to the chemical environment.

The post edge data was not analysed due to known sulfate contamination, as observed in the XPS data (Figure 7, Figure 8).

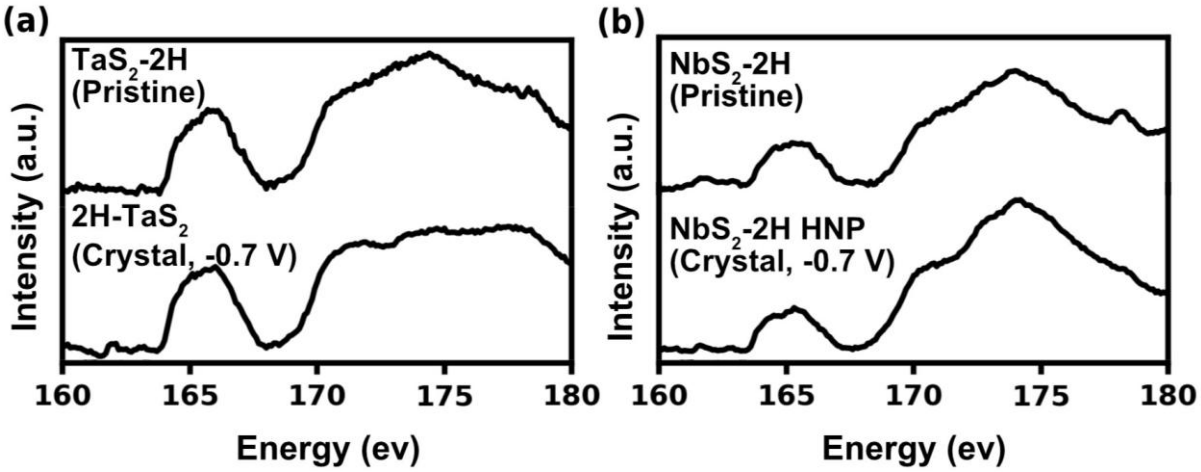


Figure 9. Soft-XAS (NEXAFS) of 2H-TaS_2 and 2H-NbS_2, examined both in the pristine and after application of strongly reducing potential. The sulfur edges at ~164 eV are broadly similar and evidences the presence of S^{2-} [18,19]. The complexity of the post edge peaks provide limited information due to the known sulfate contamination in these systems, which is expected to show between 170 and 180 eV[20].

7.4 X-Ray diffraction data

7.4.0 Methods

Raman, XPS and XAS data provide information about the existence, purity, oxidation state and composition of a material, however additional information is needed to understand the structural effects of strongly reducing potentials on the materials. X-ray diffraction provides information on the physical structure of the materials, and as such is an important complementary method. Data was acquired for the materials 1T-VS_2, 2H-NbS_2 and 2H-TaS_2, both from pristine and from HNP samples. XRD patterns were acquired from samples which had negative potentials applied to them in powder and in crystal form. Crystal sample integrity was notably reduced after application of an HNP and were powdered for analysis by agitating the crystal with a spatula. Patterns acquired in the Rigaku Miniflex were recorded on low-background silicon sample holders in nitrogen, while patterns acquired in the Rigaku SmartLab

machines were recorded on glass sample holders in air. Backgrounds were removed manually, and the surface of the samples were flattened by scraping with a glass slide.

7.4.1 1T-VS_2

For HNP 1T-VS_2 (Figure 10), XRD data shows slight position shifts in most peaks relating to the *c* axis (out-of-plane), with the (0 0 1), (0 0 2), (0 0 3) and (0 0 4) peaks at 2θ = 15.4°, 31.0°, 47.3° and 64.7° shifting to 2θ = 15.1°, 30.6°, 46.9° and 64.0° respectively. Changes in peak intensity are substantial, with the (0 0 *l*) peaks showing large increases in relative intensity. The peak at 2θ = 64.0° is particularly interesting, as although it is a single peak in the pristine material (at 64.7° 2θ), in the HNP material it splits into a central peak with two smaller shoulders at 2θ = 63.8° and 64.4° respectively. This behaviour is also apparent, although less obvious for the peak at 46.9° 2θ. Those in-plane peaks that are visible also show small apparent shifts. Peaks arising from the out-of-plane reflections are more apparent than those arising from the in-plane reflections. The peak shifts indicate a change to the size of the unit cell of the material and are modelled (see section 7.5.2). In this case, it indicates that part of the material is unchanged, and that most of it has expanded along the out-of-plane axis.

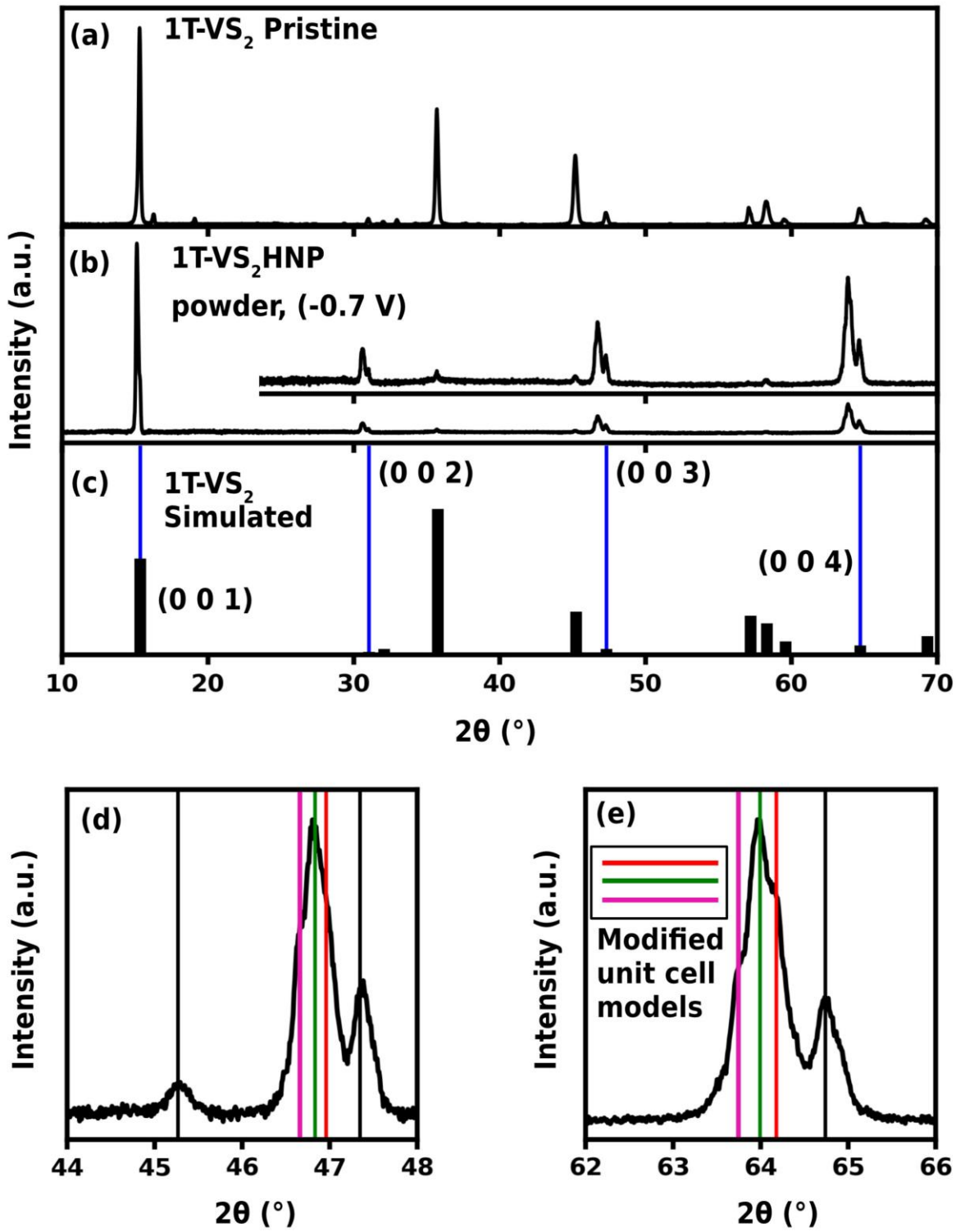

(a)
1T-VS2 Pristine
(b)
1T-VS2HNP
powder, (-0.7 V)
(c)
1T-VS2
Simulated
(0 0 1)
(0 0 2)
(0 0 3)
(0 0 4)
Intensity (a.u.)
10
20
30
40
50
60
70
2θ (°)
(d)
Intensity (a.u.)
44
45
46
47
48
2θ (°)
(e)
Modified
unit cell
models
Intensity (a.u.)
62
63
64
65
66
2θ (°)

Figure 10. XRD of 1T-VS_2 (a) and HNP 1T-VS_2, (b). The sharp, singular peaks can be seen in the pristine material while the dual peaks resulting from the strained material can be seen near 2θ = 30.6°, 46.9° (b, d) and 64.0° (b, e). The (0 0 l) peaks are marked with blue lines on the calculated reflections in (c), while (d) and (e) show the experimental data and simulated (0 0 3) and (0 0 4) peaks for the pristine (black vertical lines) and strained (magenta, red, green) unit cells. Due to some peaks having substantially higher intensities, (b) is shown zoomed in on the intensity axis, with the full pattern shown inset, and the zoomed area highlighted in red. The peak at 2θ = 45.3° in (d) arises from an in-plane reflection. Small additional peaks in the VS_2 pristine data likely arise due to the presence of iodine and lithium iodide from the delithiation process (Appendix, Section A.2.1). Pattern was acquired using a Rigaku SmartLab 9 kW.

7.4.2 TaS_2

HNP TaS_2 also shows slight shifts in its XRD pattern (Figure 11). The peak arising from the (0 0 2) reflection at 2θ = 14.6° shifts to show a shoulder at 2θ = 14.8°, while the peak arising from the (0 0 4), (0 0 6), (0 0 8) and (0 0 10) reflections shifts from 2θ = 29.4°, 44.9°, 61.2° and 79.1° to 2θ = 29.8°, 45.4°, 62.0° and 80.1°. No additional out-of-plane peak splits are observed in the data, in contrast with 1T-VS_2 which shows additional peaks and shoulders at lower values of 2θ. As with 1T-VS_2, peaks resulting from out-of-plane reflections are notably more apparent than peaks resulting from in-plane reflections, with strong peaks arising from reflections at (0 0 *l*) (*l* = 2,4,6,8) while the peaks arising from the in-plane reflections are extremely weak or not visible. The peak shifts indicate a change to the size of the unit cell of the material and has been modelled (see section 7.5.1). In contrast to VS_2, this implies the unit cell of part of the material has shrunk along its out-of-plane axis.

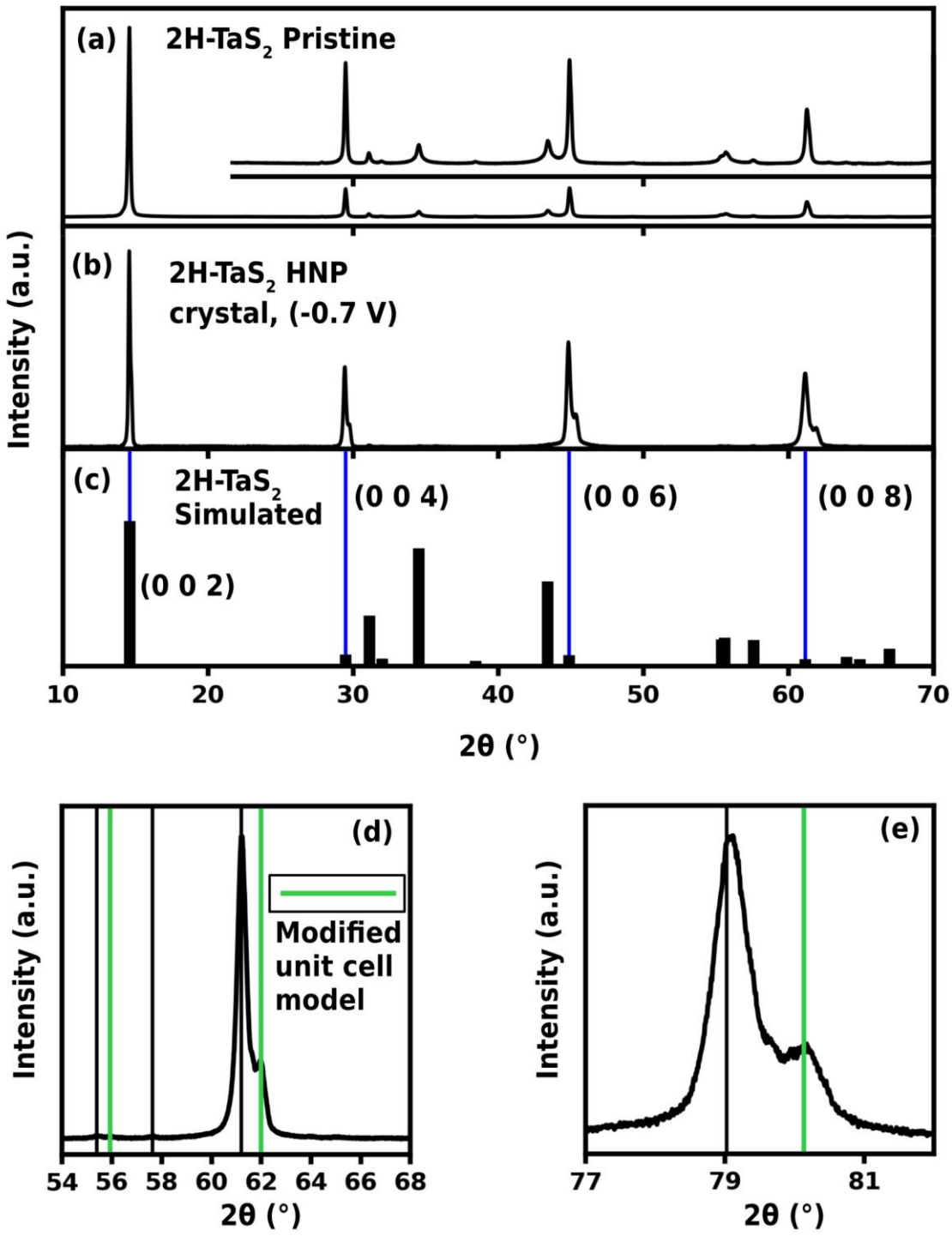

(a)
2H-TaS2 Pristine
(b)
2H-TaS2 HNP
crystal, (-0.7 V)
(c)
2H-TaS2
Simulated
(0 0 2)
(0 0 4)
(0 0 6)
(0 0 8)
Intensity (a.u.)
10
20
30
40
50
60
70
2θ (°)
(d)
Modified
unit cell
model
54
56
58
60
62
64
66
68
(e)
77
79
81

Figure 11. XRD of 2H-TaS_2 and HNP 2H-TaS_2. The sharp, singular peaks can be seen in the pristine material (a) while the dual peaks resulting from the strained material can be seen at 2θ = 29.8° (b), 45.4° (b) and 62° 2θ (b, d). The (0 0 l) peaks are marked on the calculated reflections in (c), while (d) and (e) show a closer view of the (0 0 8) and (0 0 10) peaks with the simulated positions for the pristine (black) and strained (green) unit cells shown. Pattern was acquired using a Rigaku SmartLab 9 kW.

7.4.3 NbS_2

HNP 2H-NbS_2 presents a more complex set of patterns, which change over time. The initial XRD pattern was acquired from powder samples of NbS_2 ten minutes after the application of a strongly reducing potential (-1.0 V). Acquisition was 10 minutes in length, using a 9 kW Rigaku SmartLab. The samples had a negative potential applied to them in crystal form, then were pulverised via light agitation with a spatula. The resultant powder was spread on the back of a glass sample holder. The acquired pattern (Figure 12b) shows multiple peaks, some of which can be attributed to shifts from the 2H-NbS_2 pattern, while others appear to be newly emerged. As with TaS_2 and VS_2, peaks appear to primarily arise from the out-of-plane reflections, with distinct peaks arising from the (0 0 *l*) (*l* = 2,4,6,8) reflections at 2θ = 14.8°, 29.7°, 45.5° and 62.0°, with shifted peaks appearing at 2θ = 14.6°, 29.6°, 44.8° and 61.3°. Similarly to TaS_2, only a single set of shifted peaks appear. In addition to the peaks arising from out-of-plane reflections, other peaks are visible. Peaks at 2θ = 31°, 32°, 34.5° and 55° may be attributable to in-plane reflections from the (1 0 0), (1 0 1), (1 0 2) and (1 1 0) reflections, however additional peaks are seen across the pattern. Of particular interest are the peaks at 2θ = 11.4°, 17.4°, 42.2° and 47.7°, which are strong and not obviously shifted from the pristine peaks. As with TaS_2 and VS_2, expected intensities vary, with out-of-plane reflections more intense than their in-plane counterparts.

A second XRD pattern was acquired ten minutes after the first (Figure 12c). Acquisition was 10 minutes in length. Peaks at 2θ = 14.6° and 14.8° remain, albeit with much reduced intensities, while an additional peak arises at 2θ = 15.2°. The additional peaks at 2θ = 11.4°, 17.4°, 42.2° and 47.7° remain, however in-plane peaks appear suppressed. This data implies that, like VS_2, NbS_2 expands out-of-plane, however the new peaks require their own explanation. Additionally, the in-plane peaks, particularly at the higher angle shoulder at the 31° 2θ peak indicate that 2H-NbS_2 shrinks along the in-plane axes.

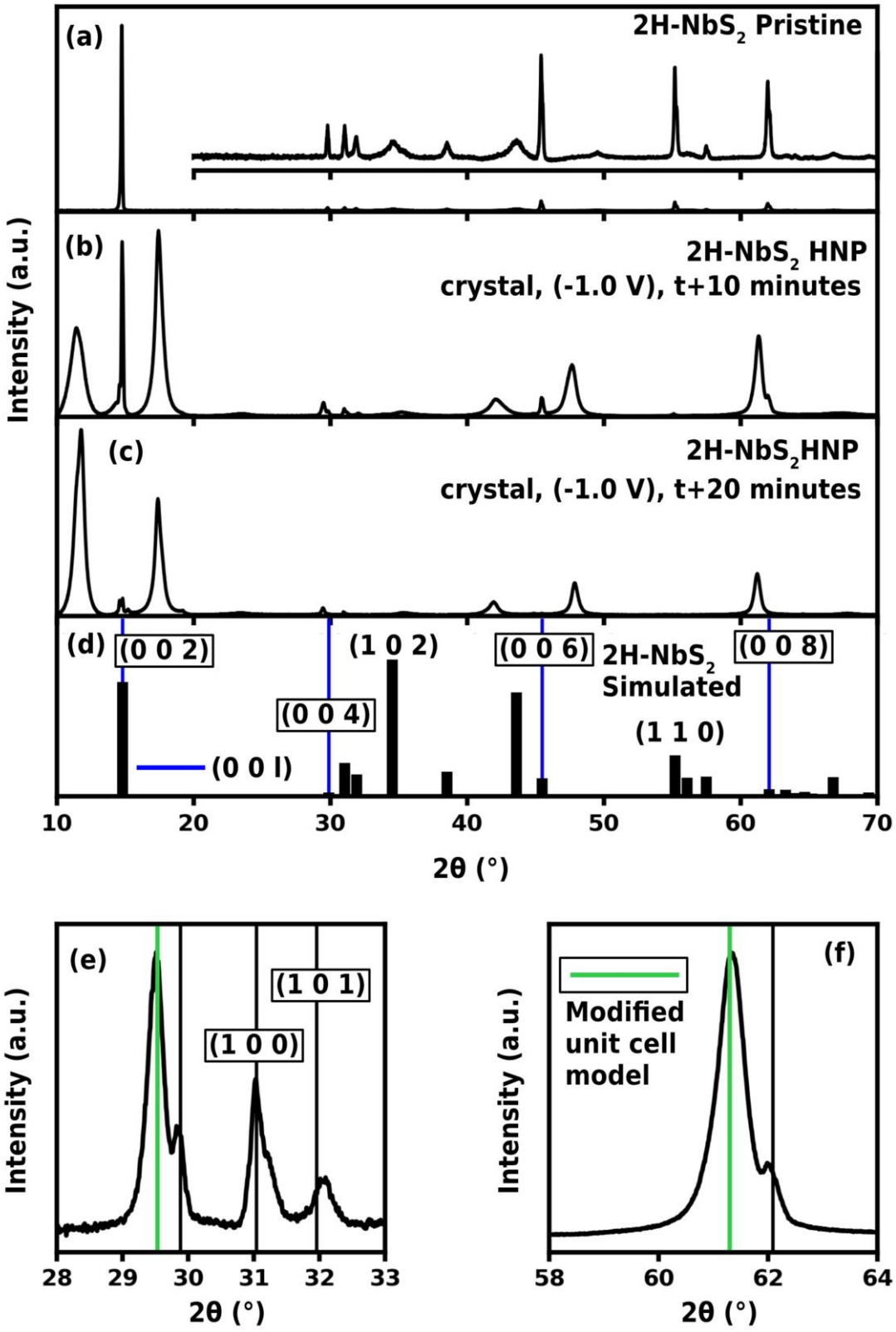

(a)
2H-NbS2 Pristine
(b)
2H-NbS2 HNP
crystal, (-1.0 V), t+10 minutes
(c)
2H-NbS2HNP
crystal, (-1.0 V), t+20 minutes
(d)
(0 0 2)
(1 0 2)
(0 0 6)
(0 0 8)
2H-NbS2
Simulated
(0 0 4)
(1 1 0)
(0 0 l)
Intensity (a.u.)
10
20
30
40
50
60
70
2θ (°)
(e)
(1 0 1)
(1 0 0)
Intensity (a.u.)
28
29
30
31
32
33
2θ (°)
(f)
Modified
unit cell
model
Intensity (a.u.)
58
60
62
64
2θ (°)

Figure 12. XRD of NbS_2 and early HNP 2H-NbS_2. The XRD of the pristine 2H-NbS_2 material is shown in (a), while (b) records the XRD pattern 10 minutes after the application of a strongly reducing potential. The XRD pattern arising from 2H-NbS_2 20 minutes after the application of a strongly reducing potential is recorded in (c). The sharp, singular peaks can be seen in the pristine material while the dual peaks resulting from the strained material can be seen at 2θ = 29.6°(b, e), 45.5° (b) and 61.3° (b, f). The (0 0 l) peaks are marked on the calculated reflections (d), while (e) and (f) show the data from and the simulated (0 0 4) and (0 0 8) peaks for the pristine(black) and strained (green) unit cells at 10 minutes. The peaks at 31.0° and 32.1° resulting from the (1 0 0) and (1 0 1) reflections also appear to have shoulders at higher values of 2θ, implying shrinking along the in-plane axes. Additional peaks unrelated to either 2H-NbS_2 or strained HNP 2H-NbS_2 can be seen in (b) and (c). Pattern was acquired using a Rigaku SmartLab 9 kW machine.

To this end, additional data was gathered from HNP crystal samples. HNP samples were acquired by applying -0.7 V to an NbS_2 crystal. Gathered crystals were washed in water then IPA, then pulverised by means of light agitation with a spatula. The initial measurement was acquired one hour after application of potential (HNP +1 hour) and subsequent measurements took place at HNP +2, +3, +7 and +11 hours, all under air. Measurements typically took 30 minutes to complete.

Initial measurements at T+1H (Figure 13a) show the presence solely of NbS_2, with peaks arising from the out-of-plane reflections. In-plane peaks are suppressed, and the peaks show evidence of amorphous character, particularly in peaks arising from the (0 0 2) and (0 0 6) reflections at 2θ = 15° and 45.7°. The peaks arising from the (0 0 4) and (0 0 8) reflections at 2θ = 29.8° and 61.6° remain sharp. At T+2H (Figure 13c) these peaks have substantially reduced in intensity or disappeared, and additional major peaks have arisen at 2θ = 16.0° (sharp), 19.6° (broad), 51.6° (broad) and 63.6° (broad). T+3H (Figure 13d) is further

inconsistent with the other patterns, with major peaks arising at 2θ = 8.5°, 17.2°, 35.0°, 44.1°, 55.7°, 63.7° and 74.2°. A further pattern of low-intensity sharp peaks can be observed between 2θ = 20° and 30°, and the broad peaks are non-Gaussian in nature, with a variety of shoulders and smaller peaks decorating them.

The pattern acquired at T+7H (Figure 13e) is similar to that at T+3H. The large peak at 2θ = 8.5° sees an apparent further expression of the shoulder at 2θ = 9.5°, dominating the peak overall, while the sharp peak at 2θ = 17.8 °develops a shoulder at 2θ = 18.6°. The large peaks from 2θ = 35.0°, 44.1°, 55.7°, 63.7° and 74.2° remain visible, although they develop substantially larger sub-peaks as well as three additional peaks at 2θ = 40.0°, 50.6° and 62.0°. The peak at 2θ = 74.2° appears to shift to 74.0° and broaden. The sharp peaks between 2θ = 20° to 30° increase in intensity. T+11H (Figure 13f) sees fewer changes still, with the intensity of the additional peaks on the major peaks decreasing while the peaks between 2θ = 5° and 20° remain in the same position while the peak at 2θ = 9.5° sharpens. This data strongly suggests that multiple additional phases form alongside NbS_2, particularly suggested by the different peak shapes of these different phases, where some are broad while others (Figure 13, marked with an x) are sharp. This is further discussed in section 7.5.3.

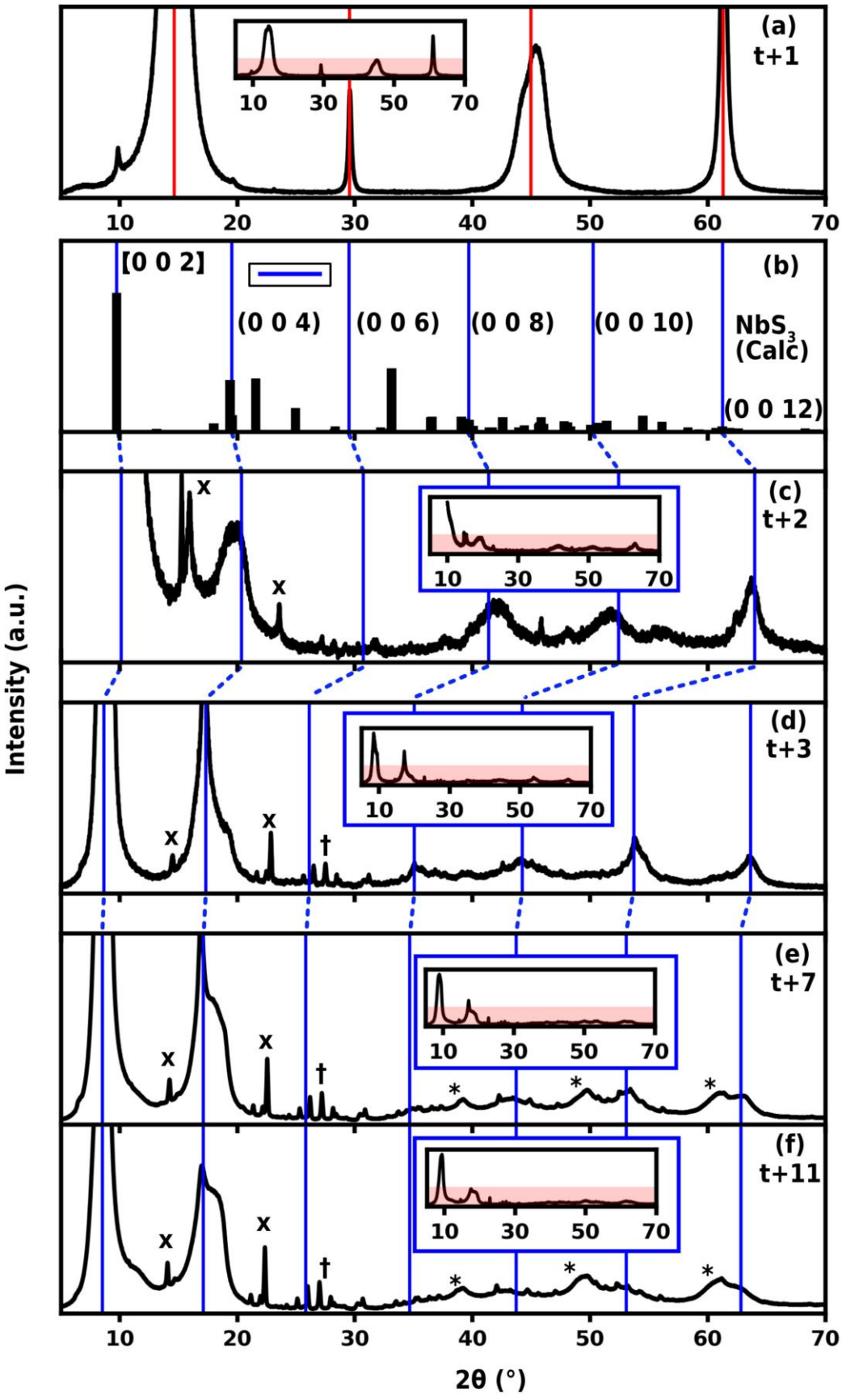

(a)
t+1
(b)
[0 0 2]
(0 0 4)
(0 0 6)
(0 0 8)
(0 0 10)
(0 0 12)
NbS3
(Calc)
(c)
t+2
(d)
t+3
(e)
t+7
(f)
t+11
x
†
*
Intensity (a.u.)
2θ (°)

*Figure 13. XRD pattern evolution of HNP (-0.7 V) 2H-NbS_2 under nitrogen. Patterns were acquired using the Rigaku Miniflex. The potential was applied while the NbS_2 was in crystalline form, and the resultant material lightly agitated to produce a powder. Patterns are shown with a letter (a,b,c…) and the time the pattern capture began (t+n, where n is number of hours since application of potential). Calculated (0 0 l) positions for strained NbS_2 are shown with red lines in (a), while calculated (0 0 l) positions for NbS_3 both strained (d-f) and less strained (c) are shown with blue lines. (a) shows a strained 2H-NbS_2 material, while (c) shows strained 2H-NbS_2 (x marks) and strained NbS_3. (d)-(f) show a variety of materials, with peaks likely arising from intercalated/strained 2H-NbS_2 marked with x, additional unknown phases marked with † and the peaks likely arising from some form of strained/intercalated NbS_3, but which have not been able to be directly assigned to strained NbS_3 are marked with a *.*

7.5 Discussion

7.5.1 The structure and characterisation of HNP 2H-TaS_2

TaS_2 provides a template material to understand the general effect of strongly reducing potentials on group V TMDCs. From XRD, the out-of-plane peaks fit well to a strained 2H-TaS_2 cell that is contracted out-of-plane (*c*-axis) with a change in size from 12.1 Å to 11.9 Å. Evidence for in-plane (*a,b* axes) strain is sparse, coming solely from a small peak at $2\theta = 55.9°$, however its origin is difficult to determine. The sharpness of the obtained peaks evidences that some crystallinity is retained despite the change in axis size.

The disproportionate intensities of the peaks arising from the out-of-plane reflections cannot be solely explained by the preferred orientation effect. Peak intensity ratios, particularly between the peaks arising from the (0 0 2) reflection and the (0 0 *l*) reflections (*l* = 4,6,8) are not consistent with the expected intensity ratios, with the (0 0 2) peaks notably less intense than expected. This phenomenon can be explained by understanding the material as nanostructured,

consisting of many nanosheets and some monolayers that are tightly aligned. The (0 0 2) reflection is thus more affected by changes to the interlayer distance than the other reflections (Figure 11). This phenomenon is seen with other nanomaterials[21,22].

The cell strain hypothesis is further supported by the Raman spectroscopy data. All Raman peaks are broadened, in line with a less crystalline and more nano-structured material. The A_{1g} peak at 400 cm^{-1} [13] (Figure 3(ii)) sees a downshift, with the apparent appearance of two peaks, one slightly shifted (400 to 391 cm^{-1}) and one more shifted (400 to 380 cm^{-1}), appearing as a shoulder. The slightly shifted peak can be reasonably assigned to few-layer pristine 2H-TaS_2, as small shifts are expected as layer numbers decrease[23], such as here where nanosheets may be created, while the more shifted peak (or shoulder) can be assigned to the strained HNP 2H-TaS_2 A_{1g}, with the larger shift more typical of a change in cell dimensions[24]. This correlates well with the contraction of the out-of-plane axis. A similar effect can be seen in the E_g mode at 290 cm^{-1} (Figure 3(i)), which sees an additional two peaks at 308 and 326 cm^{-1} [13], with no substantial shift for the main peak at 290 cm^{-1}. These two peaks are consistent with expansions to the in-plane axes of the unit cell that are otherwise difficult to extract with XRD due to preferred orientation. The peak at 170 cm^{-1}, typically attributed to two-phonon scattering[25], sees no substantial shift, although the relative intensity of the shoulder at 193 cm^{-1} does decrease. The peak at 780 cm^{-1} remains unassigned but may be associated additional phonon modes that arise from the change to the unit cell.

As expected from a strained unit cell, the XPS (Figure 6, Figure 8) and XAS (Figure 9) indicate no change in sulfur or metal oxidation state, remaining in the sulfide S^{2-} and Ta^{4+} state respectively.

7.5.2 The structure and characterisation of HNP 1T-VS_2

Similar modelling of the XRD of strained VS_2 unit cells can help to explain the changes seen in HNP 1T-VS_2. XRD from 1T-VS_2 fits with three changes to the out-of-plane (c axis), suggesting three separate strained materials being formed with different c-axes. For HNP 1T-VS_2, the c-axes are expanded as compared to the pristine material, rather than contracted as with HNP 2H-TaS_2. The existence of three HNP structures becomes more apparent at higher values of 2θ, where the separation is sufficient to distinguish between them. These structures have strained out-of-plane (*c*) axes measuring 5.82, 5.80 and 5.84 Å respectively as compared to the value for pristine 1T-VS_2 of 5.76 Å.

Raman evidence for the structure of the HNP 1T-VS_2 is limited without a reliable baseline to compare to. Nevertheless, we are able to build some level of understanding using the known behaviour of similar 2H-TaS_2 as a comparison, as well as the known behaviour of other Raman spectra. Additionally, the phonon calculations and assignments (Chapter 4 & Appendix, section A.2) allow some insight into the expected peak positions. On this basis, peaks that are consistently present across multiple spectra are analysed and assigned.

Raman calculations for 1T-VS_2 (Figure 4, calculation details in Chapter 4, assignment details in Appendix, section A.2) predict an A_{1g} and A_{2u} mode, at 362 and 525 cm^{-1} respectively, however due to theoretical limitations, Raman intensities cannot be calculated. The A_{2u} mode is expected to be Raman inactive, and the non-visibility of the vibration mode at 525 cm^{-1} can therefore be easily explained. The experimental peak at 373 cm^{-1} (Figure 4 (vi), blue) is well within the expected error for such calculations[26], correlating to the predicted peak at 362 cm^{-1}. Additionally, a peak shift of ~10 cm^{-1} is also expected for the A_{1g} mode due to the formation of nanosheets. The experimental peak at 402 cm^{-1} (Figure 4 (vi), red) is therefore assigned as a strain-induced (expansion) shift from the peak at 373 cm^{-1}, arising from the A_{1g} mode in the strained phase.

The E_g and E_u modes are predicted to be found at 258 and 343 cm^{-1}. These are tentatively assigned as the experimental peaks at 272 and 317 cm^{-1} (Figure 4(iv, v)), falling within expected errors for these calculations. The experimental peaks at 285 (Figure 4(v) red) and 242 cm^{-1} have similar intensities and appear to be strain-induced (contraction) 30 cm^{-1} shifts from the experimental peaks at 317 cm^{-1} and 272 cm^{-1}, which is broadly consistent with the strain induced shifts from cell changes in TaS_2 (Figure 3), which sees peak shifts of 18 and 36 cm^{-1}. While ordinarily the E_u mode would not be expected to be Raman active, material strain, the formation of few-layer sheets, or interactions arising from various structural distortions could well explain changes in symmetry and the appearance of the E_u mode. Additional experimental peaks at ~200, ~155 cm^{-1} and below cannot be easily assigned from the calculations and are speculated to be two-phonon peaks as in TaS_2. The intensity of the TaS_2 two-phonon peaks is speculated to be due to charge density wave (CDW) formation in the crystal[13], which is a phenomenon that has also been reported for VS_2 and VS_2-like structures[16,27]. As with HNP 2H-TaS_2, this indicates that the out-of-plane and in-plane strain are in opposing directions, although in this case the c-axes expand while the a and b axes contract.

Typically, 1T-VS_2 has no observable Raman spectrum. This may be due to low polarisability, and is empirically similar to 1T-VSe_2, which requires extremely long acquisition times for a useful signal[28]. The detection of VS_2 peaks after application of a strongly reducing potential is a phenomenon that deserves further study and theoretical justification. Despite a limited theoretical basis, the effect is empirically similar to the increased intensity seen in HNP 2H-NbS_2, where NbS_2 peak definition improves.

7.5.3 The structure and characterisation of HNP 2H-NbS_2

In contrast to HNP 2H-TaS_2 and 1T-VS_2, 2H-NbS_2 exhibits a range of complex structures. Initial data (Figure 12b) shows no presence of unmodified 2H-NbS_2. As with the other two observed HNP phases, modified unit cells do explain some of the additional peaks in the

patterns acquired. The peaks show as double peaks at or near the expected positions for peaks resulting from pristine 2H-NbS_2 (2θ = 14.7-15.0° (0 0 2), 29.6-30° (0 0 4), 45.7° (0 0 6), 61.5-62.2° (0 0 8)), indicating out-of-plane (*c*-axis) expansion, with unit cells measuring at 11.94 (pristine) and 12.10 (strain) Å as compared to the ideal cell c-axis of 11.95 Å. The air-exposed XRD data also provides the in-plane unit cell parameters with the peaks at 2θ = 31.0° and 32.1° corresponding to in-plane (a,b) axis lengths of 3.33 Å (pristine) and 3.31 Å (strain) respectively.

The broad peaks at 2θ = 23.5°, 35.3°, 47.9° and 67.5° could not be fit to any known materials in the niobium-sulfur or elemental sulfur systems. Fortunately, the patterns acquired over time under nitrogen can provide insight into what material is being formed. The patterns of the HNP NbS_2 under nitrogen seem to undergo a similar change of pattern to resemble those measured under air. Peaks initially (T+1 hour) appear to be a strained 2H-NbS_2, similar to that of the samples measured under air. At T+2 hours, the strained 2H-NbS_2 peaks diminish and peaks similar to the additional peaks at 2θ = 11.4°, 17.4° in samples measured under air appear. Additional unidentified broad peaks similar to those at 2θ = 23.5°, 35.3°, 47.9° and 67.5° also appear. At T+ 7 and T+11 hours, the XRD broadly matches, and the unknown peaks appear to stabilise at the expected reflections for slightly strained NbS_3, with the out-of-plane reflections matching the expected peak positions. The pattern from T+3 hours represents a strained NbS_3, with earlier patterns representing increasing strain. The NbS_3 is somewhat amorphous and like HNP 2H-NbS_2, HNP 2H-TaS_2 and HNP 1T-VS_2, the peak intensities do not conform to the predicted results from modelling of the preferred orientation effect, indicating that both the HNP-NbS_2 and the HNP NbS_3 are nanostructured. The extent of the strain at T+3 hours (~10%) is likely evidence of an additional structural component, along with the additional broad peaks appearing at T+7 hours. It can be speculated that this is due to some form of self-intercalation

of the excess niobium, which might reasonably produce apparent strains of that magnitude. This would also explain the additional peaks present.

The XPS spectra are also compatible with the presence of NbS_3, whose sulfur atoms are known to exist in the sulfide S^{2-} state. The NbS_3 sulfurs can be reasonably assigned to the first (reduced) sulfur state (Figure 7c-d, green component), which is also consistent with known XPS values for trisulfides. The second state (Figure 7c, blue component) remains consistent with 2H-NbS_2. One of the HNP samples (Figure 7e) shows a notably shifted sulfur region at 163.4 and 164.6 eV, which is where elemental sulfur might be expected to appear. Elemental sulfur would be expected to have an extremely strong Raman signal, which is not apparent in the acquired Raman spectra (Figure 2). One possible explanation is that the sulfur is amorphous, with consequent reduced Raman intensities. It may originate from left-over intercalated sulfur from synthesis.

Raman shows minor shifts in the A_{1g} and E_g peaks of approximately 5 cm^{-1} consistent with a strained cell as seen in the XRD and the Raman of HNP 1T-VS_2 and HNP 2H-TaS_2. Additional peaks in the acquired spectra (Figure 2) are not immediately assignable, although the peaks at 156, 220 and 340 cm^{-1} (Figure 2, green arrows) are partly consistent with NbS_3[29], albeit potentially with some change due to strain.

Ultimately, it is evident from the data that the application of a strongly reducing potential to 2H-NbS_2 strains the 2H-NbS_2 in a similar fashion to HNP 1T-VS_2 and 2H-TaS_2. This in turn causes the formation of strained NbS_3, which over time undergoes shifts in structure, potentially to an entirely different phase. Additional materials appear to form over time, with self-intercalated NbS_3, NbS_2 and elemental sulfur all tentative candidates for those materials. As with HNP 2H-TaS_2 and HNP 1T-VS_2, the in-plane and out-of-plane strains appear to be in opposition to each other, indicated both by the Raman and XRD data.

There are substantial differences in apparent relative quantities of material when evaluating the XPS, XRD and Raman. The XRD patterns (Figure 12, Figure 13) indicate the presence of both NbS_3 and the unknown phases, while the Raman spectra (Figure 2) indicate an overwhelming presence of 2H-NbS_2 and strained 2H-NbS_2, with minimal presence of NbS_3 and unknown phases. The XPS spectra meanwhile indicate similar quantities of NbS_3 and 2H-NbS_2 (Figure 7). This is due to the limitations of each technique. It is presumed, due to the formation of NbS_2 nanosheets and monolayers, that the XRD signal is much weakened compared to the NbS_3. Therefore, in this case the XRD technique is limited in its ability to evaluate quantity. XPS, too, is extremely surface sensitive, where most of the catalysis and therefore HNP 2H-NbS_2 formation might be expected to take place. This makes it difficult to definitively quantify the relative quantities of material. However, evidence from the literature[12] indicates that substantial quantities of nanosheets of the pristine material remain present, with their small size and increased amorphousness responsible for the loss of XRD signal. Raman is therefore able to provide approximate quantifications, evidencing that substantially more pristine material is present in samples of HNP 2H-NbS_2 and HNP 1T-VS_2, and an approximately equal quantity of strained and pristine material is present for HNP 2H-TaS_2. This does not apply to quantification of NbS_3, whose structure is sufficiently dissimilar to NbS_2 as to expect a different Raman cross-section.

7.5.4 Towards an understanding of the cause of HNP phase change

Throughout the various techniques in this chapter, there does not appear to be an appreciable difference between the behaviour of materials processed as crystals and materials processed as powders. This indicates some mechanism that is not reliant on the large scale of the crystal to occur.

Insight into the development of cell strain can be also gained from the XPS data. The XPS data, with near-identical environments between the HNP and non-HNP materials indicates along

with the XAS that there is no oxidation state change to the material. The exception, 2H-NbS_2 has its additional environments well explained by the presence of NbS_3 or elemental sulfur. The possibility of significant metal self-intercalation as a cause of the changes is argued against by the lack of visible bonding as with 3R-NbS_2, where the different environments from intercalation are apparent from the obtained XPS. NbS_3 is expected to form as a separate phase from 2H-NbS_2.

The non-bonding intercalation of hydrogen rich moieties and water in group V TMDCs is established in the literature[9] and further evidenced in Chapter 6. The unit cell strain observed may arise from hydrogen bubble formation in between the layers (Figure 14), which can occur without permanent oxidation state changes. In this understanding, the application of a strongly reducing potential leads to the separation of the layers by the bubble formation. 2H-TaS_2 resembles the classical case of this, with the strained unit cell contraction of the out-of-plane axis and expansion of the in-plane axes in line with what would be expected for bubble-strained 2H-TaS_2[30]. The acquired Raman spectra (Figure 3) and XRD patterns (Figure 11) are also in line with literature reports of other bubble-strained TMDCs[24,31].

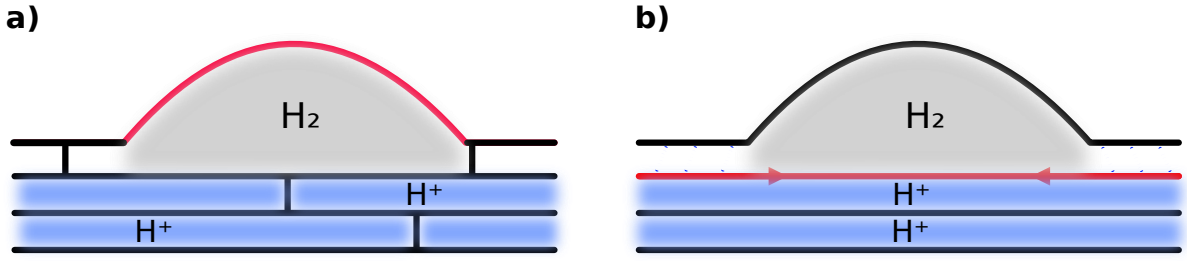


Figure 14. Illustration of the behaviour of some group V TMDCs at strongly reducing potentials. The formation of bubbles in between layers causes strain in the layers. In less intercalated structures (b), bubble strain is relieved via the hoop-compression effect, where interlayer bonds cause the interface layer (red) between the bubble and the bulk to compress.

In more intercalated materials (a), the interface layer is held in place by intercalants, so that the bubble layer undergoes strain (red).

Additional evidence for the intercalation-free strain hypothesis is found in the Raman spectra for the materials, where the frequency shifts arising from in-plane and out-of-plane vibrations occur in opposite directions, evidencing that the in-plane and out-of-plane strains oppose each other. This can be expected for strain resulting from hydrogen bubbles. Both 2H-NbS_2 and 1T-VS_2 present slightly counter-intuitive behaviour for hydrogen bubble effects, since the apparent expansion is out-of-plane and the contraction is in-plane. This behaviour is not unknown however[31]. One explanation for this behaviour may be the hoop compression effect, which is known in 2D crystals[32]. This is where the material under the bubble is compressed due to adhesion between the top and bottom layer of the material (Figure 14). This understanding is backed by the slight unit cell strain in the "pristine" component of 2H-NbS_2, which expands slightly, relieving the strain arising from the hoop compression. The strain in 2H-NbS_2 also destabilises it and causes the formation of NbS_3. This phase change has been previously reported for some TMDCs[33,34].

While hydrogen bubbles explain the behaviour of the strained unit cells, the differences in which mechanism dominates the observed data, whether hoop compression or bubble strain, must be understood. The 2H-TaS_2 appears to shrink along the out-of-plane axes, while the 1T-VS_2 and 2H-NbS_2 expand, and the 1T-TaS_2 and 3R-NbS_2 do not expand at all.

It is notable that behaviour appears to follow the extent of reported material self-intercalation. 2H-NbS_2 is produced in a highly sulfur-rich environment, and there is no evidence of niobium self-intercalation in the resulting XPS. Similarly, 1T-VS_2 is produced by the competitive intercalation of lithium, replacing vanadium self-intercalation. By contrast both 2H-TaS_2 and 1T-TaS_2 are formed in relatively sulfur-poor environments. These sulfur-poor environments

ensure some Ta intercalation[35,36], although the ease of exfoliation and limited XPS and XRD contributions indicates that this is not significant or crystalline. Finally, 3R-NbS_2 is highly intercalated, albeit with limited order, as evident from literature[15], XRD and XPS evidence.

The extent of self-intercalation may play a role in this different response to bubble formation. Since the formation takes place in large crystals rather than the more typical[30] thin- or mono-layer construction, metal self-intercalant interlayer pinning in TaS_2 likely prevents the hoop compression seen in the other crystals. By contrast, fewer self-intercalants in 2H-NbS_2 and 1T-VS_2 allows for thinner nanosheet formation and interlayer shearing, making hoop compression more favourable.

This effect of self-intercalation could also explain 1T-TaS_2 and 3R-NbS_2 behaviour. 3R-NbS_2, with its high number of self-intercalants is held together by covalent bonds rather than Van-der-Waals forces and consequently does not undergo exfoliation or structural change of any kind due to the inability of the hydrogen to effectively separate the layers and form bubbles. 1T-TaS_2 may not undergo a structure change due to poor hydrogen production (as outlined in Chapter 6), or may be more highly intercalated, or both, preventing the exfoliation necessary for strain.

7.6 A protocol for detecting thin film VS_2

There are many reports of the production of thin-film 1T-VS_2 at high temperatures (see Appendix, sections A.1, A.2). Due to the fact that at the deposition temperatures and pressures the vanadium sulfur system preferentially produces V_5S_8, reports of VS_2 production remain unconfirmed. XRD has limited utility in this application, as the materials have similar patterns and thin-film XRD has extremely poor peak resolution. While Raman can eliminate the production of other vanadium-sulfur phases, such as VS_4, V_3S_4 and V_5S_8, it is unable to definitively confirm the presence of VS_2.

It is therefore suggested that to allow for the positive identification of VS_2 several samples of the thin film are created. One of those samples can be subjected to a strongly reducing potential (approximately -1 V vs RHE), and the resulting sample examined with Raman spectroscopy. The expected result is shown in Figure 4 and can allow for the positive, albeit destructive, identification of VS_2 via Raman.

7.7 Conclusion

A novel phenomenon by which the phases 2H-NbS_2, 2H-TaS_2 and 1T-VS_2 undergo colour changes and structure changes is reported. 2H-NbS_2 is initially strained, as evidenced by XRD (Figure 13), with some transformation to NbS_3, while 2H-TaS_2 and 1T-VS_2 solely strain, with the unit cell expanding and contracting along different axes. Materials either expand along the out-of-plane axis while contracting along the in-plane axes (2H-NbS_2, 1T-VS_2) or vice versa (2H-TaS_2). Both 2H-NbS_2 and 2H-TaS_2 undergo self-exfoliation at sufficiently high potentials or long application of potential. 3R-NbS_2 and 1T-TaS_2 do not undergo phase transformation or self-exfoliation. The basis of the self-exfoliation and strain formation is attributed to interlayer hydrogen formation, while the differences in behaviour of these materials are attributed to the different self-intercalation behaviour of the materials, with 3R-NbS_2 as a highly self-intercalated material not undergoing phase transformations at all, while 1T-TaS_2 and 2H-TaS_2 behaviour can be attributed to similar extents of intercalation but different extents of hydrogen production. 1T-VS_2 and 2H-NbS_2 have minimal self-intercalants and consequently undergo out-of-plane expansion as part of the large-scale formation of nanosheets. This provides insight into the behaviour of these materials at strong reducing potentials. Strain engineering from these techniques may have potential in future catalyst engineering and modifications. Ultimately, a practical lower potential limit for these materials and the cause of this limit is established, while 3R-NbS_2 intercalation provides a fruitful avenue for mitigation of this issue.

Due to the appearance of a Raman spectrum upon the application of a highly reducing potential to 1T-VS_2, this is proposed as a possible protocol to allow the identification of thin-film 1T-VS_2 which can otherwise be a significant challenge.

7.8 References

(1) Zhong, H.; Zhang, Q.; Yu, J.; Zhang, X.; Wu, C.; Ma, Y.; An, H.; Wang, H.; Zhang, J.; Wang, X.; Xue, J. Fundamental Understanding of Structural Reconstruction Behaviors in Oxygen Evolution Reaction Electrocatalysts. *Advanced Energy Materials* **2023**, *13* (31), 2301391. https://doi.org/10.1002/aenm.202301391.

(2) Brandes, B. A.; Krishnan, Y.; Buchauer, F. L.; Hansen, H. A.; Hjelm, J. Unifying the ORR and OER with Surface Oxygen and Extracting Their Intrinsic Activities on Platinum. *Nat Commun* **2024**, *15* (1), 7336. https://doi.org/10.1038/s41467-024-51605-1.

(3) Wang, L.; Hao, Y.; Deng, L.; Hu, F.; Zhao, S.; Li, L.; Peng, S. Rapid Complete Reconfiguration Induced Actual Active Species for Industrial Hydrogen Evolution Reaction. *Nat Commun* **2022**, *13* (1), 5785. https://doi.org/10.1038/s41467-022-33590-5.

(4) Benck, J. D.; Chen, Z.; Kuritzky, L. Y.; Forman, A. J.; Jaramillo, T. F. Amorphous Molybdenum Sulfide Catalysts for Electrochemical Hydrogen Production: Insights into the Origin of Their Catalytic Activity. *ACS Catal.* **2012**, *2* (9), 1916–1923. https://doi.org/10.1021/cs300451q.

(5) Tsai, C.; Li, H.; Park, S.; Park, J.; Han, H. S.; Nørskov, J. K.; Zheng, X.; Abild-Pedersen, F. Electrochemical Generation of Sulfur Vacancies in the Basal Plane of MoS2 for Hydrogen Evolution. *Nat Commun* **2017**, *8* (1), 15113. https://doi.org/10.1038/ncomms15113.

(6) Gan, X.; Lee, L. Y. S.; Wong, K.; Lo, T. W.; Ho, K. H.; Lei, D. Y.; Zhao, H. 2H/1T Phase Transition of Multilayer MoS2 by Electrochemical Incorporation of S Vacancies. *ACS Appl. Energy Mater.* **2018**, *1* (9), 4754–4765. https://doi.org/10.1021/acsaem.8b00875.

(7) Wu, F.; Yang, R.; Lu, S.; Du, W.; Zhang, B.; Shi, Y. Unveiling Partial Transformation and Activity Origin of Sulfur Vacancies for Hydrogen Evolution. *ACS Energy Lett.* **2022**, *7* (12), 4198–4203. https://doi.org/10.1021/acsenergylett.2c02229.

(8) Escalera-López, D.; Iffelsberger, C.; Zlatar, M.; Novčić, K.; Maselj, N.; Van Pham, C.; Jovanovič, P.; Hodnik, N.; Thiele, S.; Pumera, M.; Cherevko, S. Allotrope-Dependent Activity-Stability Relationships of Molybdenum Sulfide Hydrogen Evolution Electrocatalysts. *Nat Commun* **2024**, *15* (1), 3601. https://doi.org/10.1038/s41467-024-47524-w.

(9) Liu, Y.; Wu, J.; Hackenberg, K. P.; Zhang, J.; Wang, Y. M.; Yang, Y.; Keyshar, K.; Gu, J.; Ogitsu, T.; Vajtai, R.; Lou, J.; Ajayan, P. M.; Wood, B. C.; Yakobson, B. I. Self-Optimizing, Highly Surface-Active Layered Metal Dichalcogenide Catalysts for Hydrogen Evolution. *Nat Energy* **2017**, *2* (9), 1–7. https://doi.org/10.1038/nenergy.2017.127.

(10) Yang, J.; Mohmad, A. R.; Wang, Y.; Fullon, R.; Song, X.; Zhao, F.; Bozkurt, I.; Augustin, M.; Santos, E. J. G.; Shin, H. S.; Zhang, W.; Voiry, D.; Jeong, H. Y.; Chhowalla, M. Ultrahigh-Current-Density Niobium Disulfide Catalysts for Hydrogen Evolution. *Nat. Mater.* **2019**, *18* (12), 1309–1314. https://doi.org/10.1038/s41563-019-0463-8.

(11) Najafi, L.; Bellani, S.; Oropesa-Nuñez, R.; Martín-García, B.; Prato, M.; Mazánek, V.; Debellis, D.; Lauciello, S.; Brescia, R.; Sofer, Z.; Bonaccorso, F. Niobium Disulphide (NbS2)-Based (Heterogeneous) Electrocatalysts for an Efficient Hydrogen Evolution Reaction. *J. Mater. Chem. A* **2019**, *7* (44), 25593–25608. https://doi.org/10.1039/C9TA07210A.

(12) Si, J.; Zheng, Q.; Chen, H.; Lei, C.; Suo, Y.; Yang, B.; Zhang, Z.; Li, Z.; Lei, L.; Hou, Y.; Ostrikov, K. (Ken). Scalable Production of Few-Layer Niobium Disulfide Nanosheets via

Electrochemical Exfoliation for Energy-Efficient Hydrogen Evolution Reaction. *ACS Appl. Mater. Interfaces* **2019**, *11* (14), 13205–13213. https://doi.org/10.1021/acsami.8b22052.

(13) Joshi, J.; Hill, H. M.; Chowdhury, S.; Malliakas, C. D.; Tavazza, F.; Chatterjee, U.; Hight Walker, A. R.; Vora, P. M. Short-Range Charge Density Wave Order in 2H-TaS2. *Phys. Rev. B* **2019**, *99* (24), 245144. https://doi.org/10.1103/PhysRevB.99.245144.

(14) Saitoh, Y.; Kobayashi, K.; Fujimori, A.; Yamamura, Y.; Koyano, M.; Tsuji, T.; Katayama, S. Photoemission and Core-Level Absorption Spectroscopy of FexNbS2. *Journal of Electron Spectroscopy and Related Phenomena* **2005**, *144–147*, 829–832. https://doi.org/10.1016/j.elspec.2005.01.186.

(15) Huang, D. Probing the Interlayer Coupling in 2H-NbS2 via Soft-x-Ray Angle-Resolved Photoemission Spectroscopy. *Phys. Rev. B* **2022**, *105* (24). https://doi.org/10.1103/PhysRevB.105.245145.

(16) van Efferen, C.; Hall, J.; Atodiresei, N.; Boix, V.; Safeer, A.; Wekking, T.; Vinogradov, N. A.; Preobrajenski, A. B.; Knudsen, J.; Fischer, J.; Jolie, W.; Michely, T. 2D Vanadium Sulfides: Synthesis, Atomic Structure Engineering, and Charge Density Waves. *ACS Nano* **2024**, *18* (22), 14161–14175. https://doi.org/10.1021/acsnano.3c05907.

(17) Sonntag, B.; Brown, F. C. Soft-x-Ray Response of Transition-Metal Layer Compounds. *Phys. Rev. B* **1974**, *10* (6), 2300–2306. https://doi.org/10.1103/PhysRevB.10.2300.

(18) Sugiura, C.; Muramatsu, S. Sulfur KX-Ray Absorption-Edge Structures and Electronic States of Transition-Metal Sulfides MS and MS2 (M= Fe, Co, Ni). *physica status solidi (b)* **1985**, *129* (2), K157–K161.

(19) Hallmeier, K. H.; Uhlig, I.; Szargan, R. Sulphur L2,3 and L1 XANES Investigations of Pyrite and Marcasite. *Journal of Electron Spectroscopy and Related Phenomena* **2002**, *122* (1), 91–96. https://doi.org/10.1016/S0368-2048(01)00362-0.

(20) Li, D.; Bancroft, G. M.; Kasrai, M.; Fleet, M. E.; Feng, X.; Tan, K. S K-and L-Edge X-Ray Absorption Spectroscopy of Metal Sulfides and Sulfates; Applications in Mineralogy and Geochemistry. *The Canadian Mineralogist* **1995**, *33* (5), 949–960.

(21) Jiang, A.; Tyson, T. A.; Axe, L.; Gladczuk, L.; Sosnowski, M.; Cote, P. The Structure and Stability of β-Ta Thin Films. *Thin Solid Films* **2005**, *479* (1), 166–173. https://doi.org/10.1016/j.tsf.2004.12.006.

(22) Shazad, H. K.; Huang, Z.; Ghashghaie, S.; Liu, H.; Muhyodin, G.; Tamtaji, M.; Li, H. L.; Chan, F. C.; Chung, C. Y. Systematic Analysis of Reaction Parameters Driving the Hydrothermal Growth of Layered VS2. *CrystEngComm* **2025**, *27* (18), 2858–2871. https://doi.org/10.1039/d4ce01161a.

(23) Liang, L.; Meunier, V. First-Principles Raman Spectra of MoS2, WS2 and Their Heterostructures. *Nanoscale* **2014**, *6* (10), 5394–5401. https://doi.org/10.1039/C3NR06906K.

(24) Luo, H. Simultaneous Generation of Direct- and Indirect-Gap Photoluminescence in Multilayer MoS2 Bubbles. *Phys. Rev. Mater.* **2020**, *4* (7). https://doi.org/10.1103/PhysRevMaterials.4.074006.

(25) Dumke, W. P. Two-Phonon Indirect Transitions and Lattice Scattering in Si. *Phys. Rev.* **1960**, *118* (4), 938–939. https://doi.org/10.1103/PhysRev.118.938.

(26) Bagheri, M.; Komsa, H.-P. High-Throughput Computation of Raman Spectra from First Principles. *Sci Data* **2023**, *10* (1), 80. https://doi.org/10.1038/s41597-023-01988-5.

(27) Kim, H. J.; Choi, B. K.; Lee, I. H.; Kim, M. J.; Chun, S.-H.; Jozwiak, C.; Bostwick, A.; Rotenberg, E.; Chang, Y. J. Electronic Structure and Charge-Density Wave Transition in Monolayer VS2. *Current Applied Physics* **2021**, *30*, 8–13. https://doi.org/10.1016/j.cap.2021.03.020.

(28) Falke, Y.; Ehlen, N.; Marini, G.; Fedorov, A. V.; Voroshnin, V. Y.; Senkovskiy, B. V.; Nikonov, K.; Hoesch, M.; Kim, T. K.; Petaccia, L.; Di Santo, G.; Szkopek, T.; Profeta, G.; Grüneis, A. Coupling to Zone-Center Optical Phonons in VSe 2 Enhanced by Charge Density Waves. *Phys. Rev. B* **2021**, *104* (23), 235137. https://doi.org/10.1103/PhysRevB.104.235137.

(29) Abdel-Hafiez, M. Pressure-Induced Reentrant Transition in NbS3 Phases: Combined Raman Scattering and x-Ray Diffraction Study. *Phys. Rev. B* **2019**, *99* (23). https://doi.org/10.1103/PhysRevB.99.235126.

(30) Sanchez, D. A.; Dai, Z.; Lu, N. 2D Material Bubbles: Fabrication, Characterization, and Applications. *Trends in Chemistry* **2021**, *3* (3), 204–217. https://doi.org/10.1016/j.trechm.2020.12.011.

(31) Cao, Y.; Assefa, T.; Banerjee, S.; Wieteska, A.; Zi-Ren Wang, D.; Pasupathy, A.; Tong, X.; Liu, Y.; Lu, W.; Sun, Y.-P.; He, Y.; Huang, X.; Yan, H.; Chu, Y. S.; Billinge, S. J. L.; Robinson, I. K. Complete Strain Mapping of Nanosheets of Tantalum Disulfide. *ACS Appl. Mater. Interfaces* **2020**, *12* (38), 43173–43179. https://doi.org/10.1021/acsami.0c06517.

(32) Dai, Z.; Rao, Y.; Lu, N. Two-Dimensional Crystals on Adhesive Substrates Subjected to Uniform Transverse Pressure. *International Journal of Solids and Structures* **2022**, *257*, 111829. https://doi.org/10.1016/j.ijsolstr.2022.111829.

(33) Duerloo, K.-A. N.; Li, Y.; Reed, E. J. Structural Phase Transitions in Two-Dimensional Mo- and W-Dichalcogenide Monolayers. *Nat Commun* **2014**, *5* (1), 4214. https://doi.org/10.1038/ncomms5214.

(34) Qi, K.; Cui, X.; Gu, L.; Yu, S.; Fan, X.; Luo, M.; Xu, S.; Li, N.; Zheng, L.; Zhang, Q.; Ma, J.; Gong, Y.; Lv, F.; Wang, K.; Huang, H.; Zhang, W.; Guo, S.; Zheng, W.; Liu, P. Single-Atom Cobalt Array Bound to Distorted 1T MoS2 with Ensemble Effect for Hydrogen Evolution Catalysis. *Nat Commun* **2019**, *10* (1), 5231. https://doi.org/10.1038/s41467-019-12997-7.

(35) Agarwal, N.; Sung, S. H.; Schwartz, J.; Schnitzer, N.; Xi, Z.; Hung, J.; Baggari, I. E.; Kourkoutis, L. F.; Qi, L.; Van der Ven, A.; Hovden, R. Native Intercalant Order in TaS2 Achieved Through in Situ Thermal Heating. *Microanal* **2023**, *29* (Supplement_1), 1583–1584. https://doi.org/10.1093/micmic/ozad067.814.

(36) Hall, J.; Ehlen, N.; Berges, J.; van Loon, E.; van Efferen, C.; Murray, C.; Rösner, M.; Li, J.; Senkovskiy, B. V.; Hell, M.; Rolf, M.; Heider, T.; Asensio, M. C.; Avila, J.; Plucinski, L.; Wehling, T.; Grüneis, A.; Michely, T. Environmental Control of Charge Density Wave Order in Monolayer 2H-TaS2. *ACS Nano* **2019**, *13* (9), 10210–10220. https://doi.org/10.1021/acsnano.9b03419.

Chapter 8. Summary and Future work

8.1 Summary

This thesis has focused on attaining a greater understanding of the factors affecting the catalytic activity and behaviour of the group V transition metal dichalcogenides. Chapters 1 and 2 introduced electrochemistry and the group V TMDCs and set the stage for why the study of large crystal group V TMDCs is necessary. Chapter 3 introduced the experimental techniques and outlined the methods used to study these materials in this thesis, while Chapter 4 introduced the computational background and methods that were also used to study and construct descriptors of these materials.

Chapter 5 investigated the CVT synthesis and spectroscopies of the group V TMDCs TaS_2 and NbS_2. It found that the edges of crystals exposed to air oxidised rapidly, and to a greater extent than the basal plane. From this it can be understood that the edges of few-layer TMDCs are also more likely to oxidise, changing the apparent catalytic activity and allowing understanding of the nature of the more typical catalytic powder.

Having established the extent of oxidation of the edges and basal planes of the large TMDC crystal, Chapter 6 employed those crystals to find the specific capacitance and exchange current density of the materials 2H-NbS_2, 3R-NbS_2, 2H-TaS_2 and 1T-TaS_2. This provided insight into the intrinsic catalytic performance of the materials. The electronic structure of these materials was also modelled, and the results compared to the specific capacitance. It was found that the specific capacitance correlated to the electronic structure of the materials. 1T-TaS_2 with an electronic structure different from that of the other materials was found to have a specific capacitance distinctly different from that of the other materials, while the other three were broadly comparable. The obtained specific capacitance was then applied to the polarisation

plots of the materials, allowing for the reporting of accurate overpotentials and exchange current densities, and effective comparison of future samples with other materials.

As with the specific capacitance, the exchange current density was found to correspond well with the electronic structure. Both the exchange current density and specific capacitance appear to correlate with the intrinsic catalytic activity, which is constrained by the energy of hydrogen adsorption independent of factors such as conductivity. As such, the specific capacitance and exchange current density have been proposed as experimental descriptors for the intrinsic catalytic activity of these materials, which has utility for more direct comparison to computational descriptors.

The thesis then examines the behaviour of these materials at hitherto under-reported potentials. Chapter 7 reports on the changes in structure and properties that some of the materials undergo when exposed to strongly negative potentials at or below -0.7 V vs RHE. It was found that only some of the materials, namely 2H-NbS_2, 2H-TaS_2 and 1T-VS_2 undergo these changes. It was theorised that these changes are a result of the electrochemically induced formation of hydrogen between the layers, causing substantial delamination and the formation of both nanosheets and trapped bubbles of hydrogen gas between layers of the TMDCs. These trapped bubbles strain the TMDCs, causing changes to the Raman spectrum of the materials and in the case of 2H-NbS_2 triggering a phase transformation to NbS_3 and other materials. The specific response of the materials appears to depend on the extent of intercalation and intrinsic catalytic performance of the materials and offers a potential path to mitigation.

Thanks to the change in the Raman spectrum of the materials, a Raman response is obtained from VS_2 samples. The peaks in that spectrum were tentatively assigned to VS_2 and strained

VS_2 respectively, and a protocol constructed to allow for the (destructive) detection of thin film VS_2, which has been heretofore extremely difficult.

8.2 Future work

For Chapter 5, while the oxidised state of the edges has been well established, understanding precisely the impact on performance is of great interest. This can be done via scanning electrochemical microscopy (SECM) and would allow for decoupling of the edge and basal plane contributions. This would be of particular interest if accompanied by tip enhanced Raman spectroscopy (TERS) which could determine the edge composition at the nanoscale. Additionally some exploration of the 3R-NbS_2 hair-like growth origin is warranted.

Chapter 6 indicates the specific capacitance of a material can be directly correlated to its electronic structure and intrinsic catalytic performance. This can be tested in other systems, such as transition metal single crystal surfaces and other TMDCs. The chapter also highlights that the specific capacitance and exchange current density, as descriptors, are independent of the conductivity of the materials. Testing this on simpler, blocking electrodes with low conductivity would be of great interest to establish this theory further. The methods used to establish these specific capacitances should be expanded to other basal plane active TMDCs, such as 1T-MoS_2 and $NbSe_2$, and tested against various computational descriptors to establish which is correct. SEM would also permit for the characterisation and confirmation of the cracks and flaws of the larger crystals.

For Chapter 7, further confirmation of the bubble structures in the strained materials can be obtained via SECM of specific positions on a high-quality sample, which would permit the targeted growth and detection of the bubble, as well as nano-XRD and TERS to confirm macro-observations. A combination of SEM (for large area checks) and AFM (for examination of specific bubbles) would also permit for observation of already formed bubbles. Spinning the

samples under XRD should also permit for the reduction of the preferred orientation effect and allow the confirmation of the in-plane axis expansion/contraction. Additionally, it is important to try and establish the nature of the materials that form from strained 2H-NbS_2.

Appendix. Synthesis and characterisation of VS_2

A.0 Abstract

The synthesis of 1T-VS_2 has been claimed in the literature via two methods, chemical vapour deposition and hydrothermal synthesis. However, the spectra reported from these methods differ. To that end, establishing an effective synthesis and understanding the spectroscopy of 1T-VS_2 is essential for further study of the group V transition metal dichalcogenides. This appendix identifies the source of commonly reported literature Raman spectra for 1T-VS_2 as having originated from V_5S_8 and V_2O_5 respectively. It subsequently discusses the hitherto unreported spectrum of the material and examines the hydrothermal synthesis of 1T-VS_2 with a view to improving crystallinity and purity.

A.1 Introduction

VS_2 suffers from some disagreement in the literature as to the nature of its Raman spectrum. VS_2 synthesised via hydrothermal methods[1,2] is commonly reported with a different Raman spectrum from those reported to be VS_2 synthesised via CVT[3,4]. While reports of large VS_2 single crystals do exist, they cannot yet be reliably obtained. However, insufficient evidence of the crystal chemistry and purity[5,6] have been published, which is particularly important for VS_2 which exists in sub-stoichiometric $V_{1+x}S_2$ forms.

VS_2 can be synthesised via the reaction of the elements in the presence of lithium at high temperatures, followed by de-intercalation[7,8]. However, the literature most commonly employs a hydrothermal/solvothermal method of synthesis[8]. These syntheses typically produce VS_2 in nanoparticle form, however literature reports using similar conditions to the production of VS_2 have reported the production of VS_4 or mixed VS_2/VS_4 instead[9,10].

The utilisation and potential improvement of VS_2 as a catalyst requires an adequate understanding of its spectroscopic properties and synthesis. To this end, this appendix assigns

and explains hitherto inaccurately/inconsistently reported Raman features for this material and reports on the VS_2 Raman response. The appendix also explores certain conditions under which VS_2 or VS_4 form, and a new method for increasing the purity and crystallinity of the VS_2 hydrothermal synthesis.

A.2. Understanding the Raman spectroscopy of vanadium disulfide

A.2.1 Synthesis of VS_2 related vanadium sulfides.

VS_2 was synthesised via solid-state synthesis utilising a lithium intercalation method[8]. $LiVS_2$ was initially synthesised by heating (800 °C) under vacuum Li_2S, sulfur, and vanadium at stoichiometric ratios. The $LiVS_2$ was then de-lithiated by the addition of the powder to a solution of iodine in dimethyl carbonate (DMC) under argon. The solution initially turned purple, clearing over time as the lithium reacted with the iodine to form lithium iodide. Iodine was then added to excess and the solution stirred under argon for 48h before the lithium iodide was diluted out via 3 decants and refills, and the solution evaporated away in vacuum. A black powder was produced. The resulting XRD from the produced powder is shown in Figure 1 and showed reflections at 15.4, 35.5 and 55-60°, confirming the structure in line with literature[7,11–13]. A slight preferred orientation effect was observed, as well as some additional peaks, which arose due to the presence of various lithium, iodine and carbon compounds present due to the synthesis process. These peaks are not present after immersion in acid and the application of a negative potential, indicating they are not intrinsic to the material (Chapter 7).

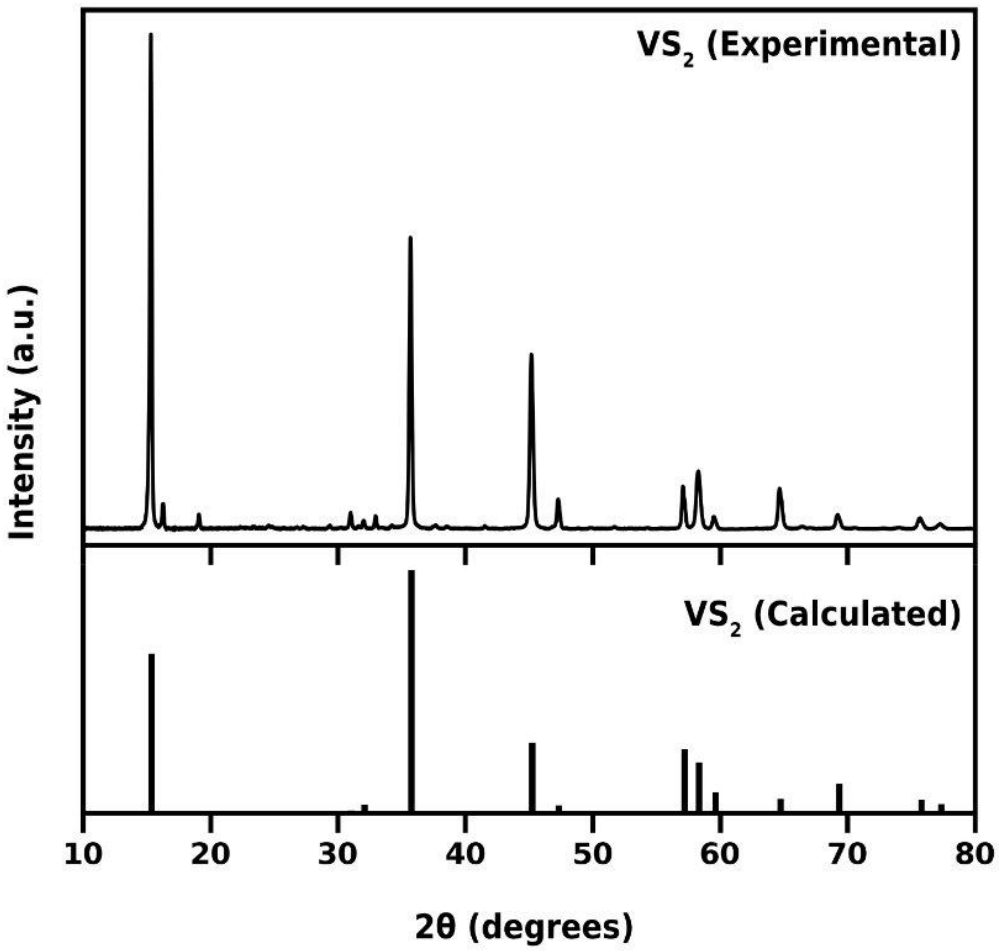


Figure 1. XRD of VS_2. Shown above is the obtained XRD pattern for VS_2 as compared to the calculated reflections below. The preferred orientation effect explains the increased height of the peak at 15 degrees 2θ as well as the peak at 45 degrees 2θ, and the distorted heights of the peaks between 55-60 degrees 2θ.

V_5S_8 was synthesised via solid-state synthesis and chemical vapour transport (CVT). In solid-state synthesis, vanadium and sulfur in a 1:2.01 ratio was added under vacuum to a sealed quartz tube. Iodine was added as a mineralising agent[14]. Materials were heated up to 450 °C at 1 °C/min, then kept at temperature for 24 hours and allowed to cool. Produced material was extracted under argon. For the CVT reaction, the same materials were placed in a 19 mm diameter quartz tube of length 200 mm. The source was at 950 °C, while the sink was at 850 °C. Sufficient iodine was added to ensure a calculated pressure of 1 bar at source temperature.

V_5S_8 crystals formed dark hexagonal crystals ~5 mm in diameter, while the solid-state synthesis produced a dark black powder. Structure was confirmed using XRD (Figure 2) and showed characteristic reflections as predicted by material models and reported in the literature[11,15–17].

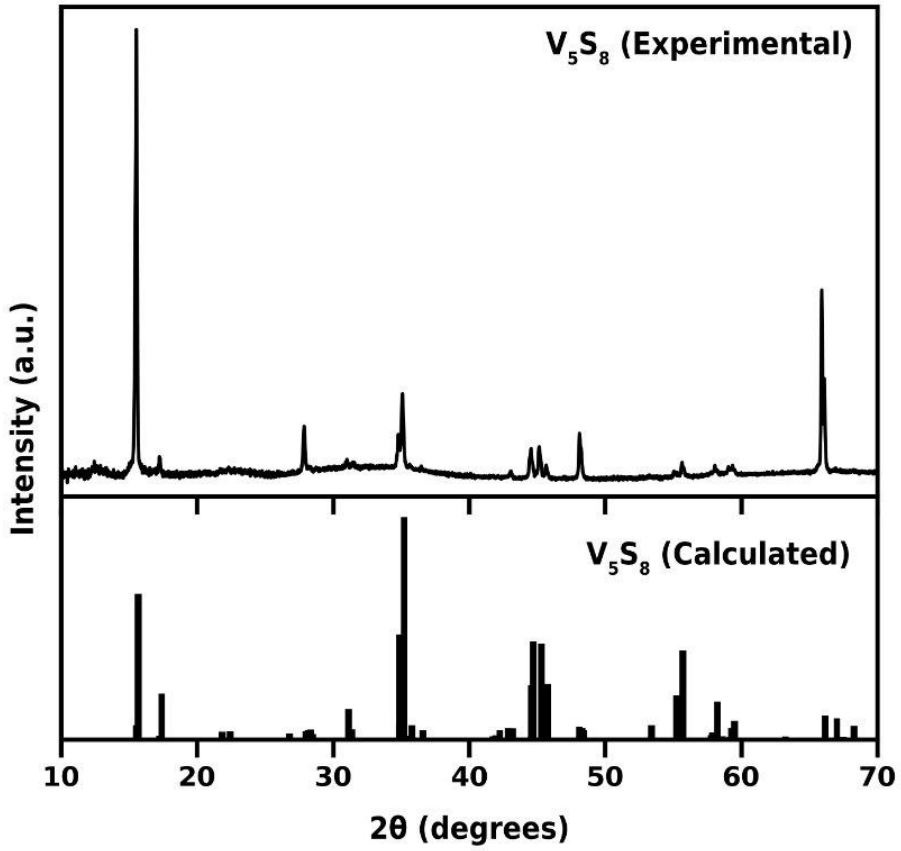


Figure 2. XRD of V_5S_8. The distortion due to the preferred orientation effect is particularly distinct in the peaks at ~15 degrees 2θ and between 55-60 degrees 2θ. The V_5S_8 pattern is similar to the VS_2 pattern, resembling a distorted VS_2 pattern with some additional weak peaks. Those peaks can be suppressed further by the preferred orientation effect and low signal, enhancing the similarities.

A substantial preferred orientation effect was observed, particularly for the peaks at ~15 degrees 2θ and between 55-60 degrees 2θ. Synthesis was further confirmed with Raman spectroscopy (Figure 3) with characteristic peaks at 124, 170, 185 and 329 cm^{-1}.

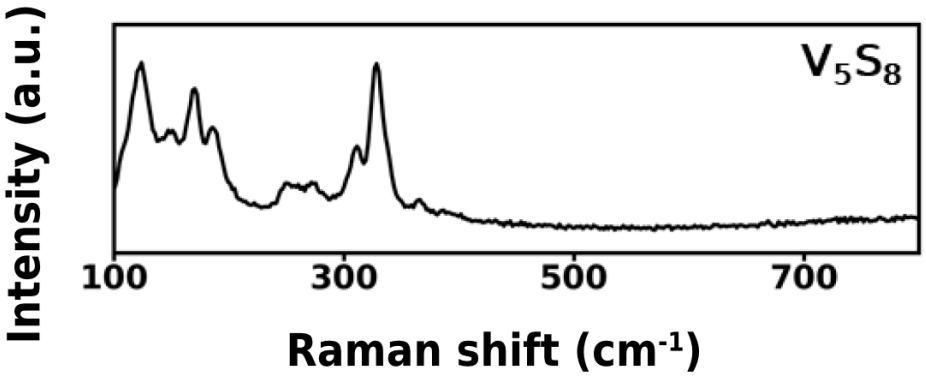


Figure 3. Acquired Raman spectrum of V_5S_8

As with other materials (Chapter 5), V_5S_8 suffered from a preferred orientation effect in its XRD. It is the preferred phase that forms from the high temperature reaction of the solids (sulfur, vanadium) and consists of vanadium disulfide sheets with intercalated, bonded vanadium atoms[17].

A.2.2 Predicted VS_2 Raman spectrum and the Raman response of VS_2

Vanadium disulfide exists in the 1T form and as a member of the space group P-3m1[7,12] and belongs to the space group D_{3d}^3. Via nuclear site analysis[18], it can be determined that the vanadium atoms have symmetry D_{3d} while the sulfur atoms have symmetry $C_{3v\ and}$ therefore contribute vibration modes $A_{2u}+E_u$ and $A_{1g}+E_g+A_{2u}+E_u$ respectively. The sum of these gives $A_{1g}+E_g+2A_{2u}+2E_u$ vibration modes, from which the acoustic (translational) modes are subtracted giving $A_{1g}+E_g+A_{2u}+E_u$ modes, of which in theory only the A_{1g} and E_g modes are Raman-active.

The phonon modes were calculated using CASTEP[19] as outlined in Chapter 4, finding modes existing at 258, 343, 362 and 525 cm^{-1}, of which the E_g and E_u (each doubly degenerate) modes are at 258 and 343 cm^{-1}, with atoms moving in the axes parallel with the basal plane, while the

A_{1g} and A_{2u} modes at 362 and 525 cm^{-1} see atoms moving in the z axis, perpendicular to the basal plane (Figure 4). CASTEP calculated results were in line with the nuclear site analysis.

Raman spectra were sought from both hydrothermal and solid-synthesis samples. Long duration spectra from the hydrothermal samples revealed minor VS_4 contamination, but no apparent VS_2 Raman spectrum. For the material produced via lithium intercalation, no Raman spectrum was observed at all. Raman spectra at multiple wavelengths (785, 633 and 532 nm) were collected under argon in a sealed cell and air (Figure 4). The spectra showed no peaks, sharp or broad. Materials were measured under air and under argon at varying laser power. While unexpected, this result is consistent with a recent report by Masaityte[8].

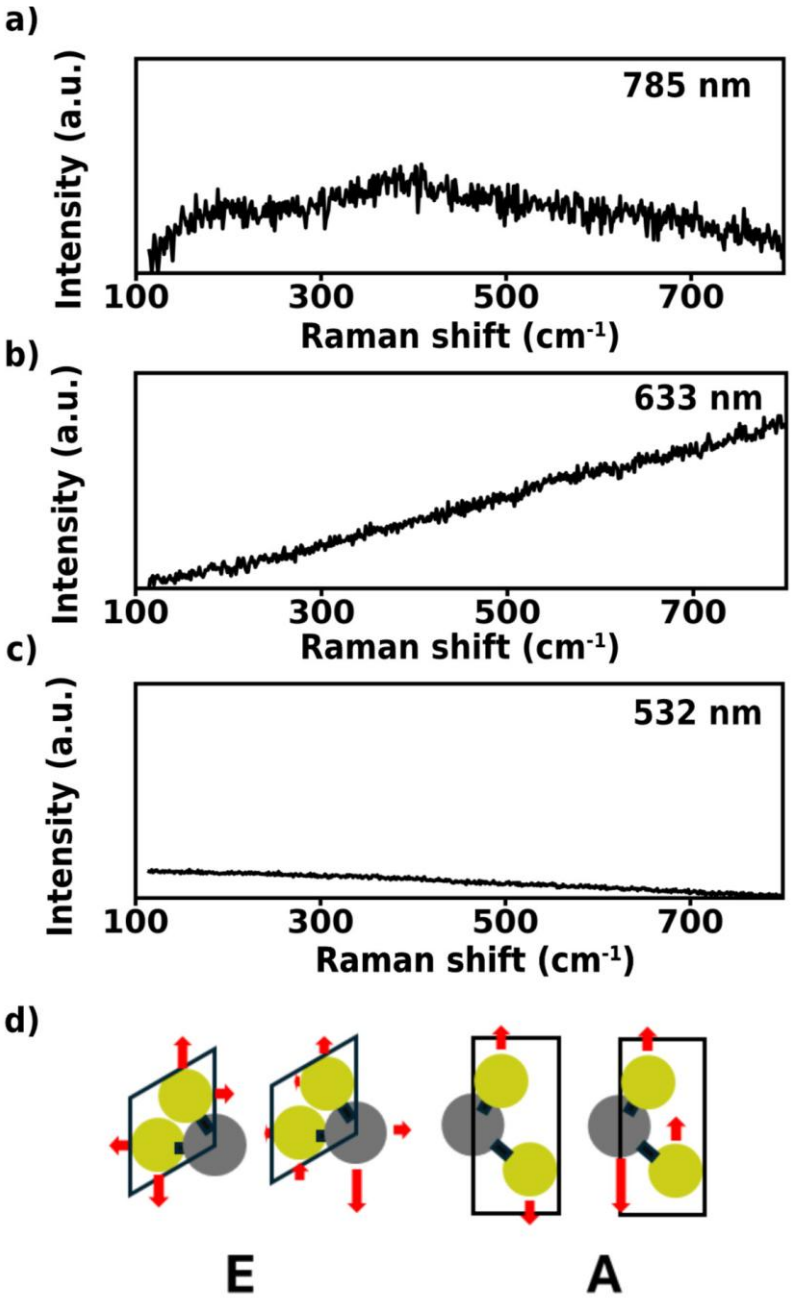


Figure 4: Raman response of VS_2. (a), (b) and (c) shows the obtained Raman response for VS_2 solid-state synthesis samples under argon. (a) has the glass background subtracted, and the resulting shallow bump between 300 to 500 cm^{-1} is likely a background subtraction feature. (b) and (c) show no features. (d) shows the approximate vibrations assigned to each phonon mode type (E_x, A_x) of VS_2.

A.2.3 Understanding reported Raman spectra for VS_2

The lack of an obtainable VS_2 spectrum is in conflict with reports that show a series of different spectra from across the literature[1–4,20–25]. Two sets of spectra are typically reported in the literature and differ by method of VS_2 synthesis. For hydrothermally synthesised VS_2, the typical reported Raman spectrum resembles that shown in Figure 5a, with characteristic peaks at 145, 285, 405, 528, 701 and 996 cm^{-1}. This spectrum is not that of VS_2 but that of α-vanadium oxide[26–28] indicating that the reported spectra are sulfides, such as VS_2, VS_4 and V_5S_8 that have been oxidised. A potential cause of this is the laser from the Raman measurement, as the α-V_2O_5 spectrum was reproduced by subjecting VS_2, V_5S_8, or VS_4 to lab-based lasers under atmosphere (Figure 5b, c). This occurs at a notably lower power than analogous TMDCs from other metals in group V. When measured under an argon atmosphere, regardless of laser power, this spectrum is not observed.

For VS_2 produced via APCVD, the typically reported Raman spectrum matches that of V_5S_8. This is explained by the phase diagram of the vanadium-sulfur system compiled by Moutaabbid et al.[17], who showed that at temperatures above 600 °C, the V_5S_8 phase forms very preferentially, requiring extreme pressures to obtain VS_2. This is also supported by reported degradation of VS_2 to V_5S_8 at temperatures above 350 °C[29]. The XRD of V_5S_8 and VS_2 are similar, with peaks in the pattern jointly appearing at 15, 35 and 55°. Due to the inevitable low quality of thin film XRD due to low mass loading, it is very difficult to distinguish the phases using this technique, and consequently other methods are recommended for structure determination (Chapter 7).

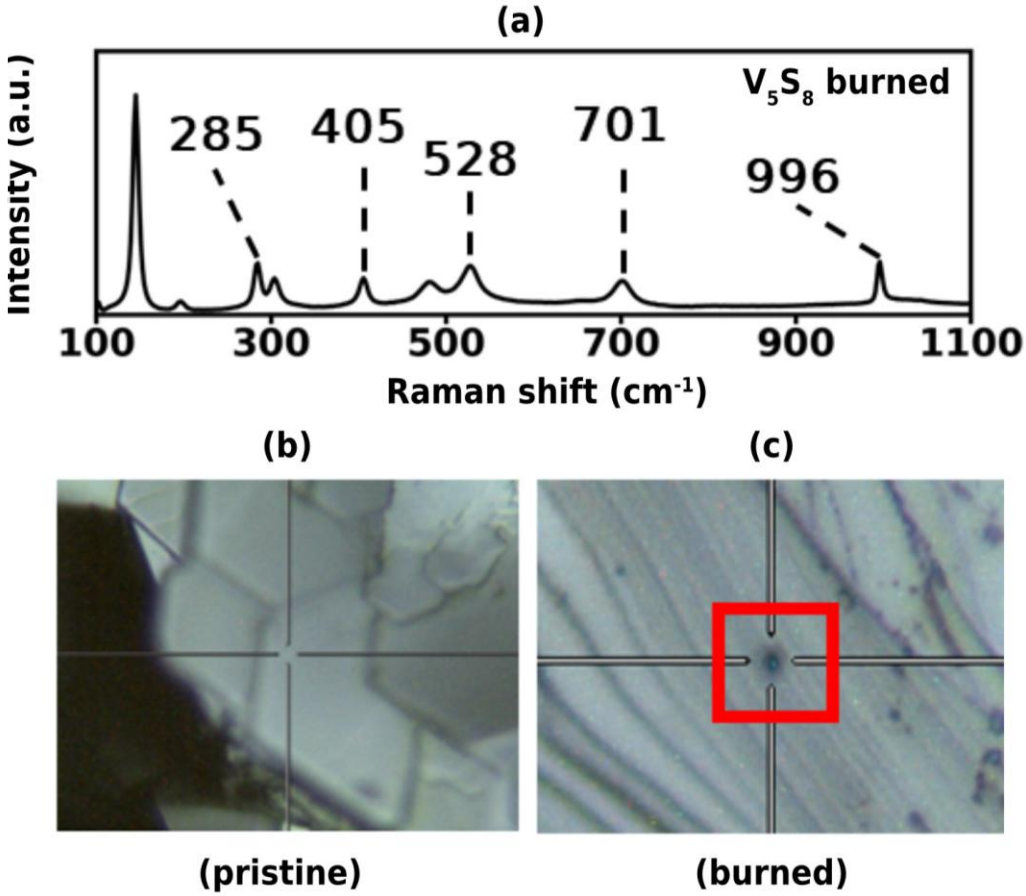


Figure 5. (a) shows the obtained Raman spectrum for laser heated V_5S_8. This resembles closely the Raman spectrum of V_2O_5, and the spectra for laser heated VS_2 and VS_4. (b) and (c) show the V_5S_8 crystal and the V_5S_8 crystal with a dark V_2O_5 region ringed by the red box obtained from laser-induced oxidation. Raman peak positions are labelled above the dashed lines. The units, cm^{-1} are omitted for space.

A.3 Improving VS_2 yields in the hydrothermal method.

A.3.1 C276 and the role of reactor vessel walls

VS_2 was synthesised in both a stainless-steel reactor and a reactor constructed of Hastelloy C-276, a high-performance corrosion-resistant alloy[30]. In a typical reaction, 5 mmol of ammonium metavanadate (NH_4VO_3) is reacted with 25 mmol of thioacetamide in 24 ml of water and 6 ml of 30% NH_3(aq). In the C276 reactor, reactions were conducted with and

without NH_3 as an addition to the synthesis solution, while in the stainless-steel reactor, reactions were conducted both with and without cetyltrimethylammonium chloride (CTAC) as a co-catalyst.

The hydrothermal reaction of ammonium metavanadate and thioacetamide in the presence of NH_3 in a C276 reaction vessel produced VS_4. The same reaction without ammonia also produced VS_4 (Figure 6).

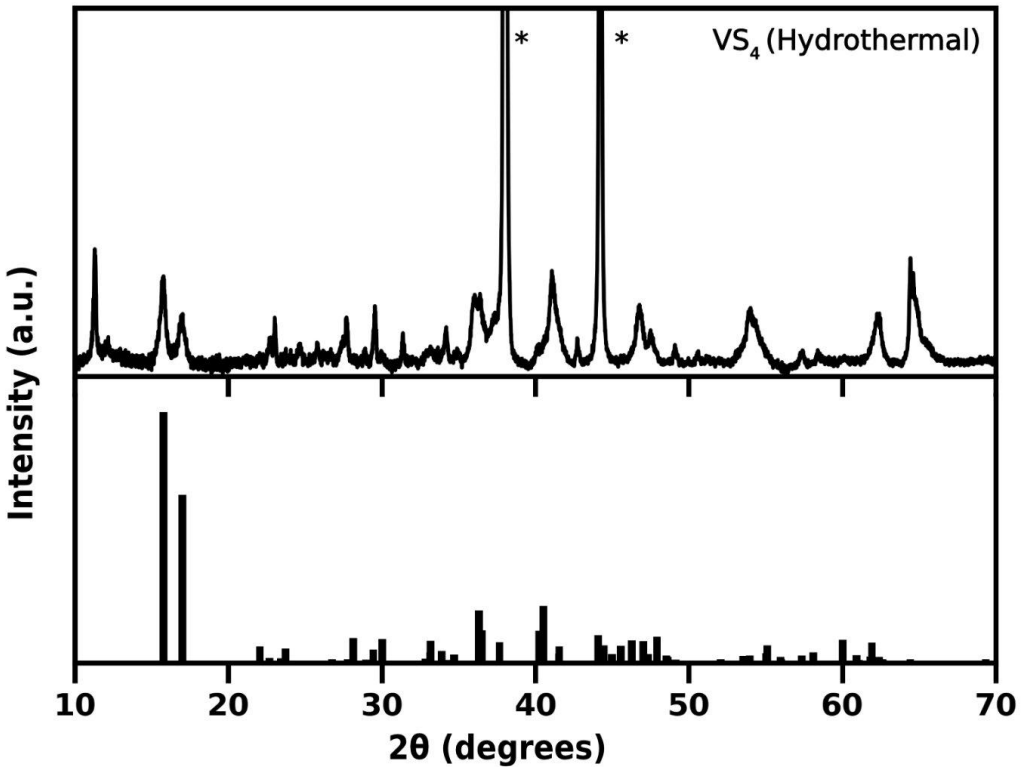


Figure 6. XRD pattern resulting from VS_4 produced without the presence of NH_3 in a reactor of C276. The peaks marked with a star arise from the aluminium sample holder. Other side reactions have likely occurred.

Comparatively, in a stainless-steel vessel in the presence of ammonia, the reaction produced VS_2. (Figure 7).

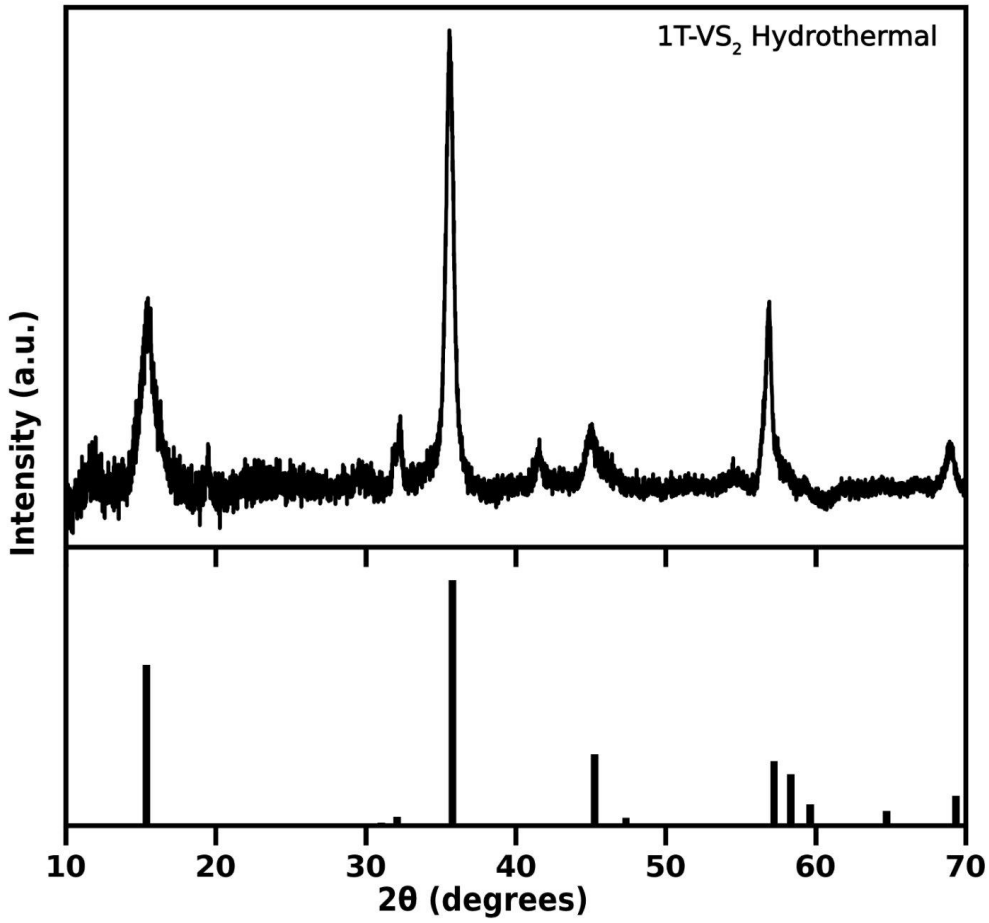


Figure 7. The XRD pattern obtained from VS_2 produced in a stainless-steel reactor in the presence of NH_3

C-276 may act similarly to NH_3, which enables the low temperature degradation of thioacetamide[31]. Higher quantities of available sulfur in the solution would likely favour the production of VS_4, while lower quantities favour VS_2. Supporting evidence for this behaviour was obtained by using a nested sub-reaction vessel made of borosilicate glass which isolated the reaction solution from the C276 alloy reactor walls without the presence of ammonia. The sub-reaction vessel produced a mix of VS_2 and VS_4 (Figure 8). Some contact is still expected between the reactant vapours and reaction walls; however the reduced contact appears to have permitted for the partial production of both materials.

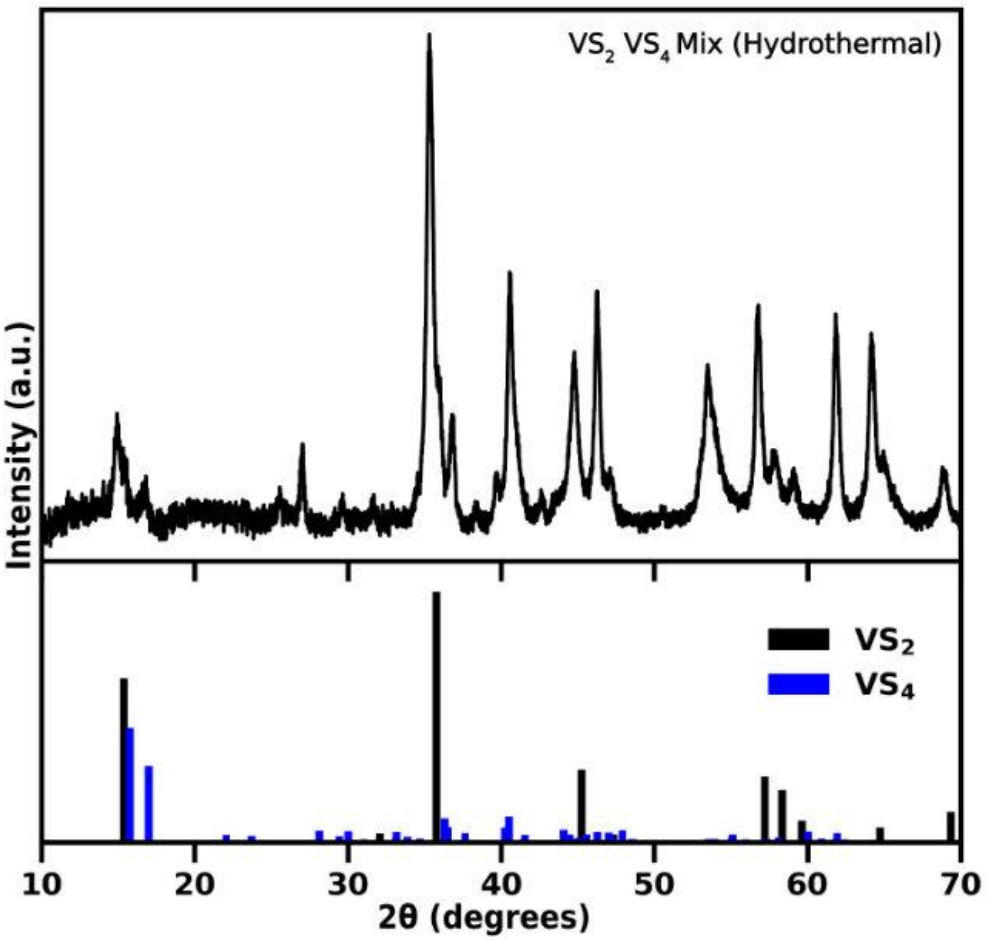


Figure 8. XRD of a mixture of VS_4 and VS_2 produced in a nested C276 reactor without the presence of NH_3.

The possibility of intercalation of materials from the C276 reactor causing the production of VS_4 was checked via EDX and SEM (Figure 9), showing no evidence of the presence of materials other than vanadium, sulfur and potentially oxygen from oxidised VS_4.

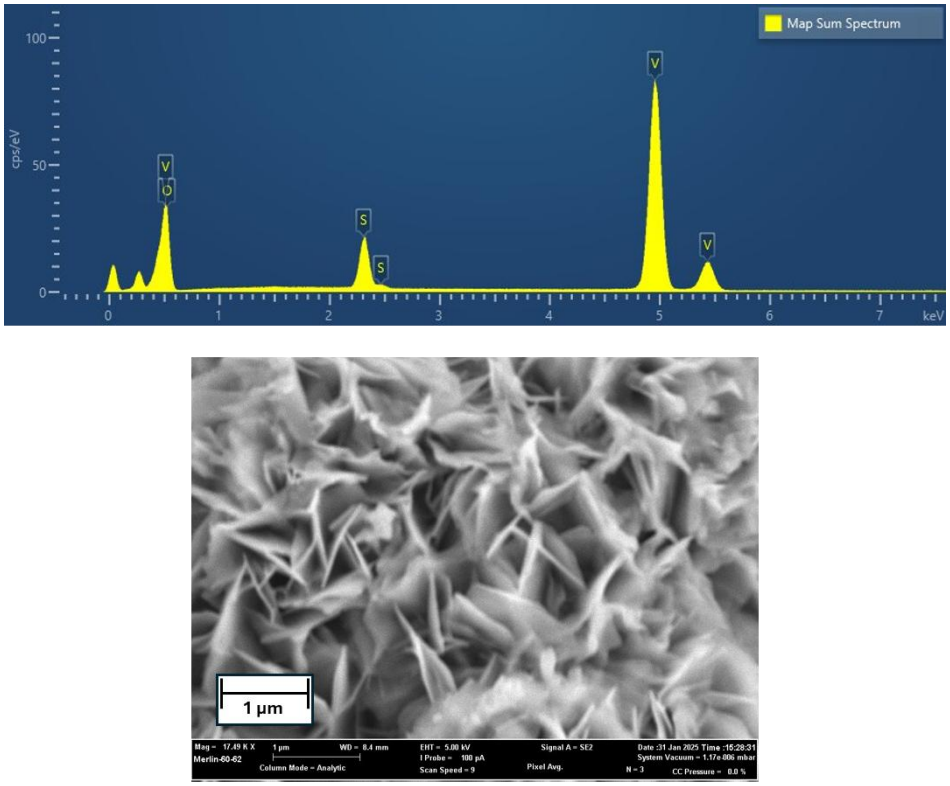


Figure 9. EDX (top) and SEM (bottom) of the VS_4 sample produced in the C276 reactor. The EDX shows no evidence of materials other than vanadium, sulfur and the possible presence of oxygen, which likely arises from the oxidation of the VS_4 material.

While isolating the reactor wall from the solution allowed for the production of VS_2, the production of VS_4 could not be prevented in the C276 reactor. It is therefore important to recognise that the role of the components in the reactor may not be limited to the parts that are in contact with the solution. It is essential to ensure all system components consist of materials that will not affect the reaction. For this system, stainless steel is well examined in the literature[13,32] and is recommended for use.

A.3.2 Improving hydrothermal VS_2 crystallinity and purity

Literature[13,32] and experimental evidence indicate a trade-off between VS_2 crystallinity and purity in hydrothermal synthesis. Figure 7 shows the XRD of the produced material in a stainless-steel reactor with NH_3, which yields almost solely VS_2, however the crystallinity is

low, as shown by the broad peaks in the pattern. Particularly of interest are the peaks from 55-60°, which should show as three distinct peaks, but appear as a single asymmetric peak. By contrast, high-sulfur reactions, such as the mixed production of VS_2 and VS_4 can produce high crystallinity materials, such as in the nested reactor synthesis of VS_2 and VS_4. Further evidence can be seen from a high-sulfur reaction in the stainless-steel reaction vessel, with thioacetamide quantity increased to 37.5 mmol (Figure 10). Out-of-plane peaks (15.3, 58.3°) show broadening but remain well defined, while peaks associated with the basal plane (*a,b* axis) are narrower still, indicating better crystallinity.

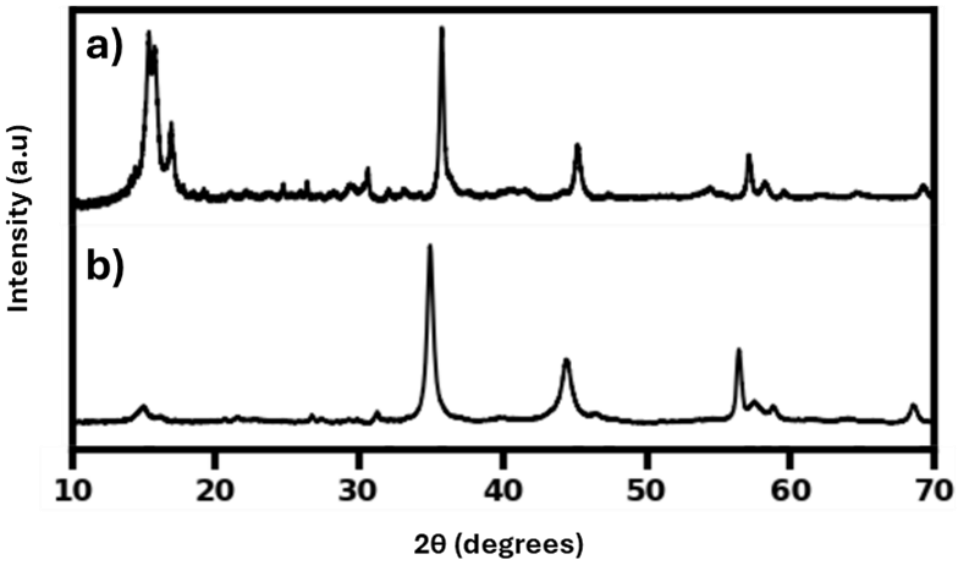


Figure 10. XRD of various produced materials. (a) shows the XRD pattern of a mixed VS_2 and VS_4 sample produced in a 37.5 mmol thioacetamide (sulfur rich) solution while (b) shows the pattern resulting from a 25 mmol solution with CTAC added.

While adjusting reaction parameters offers limited improvement, co-catalysts can enhance both crystallinity and purity. CTAC was explored as one such candidate material. CTAC contains a quaternary ammonium group, analogous to NH_3, but with methyl substituents and a long alkyl chain. As such it may be able to act both as a surfactant and as a thioacetamide degradation catalyst. The XRD of the CTAC material in Figure 10 shows improved crystallinity along the

basal plane with sharp, distinct reflections at 55-60° in comparison to the other processes in both steel and C276, where those reflections are broader and less distinct. Nevertheless, the broadening of the peak at 15.3° indicates some crystallinity reduction along the vertical (c) axis. The CTAC assisted process also appeared to reduce the VS_4 contamination, with the peaks from VS_4 not appearing in the XRD pattern. Despite the improved crystallinity and purity, VS_4 contamination was still observed with long Raman exposure (Figure 11), indicating production of trace quantities of VS_4.

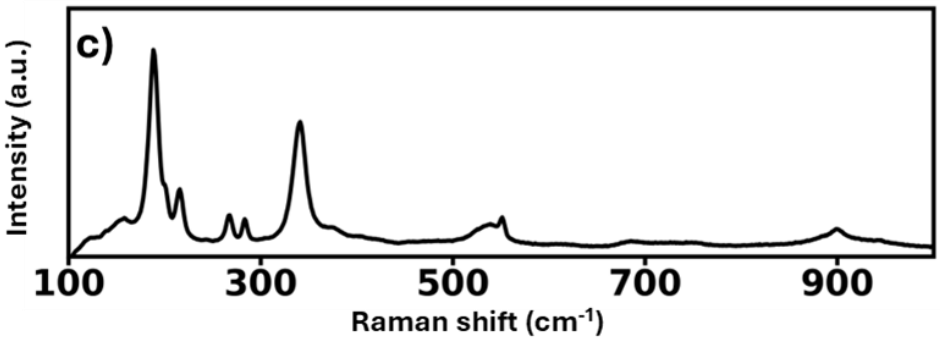


Figure 11. Raman spectrum of CTAC growth-assisted VS_2

A.4 Conclusion

High-purity and crystallinity vanadium disulfide was synthesised using high temperature solid-state synthesis via lithium intercalation. XRD was used to confirm the structure, however Raman under argon atmosphere revealed no apparent Raman spectrum. Reports of VS_2 Raman spectra across the literature were investigated and found to either be V_2O_5 formed from VS_2 oxidised by the Raman laser, typically found for samples made via the hydrothermal synthesis method, or to be V_5S_8, typically from samples formed via high temperature CVT and difficult to distinguish from VS_2 when lab-XRD with low resolution is used, due to the poor response from low-mass thin films.

Finally, insight was gained into the presence of VS_4 contamination in the hydrothermal synthesis of VS_2. The role of C276 alloy in accelerating the production of VS_4 was suggested, and subsequently, CTAC was demonstrated as an effective co-catalyst that improves both the crystallinity and purity of the VS_2.

A.5 References

(1) Mandal, A.; Yadav, A. K.; Pandey, S. K.; Chakrabarti, S. Fabrication of 1T VS2 Electrode-Based In-Plane Micro-Supercapacitor Using a Cost-Effective Mask-Assisted Printing Technique. *Phys. Status Solidi A* **2023**, *220* (20), 2300274. https://doi.org/10.1002/pssa.202300274.

(2) Liang, H.; Shi, H.; Zhang, D.; Ming, F.; Wang, R.; Zhuo, J.; Wang, Z. Solution Growth of Vertical VS2 Nanoplate Arrays for Electrocatalytic Hydrogen Evolution. *Chem. Mater.* **2016**, *28* (16), 5587–5591. https://doi.org/10.1021/acs.chemmater.6b01963.

(3) Hossain, M.; Wu, J.; Wen, W.; Liu, H.; Wang, X.; Xie, L. Chemical Vapor Deposition of 2D Vanadium Disulfide and Diselenide and Raman Characterization of the Phase Transitions. *Adv. Mater. Interfaces* **2018**, *5* (16), 1800528. https://doi.org/10.1002/admi.201800528.

(4) Avilés, M. O.; Jelken, J.; Lagugné-Labarthet, F. Periodic Spiral Ripples on VS_2 Flakes: A Tip-Enhanced Raman Investigation. *J. Phys. Chem. Lett.* **2022**, *13* (41), 9771–9776. https://doi.org/10.1021/acs.jpclett.2c02555.

(5) Mulazzi, M.; Chainani, A.; Katayama, N.; Eguchi, R.; Matsunami, M.; Ohashi, H.; Senba, Y.; Nohara, M.; Uchida, M.; Takagi, H.; Shin, S. Absence of Nesting in the Charge-Density-Wave System 1T-VS2 as Seen by Photoelectron Spectroscopy. *Phys. Rev. B* **2010**, *82* (7), 075130. https://doi.org/10.1103/PhysRevB.82.075130.

(6) Lee, S.-H.; Chang Park, Y.; Chae, J.; Kim, G.; Jin Kim, H.; Ki Choi, B.; Hak Lee, I.; Jun Chang, Y.; Chun, S.-H.; Jung, M.; Seo, J.; Lee, S. Strong Electron–Phonon Coupling Driven Charge Density Wave States in Stoichiometric 1T-VS2 Crystals. *J. Mater. Chem. C* **2022**, *10* (44), 16657–16665. https://doi.org/10.1039/D2TC04186C.

(7) Murphy, D. W.; Cros, C.; Di Salvo, F. J.; Waszczak, J. V. Preparation and Properties of LixVS2. *Inorg. Chem.* **1977**, *16* (12), 3027–3031. https://doi.org/10.1021/ic50178a008.

(8) Masaityte, L. Synthesis and Investigation of MX2 (M = Ti, V, Cr; X = S, Se) as Electrocatalysts for the Hydrogen Evolution Reaction, Ph.D. Thesis, University of Glasgow, 2022.

(9) Rout, C. S.; Kim, B.-H.; Xu, X.; Yang, J.; Jeong, H. Y.; Odkhuu, D.; Park, N.; Cho, J.; Shin, H. S. Synthesis and Characterization of Patronite Form of Vanadium Sulfide on Graphitic Layer. *J. Am. Chem. Soc.* **2013**, *135* (23), 8720–8725. https://doi.org/10.1021/ja403232d.

(10) Lui, G.; Jiang, G.; Duan, A.; Broughton, J.; Zhang, J.; Fowler, M. W.; Yu, A. Synthesis and Characterization of Template-Free VS4 Nanostructured Materials with Potential Application in Photocatalysis. *Ind. Eng. Chem. Res.* **2015**, *54* (10), 2682–2689. https://doi.org/10.1021/ie5042287.

(11) Zagorac, D.; Müller, H.; Ruehl, S.; Zagorac, J.; Rehme, S. Recent Developments in the Inorganic Crystal Structure Database: Theoretical Crystal Structure Data and Related Features. *J. Appl. Crystallogr.* **2019**, *52* (5), 918–925. https://doi.org/10.1107/S160057671900997X.

(12) Wiegers, G. A. Physical Properties of First-Row Transition Metal Dichalcogenides and Their Intercalates. *Phys. BC* **1980**, *99* (1), 151–165. https://doi.org/10.1016/0378-4363(80)90225-9.

(13) Shazad, H. K. A Systematic Approach Towards the Hydrothermal Synthesis of Vanadium Disulfide Nanosheets for Cathode Application in Lithium-Sulfur Battery, Ph.D. Thesis, City University of Hong Kong, 2023.

(14) Binnewies, M.; Glaum, R.; Schmidt, M.; Schmidt, P. *Chemical Vapor Transport Reactions*:; DE GRUYTER, 2012. https://doi.org/10.1515/9783110254655.

(15) Bensch, W.; Koy, J. The Single Crystal Structure of V5S8 Determined at Two Different Temperatures: Anisotropic Changes of the Metal Atom Network. *Inorganica Chim. Acta* **1993**, *206* (2), 221–223. https://doi.org/10.1016/S0020-1693(00)82870-4.

(16) Kawada, I.; Nakano-Onoda, M.; Ishii, M.; Saeki, M.; Nakahira, M. Crystal Structures of V3S4 and V5S8. *J. Solid State Chem.* **1975**, *15* (3), 246–252. https://doi.org/10.1016/0022-4596(75)90209-1.

(17) Moutaabbid, H.; Le Godec, Y.; Taverna, D.; Baptiste, B.; Klein, Y.; Loupias, G.; Gauzzi, A. High-Pressure Control of Vanadium Self-Intercalation and Enhanced Metallic Properties in 1T-V1+xS2 Single Crystals. *Inorg. Chem.* **2016**, *55* (13), 6481–6486. https://doi.org/10.1021/acs.inorgchem.6b00532.

(18) Rousseau, D. L.; Bauman, R. P.; Porto, S. P. S. Normal Mode Determination in Crystals. *J. Raman Spectrosc.* **1981**, *10* (1), 253–290. https://doi.org/10.1002/jrs.1250100152.

(19) Clark, S. J.; Segall, M. D.; Pickard, C. J.; Hasnip, P. J.; Probert, M. I. J.; Refson, K.; Payne, M. C. First Principles Methods Using CASTEP. *Z. Für Krist. - Cryst. Mater.* **2005**, *220* (5–6), 567–570. https://doi.org/10.1524/zkri.220.5.567.65075.

(20) Lahiri, S.; Kumar, M.; Parashar, U. B.; Thangavel, R. Insights into the Magnetic Signature in VS2 Nanosheets for Spintronics Applications: An Experimental and Ab Initio Approach. *Journal of Physics D: Applied Physics* **2024**, *57* (48), 485306.

(21) Ji, Q.; Li, C.; Wang, J.; Niu, J.; Gong, Y.; Zhang, Z.; Fang, Q.; Zhang, Y.; Shi, J.; Liao, L.; Wu, X.; Gu, L.; Liu, Z.; Zhang, Y. Metallic Vanadium Disulfide Nanosheets as a Platform Material for Multifunctional Electrode Applications. *Nano Lett.* **2017**, *17* (8), 4908–4916. https://doi.org/10.1021/acs.nanolett.7b01914.

(22) Yuan, J.; Wu, J.; Hardy, W. J.; Loya, P.; Lou, M.; Yang, Y.; Najmaei, S.; Jiang, M.; Qin, F.; Keyshar, K.; Ji, H.; Gao, W.; Bao, J.; Kono, J.; Natelson, D.; Ajayan, P. M.; Lou, J. Facile Synthesis of Single Crystal Vanadium Disulfide Nanosheets by Chemical Vapor Deposition for Efficient Hydrogen Evolution Reaction. *Adv. Mater.* **2015**, *27* (37), 5605–5609. https://doi.org/10.1002/adma.201502075.

(23) M. Masikhwa, T.; Barzegar, F.; K. Dangbegnon, J.; Bello, A.; J. Madito, M.; Momodu, D.; Manyala, N. Asymmetric Supercapacitor Based on VS2 Nanosheets and Activated Carbon Materials. *RSC Adv.* **2016**, *6* (45), 38990–39000. https://doi.org/10.1039/C5RA27155J.

(24) Zhou, J.; Wang, L.; Yang, M.; Wu, J.; Chen, F.; Huang, W.; Han, N.; Ye, H.; Zhao, F.; Li, Y.; Li, Y. Hierarchical VS2 Nanosheet Assemblies: A Universal Host Material for the Reversible Storage of Alkali Metal Ions. *Adv. Mater.* **2017**, *29* (35), 1702061. https://doi.org/10.1002/adma.201702061.

(25) Guo, Z.; Yang, L.; Wang, W.; Cao, L.; Dong, B. Ultrathin VS2 Nanoplate with In-Plane and out-of-Plane Defects for an Electrochemical Supercapacitor with Ultrahigh Specific Capacitance. *J. Mater. Chem. A* **2018**, *6* (30), 14681–14688. https://doi.org/10.1039/C8TA03812K.

(26) Baddour-Hadjean, R.; Smirnov, M. B.; Smirnov, K. S.; Kazimirov, V. Y.; Gallardo-Amores, J. M.; Amador, U.; Arroyo-de Dompablo, M. E.; Pereira-Ramos, J. P. Lattice Dynamics of β-V2O5: Raman Spectroscopic Insight into the Atomistic Structure of a High-

Pressure Vanadium Pentoxide Polymorph. *Inorg. Chem.* **2012**, *51* (5), 3194–3201. https://doi.org/10.1021/ic202651b.

(27) Shvets, P.; Dikaya, O.; Maksimova, K.; Goikhman, A. A Review of Raman Spectroscopy of Vanadium Oxides. *J. Raman Spectrosc.* **2019**, *50* (8), 1226–1244. https://doi.org/10.1002/jrs.5616.

(28) Zibrov, I. P.; Filonenko, V. P.; Lyapin, S. G.; Sidorov, V. A. The High Pressure Phases β- and δ-V2O5: Structure Refinement, Electrical and Optical Properties, Thermal Stability. *High Press. Res.* **2013**, *33* (2), 399–408. https://doi.org/10.1080/08957959.2013.796375.

(29) Poddar, P.; Rastogi, A. K. Metastability and Disorder Effects in Nonstoichiometric VS2. *J. Phys. Condens. Matter* **2002**, *14* (10), 2677. https://doi.org/10.1088/0953-8984/14/10/317.

(30) Shi, H.; Gao, Z.; Fan, Z.; Ding, Y.; Qiao, Y.; Zhu, Z. Corrosion Behavior of Alloy C-276 in Supercritical Water. *Adv. Mater. Sci. Eng.* **2018**, *2018* (1), 1027640. https://doi.org/10.1155/2018/1027640.

(31) Peters, D. G.; Salajegheh, A. Spectrophotometric Study of the Ammonia-Thioacetamide Reaction. *Anal. Chem.* **1966**, *38* (13), 1824–1828. https://doi.org/10.1021/ac50155a037.

(32) Zhan, W.; Liu, G.; Lang, L.; Gao, X.-S.; Zheng, B.; Zhang, J.; Luo, G.; Hu, L.; Chen, W. Sulfur Vacancy Riched Pure 2H Phase VS2 for Efficient Electrocatalytic Hydrogen Evolution. *J. Electroanal. Chem.* **2024**, *971*, 118609. https://doi.org/10.1016/j.jelechem.2024.118609.